TECHNISCHE UNIVERSITÄT MÜNCHEN

Lehrstuhl für Nanoelektronik

Scalable Thin-Film Manufacturing Technologies for Organic Electronics

Alaa Abdellah

Vollständiger Abdruck der von der Fakultät für Elektrotechnik und Informationstechnik der Technischen Universität München zur Erlangung des akademischen Grades eines

Doktor-Ingenieurs

genehmigten Dissertation.

Vorsitzender:	Univ.-Prof. Dr.-Ing. habil. Dr. h.c. Alexander W. Koch	
Prüfer der Dissertation:	1.	Univ.-Prof. Paolo Lugli, Ph.D.
	2.	Prof. Aldo Di Carlo, Università degli Studi di Roma "Tor Vergata", Italien

Die Dissertation wurde am 25.01.2012 bei der Technischen Universität München eingereicht und durch die Fakultät für Elektrotechnik und Informationstechnik am 28.03.2012 angenommen.

To my mother, Soheir Mansour,
my father, Galal Abdellah,
and my brother, Amr Abdellah.

Thank you for your continuous support, encouragement, and patience.

Table of Contents

Abstract

The interest in novel electronic devices based on organic semiconducting materials has dramatically increased due to the great potential of this new technology for a wide range of engineering applications. Throughout the last decades, research in the field of solution-processable organic electronics has primarily targeted the development of more efficient and stable materials along with the optimization of parameters and conditions within common techniques, with the aim of achieving more competitive device performance. The development of novel processing technologies required for enabling industrial-scale, large-area and high-throughput manufacturing were consequently given less attention among researchers. However, it is only through continuous and simultaneous development of scalable processing technologies that rapid product development and prototyping of organic electronic components can be granted. Here we introduce a generalized framework for the development of innovative processing technologies suitable for scalable manufacturing of solution-processable organic thin-film electronics.

We focus on three promising technologies, nanoimprint lithography, transfer printing, and spray deposition, rendering the core of this thesis. Their evaluation is performed within the context of application to polymer and carbon nanotube (CNT) thin-film technologies. Nanoimprint lithography is utilized for direct patterning of the photoactive polymers on a nanometer scale. A simple and reliable transfer printing process is developed to enable a solvent-free deposition of organic semiconducting thin-films for the fabrication of bilayer/multilayer based device architectures. Further, a scalable spray deposition process is developed for the fabrication of various polymer thin-films which are primarily incorporated into organic photodetectors. The same process is successfully applied to the fabrication of highly uniform CNT thin-films with extremely low surface roughness. Such CNT films can be transfer printed onto flexible plastic substrates in cases where direct deposition is problematic. Finally, spray deposited CNT films are incorporated as resistive elements in gas sensing devices, exhibiting high sensitivities for different test gases.

Chapter 1

Introduction

The discovery of conducting polymers in the 1970s paved the way for a variety of new applications. Recognizing it with the 2000 Nobel Prize in Chemistry indicates its importance to science and technology. One of the most significant fields attributed to this discovery is now referred to as organic electronics. Similarly, carbon nanotubes (CNTs) have been gaining increasing importance to the field of printed electronics ever since their discovery in 1991. Using organic materials as an alternative for, or in combination with, conventional inorganic semiconductors gives rise to new electronic, optical and mechanical properties for novel devices.

1.1 Background and Motivation

In recent years research and development in the field of organic electronics have experienced great advances. The interest in novel electronic devices based on organic semiconducting materials has dramatically increased due to the great potential of this new technology for a wide range of engineering applications [1–5].

Components based on organic semiconductors are diverse and include light emitting diodes [6], [7], solar cells [8–10], thin-film transistors [11–13], sensors [14–18]and more. Several examples of products containing organic thin-film electronics are shown in Fig. 1.1, demonstrating at the same time its capability of being processed on flexible substrates. Especially in the field of optoelectronics, organic materials seem to be very attractive for research and industry. This becomes clear when considering that the first

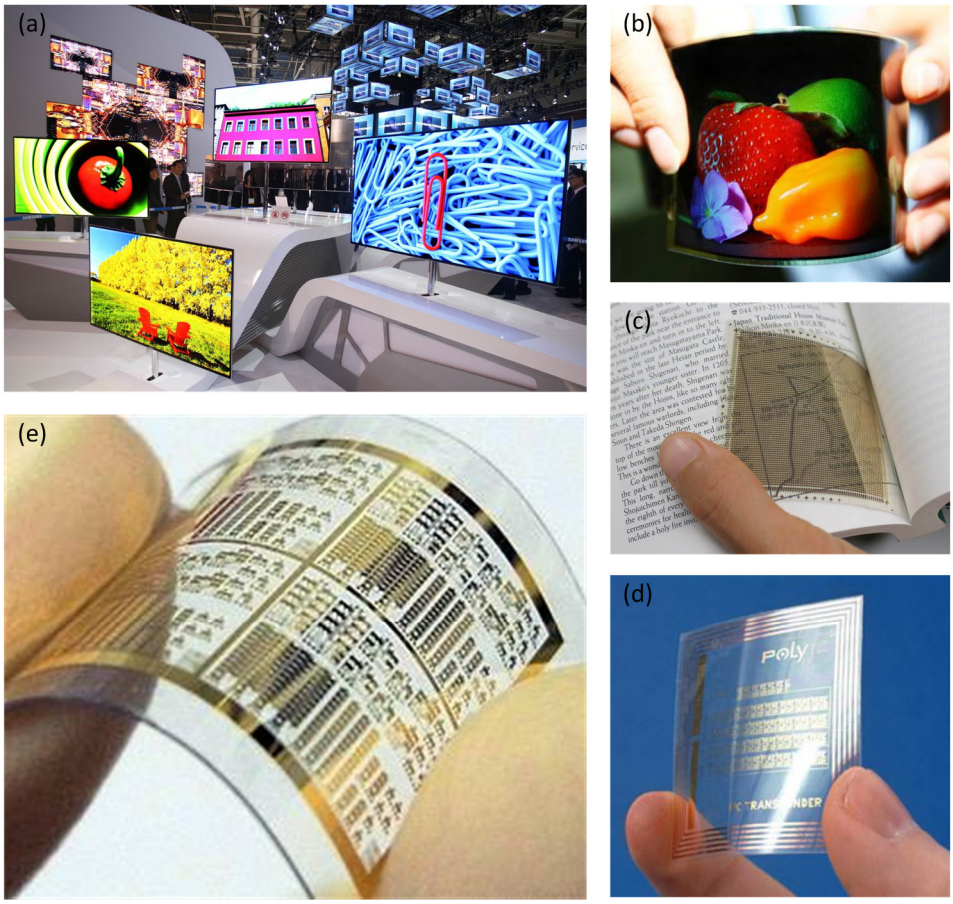

Figure 1.1: Examples of products containing organic thin-film electronics. (a) Largest (55") commercialized OLED TV introduced by Samsung at the CES 2012. (b) Samsung Mobile Display introduces a 4.5" flexible AMOLED display with WVGA resolution at the FPD-International 2010. (c) Photo of a sheet image scanner that can conform to the bent page of a book (Takao Someya Group, University of Tokyo) (d) Printed RFID tag from PolyIC GmbH. (e) Photograph of a CNT-based integrated circuit deposited on a plastic support (NPG Asia Materials featured highlight).

commercial products available belong to the class of optoelectronic devices, e.g. OLED displays for different portable electronic devices [3].

Certainly, one of the strongest advantages of organic technologies is their promise for low-cost and large-area fabrication [2]. Being able to manufacture electronic components on flexible plastic substrates by simple coating and printing techniques is not only a fascinating vision, but also interesting from an economic point of view. Solution-processable thin-film electronics have the potential to fulfill these requirements in addition to providing the possibility of chemical tailoring, allowing flexibility in the synthesis of organic materials with desired properties. In the following some of the most attractive features of this technology are summarized:

- potential to be flexible and semitransparent,
- potential to be manufactured in a continuous low-cost printing process,
- potential for large-area manufacturing,
- easy integration in different devices,
- significant cost reduction compared to traditional solutions,
- substantial ecological and economic advantages.

The key factors for commercial success of organic electronic components are efficiency, lifetime and cost [19]. Efficiency and lifetime are generally inferior when compared to traditional inorganic devices and are therefore at the same time major drawbacks. Hence, most research conducted so far has been driven by the motivation to overcome these problems. It is worth mentioning that some state-of-the-art organic devices already provide sufficient performance for certain applications. However, a major issue of equal importance, which has been largely neglected in literature, is the processing technology enabling industrial-scale, large-area and high-throughput manufacturing. It is only through the development of scalable processing technologies that rapid product development and prototyping of solution-processable thin-film electronics can be granted, thereby targeting the missing aspect of cost.

1.2 Outline of the Thesis

As mentioned in the previous section, one of the most promising prospects of solution-processable organic electronics lies in the high potential of low-cost, large-scale fabrication and integration of various components onto rigid or flexible substrate materials. The main aim of this thesis is to present a generalized framework for the development of innovative processing technologies suitable for scalable manufacturing of solution-processable thin-film electronics. It is therefore necessary to gain insight into the working principles of different film formation and film modification techniques and evaluate their performance within the context of selected device applications.

The significance of scalable processing technologies for rapid product development and prototyping is discussed in Chapter 2. We briefly describe some of the common techniques suitable for small to medium-scale film deposition. Different film deposition as well as film patterning techniques are then classified according to a proposed scheme, while highlighting the three core processing technologies, nanoimprint lithography, transfer printing, and spray deposition, utilized and developed within this work.

In Chapter 3, we use thermal and room-temperature nanoimprint lithography (NIL) for directly patterning the photoactive polymer poly(3-hexylthiophene-2,5-diyl) (P3HT) in the sub-50-nm region. Good pattern transfer is achieved independent of the presence of other underlying polymer layers or the type of substrate incorporated. Further, we discuss the future application of nanoimprint technology to the fabrication of ordered heterojuction organic photosensitive devices and demonstrate that the NIL process involved does not damage the polymer or alter its chemical or electrical properties. Additionally, in order to exploit any possible efficiency enhancement via controlled patterning of the active layer in organic photosensitive devices, a simple and reliable transfer printing process is developed to enable a solvent-free deposition of organic semiconducting thin-films for the fabrication of bilayer/multilayer based device architectures.

One very promising, yet little examined, deposition technique compatible to large-area industrial-scale processes is provided by spray technology. In Chapter 4 we present a detailed investigation on the layer formation process during spray deposition of organic thin-films and its relation to solution properties and process parameters. The technological framework developed here is successfully applied to the fabrication of organic photo-detecting devices as well as organic thin-film transistors. Moreover, we report an alternative approach for the preparation of organic heterojunction photoactive layers by successive spray deposition of the donor material and acceptor material. It is shown that organic photodiodes comprising photoactive layers prepared using this fabrication method exhibit a performance comparable to conventional BHJ devices in which the active layer is rigorously blended in advance. Separate handling of the individual materials and their deposition from distinct solutions enables an enhanced control of the active layer composition and hence increases the ability of tuning device characteristics.

In Chapter 5, we demonstrate a reliable and reproducible spray deposition process for the fabrication of highly uniform CNT films exhibiting state-of-the-art performance. CNT films with average surface roughness as low as 5.8 nm are presented. A good trade-off between sheet resistance and transmittance is achieved with best films having 100 Ω/sq at 80 %. Further, a transfer printing process is introduced for the fabrication of CNT thin-films on plastic. A comparison to films fabricated by direct spray deposition onto the same type of substrate material is conducted. Incorporating this kind of high quality films as resistive networks for gas detection in gas sensors, yields devices with high sensitivities. We report CNT-based gas sensors with exceptionally high sensitivities and fast response to various test gases. Highly uniform CNT thin-films, prepared using a reliable and reproducible low-cost spray deposition process, are utilized as resistive networks for gas detection. Sensors show a clear and immediate change in resistance as a response to test gas exposure.

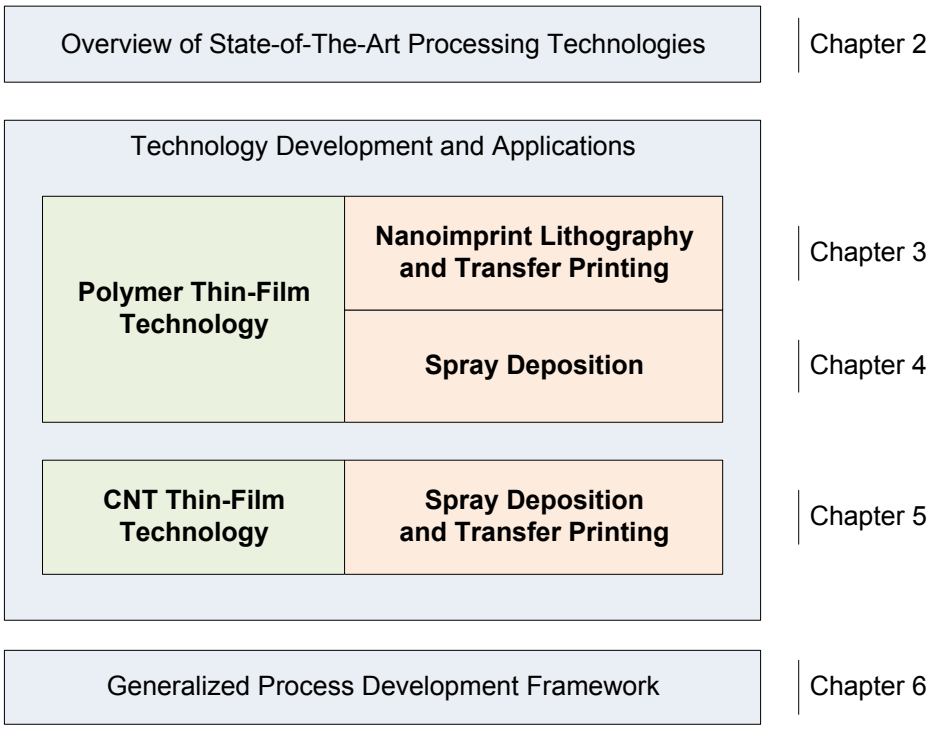

Figure 1.2: Chart summarizing the general structure of the thesis, based on the main research plan followed throughout the work carried out here. It depicts the three scalable processing technologies central to the thesis, applied to the fields of polymer and carbon nanotube thin-film technology.

Some major aspects of processes involved in manufacturing of solution-processable organic thin-film devices are discussed in Chapter 6, where we present a generalized framework for process development. This framework is developed based on the know-how accumulated from all individual processes previously presented as well as literature. An example of use is given for the development of a process for the fabrication of electronic devices based on CNT thin-films deposited from solution.

Conclusions and an outlook on future work are finally presented in Chapter 7. The main findings are summarized here, while some novel ideas relevant to the continuation of this work are introduced. The general structure of the thesis is summarized in the simplified chart illustrated in Fig. 1.2, which was created based on the main research plan followed throughout the work carried out here.

Chapter 2

Processing Technology and Scalability

In this chapter, the significance of scalable processing technologies for rapid product development and prototyping is discussed. In this context, some essential manufacturing differences between conventional and solution-processable thin-film electronics are presented. We briefly describe some of the common techniques suitable for small to medium-scale film deposition. Different film deposition and film patterning techniques are classified according to a proposed scheme, while highlighting the three core processing technologies utilized and developed within this work, nanoimprint lithography, transfer printing, and spray deposition. Their general working principles are presented in order to acquire some fundamental understanding necessary for their subsequent evaluation.

2.1 General Aspects of Processing

In the early development phases of a new technology most efforts are focused on few particular aspects related to the improvement of essential performance figures as well as establishing a fundamental understanding of underlying working principles. Throughout the last decade research in the field of solution-processable organic electronics has primarily targeted the development of more efficient materials along with the optimization of process-specific parameters and conditions necessary to achieve higher, more competitive device performance within a given application [20–22]. Additionally, there has been continuously growing interest in material stability, as in to increase operational lifetime of the corresponding devices [19], [23–25]. Research efforts underlining the progress in these two major aspects of development, efficiency and lifetime, can be justified by their significance for a successful commercialization. However, a third major

aspect of equal importance, which has been largely neglected, is the processing technology required to enable industrial-scale, large-area and high-throughput manufacturing. This is somehow surprising, considering that the main concept, on which the entire field of solution-processable organic electronics relies, is the prospect of low-cost, large-scale fabrication and integration of various components onto rigid or flexible substrate materials. Hence, waiting for materials and components to reach sufficient efficiency and lifetime before targeting the aspect of reliable and reproducible processing is counterproductive. It is only through the continuous and simultaneous development of scalable processing technologies that rapid product development and prototyping of organic electronics can be granted.

2.1.1 Differences in Manufacturing

There are several essential manufacturing differences between conventional and solution-processable organic electronics. In general, these distinctive differences apply to printed electronics of any category, whether based on organic, inorganic, or hybrid materials. While manufacturing of conventional electronics relies largely on subtractive processing, printing and coating techniques used in manufacturing of printed electronics are additive processes [26]. Subtractive processing involves process steps with considerable material consumption, such as lithography and etching. These processes inherently generate large amounts of waste. The omission of such steps in additive processing reduces material consumption and waste, which offers cost reduction in addition to obvious environmental benefits. An overview of the most important differences is given in Table 2.1.

2.1.2 Common Film Deposition Techniques

Although many different film deposition techniques are well known and developed, only a limited selection has been widely explored in the fabrication of solution-processable organic electronics [4], [19]. One of the main reasons for this is associated with the fact that many of the techniques with high-volume production capability consume large amounts of material, rendering them unsuitable for adoption in small-scale research laboratory environments. Moreover, achieving good reproducibility in short runs can be rather complicated with some of these techniques. The most widely explored and used methods are therefore ones which are practical for small-scale processing of individual samples. Typical examples are spin-coating, doctor-blading, and simple casting. Spin-coating, being a standard technique employed in manufacturing of conventional electronics, is without doubt the most commonly used in most research laboratories. The techniques selected and discussed in this section are predominantly suitable for sheet-fed processing. More deposition techniques, including ones purely relying on web-fed (roll-to-

	Conventional Electronics	Organic Electronics
General Approach	Subtractive	Additive
Operation Mode	Batch, long production runs	Continuous, short production runs
Conditions	High temperature, low pressure	Moderate temperature, atmospheric pressure
Substrate Type	Limited	Variable (rigid/flexible)
Process Environment	Cleanroom, highly controlled	Ambient, partially controlled
Cost	High initial cost, high operational cost	Low initial cost, low operational cost

Table 2.1: Overview of major differences in manufacturing of conventional electronics and novel solution-processable organic electronics.

roll) processing, are reviewed extensively in an article by Krebs [19]. While sheet-fed processing originally refers to individual sheets of paper being fed into a press, web-fed processing refers to the use of rolls of paper continuously supplied. In general, sheet-fed processes offer higher flexibility regarding sheet size and format, whereas web-fed processes are faster and more suitable for large runs. In the following we briefly describe four common techniques, which are representative for small to medium-scale deposition. A photograph of the equipment required for each of the four techniques can be found in Fig. 2.1.

Spin-Coating

Spin-coating provides a highly reproducible process to apply uniform thin-films to flat substrates. It is extensively used in the microelectronics industry during application of photoresists to silicon wafers [27]. Despite the underlying complexity of the film formation process, deposition of highly uniform films can be achieved on substrates with diameters of up to a few tens of centimeters. Typically the process of spin-coating involves the application of an excess amount of solution onto the substrate to be coated, which is then rotated at high speeds to achieve uniform spreading of the fluid. The characteristics of the final film, such as thickness and surface topography, are highly reproducible for the same material, given that solvent and material concentration are fixed. Achieving the desired film specifications can be challenging, since the tunable range of thickness and surface

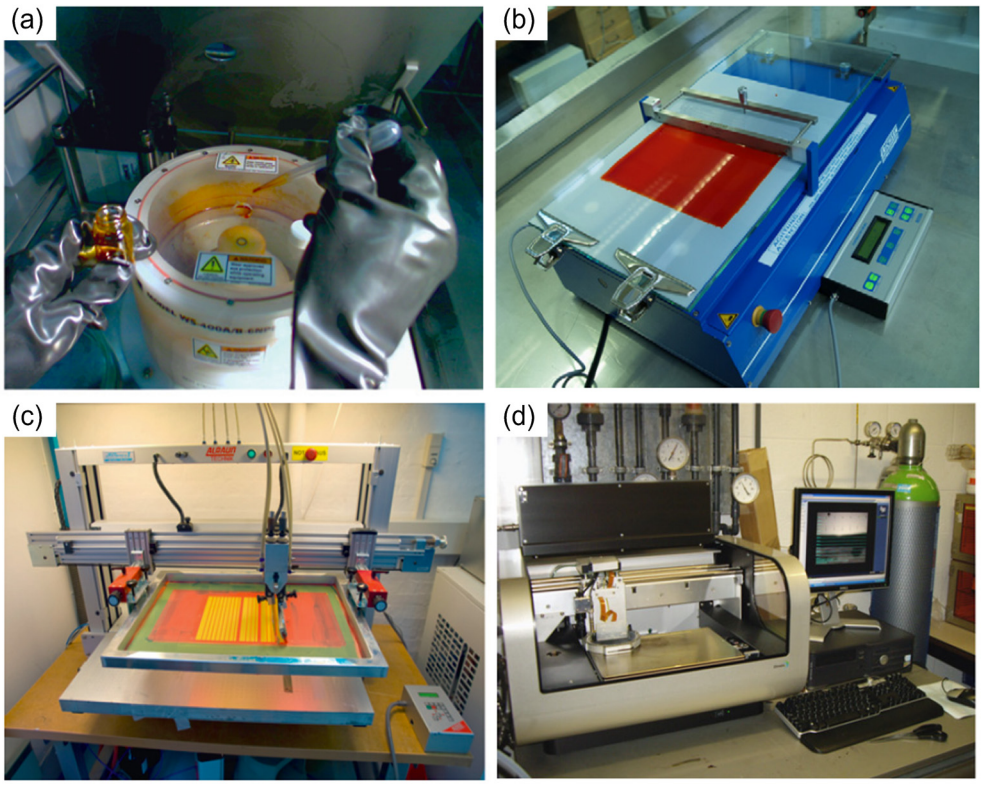

Figure 2.1: Photographs of the equipment required for four of the most commonly employed film deposition techniques, spin-coating (a), doctor-blading (b), screen printing (c), and inkjet printing (d) [19].

topography is limited and strongly dependent on processing parameters and solution properties. Rotational speed, fluid viscosity, volatility of the chosen solvent, molecular weight of the material, and concentration of the solution are factors of influence [28]. In general, it can be difficult to achieve high film thicknesses, which is desired in certain applications. Examples are given in Chapter 4 for the photoactive layer in organic bulk heterojunction photodetectors and in Chapter 5 for carbon nanotube (CNT) thin-films, where spin-coating is only useful for generating films of a few monolayers due to the typically low viscosity of CNT solutions. Another problem of spin-coating is the ejection of most of the applied solution during the film formation process, where roughly 90 % of the material is wasted. Nevertheless, due to the small volume of solution required to process individual small-scale samples, this deposition technique has been successfully applied to the field of solution-processable electronics in many research laboratories.

Doctor-Blading

Doctor-blading, also referred to as tape-casting, is a widely used deposition technique for producing thin-films on large-area surfaces. In contrast to spin-coating, this technique has been only marginally studied within the context of printed organic electronics [29], [30]. It is considered to be very economical in terms of material consumption, since losses in

solution can reach down to 5 %. The basic setup involves a sharp blade placed at a fixed distance from the substrate surface to be coated. When a constant relative movement between blade and substrate is introduced, the coating solution placed on the substrate beyond the blade is spread out to form a thin wet film of the coating material. Typically, the blade represents the moving part of the setup, whereas the substrate is stationary. The thickness of the resulting wet film depends mostly on the gap height between blade and substrate as well as solution and surface properties. While it is possible to obtain uniform films even with small amounts of material, finding reasonable processing parameters is time consuming and results in a large initial loss of coating solution. Thus it does not offer any substantial advantages over spin-coating, except when higher film thicknesses are required. Note however that doctor-blading can be readily adapted from a sheet-fed process to a web-fed (roll-to-roll) process, where it is termed knife-over-edge coating.

Screen Printing

Screen Printing is a rather inexpensive and versatile printing technique that consumes little amounts of material with almost no loss of coating solution. It requires high viscosity, low volatility coating solutions and produces wet films with relatively large thicknesses compared to other coating and printing techniques. The process typically involves a woven mesh to support an ink-blocking stencil, which forms open areas of mesh permeable to the printing material. A coating solution is filled onto the screen stencil and brought into proximity of the substrate. By moving a so-called squeegee linearly across the screen, material is forced or pumped through the threads of woven mesh in the open areas onto the substrate in a manner reproducing the screen pattern. The wet thickness of the coated film depends primarily on the volume between the threads of the mesh and the thickness of the stencil. It varies however with the force applied to the squeegee during coating, the speed of the squeegee and the viscosity of the solution. This technique is currently used in a diversity of fields, ranging from simple printing of text to printing conductors for flexible electronics and keypads. Several reports can be found regarding its use in the context of polymer thin-film electronics as well [31–33]. Although screen printing is inherently operated in a sheet-fed process, it is highly compatible with roll-to-roll (R2R) processes. Rotary screen printing, where the screen is cylindrical with a squeegee on the inside, represents a variation fully adapted to a R2R process. One example of large-scale industrial production of polymer solar cells, where all layers of the device were processed using screen printing was demonstrated by Krebs et al. [20].

Inkjet Printing

Inkjet printing is a non-contact deposition method using an ink jetted repeatedly from a printing head to form small droplets, which can be accurately directed onto the substrate. Recently, industrial inkjet printers offering the possibility to choose from different types of

solvents have become commercially available. Special printing heads resistant to organic solvents enable an employment of this technique in the production of solution-processable organic electronics. One of the main advantages inherent to inkjet printing lies in its capability of generating high resolution patterns (up to 1200 dpi) directly from a digital source image, eliminating the need for any master. The dry film thickness is adjusted through the number of droplets released onto a given area. There are two main modes of operation by which inkjet printing techniques can be classified, continuous-mode (CIJ) and drop-on-demand (DOD). In a CIJ process only a part of the continuously generated stream of droplets is directed to the substrate according to the source image, whereas in a DOD process droplets are only generated if required by the source image. According to the method employed for droplet formation in a DOD printing head, it is possible to further distinguish between thermal, piezoelectric, electrostatic, and acoustic techniques. All this adds constraints on the ink formulations needed to achieve desired droplet characteristics, introducing further complexity to solution preparation. In general, inks are required to be of low viscosity and high surface tension to facilitate droplet formation. There are only few scientific report on the use of inkjet printing in polymer thin-film deposition [34–36]. Recently however, there have been numerous reports about inkjet printing of CNT thin-films [37–39].

2.2 Selected Core Processing Technologies

Three core processing technologies, nanoimprint lithography, transfer printing, and spray deposition, are investigated throughout this work as promising alternatives for scalable manufacturing of solution-processable thin-film electronics. In the following, the general working principles are presented in order to acquire some fundamental understanding. The evaluation within the context of selected applications is however performed in the respective chapter.

2.2.1 Nanoimprint Lithography

A crucial aspect contributing to the advancement of micro- and nanotechnology is the ability to reliably fabricate micrometer and nanometer scale structures in an industrially relevant process. Nanoimprint lithography represents one of the most promising high-throughput techniques for patterning of polymer nanostructures with high reproducibility and at low-cost [40–42]. In contrast to conventional photolithographic techniques, the achievable resolution with nanoimprint lithography is not limited by diffraction. The parallel nature of the process is a clear advantage over time-consuming sequential

alternatives based on particle beam lithography, which are capable of achieving similar feature dimensions.

The working principle of nanoimprint lithography is rather simple and relies on reproducing the topography of a mostly rigid mold containing micro- to nanometer scale surface relief structures. Such a mold is pressed into a polymeric material coated on top of a substrate at controlled pressure and temperature. This creates a thickness contrast in the polymeric material corresponding to a negative of the mold features. Typically, a thin residual layer of the polymeric material remains between mold and substrate, preventing a direct impact of mold and substrate. For most applications this residual layer needs to be removed by reactive ion etching (RIE) to complete the process of pattern definition [41]. Due to its simplicity nanoimprint lithography has been applied to several applications other than nanoelectronic devices based on conventional semiconductor technology, including organic electronics and photonics, which will be discussed in Chapter 3.

Most imprints presented here are performed using a commercially available state-of-the-art 2.5” NIL tool (Obducat, Sweden). To perform an imprint, mold and substrate are stacked onto each other with the polymer coated side facing the surface relief structures. The smaller of the two has to be placed on top, such that damage to the stack under pressure is avoided. After placing the stack into the imprint chamber and sealing it with an aluminum foil to keep it in place during imprint, the setup is heated under slight pressure until the desired imprint temperature is reached. Temperature is adjusted to a value higher than the glass transition temperature T_g of the polymer to be imprinted. The necessary imprint pressure is then applied to the small volume of air inside the imprint chamber while keeping the elevated imprint temperature constant. Pressure and temperature are kept throughout the desired imprint duration. The setup is then cooled down to an appropriate demolding temperature below T_g, before the imprint pressure is released. Finally, after removing the stack from the chamber, mold and substrate are separated again leaving behind the substrate with a patterned polymer layer. A simplified cross-sectional schematic of the imprint chamber including mold/substrate stack is shown in Fig. 2.2(a). The basic steps involved in the nanoimprint process are illustrated in Fig. 2.2(b).

2.2.2 Transfer Printing

Transfer printing is a useful tool in micro- and nanofabrication for transferring a given material from a patterned stamp onto a target substrate [43]. Microcontact printing is a known process where molecules are transferred from a patterned polymethylsiloxane (PDMS) stamp to a substrate by the formation of covalent bonds [44], [45]. A solution of molecules is inked onto the surface of the PDMS stamp, which is then brought into conformal contact with an appropriate substrate. The material is selectively transferred

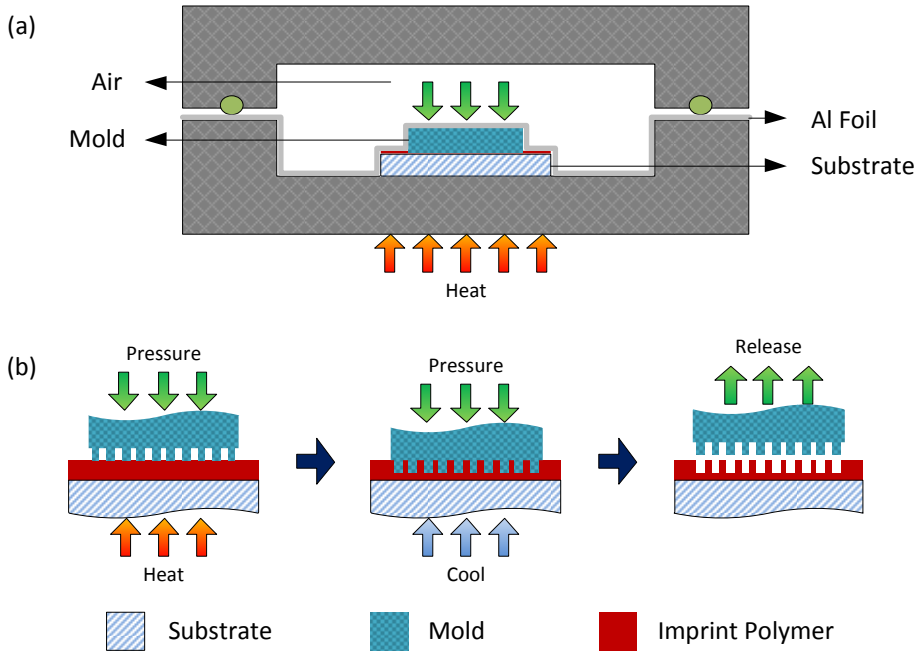

Figure 2.2: (a) A simplified cross-sectional schematic of the imprint chamber including mold/substrate stack, where the necessary imprint pressure is applied to the small volume of air inside the imprint chamber. (b) Illustration of the basic steps involved in nanoimprint lithography.

according to the topography of the stamp. Previously patterned masters used for producing the stamps are prepared lithographically or commercially available templates. The stamp is usually fabricated by pouring an elastomeric solution onto the master, which is then simply peeled off after curing, resulting in a negative replica of the master. Flexibility of the PDMS stamp and its ability to achieve excellent conformal contact with the substrate enable printing over large areas and even curved surfaces. Figure 2.3 shows a schematic of the general steps involved in transfer printing.

The transfer printing process described here involves the transfer of an organic layer from a source substrate to the desired target substrate using a flexible PDMS stamp. Although it is in principle possible to directly deposit the desired organic layer onto the PDMS stamp, this often requires additional treatment in order to render its surface hydrophilic and hence achieve acceptable layer uniformity. An oxygen plasma treatment can be used to alter the surface properties of the PDMS stamp such as to serve this purpose [46]. However, this can damage the surface and introduce cracks [47]which negatively influence the quality of the transferred organic layer. Therefore special care has to be taken when choosing the treatment conditions in order not to damage the PDMS stamp. In addition to any potential damage introduced through the surface treatment, the hydrophobic nature and hence low adhesion of the PDMS surface is a desirable property to achieve reliable and high-yield transfer to any target substrate. For this reason it is beneficial to first deposit the organic

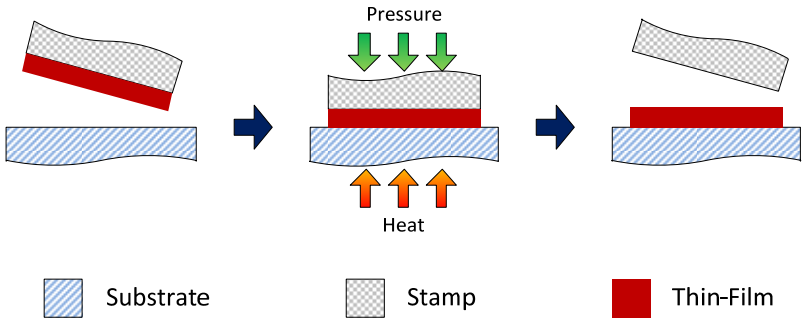

Figure 2.3: A schematic of the general steps involved in transfer printing, where the stamp utilized can either be rigid or flexible. The transfer printing process described here involves transfer of an organic thin-film to a target substrate using a flexible PDMS stamp.

layer onto a temporary glass substrate by spin-coating the corresponding solution using common process parameters, which is then transferred to the PDMS stamp by float-off from the source substrate, which is discussed more detailed in Chapter 3. This approach enables a reliable and reproducible transfer of the organic layer without altering the desirable surface properties of the PDMS stamp.

2.2.3 Spray Deposition

The process of breaking up bulk liquid into droplets is often referred to as atomization. This is usually the process by which a spray, a dispersed stream of droplets, is formed. A spray or atomizer nozzle is a device that enables the formation of this liquid spray. Spray technology is used in a wide variety of applications such as surface coating, humidification, combustion and others. Atomization can be achieved by disintegrating the liquid jet or sheet using the kinetic energy of the liquid itself, by exposure to a high-velocity gas stream, or as a result of mechanical energy. According to the different atomization methods, spray nozzles can be divided into several categories, out of which the following two are of greater interest to our specific application: Air-assisted and Ultrasonic. In the following we will briefly discuss the working principle of each of these atomization concepts.

Air-assisted nozzles, typically referred to as air spray nozzles, rely on a high speed air stream (or any other gas, e.g. N_2) to produce atomization. The fluid, which can be under pressure or fed to the material nozzle by gravity, is mixed at the orifice into the gas stream. The energy contained within the gas stream disrupts the fluid causing atomization. Note that, in airless as well as air-assisted nozzles, atomization is a result of the relative velocity between fluid and air. In airless atomization the air speed is low and the fluid speed high whereas in air-assisted atomization the air speed is high and the fluid speed low. In

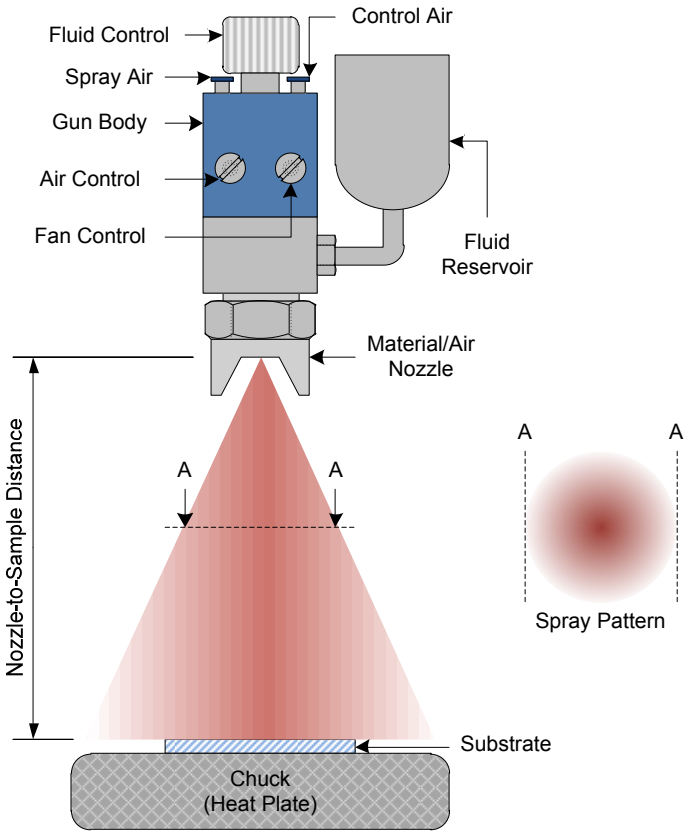

Figure 2.4: Illustration of the implemented experimental setup for spray deposition, showing the basic components and indicating the vertical arrangement of nozzle and substrate. All important elements and controls of the air atomizing spray nozzle are pointed out and labeled, while the typically resulting spray pattern is visualized.

general, air-assisted nozzles are capable of producing finer droplets. Further, the range of flow rates at which fine atomization can be achieved is independent of the fluid pressure, unlike airless atomization. The static experimental spray system implemented here utilizes an automatic air atomizing spray gun (Krautzberger GmbH, Germany) and is illustrated in Fig. 2.4. All important elements and controls of the air atomizing spray nozzle are pointed out and labeled while the typically resulting spray pattern is visualized.

Ultrasonic nozzles utilize an entirely different approach for achieving atomization. The nozzle body vibrates at ultrasonic frequencies based on a piezoelectric transducer which is driven by an electronic power generator. The fluid is delivered through the liquid passage to the atomizing surface (vibrating surface) where a liquid film is formed. This film then becomes unstable causing a mist of small droplets to be ejected from the surface. Hence, the atomization process occurs without applying any direct pressure. By changing the operating frequency, the average droplet size can be controlled, where higher frequencies produce smaller droplets. Frequencies typically range from 25 kHz to 130 kHz.

The performance of any of the spray nozzles described above is strongly dependent on its size and geometry as well as on the physical properties of the liquid being atomized and the gaseous medium surrounding the droplets. For air-assisted nozzles the diameter of the orifice is the most significant dimension for atomization. The physical properties of the liquid being atomized have a direct effect on the flow and spray characteristics of any spray nozzle. Among the most important fluid properties are density, viscosity and surface tension. As most liquids exhibit only minor differences in density, the significance of this property for atomization is rather low. However, considering that density causes a fluid to resist acceleration, higher density tends to result in a larger average droplet size. The fluid's viscosity is a measure for the intermolecular attraction. Higher viscosity is equivalent to a greater attraction, resulting in an increased resistance for molecules to move away from each other, which is exactly what occurs during liquid flow. In general, an increased viscosity tends to hinder any natural instabilities leading to fluid breakup. This results in a delayed disintegration and increased average droplet size in the spray. Surface tension is related to the behavior of molecules lying at or near the interface to a different medium. It is the force acting at the interface to minimize the potential energy of the molecules involved. While water exhibits a very high surface tension of about 72 dynes/cm at 25°C, most other liquids have lower values. In atomization, surface tension plays a very important role because it represents the force resisting the formation of new surface area. Hence it affects the droplet size as well as the spray angle. Fluids with higher surface tension tend to produce sprays with an increased average droplet size and a decreased spray angle.

A comprehensive overview of spray technology can be found in a textbook by Lefebvre [48], covering the general types of atomizers, their applications, and various mechanisms of liquid particle breakup. Additionally, mathematical and empirical relations used to characterize the distribution of drop sizes in a spray are discussed. In a textbook by Lavernia and Wu [49] the current understanding of the science and technology of spray atomization and deposition is assessed. There, a detailed discussion on fundamental principles and the application of spray atomization and deposition to a variety of structural materials are presented. Both textbooks served as a guide for the brief introduction to spray technology presented in this section.

2.2.4 Classification of Different Processing Technologies

To understand the scope of different processing technologies employed in this work and their applicability to various manufacturing settings, it is important to classify them according to certain criteria. Here, processes targeting film deposition and film patterning are of particular interest and hence constitute the primary argument for classification.

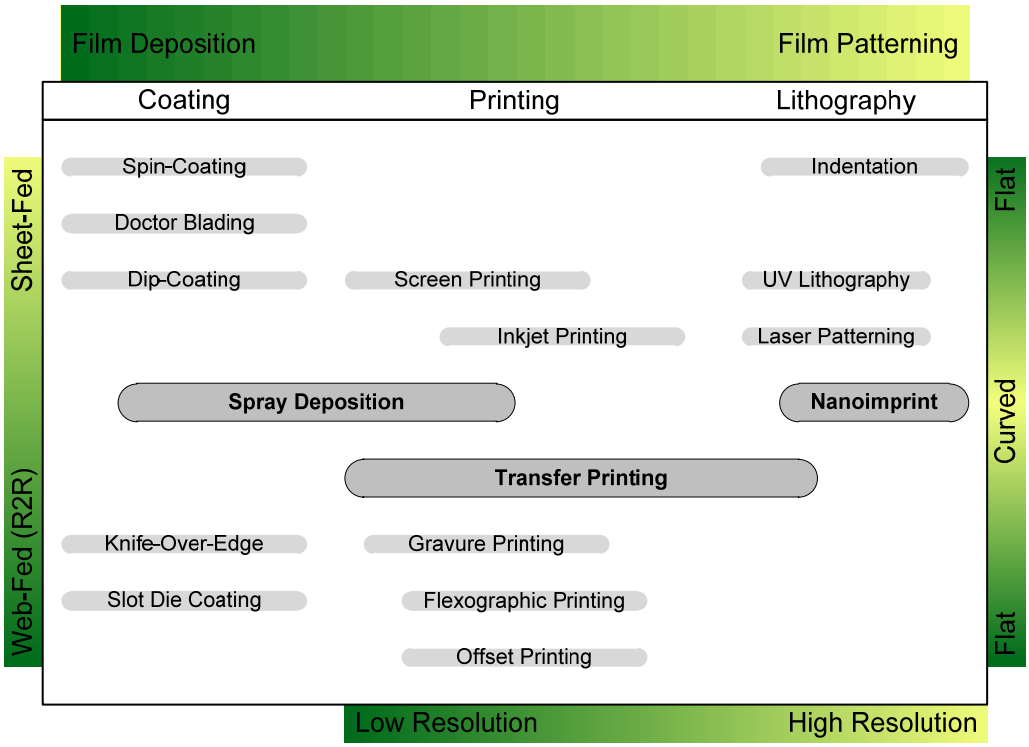

Figure 2.5: An Overview of different film deposition and film patterning techniques according to classification approach presented here. The three core processing technologies utilized and developed within this work are highlighted.

While coating refers to a process of transferring ink to a substrate covering the entire surface, printing additionally implies the formation of a certain pattern as part of the film deposition process. In this context, we define lithographic processes such as to involve techniques of post-deposition pattern formation. It is therefore understandable that a clear separation of film deposition and film patterning is in many cases not possible according to the above mentioned definitions. The amount of overlap between these processes is given by the techniques involved in manufacturing. Further classification can be performed according to the operational mode. Here we distinguish between two operational modes according to the type of substrate feed associated with any given process, which can either be sheet-fed or web-fed. Once again, since several techniques can be operated in any of the two modes with only slight modifications, a certain amount of overlap exists. Figure 2.5 shows an overview of different film deposition and film patterning techniques according to classification scheme presented here. Regarding printing and lithographic techniques, pattern resolution can be an additional argument to be considered for achieving the feature dimensions required for the application under development. Finally, while most techniques are only capable of handling flat substrate surfaces, only few are applicable also to curved substrate surfaces. Such curved substrates can range from simple convex/concave surfaces to arbitrary shaped 3D objects. The three core processing technologies utilized and

developed within this work are highlighted in Fig. 2.5, and were discussed more detailed in the previous sections. One common feature of all three is the capability of sheet-fed and web-fed operation, thereby being suitable for small-scale laboratory as well as large-scale industrial environments. Moreover, all three can handle curved substrate surfaces to different extents, with spray deposition being the most flexible in this context.

2.3 Summary

In this chapter we highlighted the importance of scalable processing technologies for rapid product development and prototyping of solution-processable thin-film electronics. In this context, some essential manufacturing differences between conventional and organic electronics were discussed. We briefly described four common techniques, which are representative for small to medium-scale film deposition. The three core processing technologies, nanoimprint lithography, transfer printing, and spray deposition, investigated throughout this thesis as promising alternatives for scalable manufacturing of solution-processable organic electronics were highlighted and described in more detail. These were then classified along with other film deposition and film patterning techniques according to a proposed scheme.

Chapter 3

Nanoimprint and Transfer Printing

We use thermal and room-temperature nanoimprint lithography (NIL) for directly patterning the photoactive polymer poly(3-hexylthiophene-2,5-diyl) (P3HT) in the sub-50-nm region. Different types of molds were used to directly imprint the desired structures into P3HT thin-films. Good pattern transfer is achieved independent of the presence of other underlying polymer layers or the type of substrate incorporated. Further, we discuss the future application of this technology to the fabrication of ordered heterojuction organic photovoltaic devices and demonstrate that the NIL process involved does not damage the polymer or alter its chemical or electrical properties.

In order however to exploit any possible enhancement through targeted patterning of the active layer in organic photosensitive devices, it is necessary to develop a process for the fabrication of true bilayers in which the integrity of an underlying layer is maintained. A simple and reliable transfer printing process was developed to enable a solvent-free deposition of organic semiconducting thin-films for the fabrication of bilayer/multilayer based device architectures. P3HT and PCBM thin-films were successfully transfer printed using a supporting PDMS stamp.

3.1 Nanoimprint for Polymer Thin-Film Devices

Electronic and optoelectronic devices based on organic semiconductors are increasingly attracting the attention of a steadily growing number of industrial and academic research groups, driven by their potential for low-cost applications with relaxed constraints with respect to their inorganic counterpart [50], [51]. Of special interest are devices based on solution-processable polymeric materials, and among those regioregular poly(3-

hexylthiophene) (P3HT) is one of the most promising conducting polymers with a relatively high electrical conductivity and nonlinear optical properties [52], [53]. Being able to pattern organic materials in the micron range and below is essential: for electronic devices an improvement of device performances in terms of operations speed can be achieved, whereas for optoelectronic devices the interaction between matter and light at the nanometer scale can be further exploited [54], [55]. Unfortunately conventional techniques for achieving micron or sub-micron sized structures are not suitable or present some limitations when applied to organic semiconductors. Different approaches for transferring relief structures into organic materials, for example, are screen printing [56], [57], ink-jet printing [58], [59], soft lithography [60], [61], and nanoimprint lithography [62]. Austin and Chou [63] applied nanoimprint techniques for fabricating 70 nm channel P3HT organic thin-film transistors, but rather than directly patterning the semiconductor, they performed the lithographic step on the SiO_2 constituting the gate-oxide on the Si substrate. Recently two direct patterning techniques have been applied to P3HT layers. The first one used micromolding in capillaries with ice molds [64], [65], while the second one performed nano-indentation lithography on a scanning probe microscope platform [66]. It is nevertheless difficult to imagine an extension of such special techniques to those practical applications requiring large-area and low-cost compatible fabrication technologies. Nanoimprint lithography (NIL) has also been successfully applied by Kim and coworkers [67] for generating surface relief gratings on P3HT and fullerene blends which lead to improved performance of organic solar cells. Since NIL is amenable to low-cost, large-area roll-to-roll fabrication, the latter example shows the great potential of this technology for a wide range of important engineering applications.

In this section, we demonstrate thermal and room-temperature NIL for directly patterning P3HT thin-films with feature sizes down to 20 nm. For accomplishing this result, molds fabricated by molecular beam epitaxy (MBE-molds) have been used. Finally, we conclude with a discussion and summary of key results and future plans.

3.1.1 Patterning P3HT by Thermal Nanoimprint

Materials and Methods

We used a commercially available state-of-the-art NIL tool (Obducat 2.5” equipment, Obducat, Sweden) for structuring the material of interest. The structures imprinted into the polymer were defined using commercially available 2” diameter Ni and Si/SiO_2 molds (NILT Technology, Denmark) comprising approx. 100 nm deep line gratings of various lateral feature sizes ranging between 35 nm and 300 nm. Further, porous alumina templates featuring an average pore width as well as pore-to-pore distance of approx. 60 nm, which were fabricated by a collaboration partner, were used as molds for obtaining 2D pillar

structures. The samples to be imprinted were placed on the bottom plate of a gas-tight heatable as well as coolable chamber of the NIL tool with the mold manually placed upside down onto the imprint polymer layer. The imprint step was performed by pumping compressed-air into the upper section of the chamber pressing a metal foil (posed on top of the mold/substrate sandwich structure) and the mold itself down against the substrate. Thus, mold features were transferred into the polymer layer. Finally, after cooling of the substrate the mold was released from the imprint polymer layer. Imprint duration, temperature, pressure were computer-controlled, in-situ monitored, and could be preset.

The imprint polymer chosen was a highly regioregular (90 % - 93 %) poly(3-hexylthiophene-2,5-diyl) purchased from Rieke Metals, Inc. used without any further purification. The nominal molecular weight (M_w) is specified to be around 50000. Being a comb like stiff polymer with flexible hexyl side chains, P3HT cannot be strictly considered a glassy polymer like the ones conventionally used for thermal imprinting. This particular configuration leads to a semicrystalline structure, whose morphology and orientation also depend on the method used for preparing the film, like solvent casting or spin-coating. In particular the orientation in spin coated films depends on both regioregularity and molecular weight [68]. Studies of the thermodynamic phase behavior based on calorimetric measurements revealed a phase transition from a crystalline to a layered liquid crystalline state at 210 °C-225 °C in regioregular P3HT, and a glass transition temperature at -3 °C in regiorandom P3HT [69]. Thus, the phase transition temperature depends on the extent of the regioregularity of the material used and it is not surprising to find in the literature very broad order-disorder phase transitions in a temperature range well below 200 °C where hysteresis are also present [70].

Results and Discussion

The first step towards achieving proper pattern transfer is finding the optimum imprint parameters for the given polymer. To determine the best imprint temperature, a series of samples were imprinted with different temperatures while fixing pressure and time to 70 bar and 300 sec, respectively. The same procedure was then repeated to determine the best imprint pressure, this time however samples were imprinted using different pressures while fixing temperature and time to 125 °C and 300 sec, respectively. All samples were prepared by depositing P3HT from a dichlorobenzene based solution of 2 wt% concentration. The P3HT layers were deposited onto cleaned Si substrates by spin coating the samples at 1000 rpm for 90 sec, resulting in a layer thickness of approx. 100 nm. No thermal treatment of the samples was performed prior to imprint. The mold used for imprint comprised a line grating with 250 nm sized features. This relatively large feature size was chosen during optimization to facilitate the characterization of the samples. The characterization of the imprinted samples was performed using atomic force microscopy

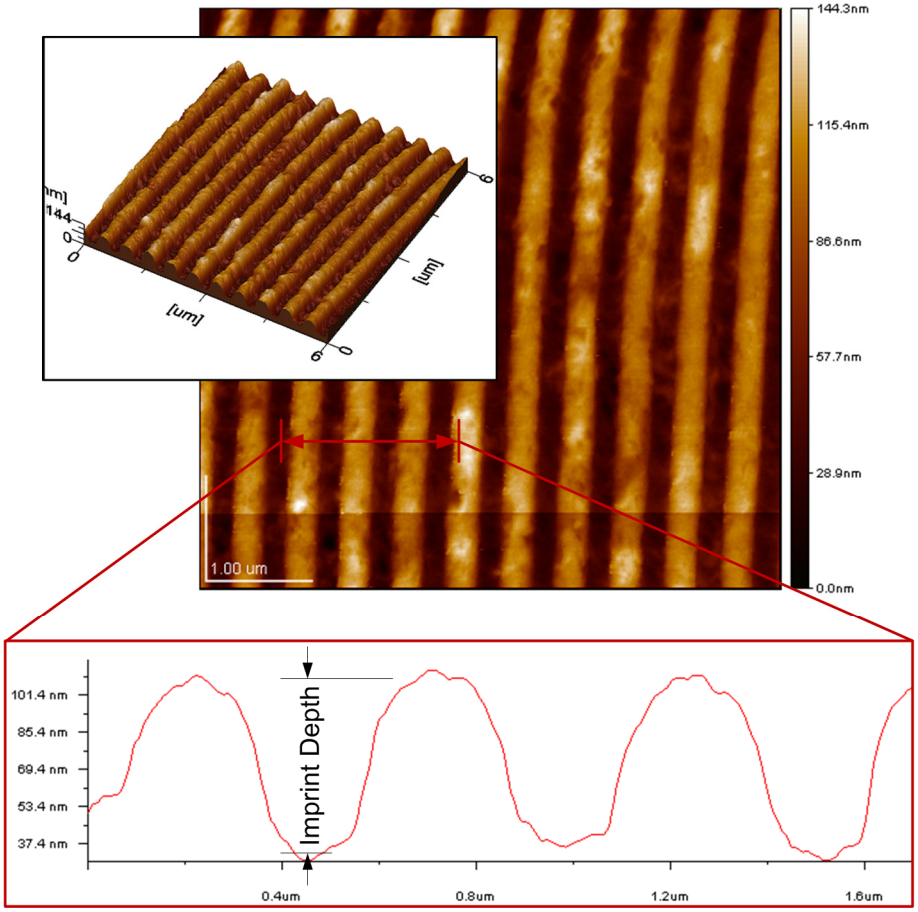

Figure 3.1: AFM scan of a P3HT/Si sample imprinted at 125°C and 70bar for 300sec, and the corresponding line profile indicating the imprint depth used for comparison.

(AFM). Imprint depth, measured from a line profile of the AFM scan, was selected to be the main criteria for judging imprint quality. Figure 3.1 shows an AFM scan of one of the samples (T=125 °C, P=70 bar, t=300 sec) and the corresponding line profile indicating the imprint depth mentioned previously. Further, the graph plotted in Fig. 3.2(a) presents the imprint depths measured for different samples as a function of imprint temperature, while Fig. 3.2(b) shows a second graph where the imprint depths are plotted against imprint pressure. In both cases several measurements were taken at different areas for each sample. The results indicate that the optimum imprint temperature for the purchased material lies between 100 °C and 125 °C. Although the sample imprinted at 150 °C showed only a slightly lower average imprint depth, the pattern transferred was of lower quality, which can also be seen in the higher deviation (larger error bar) between the different measurements at that point. This is probably caused by parts of the polymer sticking to the mold while imprinting at more elevated temperatures. On the other hand, the relation between imprint depth and imprint pressure shows a less interesting behavior, which is

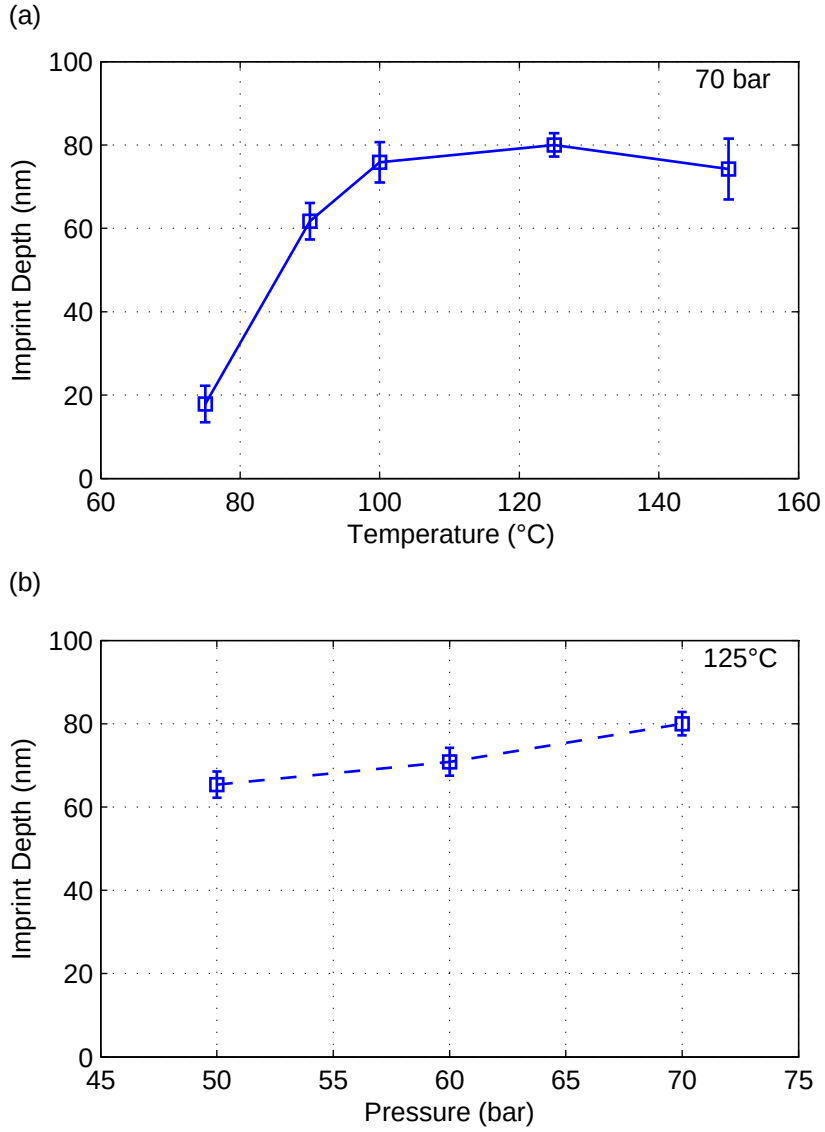

Figure 3.2: Graph presenting the imprint depth measured for different samples plotted against imprint temperature (a) as well as against imprint pressure (b).

nearly linear in the examined region. However, it reveals that reasonable pattern transfer can already be achieved at a pressure of 50 bar.

Using the results obtained from the experiments discussed above, we attempted to structure P3HT down to the sub-50-nm region. For this purpose a Si/SiO_2 mold comprising a line grating with 35 nm feature sizes over an area of approx. $1cm^2$ was used. The imprint was performed at a temperature of 120 °C and a pressure of 70 bar for 300 sec. Figure 3.3 shows an AFM topography image of the imprinted sample scanned over an area of 4µmx4µm. The line pattern transferred to the P3HT layer is clearly observed and single lines can be easily distinguished. Note that all AFM images shown here were taken in

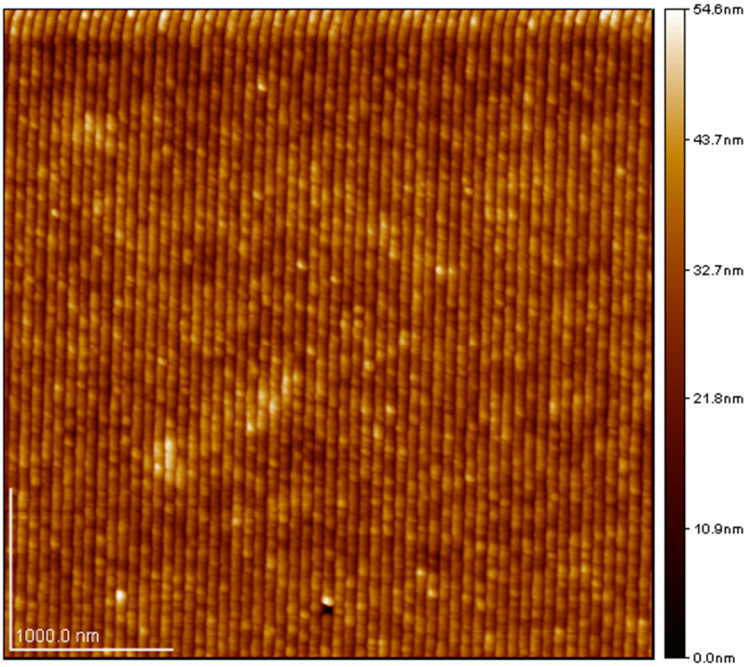

Figure 3.3: AFM topography image of an imprinted sample scanned over an area of 4µm x 4µm. The imprint was performed on a P3HT/Si sample at 120°C and 70bar for 300sec using a Si/SiO_2 mold featuring a 35nm line grating.

tapping mode using a standard SPM-tip. This is the reason why the lines appear to be touching each other with trenches in between of a depth and width smaller than expected. For a more accurate depth measurement of such small structures an ultra-sharp high aspect ratio SPM-tip is needed. Despite this issue, random scans over the imprinted area proved the imprint process to be suitable for imprinting larger areas of P3HT, which is of significant importance for its future application to active organic devices.

The most promising application of nanostructured P3HT layers is related to organic photovoltaic devices and is going to be discussed in more detail in Section 3.1.3. For this application it is of great interest to increase the surface area of the P3HT layer as much as possible. Hence, 2D nanostructures would be more favorable for increasing the surface area even further. In Fig. 3.4(a) a 3D AFM image is shown, which demonstrates successful pattern transfer of a 2D pillar structure imprinted using the porous alumina templates described before. As in the previous case, reliable pattern transfer is achieved over the entire structured area (~1cm^2) with high uniformity as indicated by the 4µmx4µm AFM scan shown. Characterizing a smaller area of 1µm x 1µm by AFM, shown in Fig. 3.4(b), visualizes the individual pillars of around 60nm diameter. As for the 35nm line structure, due to the dimensions of the SPM-tip used, the spacing between the pillars appears narrower than expected. This becomes more obvious when examining such a structure using an SEM, shown in Fig. 3.4(c), where the spacing between pillars appears wider.

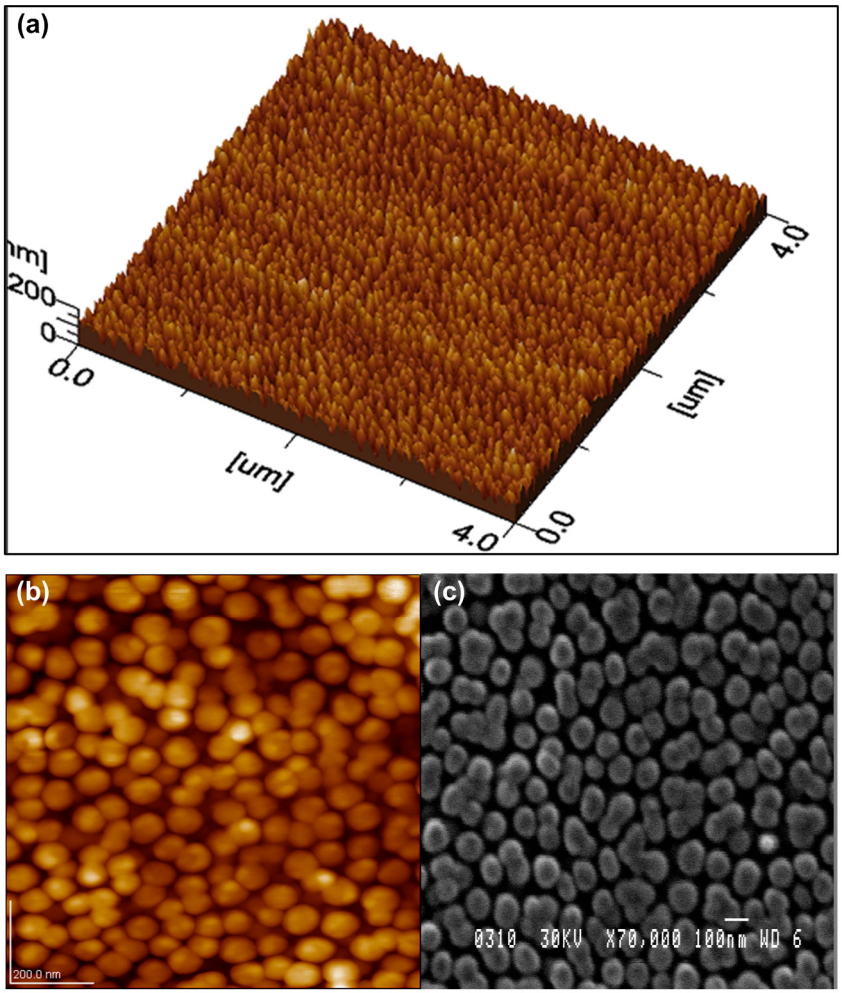

Figure 3.4: 3D AFM image demonstrating successful pattern transfer of a 2D pillar structure imprinted using the porous alumina templates with 60nm average pore width (a). Characterizing a smaller area of approx. 1 µm x 1 µm using AFM (b) and SEM (c) visualizes individual pillars of around 60 nm in diameter.

It is important to mention that similarly good imprint results were obtained when imprinting P3HT layers deposited onto plain glass, ITO/glass and PEDOT:PSS/ITO/glass substrates using the different types of molds. Being able to structure P3HT layers independent of the underlying layers and type of substrate is essential for applying this technology to organic electronic and optoelectronic devices.

3.1.2 Patterning P3HT by Room-Temperature Nanoimprint

Materials and Methods

We investigated the potential of MBE room temperature NIL (MBE-RTNIL) [71] for patterning P3HT. Room-temperature NIL (RTNIL) has two core advantages with respect

to classical thermal NIL: (a) it can be used to pattern electrically, optically or magnetically active polymer materials that may change or even lose their distinct functionality upon heating in thermal NIL processes or exposure to radiation in conventional optical, e-beam, or UV-curing lithography; (b) it allows for patterning the same area or closely neighboring areas of an imprint polymer layer through sequential step-and-repeat NIL cycles. It was for example used in conjugated polymer-based photonics [72], and to fabricate oligomer-based organic distributed feedback lasers [73] as well as near-infrared imprinted distributed feedback lasers [74]. The imprint polymer layer consisted of P3HT (Rieke Metals, Inc.) that was first dissolved in toluene to a concentration of 2 wt%. We cleaned a silicon wafer in an oxygen plasma asher for 2 min, spin-coated the P3HT/toluene solution onto it at 1000 rpm, and baked it at 140 °C for 15 min resulting in an approximately 100 nm thick P3HT layer.

Using a positive multi-line MBE-mold (we have elaborately described the mold fabrication process elsewhere [71], [75]) and a custom-built RTNIL-tool that controllably presses the MBE-mold into a stationary imprint sample applying imprint pressures of up to approx. 700 MPa we carried out the following MBE-RTNIL process: (i) imprint sample and MBE-mold were mounted in our custom-built MBE-RTNIL tool, (ii) a hardened steel plate with an ultra-flat surface was mounted between imprint sample and wafer chuck to support homogenous distribution of the force applied by the wafer chuck counteracting the imprint force during the imprint step, and (iii) the mold-holder unit was operated in such a way that the cylinder force was partly absorbed in the mold holder unit before transferred to the MBE-mold. This buffer function becomes necessary when using positive MBE-molds since stand-alone positive mold features are highly sensitive to even slightest variations of the imprint pressure. We then performed separate single-step RTNIL experiments at room-temperature under atmospheric conditions applying an imprint pressure of ~ 350 MPa (~3.5 kbar) for 10 sec.

Results and Discussion

Experimental results are shown in Fig. 3.5. The SEM images show three imprinted grooves where the 21 nm wide groove was generated by a 19 nm wide line on the mold, the 39 nm wide groove corresponds with a 36 nm wide line on the mold, and the 60 nm wide groove results from imprinting a 55 nm wide line on the mold [71]. A 3 nm thick titanium layer was evaporated onto the sample before SEM imaging to prevent charging effects.

The imprint depths in this case were ~20 nm. Sidewall and surface characteristics of imprinted P3HT patterns need to be further improved in order to establish a RTNIL process that is capable of reproducing high-quality sub-50-nm features. However, we could demonstrate that P3HT can be imprinted in the sub 50 nm region at room-temperature by performing the developed MBE-RTNIL scheme. Detailed information on latest

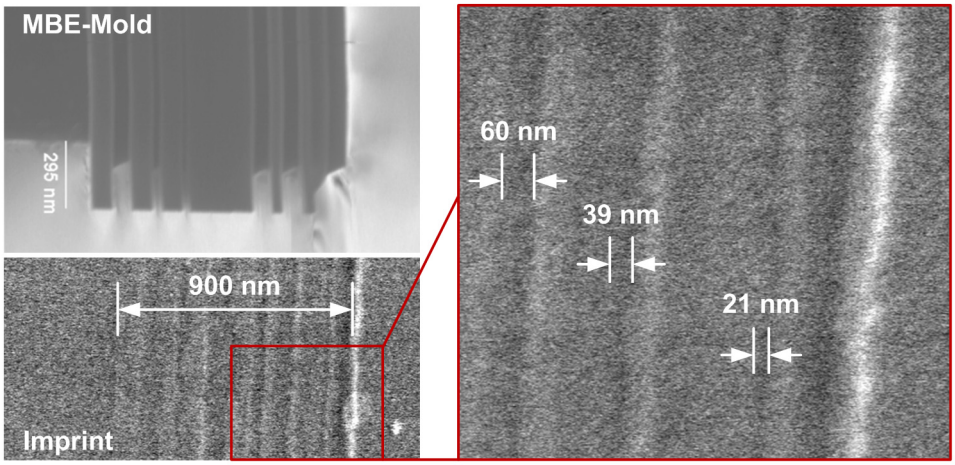

Figure 3.5: SEM images of a multi-line pattern imprinted onto a P3HT/Si sample at room-temperature and an imprint pressure of ~3.5 kbar using a positive multi-line MBE-mold.

development efforts of this technology, including process parameter optimization, patterning efficiency, yield data regarding patterning processes, yield optimization techniques, and main potential applications are presented elsewhere [76].

3.1.3 Future Application to Organic Photosensitive Devices

The results presented here can be particularly appealing for P3HT-based organic photovoltaics (OPVs) and organic photodetectors (OPDs). In such devices, an exciton (bound electron-hole pair) is created upon absorption of a photon. The energy required for the dissociation of such an exciton is introduced by the difference in ionization potentials and electron affinities at the interface between the donor and acceptor materials forming the active layer of the device. In state-of-the-art organic photovoltaic devices, P3HT and the fullerene derivative [6,6]-phenyl C61 butyric acid methyl ester (PCBM) are used as donor and acceptor materials, respectively. Efficient charge carrier separation requires large interface areas, which are obtained by the nanoscale phase separation in a blend of the two materials. The interpenetrating network of donor/acceptor interfaces formed during this process has a length scale similar to the exciton diffusion length (in the order of 10 to 20 nm), thus allowing dissociation to occur everywhere throughout the bulk before exciton lifetime is reached. The free carriers generated at the interfaces can then be driven to the contacts by the built-in electric field resulting from the different work function electrodes. The improvement in the performance of bulk heterojunction (BHJ) OPVs requires the optimization of all the processes described above, which in turns involves the choice of materials, their combination, device geometry, device structure, and several other parameters. Using nanoimprint technology, it should be possible to create controlled acceptor-donor interfaces by patterning P3HT in the sub-50nm range prior to the

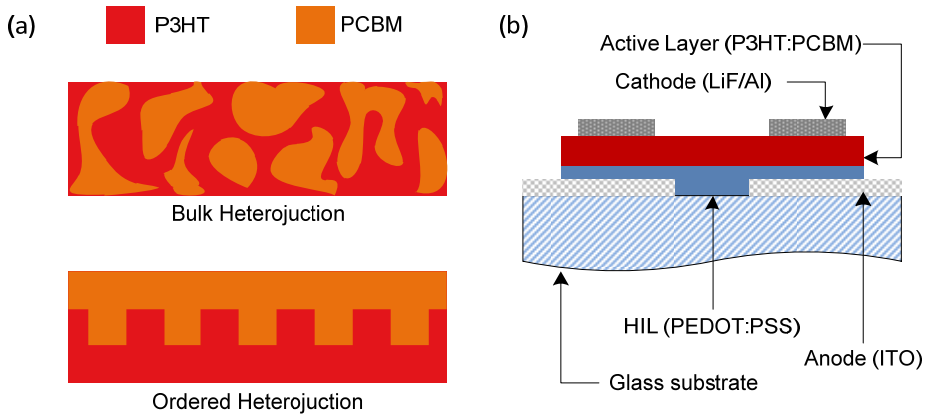

Figure 3.6: (a) Illustration of two structures for the photoactive layer based on bulk or ordered heterojunctions of P3HT and PCBM. (b) A schematic showing the general layout of the BHJ photovoltaic devices built here.

deposition of the acceptor material. Figure 3.6(a) illustrates the difference in active layer morphology of an ordered heterojunction (OHJ) structure as opposed to the conventional BHJ structure.

However, in order to seriously consider the NIL process described here for the fabrication of OHJ photovoltaic devices, the compatibility of this process to the imprint polymer (i.e. P3HT) has to be granted. This implies that the process parameters involved in this step of fabrication, such as temperature and pressure applied, do not alter its chemical, optical and/or electrical properties significantly. Building a complete OHJ device is however rather complicated and still under investigation. The problems that still have to be solved are related to the deposition of the PCBM onto the structured P3HT layer without destroying the pattern while at the same time assuring good filling of the trenches. To overcome this current limitation, we fabricated BHJ devices from a dichlorobenzene based P3HT:PCBM (1:1) blend solution with 2 wt% concentration. The active layer was deposited onto a PEDOT:PSS/ITO/glass substrate by spin coating. A reference sample was completed by a thermal annealing process at 80 °C for 180 sec followed by the evaporation of the metal top electrode. Another sample was imprinted at 80 °C and 60 bar for 180 sec using a cleaned unstructured Si wafer. This way we can assure that both polymers in the blend are exposed to the conditions (i.e. temperature and pressure) of a typical imprint step without being structured, which makes a direct comparison with the reference sample possible. The planar imprinted device was then completed by evaporation of the metal top electrode. A general layout of the BHJ photovoltaic devices prepared here is shown in Fig. 3.6(b).

Figure 3.7 shows the IV-characteristics measured for both devices under illumination with a 100 mW/cm^2 halogen lamp. Note that the data plotted is averaged over four diodes for

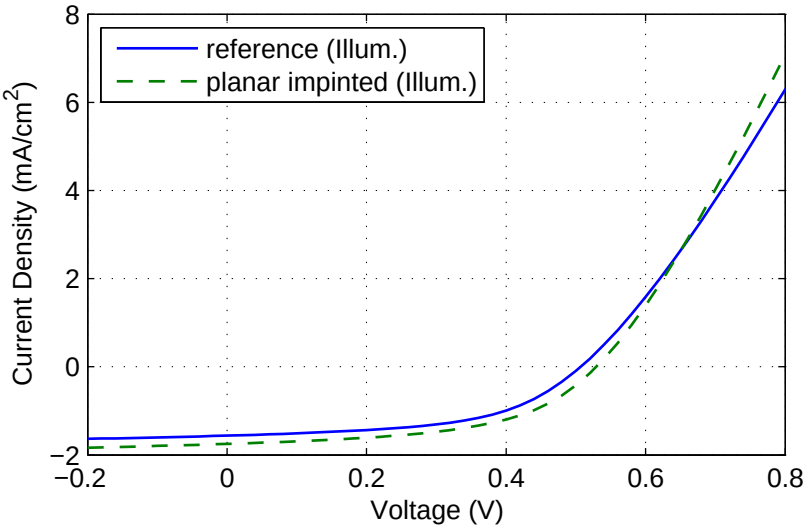

Figure 3.7: IV-characteristics comparing a reference device to a planar imprinted device, both measured under illumination with a 100mW/cm^2 halogen lamp.

	V_{oc} (V)	I_{sc} (mA/cm^2)	FF (%)	PCE (%)	R_s (Ω/cm^2)
Reference	0.50	1.56	53.5	0.42	57.95
Planar Imprint	0.52	1.75	53.1	0.48	50.79

Table 3.1: Performance parameters extracted from the illuminated IV-characteristics of the fabricated devices.

each of the two device types under comparison. This is to ensure that the conclusion taken from the outcome of this experiment represents a general trend. The presented IV-curves clearly demonstrate similarly good diode behavior for both devices. Table 3.1 compares all key performance parameters extracted from the corresponding IV-curves. Comparable open-circuit voltages and fill factors are calculated for both device types while a 10 % higher short circuit current is observed for the planar imprinted device, resulting in slightly higher power conversion efficiency. The noticeable enhancement in device performance after imprinting has been observed before by Kim et al. for TDPTD and was suggested to be due to additional chain-to-chain ordering resulting from the imprint process [55]. This issue is currently under investigation. From the presented results it is however obvious that the device performance is not deteriorated in any way by the imprint step during device fabrication. Hence, we can assume the individual materials, including P3HT, are not damaged by the imprint process.

3.2 Transfer Printing

One major challenge in the fabrication of organic electronic devices based on solution-processable polymers lies in achieving complicated layer stacks consisting of different organic materials. Since many of these materials are soluble in the same set of solvents, it becomes rather complicated to implement even simple bilayer architectures directly deposited from solution. The deposition of any additional layer on top of an existing one usually results in partial dissolving and/or swelling of the underlying layer due to the solvent present in the solution. The degree of dissolving strongly depends on solvent properties as well as deposition method involved in the process. The utilization of spray technology for this purpose will be discussed in Chapter 4, where we demonstrate that successive spray deposition of the donor and acceptor materials of the photoactive layer in an organic photodiode, using the same solvent, still leads to significant intermixing of the materials allowing the formation of an interpenetrating network required for achieving performances comparable to those of conventional blend devices.

In order however to exploit any possible enhancement through targeted patterning of the active layer in organic photosensitive devices, as presented in the previous section, it is necessary to develop a process for the fabrication of true bilayers in which the integrity of an underlying layer is maintained. Moreover, the ability to reliably fabricate even planar bilayer devices enables a more fundamental understanding of the physical principles involved in device operation for a given material system [77], [78]. Transfer printing is a very promising technique with the potential to overcome the above mentioned technological challenges. It provides an easy and powerful tool for a modular construction of complicated device stacks by adding readily prepared and dry organic layers on top of each other. The absence of any solvent during the actual deposition process preserves the integrity of any previously deposited layers.

Hines et al. previously developed a printing process for high-resolution transfer of all components for organic electronic devices on plastic substrate [79], [80].Their transfer printing process allowed fabrication of an entire device without exposing any component to incompatible processes and with reduced need for special chemical preparation of transfer or device substrates. Several other methods for transfer printing organic thin-films have been reported in recent years, particularly in the context of optoelectronic devices. Choi et al. demonstrated transfer of a complete OLED structure from a patterned mold [81]. A stamp transfer technique that allows ready fabrication of planar heterojunctions from a variety of solution-processed organic materials was reported by Ferenczi et al. [82]. Similarly, Chen et al. presented a new PDMS-stamp-based polymer transfer printing process that enables multilayer structure fabrication, which could be simultaneously used to define lateral patterns [83].

3.2.1 Materials and Methods

Transfer Printing Process

In order to transfer the desired organic layer to a target substrate, the material is first deposited from solution onto a source substrate. In principle any common deposition method can be applied to perform this step. Here we deposit the organic layer by spin-coating the corresponding solution onto a glass substrate. The sample is then left to dry for >1 h in order to remove any excess solvent from the layer. The PDMS stamp is placed carefully on top of the organic layer while applying little pressure to achieve good adhesion and avoid any air enclosures. Once the PDMS stamp is fully attached to the organic layer, the entire stack is immersed into a bath containing DI-water. After approx. 30 min the organic layer completely detaches from the source substrate and floats-off in the water bath. Excellent conformal contact to the PDMS stamp keeps the organic layer attached to the stamp, thereby supporting the sensitive film and enabling convenient handling for a high-yield transfer printing process. The inked stamp can be easily picked up from the water surface and is dried under gentle N_2 flow. Note that performing the float-off step in water renders the process presented here unsuitable for the transfer of water-soluble materials, which introduces only little limitations to the applicability of this process to a broad range of materials since most materials of interest are soluble in organic solvents. To transfer the organic layer to a given target substrate, whether plain or previously coated, the inked PDMS stamp is again placed carefully onto the substrate while applying little pressure to achieve good adhesion and avoid any air enclosures. Finally, the resulting stack is heated up for a short time interval (typically a few minutes) before the PDMS support is peeled off, leaving behind the complete organic layer attached to the target substrate. The elevated temperature is beneficial for complete transfer of the polymer film from the PDMS stamp to the substrate and hence enables a high-yield process [84–86]. Figure 3.8 shows a schematic of the major steps involved in the transfer printing process presented here.

Solution Preparation

Solutions of the pristine acceptor and donor materials were prepared in o-dichlorobenzene (o-DCB) with 2 wt% concentration using regioregular poly(3-hexylthiophene-2,5-diyl) (P3HT) (Rieke Metals Inc.) and [6,6]-phenyl C61 butyric acid methyl ester (PCBM) (Solenne B.V.), respectively. The blend solution consisting of a P3HT:PCBM (1:1) mixture, used for the fabrication of reference devices, was similarly prepared in o-DCB with 2 wt% concentration. All solutions were stirred for >12 h at a temperature of 60 °C. Filtering of the solutions is performed immediately before deposition onto the source substrate using 0.2 μm PTFE filters.

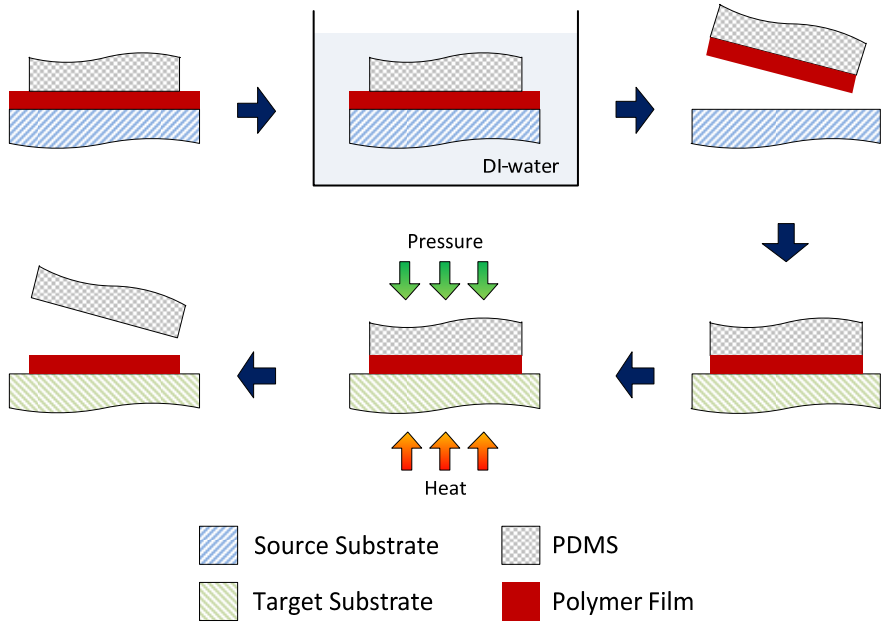

Figure 3.8: Schematic of the major steps involved in the transfer printing process presented here. P3HT and PCBM thin-films can be transfer printed using a supporting PDMS stamp.

Device Fabrication

Prepatterned ITO-glass substrates were cleaned by sonication in acetone and isopropanol in sequence. PEDOT:PSS aqueous dispersion (CLEVIOS™ P VP CH 8000) was deposited by spin coating at 2000 rpm for 20 sec and then dried on a hot plate at 150 °C for 15 min. The active layer of transfer printed device consisted of either a blend or bilayer of regioregular poly(3-hexylthiophene-2,5-diyl) (P3HT) (Rieke Metals, Inc.) and [6,6]-phenyl C61 butyric acid methyl ester (PCBM) (Solenne B.V.) as donor and acceptor materials, respectively. The P3HT:PCBM (1:1) blend, pristine P3HT, and pristine PCBM films were deposited from a solution of 2 wt% concentration in dichlorobenzene (DCB). Samples are then placed again on a hot plate for annealing unless stated otherwise. Finally, a LiF(1 nm)/Al(120 nm) cathode was thermally evaporated on top. The active area of each diode was defined by the electrodes geometries to be 9 mm^2.

3.2.2 Single Layer Investigations

Before incorporating any transferred organic layers into new device architectures it is necessary to investigate the effect of the transfer process on the material and ensure that none of the desired electrical and optical characteristics of the material being considered are altered. For this purpose the absorption spectra as well as layer roughness of transfer

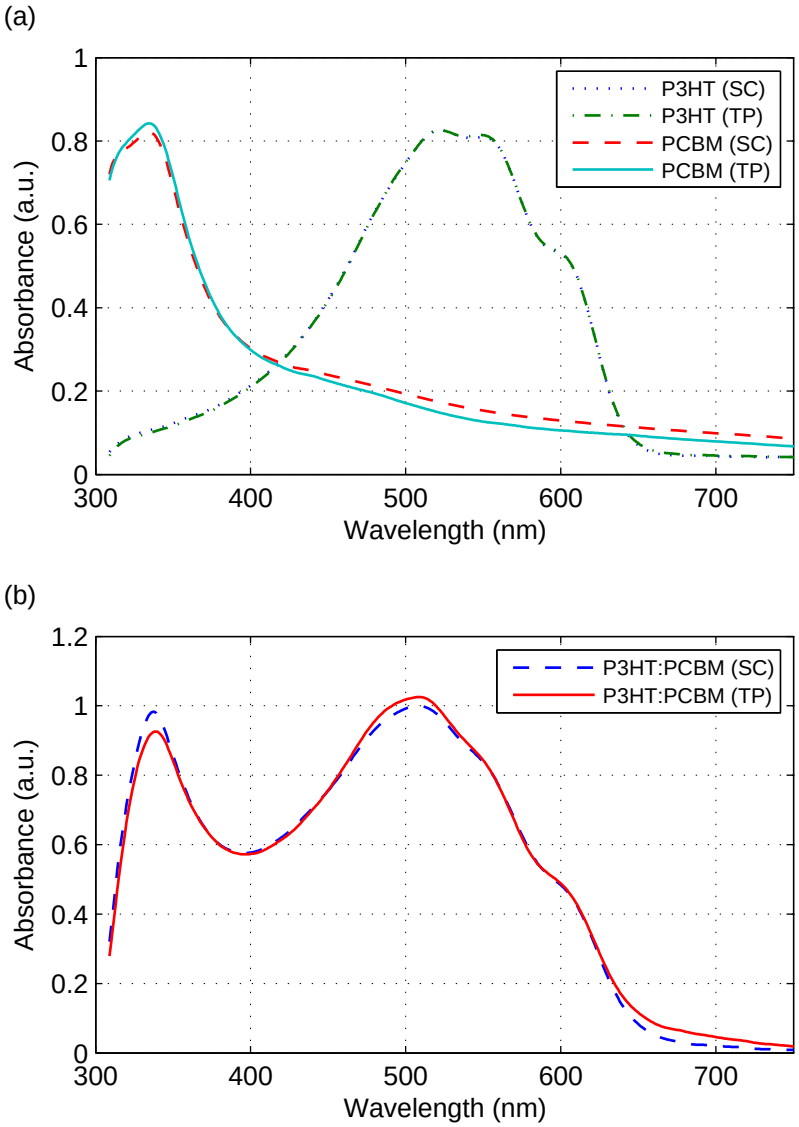

Figure 3.9: Optical absorbtion spectra of spin coated and transferred printed pristine P3HT, PCBM layers (a) as well as P3HT:PCBM blend layers (b).

printed P3HT, PCBM, and P3HT:PCBM blend layers were examined and compared to directly spin-coated ones.

Figure 3.9 shows the UV/Vis absorption spectra of P3HT, PCBM and P3HT:PCBM blend layers prepared by transfer printing and spin-coating. It can be clearly seen that the corresponding curves match very closely. The slight deviation observed between the transfer printed and spin-coated P3HT:PCBM blend layers is most likely originating from the minor annealing step inherent to our transfer process, as it is performed at elevated temperature. An increase in the absorption peak of P3HT (at approx. 510 nm) with respect

	RMS Roughness (nm)		
	P3HT	PCBM	Blend
Spin-Coating	11.7	0.4	0.7
Transfer Printing	13.1	2.5	2.0

Table 3.2: Comparison of the RMS surface roughness values measured for spin coated and transfer printed P3HT, PCBM, and P3HT:PCBM blend films.

to the PCBM absorption peak (at approx. 335 nm) is commonly observed upon annealing of such blend layers [87].

Atomic force microscopy was used to determine the surface roughness for all three types of layers as-cast onto the source substrate and after transfer printing to the target substrate. A comparison of the measured RMS roughness values for spin-coated and transfer printed layers is presented in Table 3.2. One can observe an increase in layer roughness for all three layers after transfer printing is performed. From the data presented in Table 3.2 an average increase of 1.6 nm is determined after transfer printing. The increase of surface roughness for transferred layers can be generally attributed to a lower planarization efficiency of transfer printing. For spin-coating, the direct deposition process from solution counters surface non-uniformities and works on planarization of the substrate surface. In the transfer printing process we introduce here, the planarization occurs for the source substrate during spin-coating. The subsequent transfer printing of the organic layer is only capable of limited planarization of the target substrate. Since each substrate has its unique surface topography, it is not possible for an organic layer, pre-molded by the source surface, to perfectly conform to the target surface. Hence the surface roughness of the transferred layer is increased, despite very good conformal contact between PDMS stamp and target substrate. One possibility for minimizing this effect may lie in the utilization of highly smooth surfaces as source substrates (e.g. silicon substrates) instead of the conventional glass substrates utilized here.

3.2.3 Implementation in Organic Photodetectors

Bulk Heterojuntion Devices

Besides demonstrating the preservation of the overall optical and topographical characteristics of the organic material after transfer printing, it remains necessary to validate the preservation of the electrical characteristics desired for regular device

operation. For this purpose, the electro-optical characteristics of BHJ organic photodiodes with transfer printed P3HT:PCBM blend layers are examined and compared to spin-coated ones, which serve here as well-studied reference devices and are discussed in more detail in Chapter 4. A series of photodiodes were fabricated and characterized in a voltage range between −5 V and +2 V under dark and illuminated conditions. The measurement data obtained for each type of device was averaged over several working photodiodes.

Figure 3.10(a) shows the I-V characteristics of spin-coated and transfer printed devices. The comparison of devices fabricated using the two methods under investigation reveals that dark current density and photocurrent density under reverse bias are very similar for both fabrication methods. Spin-coated devices exhibit a dark current density as low as $6.3 \cdot 10^{-5}$ mA/cm^2 and an on/off-ratio of $2.9 \cdot 10^4$ at −1 V bias, while transfer printed devices exhibit a dark current density of $5.3 \cdot 10^{-5}$ mA/cm^2 and an on/off-ratio of $3.5 \cdot 10^4$ at −1 V bias. Despite slightly enhanced performance of transfer printed devices under reverse bias, spin-coated devices show higher forward current densities. The decreased forward current density of transfer printed devices indicates an increase in series resistance (R_s). A possible reason for the increased series resistance is a poorer contact interface to the transfer printed active layer with respect to the spin-coated layer. This is caused by the lower planarization efficiency of transfer printing, described in the previous section.

Bilayer Devices

Having demonstrated that the transfer printing process developed here has no significant effect on morphological, optical, or electrical properties of the organic materials utilized, this technique can be in principle used to transfer any number of non-water-soluble layers on top of each other. Not only does this provide a powerful tool for the construction of rather complicated organic layer stacks, but it also enables the realization of simple bilayer device architectures, which are difficult to reliably implement for solution-processable material systems. Such simple bilayer architectures are needed for a fundamental understanding of the material system under investigation and represent an essential element in evaluating the possibility of realizing an ordered heterojunction to be implemented in photosensitive applications, as discussed in the first part of this chapter. Further, the examination of miscibility and interdiffusion of donor and acceptor materials and the influence of common post-deposition treatments is crucial for the optimization of the active layer morphology, which is necessary to improve device performance.

We suggest two different approaches for the fabrication of bilayer organic photodiodes using transfer printing. One possibility is to deposit the first layer of the active region (P3HT) by direct spin-coating onto the previously deposited hole injection layer (PEDOT:PSS), since the latter is only water-soluble and will therefore not be affected by a subsequent P3HT deposition. The second layer of the active region (PCBM) is then

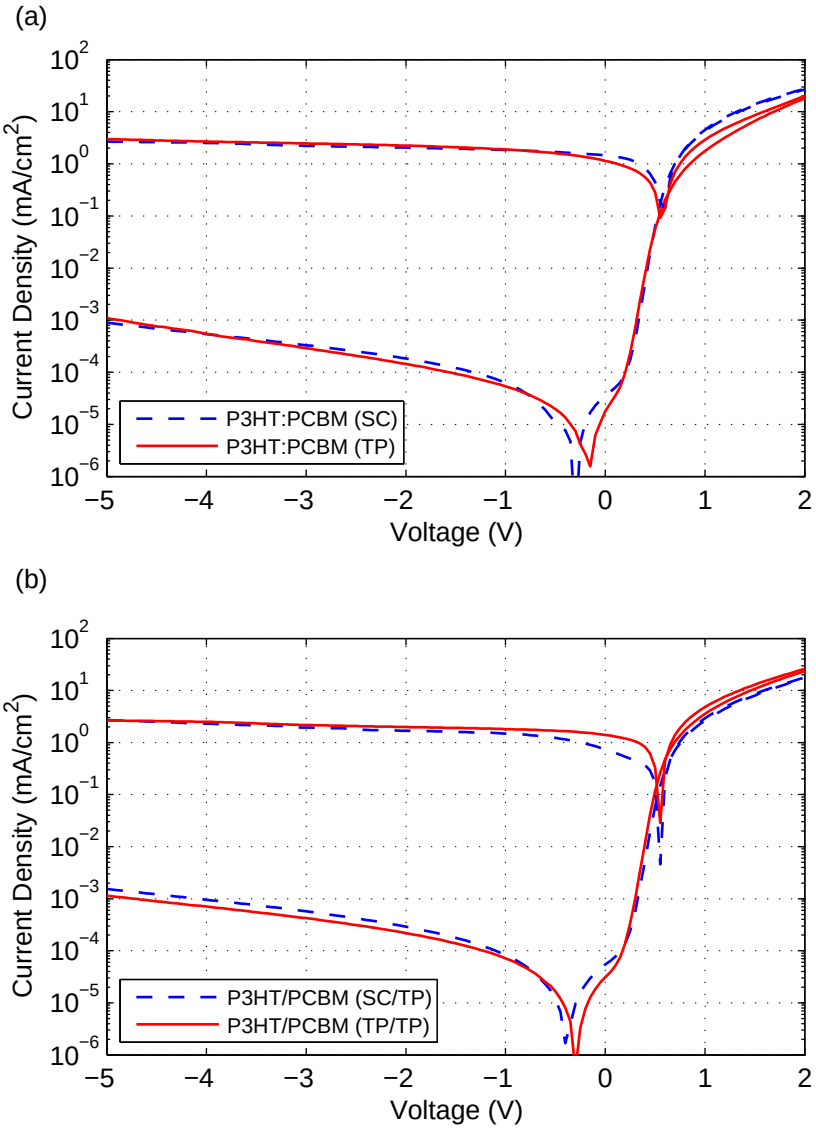

Figure 3.10: (a) IV-characteristics of conventional BHJ photodetectors containing spin-coated or transfer printed P3HT:PCBM blend films. (b) IV-characteristics of P3HT/PCBM bilayer photodetectors, where the P3HT layer is deposited either by spin-coating or transfer printing while the PCBM layer is subsequently deposited by transfer printing.

deposited on top by transfer printing, as described above. Devices fabricated following this procedure are designated by $D_{S\text{-}T}$. An alternative approach is to deposit both layers of the active region sequentially on to the PEDOT:PSS layer by transfer printing. This type of devices is designated by $D_{T\text{-}T}$. Figure 3.10(b) shows a comparison of the IV-characteristics for devices of both types. Devices $D_{S\text{-}T}$ exhibit a dark current density as low as $8.3 \cdot 10^{-5}$ mA/cm^2 and an on/off-ratio of $1.8 \cdot 10^4$ at −1 V bias, while devices $D_{T\text{-}T}$ exhibit a dark current density of $7.2 \cdot 10^{-5}$ mA/cm^2 and an on/off-ratio of $2.5 \cdot 10^4$ at −1 V bias. Those values demonstrate that bilayer devices prepared using both methods show similar performance and can be considered equivalent.

However, it is interesting to note the values measured for bilayer devices, whether of the type $D_{S\text{-}T}$ or $D_{T\text{-}T}$, are surprisingly close to those of conventional BHJ devices shown in Fig. 3.10(a). The comparable performance of bilayer and blend devices is unexpected and not in agreement with the commonly accepted theory of exciton diffusion and dissociation, which implies that diffusion of excitons is limited to a few tens of nanometers and hence the donor/acceptor interfacial area has to be maximized throughout the active layer for efficient exciton dissociation to occur. One possible explanation capable of resolving this contradiction is the occurrence of thermally-assisted intermixing and/or interdiffusion of material at the donor/acceptor interface of the bilayer, thereby forming an interpenetrating network similar to the one found in a BHJ and providing the large interfacial area needed for efficient exciton dissociation.

3.2.4 Thermally Assisted Interdiffusion

Recently, several research groups have attempted to gain insight into morphology evolution of organic bilayer photosensitive devices in order to resolve this controversial issue. Treat et al. fabricated bilayers of P3HT/d-PCBM using a float-casting technique to study the evolution of the interface between the P3HT and PCBM upon thermal annealing [88]. Fast interdiffusion of these two components was observed at low temperatures, resulting in a homogeneous system when annealed at 150 °C for 30 s. Furthermore, it was found that the diffusion of PCBM within P3HT occurs within the disordered phases of P3HT having little effect on the growth of the P3HT crystallites. Chen et al. used a similar float-off method to prepare P3HT/PCBM bilayers, pointing out that any solvent-induced interdiffusion is completely avoided and only the interdiffusion of the components by thermal annealing is observed [89]. Their results demonstrate the development of BHJ morphology by the diffusion of PCBM into P3HT after annealing at 150 °C for only a few seconds. Further, the authors suggest that PCBM can completely diffuse into the P3HT layer without perturbing the ordering of the P3HT.

Evolution of Device Characteristics

As described in the experimental section, transfer printing to the target substrate is performed at elevated temperatures. This introduces an unintentional annealing step, which may significantly alter the active layer morphology from that of a true bilayer depending on the chosen transfer temperature and duration, even in the absence of any thermal post-deposition treatment. Hence it is necessary to minimize undesired annealing during transfer printing, in order not to interfere with any subsequent annealing step. For this purpose, the lowest possible transfer temperature, still sufficient to achieve high-yield transfer and reasonable device performance, has to be investigated. Finding such parameters enables us to get as close as possible to a true bilayer architecture for as-prepared devices, while

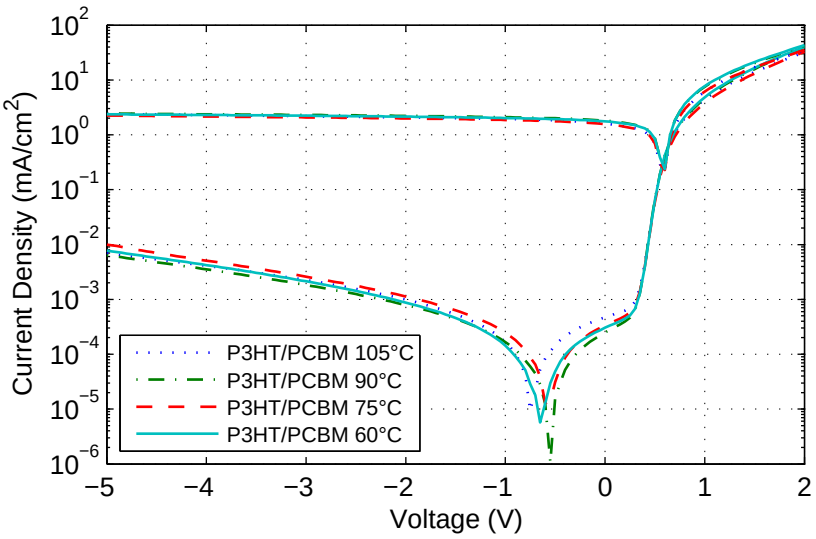

Figure 3.11: IV-characteristics of P3HT/PCBM bilayer photodetectors transfer printed at different temperatures, ranging from 105 °C down to 60 °C for a fixed duration of 3 min.

isolating the effect of thermal post-deposition treatment on morphology evolution and the corresponding device performance.

A series of bilayer devices were fabricated by transfer printing PCBM layers onto previously spin-coated P3HT at different transfer temperatures, ranging from 105 °C down to 60 °C for a fixed duration of 3 min. Several diodes for each temperature point were characterized and the averaged IV-characteristics under dark and illuminated conditions are plotted in Fig. 3.11. The curves of all four different devices match very closely, showing that high quality transfer printing of PCBM can be achieved even at transfer temperatures as low as 60 °C. For this reason, all bilayer devices presented from this point on involve the transfer printing of PCBM layers at 60°C in order to minimize any undesired annealing effects during active layer preparation.

Since the annealed bilayer devices presented previously were shown to exhibit a performance comparable to blend devices, it is important to examine the effects of thermal post-deposition treatment on the evolution of active layer morphology in such bilayer architectures and hence on the overall device performance. Therefore, a series of bilayer devices were fabricated using the minimum transfer temperature determined above for transfer printing of PCBM layers. Each group of samples was thermally annealed under inert gas conditions at temperatures of 140 °C, 120 °C, and 100 °C, respectively. Within a given group the duration of treatment was varied for different samples. Figure 3.12 shows the measured IV-characteristics, where each group of samples annealed at the same temperature are plotted together in the same graph. As-prepared devices of all three sets, labeled with 0 min annealing duration, exhibit very similar behavior with extremely low

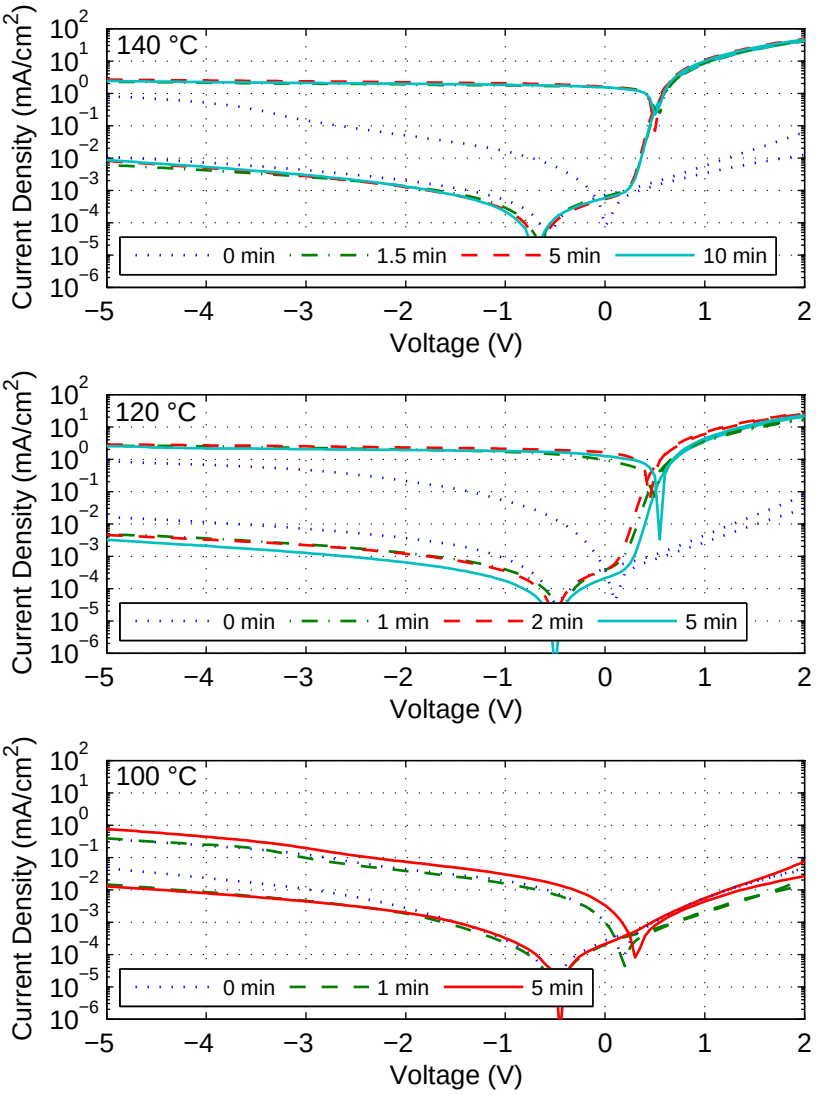

Figure 3.12: IV-characteristics of bilayer devices thermally treated at different temperatures following initial transfer printing at 60 °C. While no clear impact is observed for devices annealed at 100 °C, annealing at higher temperatures introduces significant enhancement in performance even for the shortest treatment durations.

photocurrent densities not exceeding $5 \cdot 10^{-2}$ mA/cm^2 at −1 V bias, leading to on/off-ratios below 60 at the same biasing conditions. Moreover, all diodes show poor rectification due to the low forward current densities with the highest value being approx. $6 \cdot 10^{-3}$ mA/cm^2 at +1 V bias. Considering the set of devices thermally annealed at 140 °C, reveals a strong increase in photocurrent as well as forward current densities, which is nearly independent of the treatment duration applied. Values for the photocurrent density reach up to 1.8 mA/cm^2 at −1 V bias, while the forward current density increases by almost 4 orders of magnitude to 10 mA/cm^2 at +1 V bias. Note that a decrease in dark current density is observed for annealed devices as well, however only marginal. It becomes clear from this

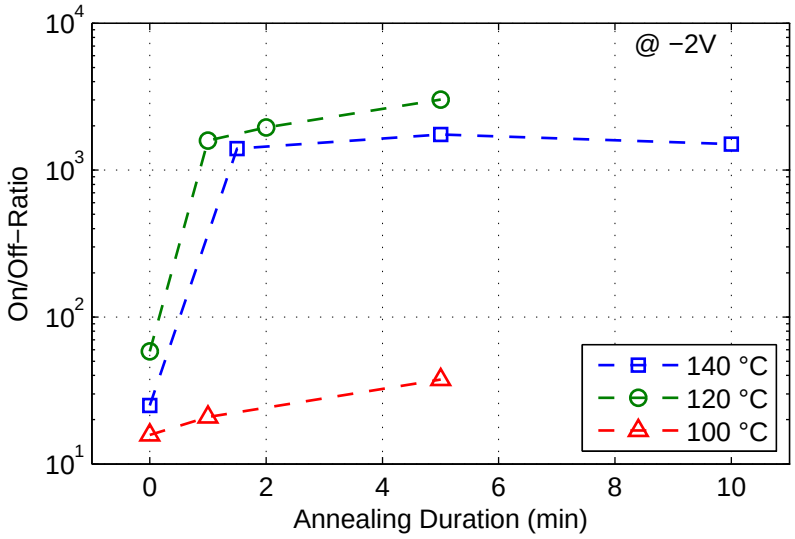

Figure 3.13: Comparison of the on/off-ratios at −2 V bias, as extracted for bilayer devices annealed at different temperatures, with respect to the treatment duration.

set of devices that at such high annealing temperatures (140 °C) even the shortest treatment duration of 1.5 min leads to drastic enhancement of the overall device performance. Samples annealed at 120 °C show in principle a similar trend only with slightly clearer changes in device performance for treatment durations between 1 min and 5 min. Only after annealing temperature is decreased to 100 °C the enhancement in device performance is only minor, at least up to a treatment duration if 5 min. The overall device performance remains poor and close to that of the as-prepared devices. Since it is assumed that the significant change in overall device performance observed here upon thermal annealing is related to major changes in active layer morphology, the results presented suggest that interdiffusion of the materials within the active layer occurs in less than one minute for annealing temperatures above 120 °C. The observation of such a rapid interdiffusion renders any attempt of demonstrating a gradual enhancement in device performance corresponding to different stages of morphology evolution rather complicated. Figure 3.13 shows a comparison of the on/off-ratios at −2 V bias, as extracted for all three sets of devices, with respect to the treatment duration. The clear and abrupt increase in on/off-ratio by several orders of magnitude for devices annealed at 140 °C and 120 °C confirms the idea of a rapid intediffusion within the first minute of thermal annealing, after which only a slight increase can be observed. This is in good agreement with findings recently published by other research groups [88], [89].

Cross-Sectional SEM Investigations

In all our previous analysis we attribute the dramatic enhancement in performance of bilayer devices upon thermal annealing to major changes in active layer morphology caused by rapid interdiffusion of the composing donor and acceptor materials, thereby

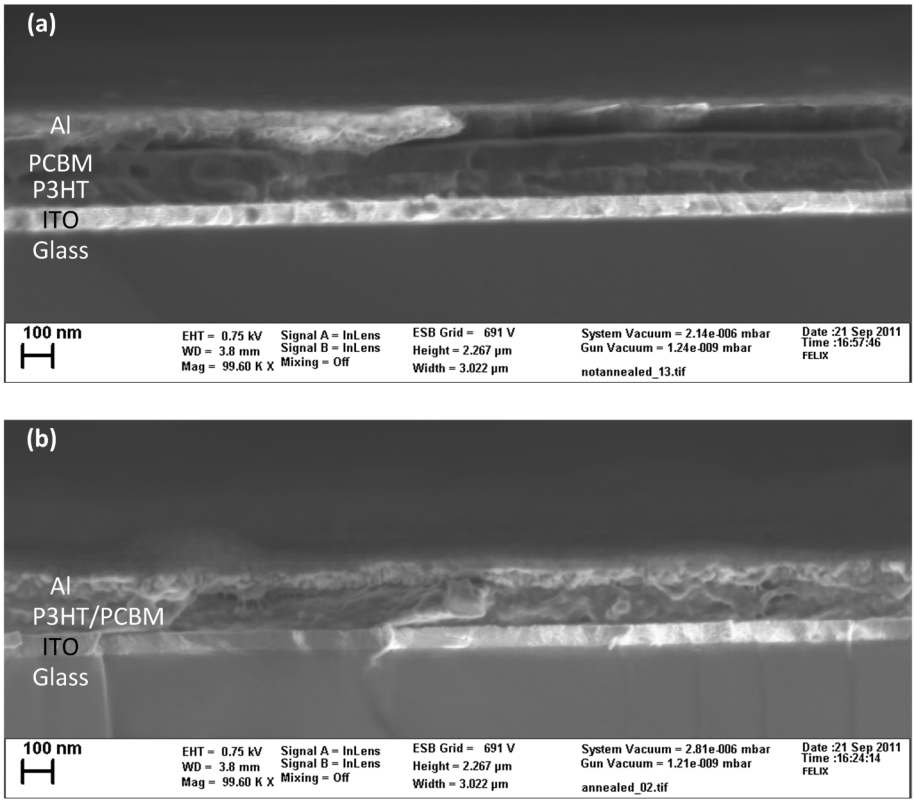

Figure 3.14: Cross-sectional SEM images of two P3HT/PCBM bilayers before (a) and after (b) thermal annealing at 140 °C for 10 min.

forming the large interfacial area necessary for efficient exciton dissociation. To be able to show the occurrence of an essential morphological change from initially true bilayer architecture towards an intermixed bulk heterojunction, cross-sectional scanning electron microscopy (SEM) investigations of as-prepared and thermally annealed samples were carried out. Two samples were prepared on ITO coated glass substrates, where P3HT was directly spin-coated onto the substrate followed by transfer printing of PCBM performed at 60 °C. The organic stack was then capped by a thermally evaporated 150nm Al layer to enhance contrast and avoid charging effects during SEM imaging. One sample was left as-prepared without any further treatment while the other was thermally annealed at 140 °C for 10 min. Cross-sections were prepared by liquid nitrogen cooling and cleaving of the samples, which were then ready for SEM imaging. Images obtained for both samples are compared in Fig. 3.14, where the different materials within the stack are labeled. There, a relatively sharp interface can be seen throughout the entire width of the active layer despite the low contrast difference, which clearly discriminates the two sequentially deposited materials and confirms the existence of a true bilayer architecture for as-prepared samples fabricated using the transfer printing process developed here. On the other hand, in the thermally annealed sample such an interface within the active layer does not exist anymore, indicating a good intermixing of the materials and giving the impression of a

homogenous layer composed of a single material. This clearly demonstrates the occurrence of intermixing and/or interdiffusion upon annealing of the given material system, which was previously suggested as the main reason behind the unexpectedly good performance of bilayer devices. Cross-sectional SEM images presented in this section were acquired by the group of Dr. Enrico Da Como, Lehrstuhl für Photonik und Optoelektronik, Department für Physik und CeNS, Ludwig-Maximilians-Universtität München.

Optical Absorption Characteristics

Gaining further insight into the nature of interdiffusion in the material system under investigation can be accomplished by examining the optical absorption spectra of the different layers considered so far. The extent of crystalline domain formation in P3HT has a strong effect on the features of its optical absorption. Strong interchain interactions in the crystalline domains lower the band gap, creating a shoulder in the absorption spectrum around 600 nm (2.1eV) that can be attributed to a π-π^* interchain transition [90]. Regiorandom P3HT is not capable to form crystallites on such a scale and hence does not exhibit a pronounced shoulder in it absorption spectrum. A similar behavior is observed also for regioregular P3HT in which the formation of crystalline domains is disrupted. It is expected that PCBM hinders the formation of such P3HT crystallites when both materials are intermixed, as in a blend layer. Fig. 3.15(a) shows the absorption spectra of pristine P3HT and PCBM layers along with that of an as-prepared P3HT/PCBM bilayer. In addition to the measured curves, a fourth curve is plotted showing the calculated sum of the two pristine materials (P3HT+PCBM). Comparing this to the spectrum of the bilayer reveals a close matching of the two spectra. This indicates that formation of crystalline P3HT domains in the bilayer is of comparable extent as in pristine P3HT layers. Additionally, since the absorption spectrum of the bilayer is almost completely identical in all features to the sum of its two composing materials, it is assumed that no significant interdiffusion has occurred within the bilayer and hence no interaction of the materials can be extracted from its absorption spectrum. This assumption is consistent with the clear interface visible in the cross-sectional SEM image of the as-prepared device as well as the poor device performance measured. In case of a thermally annealed P3HT/PCBM bilayer, which is plotted in Fig. 3.15(b) along with an unannealed P3HT/PCBM bilayer and a P3HT:PCBM blend layer, the situation becomes different. There the shoulder at 600 nm is slightly quenched with respect to that of the pristine P3HT layer. This quenching is known to occur more prominently in blend layers and is attributed to the disruption of P3HT crystalline domains by the embedded PCBM molecules. Hence, it indicates the diffusion of PCBM into the underlying P3HT layer upon thermal annealing of the bilayer. The slight reduction in intensity of the shoulder at 600 nm together with the slight blue-shift in P3HT absorption suggest however that crystalline P3HT domains are only marginally affected by PCBM diffusion. As a direct consequence it is expected that the diffusion of PCBM occurs

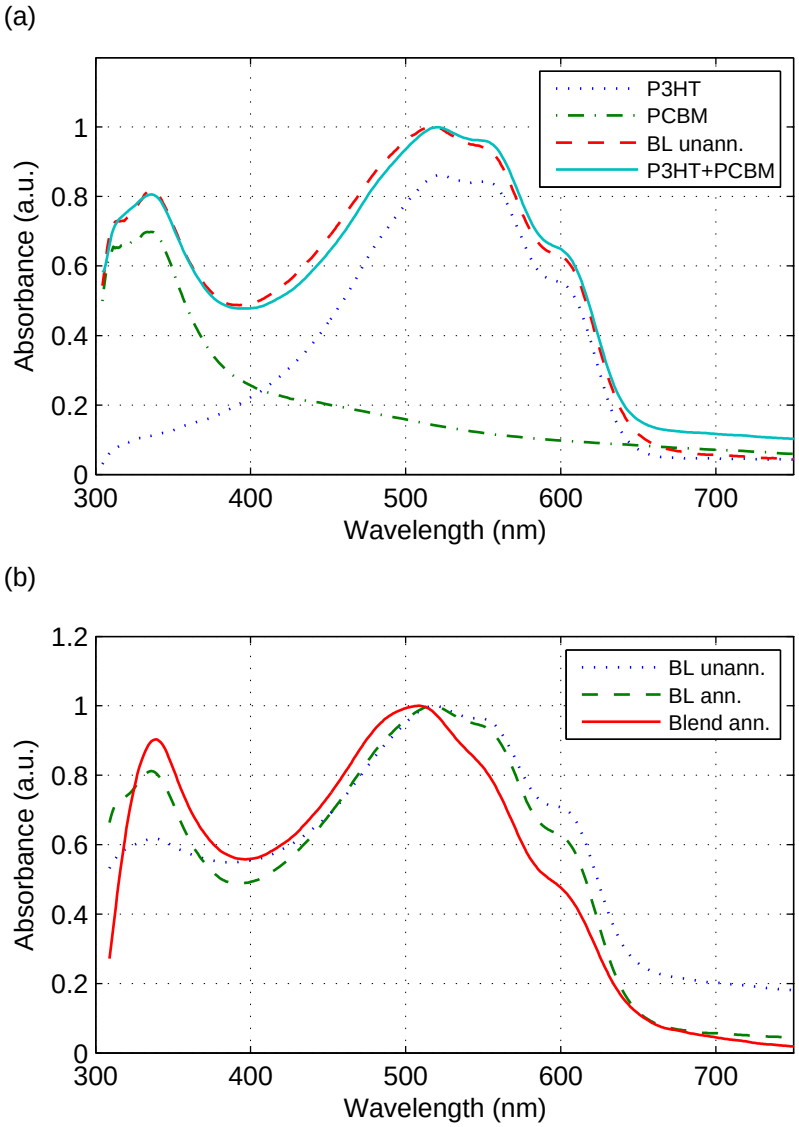

Figure 3.15: (a) Optical absorption spectra of pristine P3HT and PCBM layers along with that of an as-prepared P3HT/PCBM bilayer. The bilayer spectrum closely matches the calculated sum of the P3HT and PCBM curves. (b) Optical absorption spectra of annealed and unannealed bilayers compared to that of a blend.

predominantly into the amorphous P3HT domains, thereby causing only little change in the characteristic P3HT absorption features. This becomes even clearer when compared to the absorption spectrum of the P3HT:PCBM blend layer, where the two materials are rigorously blended in solution prior to deposition. The intimate intermixing of the materials in a blend layer causes significant disruption of P3HT crystallites and reduced interchain interactions, leading to a strong blue-shift of the P3HT absorption and severe quenching of the shoulder at 600 nm.

The thermally-assisted spontaneous formation of bulk heterojunction morphology from a P3HT/PCBM bilayer renders the idea of fabricating ordered heterojunction photosensitive devices, as proposed in the first part of this chapter, rather complicated and hardly feasible. Any thermal annealing step would basically eliminate any pattern initially generated by nanoimprint lithography of the P3HT layer. It might however be possible, by careful optimization of treatment temperature and duration, to achieve a kind of guided interdiffusion of PCBM into the patterned P3HT layer. This could combine the advantages of a tightly interpenetrating network for efficient exciton dissociation along with continuous material paths for efficient charge transport to the electrodes. Finally, applying the transfer printing process developed here to another material system can lead to different results, which render it more suitable for the preparation of ordered heterojunctions.

3.3 Summary

We demonstrated thermal NIL as well as room temperature NIL using organic semiconducting P3HT films as imprint polymer. Commercially available Ni and Si/SiO_2 molds as well as custom built MBE-molds and porous alumina templates enabled imprinting patterns with feature sizes from hundred nanometers down to 20 nm. Our experiments revealed good pattern transfer quality into P3HT layers independent of the presence of other underlying polymer layers or the type of substrate incorporated. Thermal NIL processes were carried out at imprint temperatures around 120 °C, applying a standard imprint pressure of 70 bar for 300 sec. RTNIL processes were performed at significantly higher imprint pressures, i.e. approximately 350 MPa (3.5 kbar) applied for 10 s. Samples with multi-layer structures (e.g including PEDOT:PSS) were also produced to demonstrate process compatibility within more complex device architectures in the future. The future application of this technology to the fabrication of ordered heterojunction organic photovoltaic devices was discussed in detail. Finally, we proved that the NIL step involved in the fabrication of such kind of devices would not damage the polymer or alter its chemical or electrical properties. Clearly, imprint polymer flow characteristics and the stability of MBE-molds and imprint samples under RTNIL conditions as well as sidewall and surface characteristics of imprinted features have to be further analyzed and optimized. In order to bring the MBE-RTNIL scheme down into the sub 15 nm region it is necessary to investigate the flow characteristics of P3HT and its capability to fill mold features during the imprint step.

A simple and reliable transfer printing process was developed to enable a solvent-free deposition of organic semiconducting thin-films for the fabrication of bilayer/multilayer

based device architectures. P3HT and PCBM thin-films were successfully transfer printed using a supporting PDMS stamp. We were able to demonstrate that the transfer printing process does not affect any of the desired optical or electrical properties of the materials utilized. Further, organic photodetectors incorporating P3HT/PCBM bilayers fabricated by transfer printing were shown to exhibit a device performance comparable to that of conventional BHJ devices. Device performance improved dramatically upon thermal post-deposition treatment of the bilayers. By means of cross-sectional SEM as well as optical absorption analysis of as-prepared and thermally annealed samples, this performance enhancement was attributed to morphology evolution from a true bilayer towards a bulk heterojunction by intermixing of the materials composing the active layer. Moreover, changes in the optical absorption features related to P3HT suggest that intermixing occurs due to interduffusion of PCBM into the P3HT layer, which was recently concluded from DSIMS measurements performed by Treat et al. [88]. Similar to their findings, our investigations reveal that interdiffusion occurs rapidly at annealing temperatures common for this material system. We hence conclude that according to the results presented here, the realization of an ordered heterojunction using the given material system of P3HT and PCBM is hardly feasible.

Chapter 4

Polymer Thin-film Technology

In order to fully exploit the potential of polymer electronics, large-area/low-cost processing technologies suitable for thin-film deposition on arbitrary substrate materials and geometries are necessary. One very promising, yet little examined, deposition technique compatible to large-area industrial-scale processes is provided by spray technology. In this chapter we present a detailed investigation on the layer formation process during spray deposition of organic thin-films and its relation to solution properties and process parameters. It is demonstrated that the layer formation process can be thought of as a process of successively stacking individual droplets. Microscopy investigations indicate that individual droplets in a spray-coated layer can behave to a certain extent as a continuous layer. The technological framework developed here is successfully applied to the fabrication of organic photo-detecting devices as well as organic thin-film transistors. Gaining insight into the layer formation process represents an important step towards the realization of arbitrary shaped organic electronic devices fabricated by spray deposition.

Controlling the active layer composition in organic electronic devices represents one of the major challenges in their fabrication process. In particular, the composition of mixed donor/acceptor active layers for photosensitive device applications is known to strongly influence device performance. Here we report an alternative approach for the preparation of organic heterojunction photoactive layers by successive spray deposition of the donor material, poly(3-hexylthiophene) (P3HT), and acceptor material, [6,6]-phenyl C61-butyric acid methyl ester (PCBM). Optical absorption spectra, X-ray reflectivity, as well as cross-sectional TEM investigations are utilized to indicate the penetration of PCBM into a previously deposited P3HT layer and the spontaneous formation of a bulk heterojunction (BHJ) within the active layer, which provides the large interfacial area needed for efficient exciton dissociation. It is shown that organic photodiodes comprising photoactive layers

prepared using this fabrication method exhibit a performance comparable to conventional BHJ devices in which the active layer is rigorously blended in advance. Moreover, separate handling of the individual materials and their deposition from distinct solutions enables an enhanced control of the active layer composition and hence increases the ability of tuning device characteristics. From a practical perspective, devices with state-of-the-art performance can be fabricated in simple and controllable ways using an industrially relevant high-throughput process.

4.1 Spray Deposition of Polymer Thin-Films

Electronic devices based on solution-processable polymers are among the most promising applications of organic semiconductors. Low-cost fabrication by means of simple coating and printing techniques is one of their greatest advantages. Although various deposition techniques are feasible [2], [9], spin-coating is the dominating fabrication method in most research activities related to organic thin-film devices. Despite the simplicity and effectiveness of this technique in producing high quality thin films, it lacks several aspects necessary for large-scale production. In order to fully exploit the potential of polymer electronics, large-area/low-cost processing technologies suitable for thin-film deposition on arbitrary substrate materials and geometries are necessary. One very promising, yet little examined, alternative deposition technique is provided by spray technology. The most significant advantages associated with the utilization of spray technology are related to its compatibility to large-area industrial-scale processes. Its capability of following even complicated surface contours provides means for establishing a whole new range of potential applications where direct integration of polymer electronic devices onto various types of objects is needed.

Vak et al. were among the first to show that an optimized organic bulk heterojunction solar cell fabricated by spray deposition performed comparably to reference devices, which were fabricated by spin-coating [91]. Since then some work has been conducted on examining the choice of solvents and the effects of annealing on the performance of devices prepared using spray deposition [92], the influence of the spray gun settings on the film topography [93], the reproducibility of fully spray-coated organic photodetectors with low dark current densities [94], and the surface topography of spray-coated layers based on pristine solvents and multiple solvent systems [95]. We previously investigated the feasibility of air atomizing spray technology for large-area/low-cost fabrication of organic electronic and optoelectronic thin-film devices based on solution-processable polythiophene derivatives. There, a manually operated airbrush was utilized to fabricate different devices while

comparing electrical and electro-optical characteristics, as well as film morphology and roughness of spray-coated devices to those of spin-coated ones with similar structure [96].

Here we present a detailed investigation on the layer formation process during spray deposition of organic thin-films and its relation to solution properties and process parameters. By considering layer formation to be a stacking of individual droplets onto the substrate followed by partial merging between adjacent ones, we are able to correlate deposition conditions to the electrical and electro-optical characteristics of fabricated devices. Other than in previously reported research activities, we apply the technological framework developed here not only to the fabrication of organic photovoltaic devices, but also to the fabrication of organic thin-film transistors. This work clearly demonstrates the feasibility of this deposition technology for the fabrication of diverse organic electronic and optoelectronic devices independent of substrate material and geometry.

4.1.1 Materials and Methods

Spray technology is used in a wide variety of applications such as surface coating, humidification, combustion and many more. Each application area requires different spray nozzles to fulfill the specified criteria and achieve the desired results. The layers deposited here were sprayed by an air atomizing nozzle. This type of nozzles provides, along with ultrasonic spray nozzles, the finest degree of atomization. It is worth mentioning that ultrasonic spray nozzles have also been successfully applied to the deposition of active layers [97] and hole-selective contacts [36] in organic photovoltaic devices. For our static test system, a commercially available automatic air atomizing spray gun (Krautzberger GmbH, Germany) was used. All ink containing parts of the spray gun are resistant to organic solvents and are therefore suitable for the desired application. Figure 4.1(a) shows a schematic drawing of the test setup, indicating the vertical arrangement of nozzle and substrate. The spray gun contains an internal pneumatic control system which is activated by an electromechanical 3/2-way valve connected to a timer for precise spray time adjustment. Other spray gun settings that were varied to obtain the desired spray characteristics are material flow rate, atomizing gas (N_2) pressure and nozzle-to-sample distance. The performance of any kind of spray nozzle is strongly dependent on its size and geometry as well as on the physical properties of the liquid being atomized and the gaseous medium surrounding the droplets. For air-assisted nozzles the diameter of the orifice is the most significant dimension for atomization. Here a nozzle with 0.5 mm orifice diameter was chosen. The physical properties of the liquid being atomized have a direct effect on the flow and spray characteristics in a spray nozzle. Density, viscosity and surface tension are among the most critical fluid properties. As most liquids exhibit only minor differences in density, the significance of this property for atomization is rather low. However, higher

density tends to result in a larger average droplet size. An increased viscosity tends to hinder any natural instabilities leading to fluid breakup, which results in a delayed disintegration and increased average droplet size in the spray. Surface tension plays a very important role because it represents the force resisting the formation of new surface area. Hence it affects the droplet size as well as the spray angle. Fluids with higher surface tension tend to produce sprays with an increased average droplet size and a decreased spray angle. In addition, boiling point and vapor pressure of solvents are of great significance for the drying behavior of droplets in a spray and hence the process of layer formation. The three solvents used in the work presented here are Toluene, p-Xylene and o-Dichlorobenzene (Merck KGaA, Germany) having boiling points of 110.6 °C, 138.3 °C and 180.5 °C, respectively.

Different Deposition Regimes

In all our experiments the atomizing gas pressure was kept below 1 bar in order to achieve a reasonable spray pattern and prevent the gas flow from pushing away the droplets already on the substrate before completely drying. Depending on the solution to be deposited, i.e. polymer and solvent type, the nozzle-to-sample distance can only be varied within a certain range. One can distinguish between three regimes: wet, intermediate and dry [91]. In the wet regime, the nozzle-to-sample distance is low resulting in the formation of a wet polymer layer on top of the substrate, hence producing inhomogeneous layers with no real thickness control. On the other hand, in the dry regime, when the nozzle-to-sample distance is high, the entire solvent is evaporated before reaching the sample and a polymer powder is formed. The intermediate regime is the one more suitable for the deposition of organic thin films. In this regime, homogeneous layers can be formed and the thickness can be precisely controlled by adjusting the spray time. It is important to mention, that the evaporation rate of the atomized liquid, and hence the different deposition regimes, is strongly dependent on the properties of the chosen solvent (e.g. boiling point, vapor pressure) as well as the droplet size achieved for a given set of process parameters.

Device Fabrication

The general device architectures for the organic photodetectors and thin film transistors fabricated are illustrated in Fig. 4.1(b) and Fig. 4.1(c), respectively. For the fabrication of the organic photodetectors ITO electrodes with the desired structure were patterned on glass by conventional photolithography. The structured ITO-glass substrates were then cleaned by sonication in acetone and isopropanol in sequence. PEDOT:PSS aqueous dispersion (CLEVIOS™ P VP CH 8000) was deposited by spin coating at 2000 rpm for 20 sec and then dried on a hot plate at 150 °C for 15 min. The active layer of the device consisted of a blend of regioregular poly(3-hexylthiophene-2,5-diyl) (P3HT) (Rieke Metals, Inc.) and [6,6]-phenyl C61 butyric acid methyl ester (PCBM) (Solenne B.V.) as

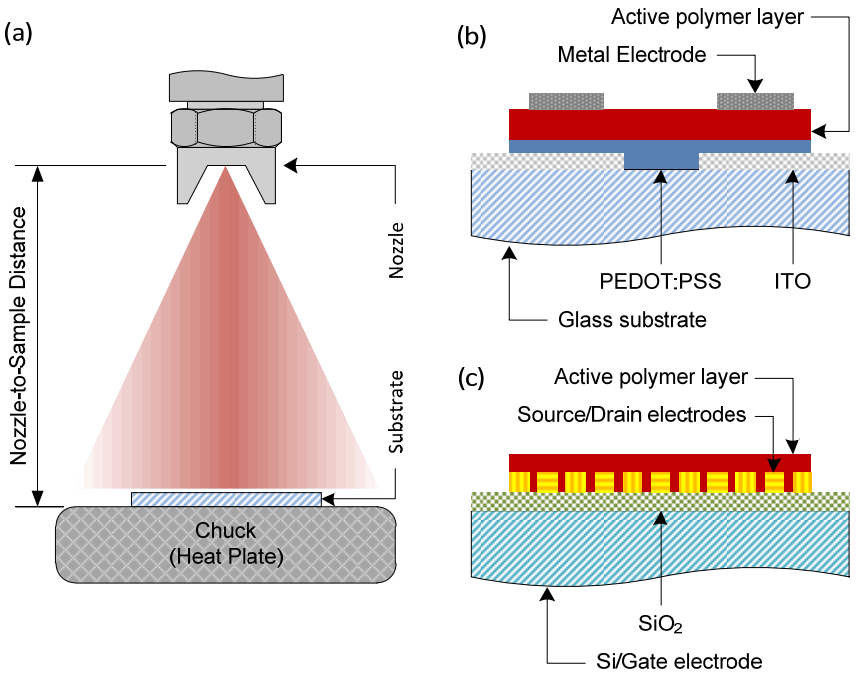

Figure 4.1: (a) Illustration of the implemented experimental setup for spray deposition, showing the basic components while indicating the vertical arrangement of nozzle and substrate. (b) General layout of an organic photodetector showing the layer stack comprising two organic layers sandwiched between two electrodes. (c) General layout of an organic thin-film transistor showing a single organic layer deposited onto an interdigitated electrode structure. For both device types the active polymer layer was spray-coated.

donor and acceptor materials, respectively. The P3HT:PCBM (1:1) blend was deposited from a solution of 0.5 wt% concentration in the different solvents. All samples were then placed again on a hot plate for annealing at 140 °C for 15 min. Finally, a LiF(1 nm)/Al(120 nm) cathode was thermally evaporated on top. The active area of each diode was defined by the ITO-electrode to be 25 mm^2. Organic Thin-Film Transistors were fabricated on highly p-type doped Si wafers, on which a 45 nm thick SiO_2 layer was thermally grown. An interdigitated electrode structure (IDES) consisting of a 2 nm thick Ti layer (to promote Au adhesion on Si) followed by a 45 nm Au layer was evaporated on top of the SiO_2. The spacing formed between the source and drain contacts of this interdigitated structure was chosen to be 20 µm. Regioregular P3HT was used as a semiconductor for the channel of our p-type TFT and was deposited on top of the sample from a solution of 0.5 wt% concentration in xylene. Device fabrication was finalized by an annealing step at 120 °C for 10 min. It should be noted that all organic layers were deposited in ambient conditions, while only annealing steps and device encapsulation were performed under inert gas atmosphere inside a glove box.

4.1.2 Selected Deposition Approach

Operating in the intermediate regime, the process of layer formation can be thought of as a process of successively stacking individual droplets onto the substrate at a certain rate. In the following we will discuss experimental results supporting this idea and correlating it to the performance of fabricated devices. By the correct choice of process parameters the effect of dissolving previously deposited droplets by new ones can be significantly minimized. This allows the fabrication of devices with more complicated layer stacks from the same solvent. However, if droplets arriving at the substrate are too dry, it can be assumed that a large portion of these droplets form separate domains and that charge transport across domain boundaries is impeded. For this reason, droplets arriving at the substrate surface should still be wet to an extent allowing a minimum of merging between individual droplets. Spray deposition from low boiling point solvents shows a higher sensitivity to process parameters and ambient condition variations due to a narrower intermediate regime and hence suffers from poor reproducibility. The lower evaporation rate of high boiling point solvents makes the deposition process less sensitive and easier to control over a larger parameter space. In order to ensure an optimal merging between droplets, we introduce a deposition approach in which we operate within the wet regime while heating up the substrate in order to speed up the drying of wet droplets arriving at the substrate. This approach allows the formation of dry layers with good thickness control over time, enhancing at the same time reproducibility, especially of devices deposited from low boiling point solvents (e.g. Toluene). The substrate heating during deposition is a very important parameter which still has to be carefully optimized. Our investigations showed that, as a rule of thumb, the substrate temperature should be close to the boiling point of the used solvent. This turned out to be valid also for spray deposition of the conducting polymer PEDOT:PSS (aqueous dispersion), which confirmed the applicability of our deposition approach to other organic conducting and semiconducting material systems in different types of solvents.

4.1.3 Organic Bulk Heterojunction Photodetectors

Spray Deposition of Photoactive Layer

Figure 4.2(a) shows a comparison of the IV-characteristics of four spray-coated organic photodetectors (OPDs) D1, D2, D3 and D4 where a dichlorobenzene based P3HT:PCBM blend was sprayed for 10, 15, 20 and 25 sec, respectively. Each device was measured under dark and illuminated (halogen light source with 100 mW/cm^2) conditions. A clear decrease of the dark current density can be observed for longer spray durations, i.e. higher layer thickness, leading to an increase in the on/off-ratio of the respective OPD. Sample D4 exhibits a dark current density as low as $3.8 \cdot 10^{-5}$ mA/cm^2 and an on/off-ratio of $8.2 \cdot 10^4$ at

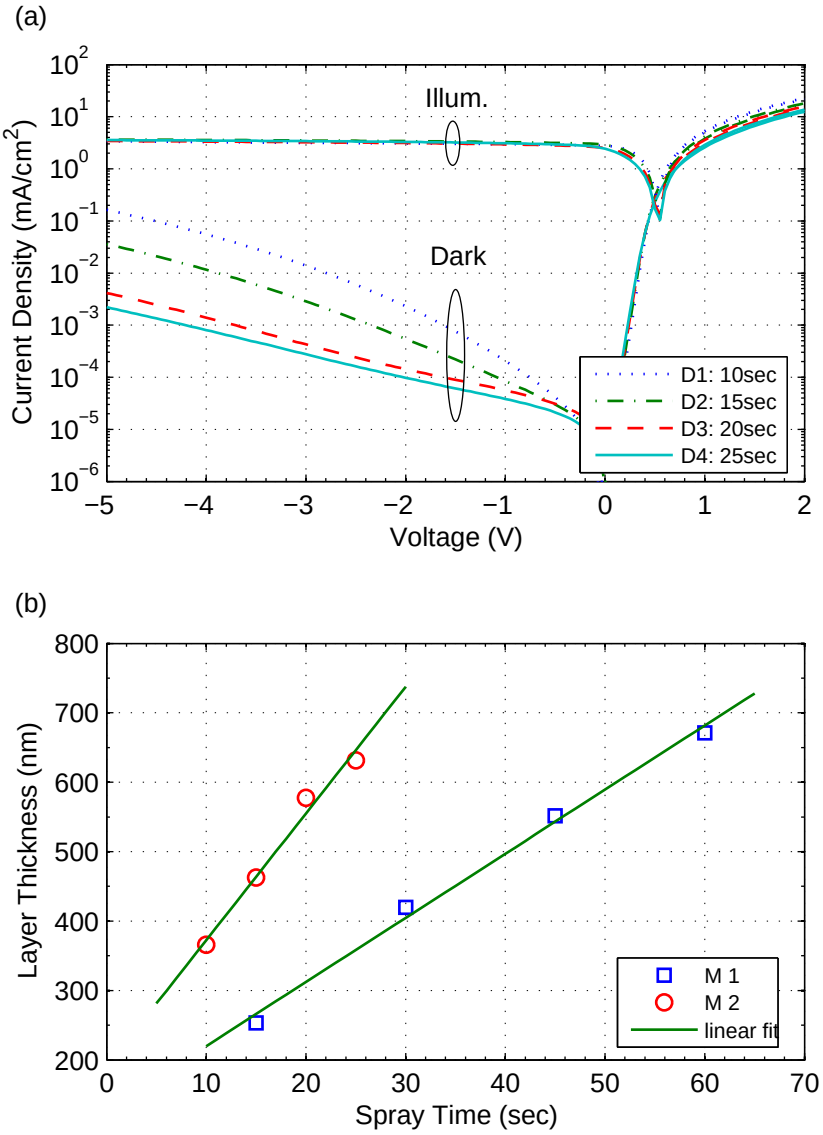

Figure 4.2: (a) Comparison of the IV-characteristics of four spray-coated OPDs D1, D2, D3 and D4 with a P3HT:PCBM blend sprayed for 10, 15, 20 and 25 sec, respectively. (b) An estimated layer thickness calculated from transmission measurements of spray-coated layers plotted versus spray duration. M1 and M2 indicate two different material flow rates, where M2>M1.

−1 V bias. This low dark current density is remarkable considering the relatively large active area of our devices compared to the ones reported by Tedde et al. [94]. Due to the increased layer thickness however, the series resistance rises from 81 Ω/cm^2 for D1 to 155 Ω/cm^2 for D4, leading to a decrease in the forward current density. Nevertheless, we are still able to achieve around one order of magnitude higher forward current densities at +2 V, with respect to devices presented by Tedde et al. [94]. This indicates an enhanced charge transport in layers prepared using our deposition approach. Due to the extremely high surface roughness, which depending on spray parameters can be above 100 nm [96],

precise layer thickness measurement using profilometry or atomic force microscopy become rather meaningless. To be able to quantify the layer thickness and gain an idea about its dependence on the spray duration, optical transmission measurements on spray deposited layers were performed and the absorption spectrum of the blend material was calculated from reference measurements carried out on spin-coated layers of known thickness. An absorption coefficient of approx. $1 \cdot 10^5$ cm^{-1} at a wavelength of 510 nm (P3HT absorption peak), which corresponds to values found in literature [98], was then used to estimate the thickness of spray deposited layers. Note that the value obtained from this calculation represents an averaged absorption thickness over the illuminated area of about 25 mm^2, which is on a significantly larger scale than that of the individual droplets. The estimated layer thickness was then plotted versus spray duration and is shown in Fig. 4.2(b). M1 and M2 indicate two different material flow rates, where M2 is higher than M1. The four measurement points shown for M2 in the figure correspond to the four devices shown in Fig. 4.2(a). By fitting a line through the measurement points it becomes clear that for the correct choice of spray parameters, the layer thickness exhibits a linear dependence on the spray duration over a wide range. In order to further verify the suggested description of the layer formation process, we examined single-coat and multiple-coat deposition. For this purpose two OPDs were fabricated, in which the P3HT:PCBM layer was deposited as a single coat of 30 sec spray duration for the first device D5 and as a double coat of 15 sec spray duration each for the second device D6. The IV-characteristics of both devices are plotted in Fig 4.3, showing almost identical behavior with only small discrepancy, which lies within the usual fabrication uncertainty and can therefore be neglected, confirming results already obtained by Tedde et al. [94] and further supporting the suggested description of the layer formation process.

Choice of Solvent

Single layers as well as complete OPDs presented so far were deposited from a dichlorobenzene based P3HT:PCBM solution. The reasons for preferring a high boiling point solvent were already discussed at the beginning of this section. Nevertheless, it is possible to fabricate devices with reasonable performance from other solvents, such as toluene and xylene. Due to the different behavior of each solvent when sprayed, most process parameters have to be entirely readjusted for each solvent. This makes a direct comparison between devices fabricated from different solvents rather misleading. Instead, we present the best device obtained out of each solvent, while applying only necessary changes to spray settings. For the same reason, we preferred to fix the substrate temperature used for spray deposition of the P3HT:PCBM blends to 150 °C for all three solvents discussed in this section. Figure 4.4 shows the IV-characteristics of three devices (D7, D8 and D9) fabricated from three different solvents. All three devices exhibit low dark current densities of around $4 \cdot 10^{-5}$ mA/cm^2 and an on/off-ratio between $4.6 \cdot 10^4$ and

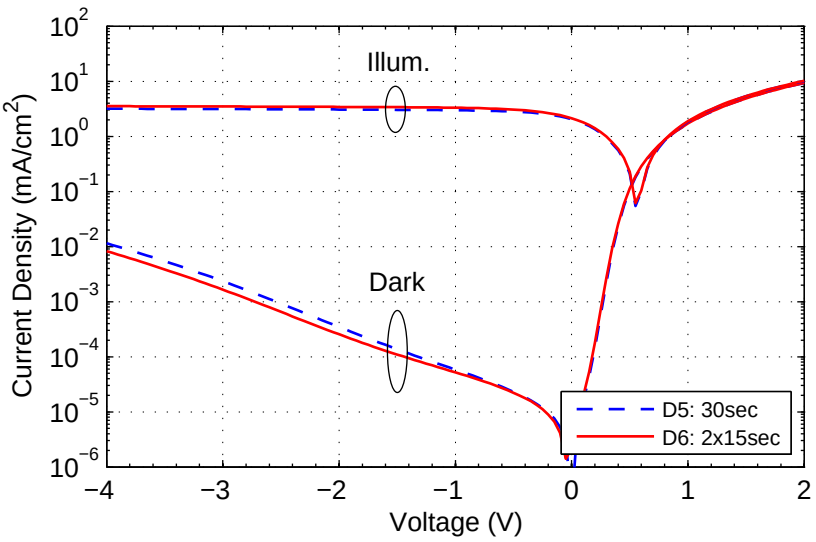

Figure 4.3: IV-characteristics of devices fabricated by depositing the blend as a single coat of 30 sec spray duration for the first device D5 and as a double coat of 15 sec spray duration each for the second device D6.

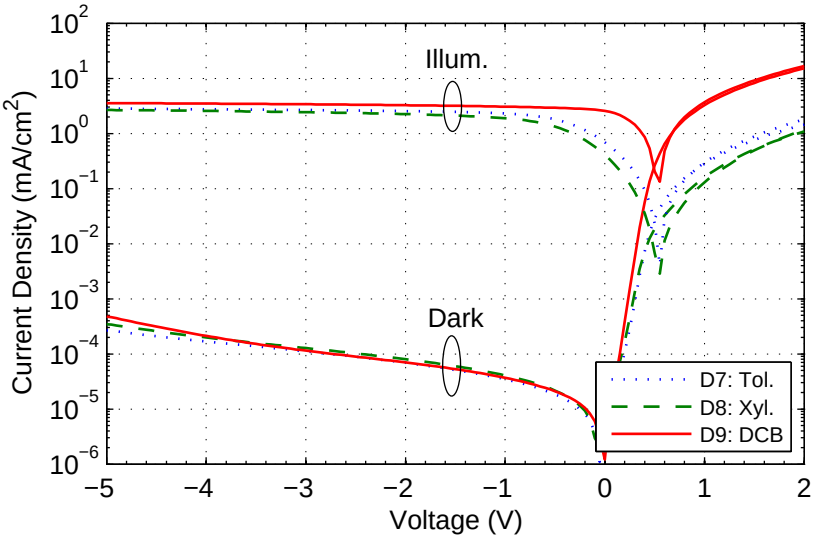

Figure 4.4: IV-characteristics of three devices (D7, D8 and D9) representing the best device obtained from each of the three solvents, toluene, xylene and dichlorobenzene.

$8.4 \cdot 10^4$ at −1 V bias, while maintaining a dark current density as low as $4.6 \cdot 10^{-4}$ mA/cm^2 and an on/off-ratio of $7.8 \cdot 10^3$ even at −5V bias in case of D9. At low reverse bias (below −1 V) and under forward bias however, the dichlorobenzene based device shows significantly higher current density, which is up to one order of magnitude higher than for the other two devices at a bias voltage above +1 V. In addition to that, the best results of devices prepared from a dichlorobenzene based solution were easier to obtain, less sensitive to variations in the process parameters and hence showed a much higher reproducibility.

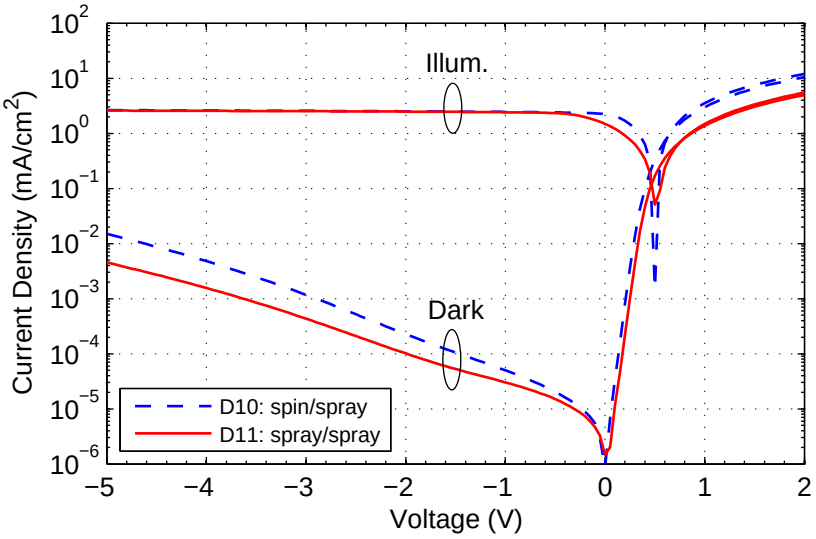

Figure 4.5: Comparison of the IV-characteristics of two OPDs where the PEDOT:PSS film is either spin-coated (D10) or spray-coated (D11), while the P3HT:PCBM blend film is spray-coated in both cases for 20 sec.

Spray Deposition of Hole Injection Layer

To demonstrate the applicability of this technique to other polymer materials involved in the fabrication of OPDs, it was applied to the deposition of the conducting polymer PEDOT:PSS (aqueous dispersion). Two devices were prepared, where the PEDOT:PSS layer was spin-coated for one of the samples (D10) and spray-coated for the other (D11), while all other processing condition were kept identical. The IV-characteristics of D10 and D11 are plotter together in Fig. 4.5, which show almost identical photocurrent under reverse bias. The reduced dark and forward current observed for spray-coated PEDOT:PSS layers are attributed to an increased effective thickness of the layer. It should be noted that, in contrast to P3HT:PCBM, spray deposition of PEDOT:PSS was not optimized within this work and hence there is still high potential for further enhancement of device performance.

4.1.4 Process of Layer Formation

Based on the linear relation of layer thickness and spray duration as well as the similarity between single-coat and multiple-coat deposition, we can confirm our view of the layer formation process proposed at the beginning of this chapter. This is further supported by examining microscopic images of spray deposited blend layers, as shown in Fig. 4.6(a). In this image individual droplets can be distinguished and a pinhole-free layer is built up by the successive stacking of such droplets. Spreading and deformation of droplets upon impact on the substrate could also be observed in other optical and atomic force

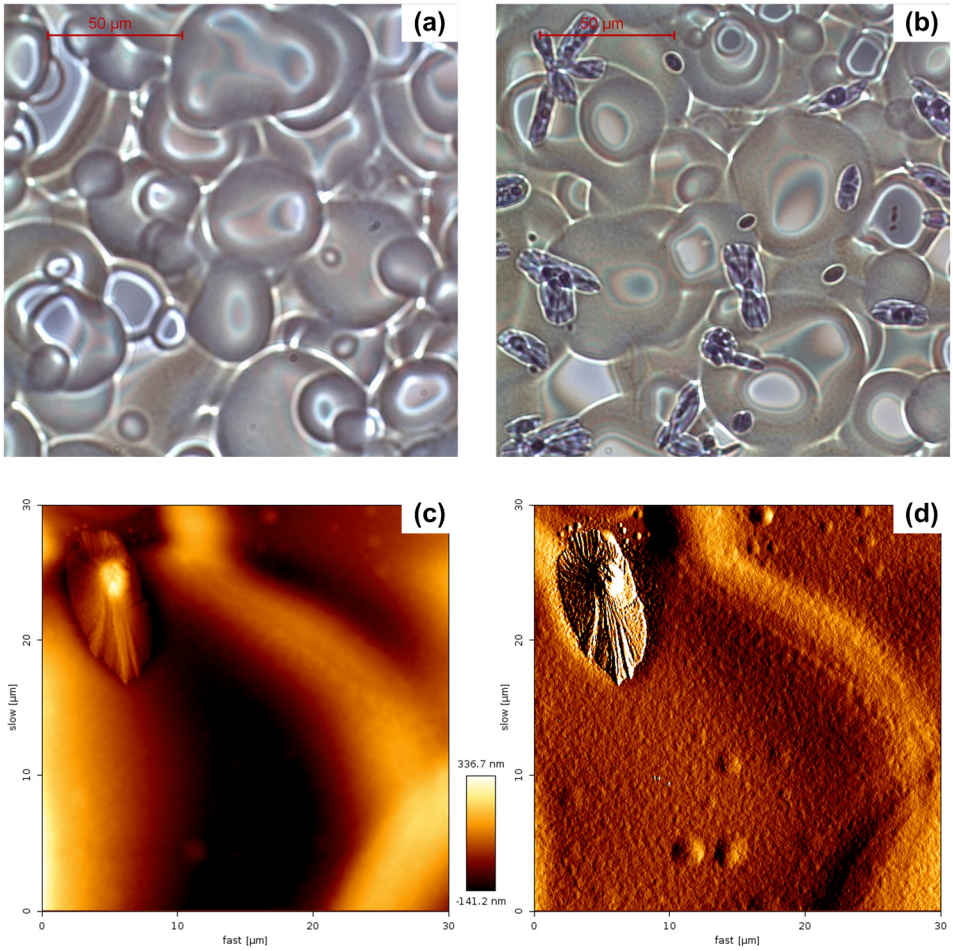

Figure 4.6: (a) Microscopic image of a spray deposited blend layer. Individual droplets can be distinguished and a pinhole-free layer is built up by the successive stacking of such droplets. (b) Microscopic image of the same layer after a thermal annealing step, which reveals the formation of the typical and well-known PCBM crystalline structures. (c) AFM height image of the spray-coated P3HT:PCBM layer after annealing, visualizing the huge height differences existing. (d) An error image of the same area, clarifying the contours of the individual droplets and indicating the formation of a PCBM crystalline structure across their boundaries.

microscopy images, which are not shown here. Droplets, which are originally assumed to be spherical, are deformed into more disk-like structures of increased diameter and heightened boundaries. This deformation is typical for spray deposited layers and is expected to depend on the droplet velocity at impact and solvent properties such as surface tension. Topography investigations carried out on spray deposited layers by atomic force microscopy reveal an extremely high surface roughness on a scale larger than the average droplet dimensions. Despite this high surface roughness, the results presented above demonstrate state of the art OPDs fabricated by spray deposition. On a sub-micrometer scale, a surface topography similar to spin-coated layers can be observed, which was suggested to indicate a similar nano-morphology and hence be one of the reasons for the good device performance [96]. Hoth et al. observed no significant difference in the ideality

factor measured for spray-coated and doctor-bladed devices. This was explained by a rather comparable distribution of the donor and acceptor interfaces throughout the bulk of the heterojunction, again indicating a similar nano-morphology [95]. Taking a closer look on optical microscopy images of the same spray deposited layer shown in Fig. 4.6(a), this time however after the thermal annealing step usually performed for all devices, reveals the formation of the typical PCBM crystalline structures well known from the annealing of spin-coated P3HT:PCBM layers [99–101]. Such an image is shown in Fig. 4.6(b). It is interesting to notice that the crystallization of PCBM does not seem to be confined only within individual droplets, but is rather randomly distributed and can occur across the droplet boundaries as well. The existence of such crystalline structures reaching even over several droplets indicates that individual droplets in a spray-coated layer can behave to a certain extent as a continuous layer depending on the degree of merging between droplets during deposition and do not necessarily act as isolated domains. This picture is consistent with our proposed view of the layer formation process and gives another possible explanation for the competitive device performance of spray-coated OPDs. Figure 4.6(c) shows an AFM height image of the spray-coated P3HT:PCBM layer after annealing measured in contact mode. There a crystalline PCBM structure can be seen while visualizing the huge height differences existing in a spray-coated layer. An error image of the same area is shown in Fig. 4.6(d), clarifying the contours of the individual droplets and the formation of the PCBM crystal across their boundaries.

4.1.5 Organic Thin-Film Transistors

Spray technology was also used to fabricate other classes of organic thin-film devices, such as organic light emitting diodes (OLED) based on MEH-PPV as the light emitting polymer and organic thin-film transistors (OTFT) based on P3HT as the p-type semiconducting polymer. Here we will present some of the results obtained for the OTFTs fabricated using spray deposition. First devices were prepared using exactly the same approach as for the OPDs, meaning that the polymer was deposited in the wet regime on a heated substrate forming a dry layer. The measured output characteristics (I_D-V_{DS}) of this kind of device are shown in Fig. 4.7(a) along with the corresponding transfer characteristics (I_D-V_{GS}) shown in Fig. 4.7(b). Upon examination of these plots, one can clearly observe a transistor-like behavior with saturating drain current. The drain current of such spray-coated OTFT is about one order of magnitude lower than what is usually expected from devices of the same structure fabricated using other deposition techniques. This is also reflected in an extracted field effective mobility of approx. $1.02 \cdot 10^{-4}$ cm^2/Vs. Further, an on/off-ratio of only $5.8 \cdot 10^{1}$ can be achieved. The lower mobility may not be surprising if the process of layer formation is taken into account, where the droplets arriving at the substrate are immediately dried. Such a fast growth of the active layer is known to have a negative

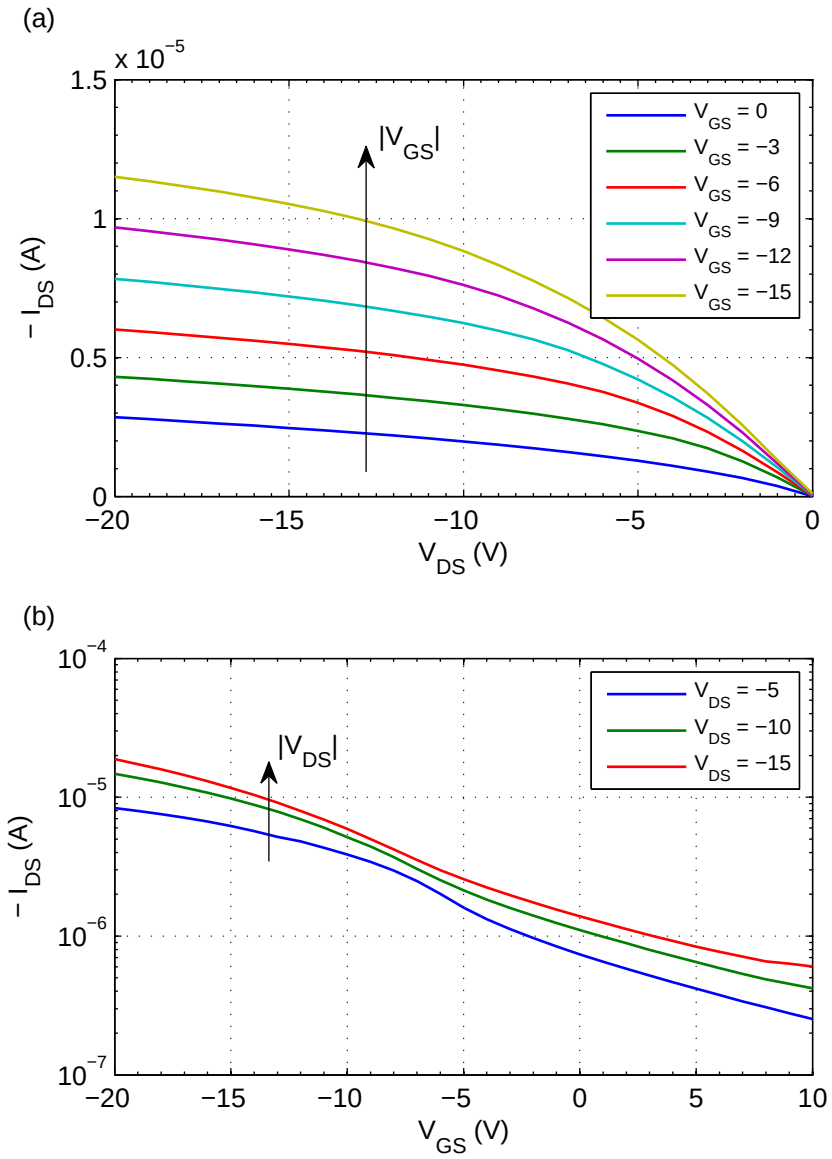

Figure 4.7: (a) Output characteristics (IDVDS) of a device where the active polymer was deposited in the wet regime on a heated substrate forming a dry layer and (b) the corresponding transfer characteristics (IDVGS).

effect on the mobility of OTFTs [102], [103]. By operating the spray gun in the wet regime without heating the substrate, a wet layer of P3HT is formed on top of the substrate. This wet layer is then left to dry for some time, thereby introducing more time for reorganization. The inhomogeneous P3HT layer resulting from this deposition approach does not cause any additional problems. This is due to the fact that the P3HT layer thickness does not play an important role in device performance as long as it is sufficiently thick to allow the formation of a channel between source and drain contacts. By applying this deposition approach, the layer formation process becomes comparable to processes such as drop casting and dip coating, where a slow growth of the layer is achieved.

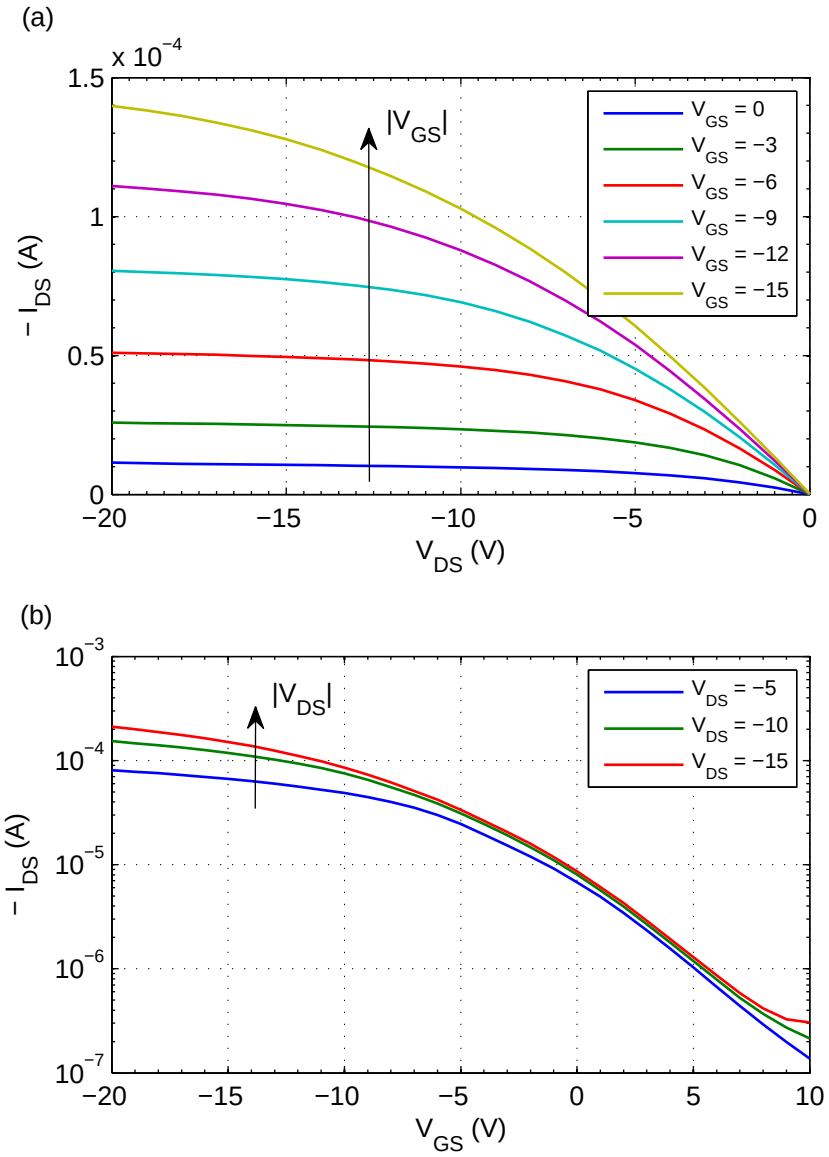

Figure 4.8: (a) Output characteristics (IDVDS) of a device fabricated using a wet deposition approach and (b) the corresponding transfer characteristics (IDVGS). A field effective mobility of approx. $1.1 \cdot 10^{-3}$ cm^2/Vs can be calculated for the wet deposited device, which is about one order of magnitude higher than for the other.

Figure 4.8(a) shows the output characteristics of an OTFT fabricated using the wet deposition approach. There significantly higher currents of up to 140 µA at −20 V drain bias and −15 V gate bias can be observed. The field effective mobility calculated from the transfer characteristics of such devices, plotted in Fig. 4.8(b), is approx. $1.1 \cdot 10^{-3}$ cm^2/Vs and an on/off-ratio of $5.8 \cdot 10^2$ can be measured at −5 V drain bias.

4.2 Successive Spray Deposition

Organic solar cells and photodiodes have been subject of extensive research in recent years. Independent of the application of the photosensitive device, designs based on the bulk heterojunction (BHJ) concept showed the best performance. There a photoactive conjugated polymer is intimately blended with an electron acceptor, usually a fullerene, to form an interpenetrating network of both materials. The large interfacial area leads to efficient exciton dissociation at the interfaces and increases external quantum efficiency. Different studies have shown that device performance strongly depends on the morphology of the blend film, which is in turn related to the processing conditions [21], [22], [104]. Major drawbacks of the BHJ approach however are related to issues of carrier extraction rather than exciton diffusion and dissociation. Paths of a single material, donor or acceptor, forming continuous connections between anode and cathode lead to a decreased shunt resistance. Isolated islands of any of the two materials lead to trapping of carriers, which then do not contribute to the photocurrent. Vertical composition gradients resulting from the segregation of the donor material towards the anode interface and the acceptor material towards the cathode interface are believed to be beneficial for device performance. This is considered to be a result of efficient exciton dissociation due to intimate intermixing of the components as well as efficient charge transport and enhanced electrode selectivity.

Campoy-Quiles et al. used optical techniques to probe the final morphology of P3HT:PCBM films fabricated using different procedures [101]. They demonstrated that different treatments of P3HT:PCBM blends all lead to a common arrangement of the components, which consists of a vertically and laterally phase-separated blend of crystalline P3HT and PCBM. A simple method for improving the unfavorable vertical composition gradients of P3HT and PCBM in the photoactive layer of BHJ solar cells was proposed by Liang et al. [105]. There a thin layer of P3HT was deposited on top of the PEDOT:PSS prior to spin-coating the P3HT:PCBM blend, resulting in enhanced electron blocking at the anode side, efficiency of photoinduced electron transfer and photocurrent of the device. PCBM was chosen by Kumar et al. as the acceptor material to be thermally deposited on top of the P3HT:PCBM active layer to achieve a vertical composition gradient in the BHJ structure [106]. The observed increase in efficiency was attributed to improved transport and extraction of electrons near the cathode. Wang et al. fabricated a polymer photovoltaic device with P3HT/PCBM bilayers as active film with a concentration gradient by choosing the proper solvent system for each layer [107]. Since the solvent for the upper PCBM layer can partially swell the bottom P3HT layer, an intermixed zone with a concentration gradient of P3HT and PCBM is created between two layers. The devices showed an enhanced photocurrent density and power conversion efficiency compared to those of the bulk heterojunction PV prepared under the same

fabrication condition. An almost identical experiment was conducted by Ayzner et al., leading to similar results but with a significantly different interpretation of those results [108]. They demonstrate that o-dichlorobenzene and dichloromethane serve nicely as a pair of orthogonal solvents from which sequential layers of P3HT and PCBM, respectively, can be spin-cast. Atomic force microscopy, various optical spectroscopies, and electron microscopy are reported to demonstrate that the act of spin-coating the PCBM overlayer does not affect the morphology of the P3HT underlayer, so that the authors claim to have a well-defined planar interface in their spin-cast P3HT/PCBM bilayers. This seems to be in strong contrast to the formation of the concentration graded bilayer shown by Wang et al. using an identical set of solvents.

Here we introduce an alternative approach for the preparation of organic heterojunction photoactive layers by successive spray deposition of the donor and acceptor materials comprising such a layer. Separate handling of the two materials and their deposition from distinct solutions provides a major degree of freedom in the formation of the active layer morphology/composition and hence in the ability of tuning device characteristics. Similar advantages were recently demonstrated by Chen et al. for organic solar cells fabricated by alternating spay deposition [109]. In contrast to their method, where the active layer is built by an alternating deposition of donor and acceptor materials to achieve intermixing of the components, we rely on a self-mixing of components inherent to our deposition routine, in addition to material interdiffusion occurring in the photoactive layer. Further, organic photodetectors with successively sprayed photoactive layers are fabricated. We demonstrate that rigorous blending of the two solutions prior to deposition is not necessary for obtaining good device performance. The blend required for the formation of a higher surface area at the heterojunction interface is shown to be created during deposition as a result of the deposition method employed here in combination with the thermal post-deposition treatment. Results presented are consistent with very recent data of morphology evolution in P3HT/PCBM bilayer model systems, where rapid interdiffusion of PCBM into P3HT upon thermal annealing is shown to result in the spontaneous formation of nanomorphologies equivalent to those in conventional BHJ systems [88], [89], [110].

4.2.1 Materials and Methods

One of the major challenges in the fabrication of organic electronic devices based on solution-processable polymers is the successive deposition of multiple layers of different organic materials. The problem arises from the fact that many of these materials are soluble in the same set of solvents, making it rather complicated to implement even simple bilayer architectures directly deposited from solution. Depositing an additional layer on top of an existing one usually results in partial dissolving and/or swelling of the underlying

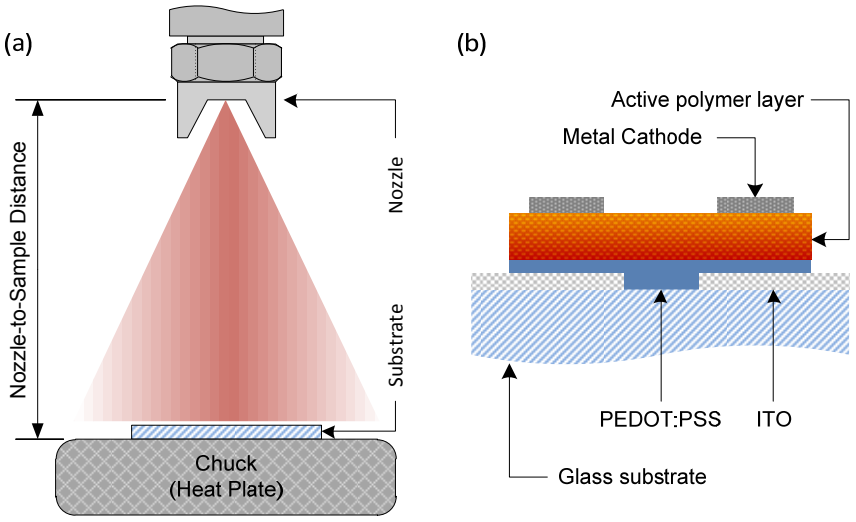

Figure 4.9: (a) Schematic drawing of the experimental setup, indicating the vertical arrangement of nozzle and substrate. (b) General device architecture of an organic photodiode illustrating the layer stack involved.

layer due to the solvent present in the solution. The degree of dissolving strongly depends on solvent properties as well as deposition method involved in the process. Spray deposition is considered to minimize this issue due to the fast evaporation of the tiny droplets arriving at the substrate [93], [96], [111]. Here we demonstrate that successive spray deposition of the donor and acceptor materials of the photoactive layer in an organic photodiode, using the same solvent, still leads to significant intermixing of the materials allowing the formation of an interpenetrating network required for achieving performances comparable to those of conventional blend devices. Figure 4.9(a) shows a schematic drawing of the experimental setup used, indicating the vertical arrangement of nozzle and substrate. The general device architecture of our organic photodiode is illustrated in Fig. 4.9(b). One of the main advantages of spray deposition for this kind of process is the uniform distribution of small-volume droplets in the area of interest which in turn gives a uniform dissolving and intermixing over time and enables high reproducibility of the fabricated devices. This is in strong contrast to other deposition methods, such as spin-coating, where a large-volume solution is usually dispensed locally causing non-uniform dissolving of the underlying layer and hence poor reproducibility due to significantly longer interaction time with the solvent.

Experimental Setup

The experimental setup used to fabricate all samples is composed of an air atomizing spray gun in a vertical static arrangement with respect to a heatable substrate. The main spray parameters to be adjusted for obtaining desired spray characteristics are material flow rate, atomizing gas (N_2) pressure, nozzle-to-sample distance and substrate temperature. A

commercially available spray gun (Krautzberger GmbH, Germany) with 0.5 mm orifice diameter is utilized for the disintegration of the organic solution. The atomizing gas (N_2) pressure was kept below 1 bar throughout all experiments in order to obtain the desired spray characteristics and a uniform spray pattern across the area of interest. More details regarding spray setup and parameters were already discussed in the first part of this chapter and published [111].

Solution Preparation

Solutions of the pristine acceptor and donor materials were prepared in o-dichlorobenzene (o-DCB) with 1 wt% concentration using regioregular poly(3-hexylthiophene-2,5-diyl) (P3HT) (Rieke Metals Inc.) and [6,6]-phenyl C61 butyric acid methyl ester (PCBM) (Solenne B.V.), respectively. The blend solution consisting of a P3HT:PCBM (1:1) mixture, used for the fabrication of reference devices, was similarly prepared in o-DCB with 1 wt% concentration.

Device Fabrication

For the fabrication of our organic photodiodes, pre-patterned ITO-glass substrates were cleaned by sonication in acetone followed by isopropanol. A PEDOT:PSS aqueous dispersion (CLEVIOS™ P VP CH 8000) was deposited by spin coating at 2000 rpm for 20 sec and then dried on a hot plate at 150 °C for 15 min. The active layers were then deposited from the desired solutions using our above described spray setup. Finally, the cathode consisting of 1 nm LiF and 100 nm Al was thermally evaporated on top. Samples were placed on a hot plate for annealing at 150 °C for 15 min. either before or after deposition of the metal top electrode. The active area of each diode was defined by bottom and top electrode geometry to be either 25 mm^2 or 9 mm^2. Note that the organic active layers were deposited in ambient conditions, while only annealing steps and device encapsulation were performed under controlled nitrogen atmosphere inside a glove box.

Active Layer Characterization

Depending on the refractive index of the materials used X-ray reflectivity measurements allow a film composition analysis parallel to the sample normal and can be used to investigate the crystallinity of the semi-crystalline P3HT. The X-ray reflectivity data were taken at a Siemens D5000 diffractometer at a wavelength of 0.154 nm (Cu-Kα radiation) in an angular range from 0° to 6° using a θ-2θ geometry. Silicon substrates were used in order to minimize the substrate influence on the recorded reflectivity curve. Since the sample preparation was identical to that of the final device prepared on ITO substrates, same film morphologies can be expected. In addition a knife edge was used to limit the beam size and to reduce the background. The reflected intensity was recorded via a point detector, which was protected by an automatic beam absorber. For analysis the reflectivity data were fitted

with the Parrat32 reflectivity simulation software [112]. X-ray reflectivity measurements presented here were carried out by the group of Prof. Peter Müler-Buschbaum, Lehrstuhl für Funktionelle Materialien, Physikdepartment E13, Technische Universität München.

For TEM investigations samples were spray coated as described above on a silicon substrate because of the relative ease of cross sectional sample preparation for a silicon substrate. In addition, for protecting the active layer from the rigors of TEM sample preparation a thin aluminum layer (~100nm) was deposited on top of the active layer. The material was cut into slices, inserted in a brass tube, and thinned by mechanical grinding and dimpling. Subsequently precision ion polishing was employed for the final thinning process using a Gatan Precision Ion Polishing System operated with argon ions at 3keV and liquid nitrogen cooling. The TEM measurements were performed on a FEI TITAN 80-300 operated at 80 and 300keV. Since the specimen were surprisingly stable upon irradiation with the electron beam, images shown in this work were acquired while operating the TEM at 300keV as it allowed investigation of thicker specimen regions. Scanning transmission electron microscopy (STEM) in high angular annular dark field (HAADF) mode was employed with a convergence semi-angle of 9.5mrad to acquire images with z-contrast dependency. In conjunction, selected area electron diffraction (SAED), energy dispersive X-ray spectroscopy (EDX) and electron energy loss spectroscopy (EELS) were employed for analytical measurements. TEM investigations presented here were carried out by the group of Prof. Christina Scheu, Professur für Transmissionselektronenmikroskopie, Department Chemie & CeNS, Ludwig-Maximilians-Universität München.

Device Characterization

Optical absorption spectra as well as external quantum efficiency (EQE) were measured using a chopped 300 W xenon arc research source passing through an Oriel Cornerstone 260 1/4 m monochromator and a calibrated silicon photodiode with pre-amplifier connected to an Oriel Merlin digital lock-in radiometry system. For the IV-characterization of the OPDs, dark current measurements were performed inside a dark box while photocurrent measurements were performed under illumination with a tungsten halogen source at 100 mW/cm^2.

4.2.2 Partial Dissolving and Intermixing

As a first step towards the realization of a heterojunction with controlled morphology and/or composition by our proposed method of successive spray deposition, it is necessary to carefully examine the extent of partial dissolving and intermixing on previously deposited underlying layers and its implications on the integrity of this layer. For this

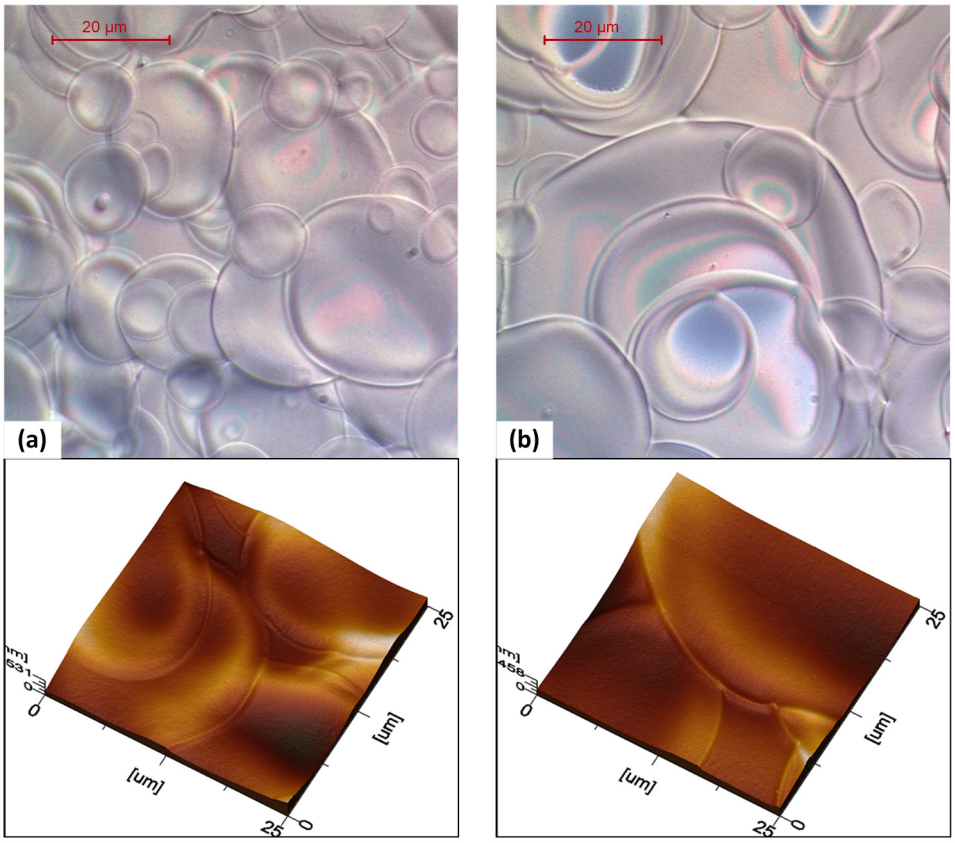

Figure 4.10: (a) Optical and atomic force microscopy images of a spray deposited layer of pristine P3HT showing typical disk-like structures with heightened boundaries originating from dried solution droplets. (b) Images of the same layer after spray deposition of pure dichlorobenzene showing changed surface features and an increased average diameter of the droplet boundaries.

purpose, P3HT was spray deposited from a o-dichlorobenzene (o-DCB) based solution directly onto a glass substrate to form a pristine layer of the donor material. In a following step, pure o-DCB was sprayed on top of the P3HT layer in a region well defined by shadow masking. Samples were then characterized by comparing optical as well as atomic force microscopy (AFM) images of unexposed and exposed regions of the P3HT layer. By spraying pure o-DCB it is possible to visualize the impact of solvent droplets hitting the surface of the polymer without having actual deposition of another material. Figure 4.10(a) shows the optical and AFM images of a protected area of the P3HT layer. One can clearly identify the typical disk-like structures with heightened boundaries formed upon impact of individual droplets on the substrate surface and their subsequent drying. The polymer layer is then built up by the stacking of such droplets which are assumed to merge to some extent by partial dissolving of previously deposited droplets [111]. For comparison, images of an unprotected area on the same sample are shown in Fig. 4.10(b). The most noticeable difference is a significantly increased average diameter of the droplet boundaries in the latter case. Changes in the general feature dimensions of the surface indicate a

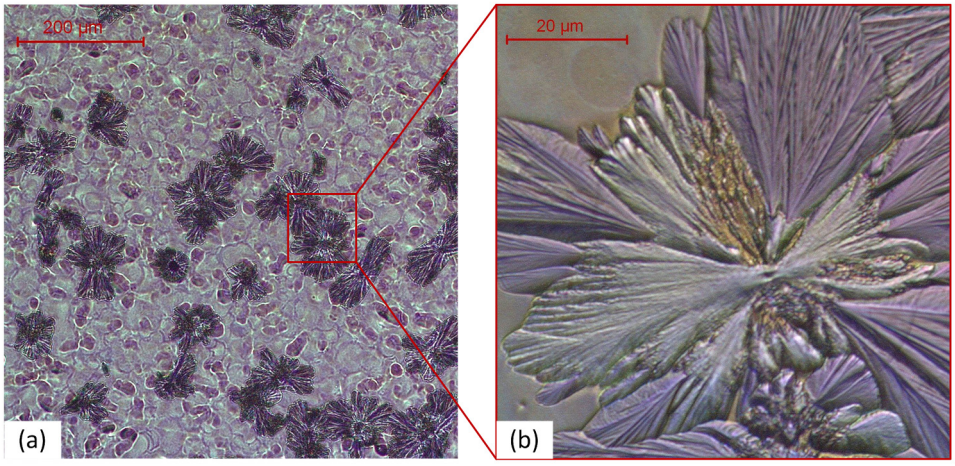

Figure 4.11: Optical microscopy image of a thermally annealed P3HT/PCBM layer prepared by successive spray deposition of the individual components (left). The details of a typical PCBM crystalline structure existing on the surface are shown in a zoom-in (right).

modification of the layer topography and/or morphology upon impact of the solvent droplets. This phenomenon is best described by the partial dissolving and subsequent resolidification of the polymer with redefined features, induced by wet solvent droplets hitting the polymer surface. Further, it can be seen that the penetration of droplets can reach the substrate at some points creating pinholes in the polymer layer. This indicates that locally the acceptor material will be directly in contact with the hole-extraction layer, in our case PEDOT:PSS. Nevertheless, globally the donor material concentration will remain predominant at this interface. Such a P3HT-rich layer at the hole-extraction interface should be beneficial for device performance as already described above. The extent of penetration and hence intermixing of the different layers strongly depends on spray parameters as well as solvent properties, providing means for tuning active layer morphology and device performance. However, an interaction with the residual solvent during deposition is expected to result in a coarse intermixing occurring at a scale close to that of the droplet dimensions.

Taking a close look at optical microscopy images of separately sprayed P3HT and PCBM layers reveals no significant difference in surface topography as both layers exhibit typical features of a spray deposited layer. This changes drastically after thermal post-deposition annealing, which does not show any visible modification of the P3HT layer while the PCBM layer shows strong crystallization over the entire area. The droplet boundaries present before annealing almost completely vanish in the thermally treated layer of PCBM. A similar behavior can be observed when spraying PCBM as acceptor material on top of a previously deposited layer of P3HT as donor material. Optical microscopy images of such a layer after thermal post-deposition treatment are shown in Fig. 4.11. There are two main characteristics to be pointed out here, the density and size of the PCBM crystalline

structures visible in the image. Compared to a conventional P3HT:PCBM blend layer spray deposited and thermally annealed under similar conditions [111], this layer shows a significantly higher density of crystalline structures on the surface. Further, the structures are more pronounced with larger dimensions of up to 100 μm, thereby being around four to five times larger than their counterparts on a blend layer. This clear increase in density as well as size of PCBM crystalline structures on the surface of the sample indicates the existence of a high acceptor material concentration at the interface to the negative electrode. Such a PCBM-rich layer at the electron-extraction interface is expected to be beneficial for device performance.

4.2.3 Characteristics of Successively Sprayed Active Layers

Optical Characteristics

Optical absorption spectra of pristine films (P3HT, PCBM) as well as composite films (pre-blended P3HT:PCBM, successively sprayed P3HT/PCBM) were examined and analyzed before and after thermal post-deposition treatment. Figure 4.12(a) shows the results obtained for pristine films while Fig. 4.12(b) shows the results obtained for composite films. In case of the sprayed pristine P3HT and PCBM films, no clear changes in the spectrum can be observed after annealing, except for a slight increase in the absorption intensity. This is in close agreement with previously reported results for spin-coated layers [113]. Considering the blend film, one can clearly distinguish two main absorption peaks originating from PCBM around 345 nm and from P3HT around 500 nm. A main difference between as-prepared and annealed films lies in a decrease of the absorption features related to PCBM and an enhancement of those attributed to P3HT. Further, the region around the absorption peak of P3HT in the spectrum of the annealed film is slightly extended towards longer wavelengths while the shoulder present at around 600 nm, supposed to be resulting from interchain interactions [90], becomes more pronounced. The presence of PCBM is known to quench the red band of the P3HT absorption while maintaining the absorption in the blue band. This is indicative for the disruption of the intermolecular packing structure of the P3HT chains and reduced density of aggregates that give rise to the red absorption [114]. The annealing process induces partial recovery of the ordered structure of the P3HT chains, which results in a red shift of the absorption features of P3HT. However, a slight blue-shift of the P3HT absorption features in the blend film also remains after annealing as compared to the pristine P3HT film. Similar behavior, but more pronounced, can be observed for the composite film prepared by successive spray deposition of the individual components. The strong blue-shift of the P3HT absorption features present in the spectrum of the as-prepared film indicates a disruption of the P3HT ordering by the PCBM. This means that the integrity of the initially sprayed P3HT film is not entirely preserved during the subsequent spraying

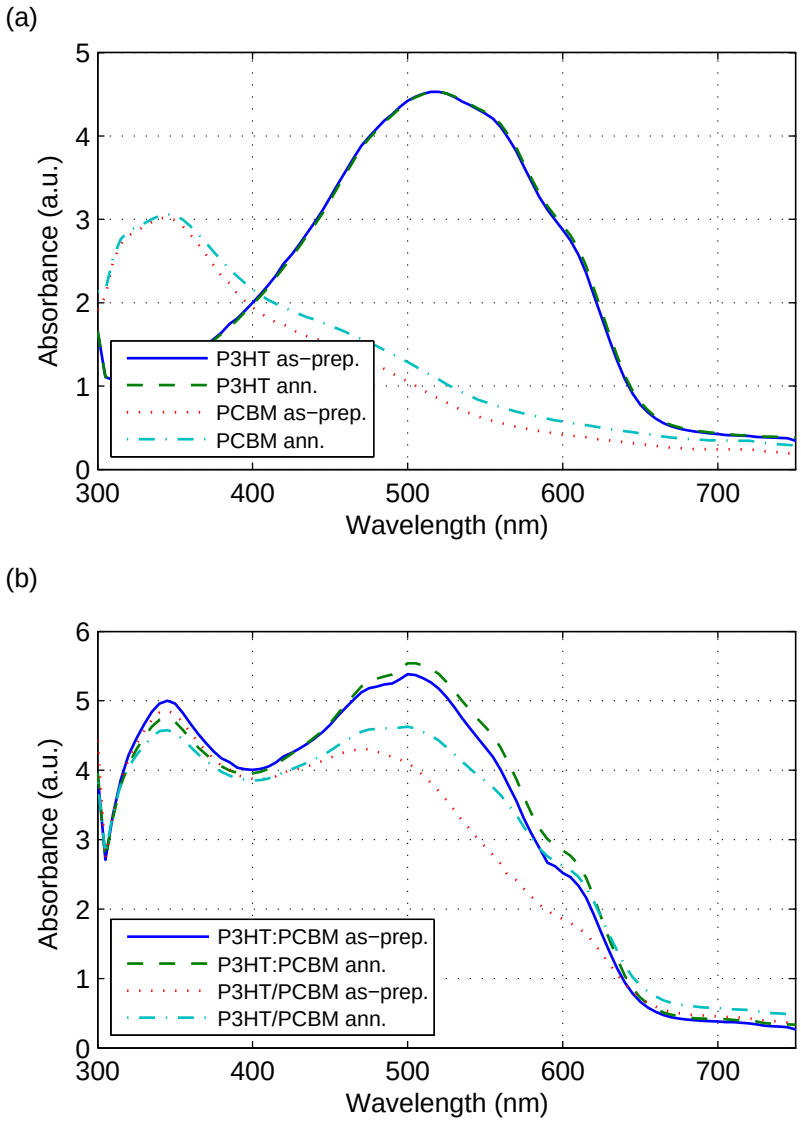

Figure 4.12: UV-Vis absorption spectra of pristine P3HT (15 sec) and PCBM (10 sec) films (a) as well as composite P3HT:PCBM (20 sec) blend and P3HT/PCBM (15/10 sec) successively sprayed films (b) obtained before and after thermal post-deposition treatment of the samples. Quenching of the red band of the P3HT absorption in the successively sprayed film can be seen as indicative for a penetration of PCBM into the P3HT layer and an intermixing of both materials.

cycle of PCBM. Quenching of the red band of the P3HT absorption in the successively sprayed film can therefore be seen as indicative for a penetration of PCBM into the P3HT layer and an intermixing of both materials. However, coarse intermixing of the materials within the photoactive layer due to interaction with residual solvent during deposition, described above to occur at a scale of a few tens of micrometers, cannot alone cause the quenching observed here. The intermixing has to occur at a nanometer scale, as to cause disruption of the P3HT chain ordering. It is therefore most likely that upon annealing, an

additional fine intermixing takes place by interdiffusion of PCBM into P3HT, resulting in the formation of a morphology close to that of the conventional BHJ. It should be noted that the annealed film exhibits a significant red-shift of the P3HT peak wavelength upon partial recovery of the polymer chain ordering, bringing it very close to the position of its counterpart in the spectrum of the blend film.

X-Ray Reflectivity Measurements

In addition X-ray reflectivity measurements have been used to investigate the intermixing of the P3HT layer with the subsequently deposited PCBM molecules. In contrast to the optical absorption spectra, X-ray reflectivity measurements allow an accurate determination of the film thickness of thin polymeric layers and reveal the inner film morphology of layered systems [115], [116]. Figure 4.13 shows the measured reflectivity curves together with the model fits for pristine and annealed P3HT films and for the layered P3HT/PCBM system. For angles larger than the critical angles of the materials used, which are in our case 0.159° and 0.146° for P3HT and PCBM, the incoming X-rays penetrate through the complete film. Therefore these measurements are not only sensitive to the bulk properties of the films but also reveal thin enrichment layers as they can be seen from the prominent long modulations in the reflectivity curves. Due to the high surface roughness of the films, the total film thickness is not seen by strong intensity modulations, which facilitates the detection of enrichment layers at the substrate. For the pristine P3HT films the corresponding Parrat simulations reveal an enrichment layer with a thickness of 2.3 nm, which increases to 2.6 nm after annealing. This enrichment layer is given by a layer of P3HT with a more dense packing, located at the substrate. Such a dense packing of P3HT polymer chains is not seen for spin-coated films and can hence be attributed to the spray coating technique, which leads to a physically accelerated deposition of the polymeric material on a hard substrate at elevated temperature. After annealing the enrichment layer gets less pronounced due to the rearrangement of the P3HT molecules. The resulting crystalline ordering of the P3HT molecules is seen from the well-defined Bragg reflection in the X-ray reflectivity curve of the annealed film (denoted with ‘B’ in Fig. 4.13). The inset in Fig. 4.13 shows the corresponding Gaussian fit on a linear scale. The Bragg peak is centered at a position with a q_z-value of 3.83 nm^{-1}. This value corresponds to a structure size of 1.64 nm and is hence in very good agreement with the (100) Bragg peak of P3HT in an edge-on arrangement as reported by Kim et al. [117]. The higher Bragg orders of this molecular arrangement appear at larger angles and cannot be resolved due to limitations in intensity. For the pure P3HT films the evolution of the Bragg peak clearly shows that the crystalline ordering can be introduced to the P3HT polymer matrix with an additional post-deposition annealing step. In contrast, for the P3HT/PCBM bilayer system an equivalent crystalline ordering as seen in the pure P3HT films was not achieved. No Bragg peak is found in the X-ray reflectivity data. Also the annealing has

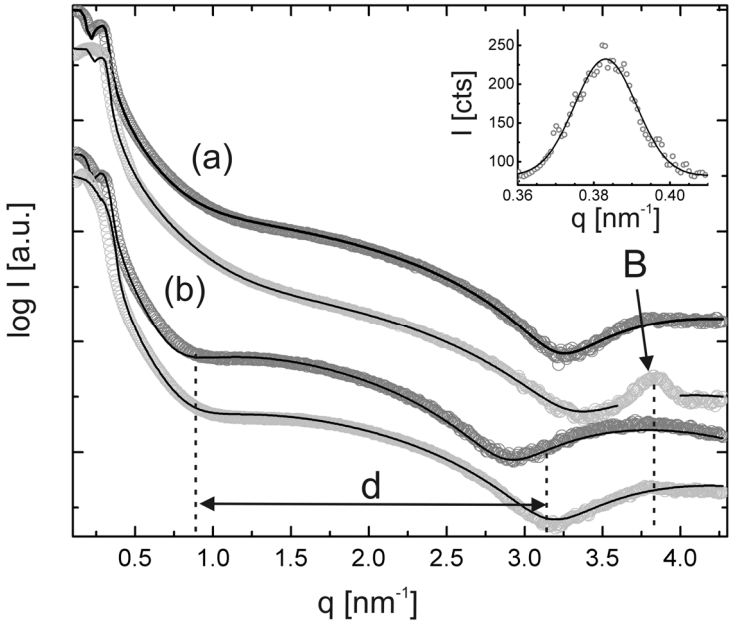

Figure 4.13: X-ray reflectivity curves of (a) pure spray coated P3HT films and (b) successive sprayed P3HT/PCBM layered films. Both, the pristine (dark grey) and the annealed (bright grey) films are shown for the single and the multi-layer films. The position of the Bragg peak from the crystalline structure of the P3HT is marked with 'B'. The thickness of a densely packed P3HT film at the substrate interface is seen in the intensity modulation marked with 'd'. The inset shows the exact position of the (100)-Bragg peak of the semicrystalline P3HT and the corresponding Gaussian fit.

only a minor influence on the crystallinity of the firstly deposited P3HT and only a very weak indication of a Bragg peak is found in the X-ray reflectivity data. The absence of a well-defined (100) Bragg peak is a strong indication for a good penetration of the PCBM molecules into the P3HT matrix, which perturb the P3HT-lattice and hence prevent a crystalline ordering even after annealing. By using grazing incidence wide angle X-ray scattering (GIWAXS) a similar behavior was also found for spin-coated P3OT/CN-PPV bulk heterojunction films, which exhibited a less crystalline ordering as compared with the pristine films [118]. The already mentioned enrichment layer is seen in the successively sprayed P3HT/PCBM samples as well and shows a similar slight increase in thickness as it was found for the pure P3HT films. Combining the results of the optical absorption and the X-ray reflectivity measurements a significant penetration of the stepwise deposited P3HT and PCBM is found, which makes this fabrication routine very interesting for device applications, where a high interfacial area between the used materials is desired.

Cross-Sectional TEM Analysis

The morphology of the active layer was further studied by TEM investigations. The active layer can easily be identified as the region between the silicon substrate and the aluminum

coating. In the active layer a percipient contrast was observed indicating the presence of two phases with an interface in the middle as shown in the TEM image Fig. 4.14(a). The same figure shows SAED patterns of two regions marked as '1' and '2'. The first region '1', located in the domain adjacent to the aluminum showed a crystalline diffraction pattern with a d-spacing of 15.4Å which matches fairly well the d-value proposed by Li et al [119]. This indicates the domain adjacent to the aluminum to be highly crystalline PCBM. The other region labeled in Fig. 4.14(a) as '2' turned out to be amorphous as is illustrated by the SAED pattern on bottom right. Subsequently, to identify the elemental composition of the active layer, EDX measurements were done in STEM mode. EDX spectra were acquired from four regions across the active layer labeled 1-4 in Fig. 4.14(b). The EDX spectra obtained, plotted in Fig. 4.15, show the composition in the domain adjacent to aluminum (region 3 and 4) to be primarily of carbon and oxygen. This matches with the chemical formula of PCBM $C_{72}H_{14}O_2$. This domain is highly crystalline and together with the SAED experiments can be identified as PCBM. Region 1 and 2 located in the domain next to silicon show predominant signal of carbon and sulfur in accordance to the elements expected for P3HT, which has a chemical formula of $[C_{10}H_{14}S]_n$. A very weak oxygen signal is visible in the EDX data of the P3HT layer, which was also confirmed by EELS measurements. This very weak oxygen signal detected within the P3HT layer might be related to interdiffusion of PCBM into this layer as suggested by [89], [110] or stem from oxidation of the sample surface prior to insertion into the microscope. To clarify that point, further investigations are required. Our TEM investigations further support the idea of PCBM diffusion into the P3HT layer. The absence of a clear diffraction pattern in the P3HT-rich region indicates the disruption of crystallinity, as proposed above by optical absorption and x-ray reflectivity analysis. We assume that the absence of any dominant oxygen signal, originating from the existence of PCBM, is due to the low concentration of PCBM throughout the entire region. DSIMS profiles of P3HT/dPCBM bilayers reported by Chen et al. showed only slight increase of PCBM concentration in the P3HT and no variation with depth upon annealing [89], which is consistent with our assumption of low PCBM concentration in the P3HT-rich region.

4.2.4 Complete Devices

In order to prove the suitability of the proposed deposition method for fabrication of complete devices with reasonable performance characteristics, we prepared a series of photodiodes fabricated using this method. The main parameter varied for tuning the composition of the active layer was the spray duration during deposition of the individual components. All other spray parameters such as solvent type, initial solution concentration, material flow rate, atomizing gas pressure, nozzle-to-sample distance and substrate temperature were kept constant. Although we consider this to be the most straightforward

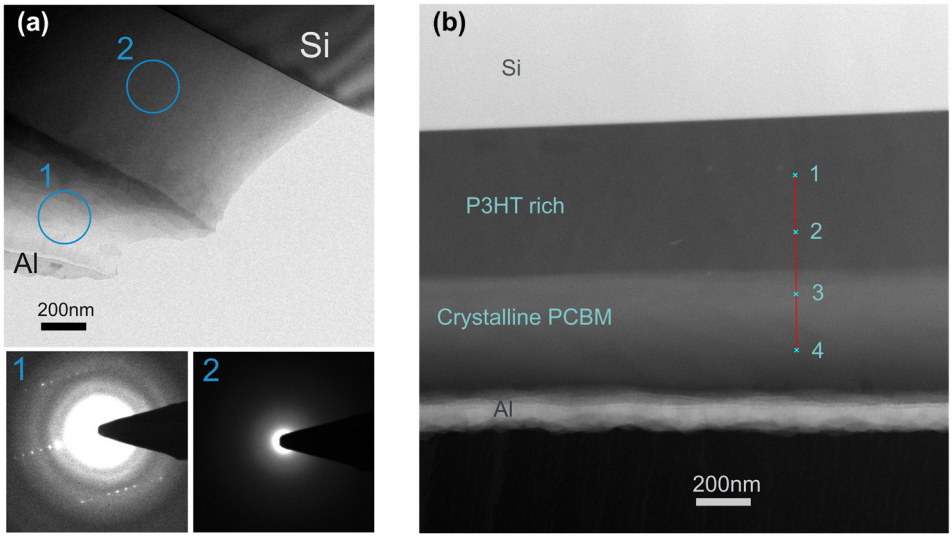

Figure 4.14: (a) Above is a TEM image from a thin region in the active layer. Diffraction patterns were obtained from regions indicated 1 and 2 and are shown below on left for 1 and on right for 2. (b)) STEM image showing the active layer and the four spots 1, 2, 3 and 4 across the active layer from where point EDX spectra were acquired.

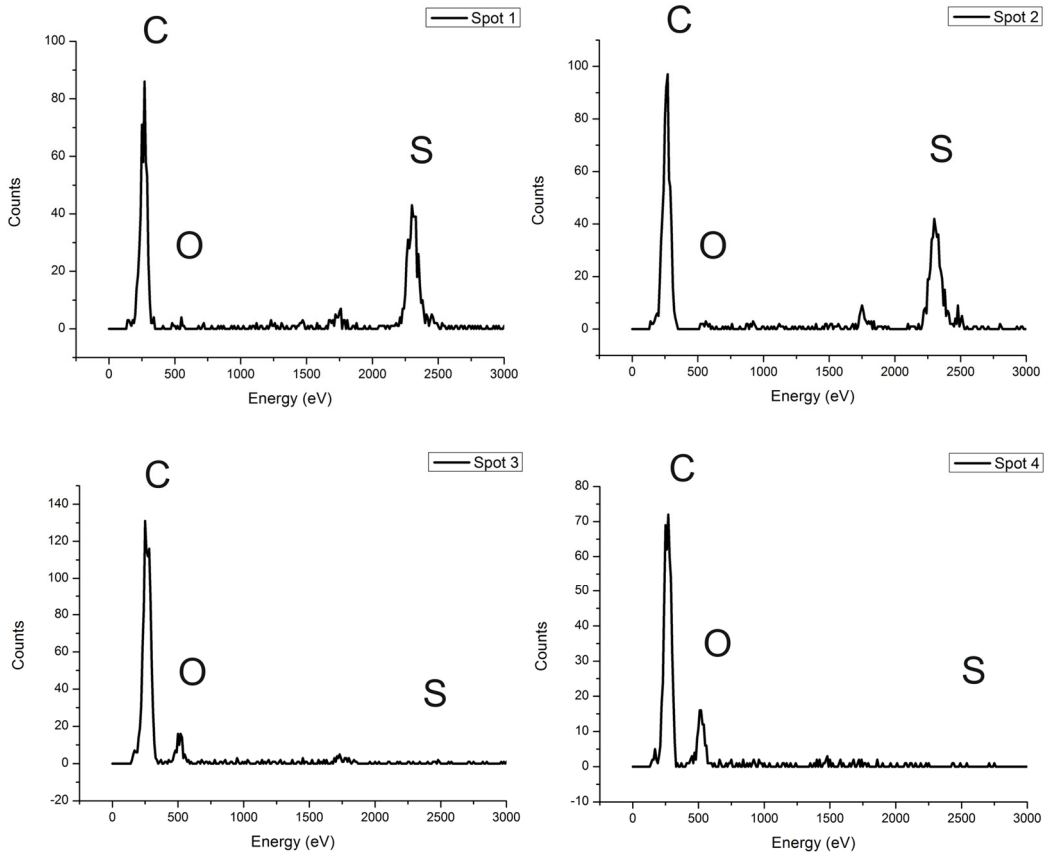

Figure 4.15: EDX spectra acquired from spots 1, 2, 3 and 4 labeled in Fig. 4.14(b).

approach, it also shows the huge parameter space still to be explored for a rigorous optimization of the layer composition. Figure 4.16 shows a comparison of the IV-characteristics of five OPDs, D1 to D5, sprayed with different durations for P3HT and PCBM. Three devices with fixed PCBM and varying P3HT spray duration of 10, 15 and 20 sec are combined together in Fig. 4.16(a). On the other hand, three devices with fixed P3HT and varying PCBM spray duration of 5, 10 and 15 sec are combined together in Fig. 4.16(b). In both graphs one can clearly observe reasonable device performance for all compositions. Considering one of the best diodes presented, such as D2, reveals highly competitive figures with an on/off-ratio of up to $1.7 \cdot 10^5$ and a dark current density as low as $1.5 \cdot 10^{-5}$ mA/cm^2 under −1 V reverse bias. This is a remarkably low dark current density considering OPDs with an active device area of 25 mm^2. For short PCBM spray durations, e.g. D1, the photocurrent drops significantly in addition to an increase in dark current density by up to one order of magnitude at high reverse bias. The low photocurrent is due to a non-ideal composition with low PCBM concentration leading to decreased exciton dissociation efficiency at the P3HT/PCBM interfaces. A low coverage of PCBM creates a large contact interface between the P3HT and the electron-extraction layers, forming more shunt paths through the device and hence increasing the leakage current.

For a comprehensive evaluation of the deposition approach described here and its potential competitiveness with more conventional pre-deposition blending approaches, devices fabricated by both techniques must be directly compared in terms of common performance parameters. A set of OPDs was fabricated by successive multilayer spray deposition while varying deposition times of P3HT and PCBM for obtaining different compositions of the active layer. This was then compared to another set of OPDs fabricated by direct spray deposition of a P3HT:PCBM (1:1) blend while varying deposition times to obtain different thicknesses of the active layer. Note that the performance of such spray-coated BHJ photodiodes matches the one of their spin-coated counterparts [94], [96]. As the two device groups rely on an essentially different process of active layer formation, a direct comparison is rather difficult. For this reason and for the purpose of proving the competitiveness of our approach, we chose the parameter combination in each group leading to almost identical performance of the corresponding devices. This is fairly easy to accomplish due to the high flexibility in tuning layer composition and device performance by successive multilayer deposition, which was already demonstrated in the previous section. Moreover, the two selected devices happened to be best out of their corresponding group. Figure 4.17(a) shows the IV-characteristics of device D6, fabricated by spraying a blend solution for 20 sec, and device D7, fabricated by spraying a P3HT solution for 15 sec followed by spraying a PCBM solution for 10 sec. Note that the data points for each device type plotted in the figure correspond to averaged values from three individually sprayed diodes. The deviation within individual diodes of the same type is comparable for both deposition approaches. At −1 V reverse bias for example, the deviation for D6 is approx.

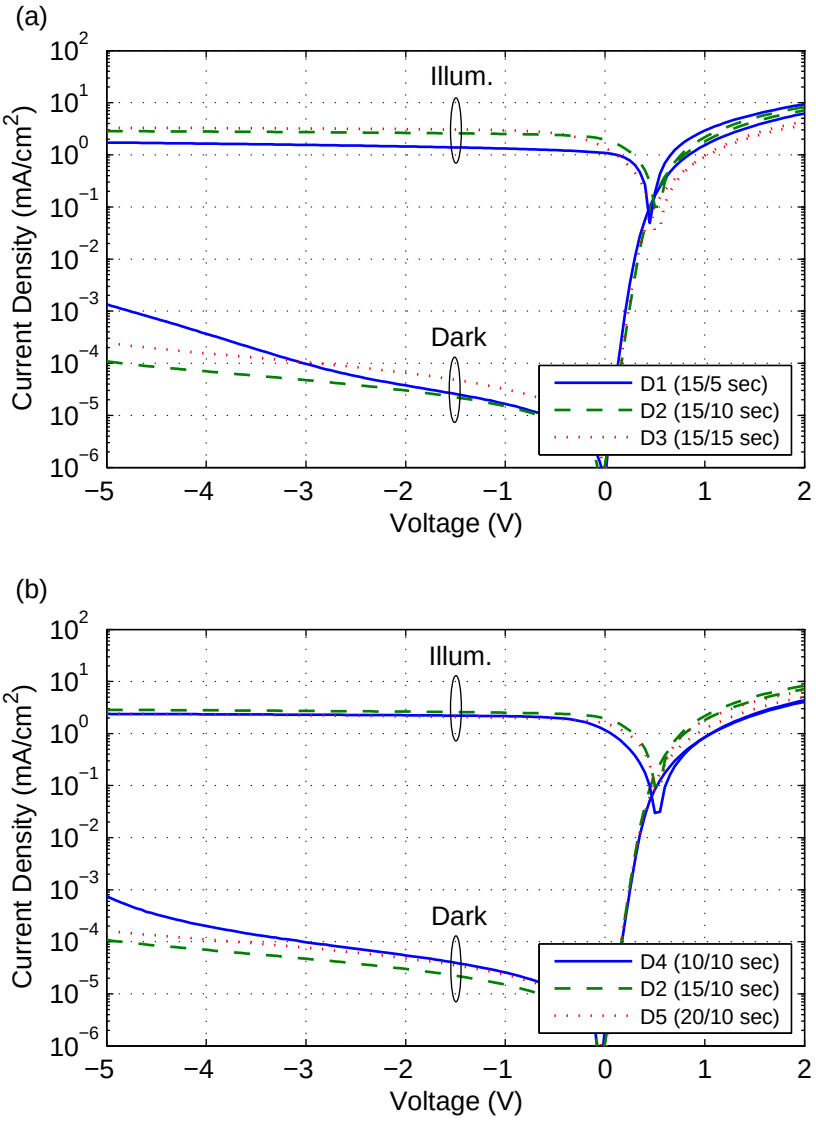

Figure 4.16: (a) IV-characteristics of three OPDs (D1, D2, D3) with fixed PCBM and varying P3HT spray duration of 10, 15 and 20 sec. (b) IV-characteristics of three OPDs (D4, D2, D5) with fixed P3HT and varying PCBM spray duration of 5, 10 and 15 sec. Both graphs show device behavior under dark as well as illuminated condition.

1.5 % in the photocurrent and 24 % in the dark current, whereas for D7 it is approx. 2.8 % and 22 % at the same conditions. This demonstrates the reproducibility and reliability of our deposition method. By looking at the IV-curves it becomes immediately obvious that both devices exhibit very similar behavior under dark as well as illuminated conditions. The conventional blend device D6 shows an on/off-ratio of around $6 \cdot 10^4$ and a dark current density of $4.3 \cdot 10^{-5}$ mA/cm^2 under −1 V reverse bias. For the successively sprayed device D7 one obtains an on/off-ratio of around $8.8 \cdot 10^4$ and a dark current density of $3 \cdot 10^{-5}$ mA/cm^2 under −1 V reverse bias, thereby slightly outperforming the blend device. However, both devices maintain a high on/off-ratio and relatively low dark current

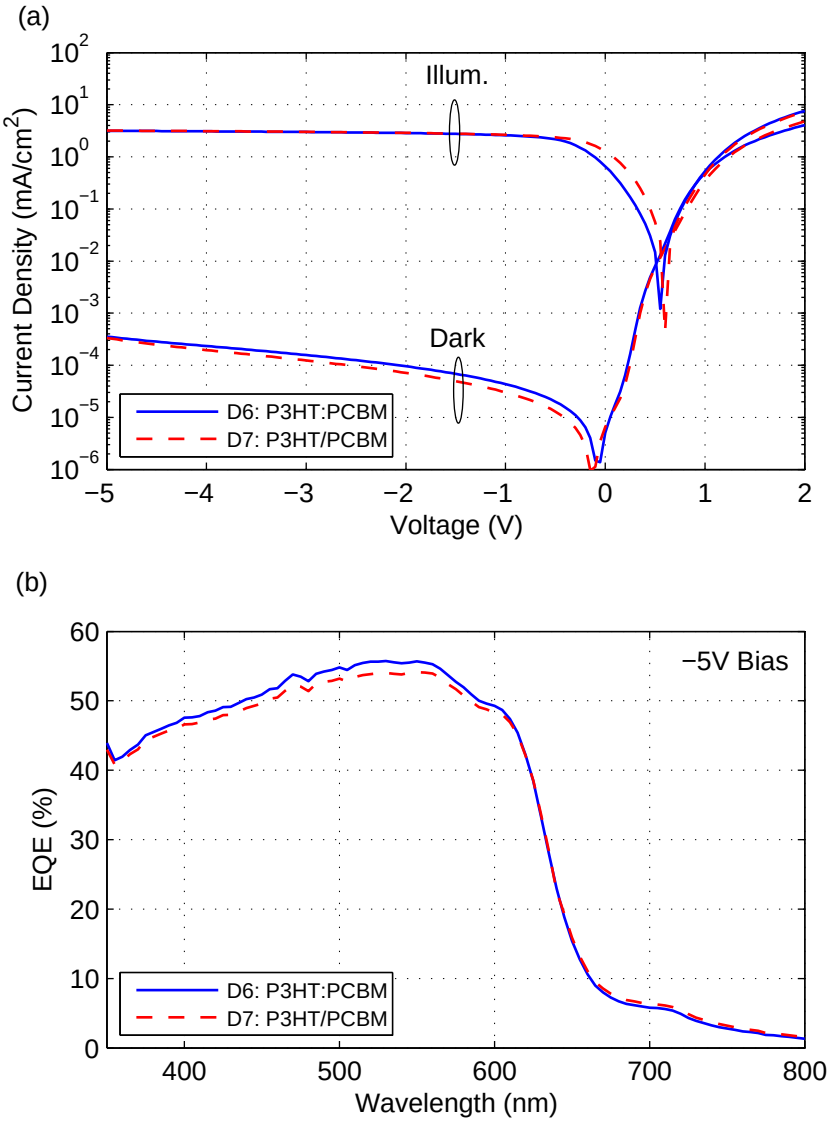

Figure 4.17: (a) IV-characteristics of OPD D6, fabricated by spraying a blend solution for 20 sec, and OPD D7, fabricated by spraying a P3HT solution for 15 sec followed by spraying a PCBM solution for 10sec. The graph shows device behavior under dark as well as illuminated condition. (b) Plot of the external quantum efficiency against wavelength for devices D6 and D7.

densities even at higher reverse bias, with on/off-ratios slightly below 10^4 and dark current densities below $4 \cdot 10^{-4}$ mA/cm^2 under −5 V reverse bias. In terms of external quantum efficiency, plotted in Fig. 4.17(b), both devices show almost identical behavior as expected. The spectral response is perfectly identical and the difference in the absolute values of up to 1 % lies within the inaccuracy of the measurement setup.

Based on these results, one can conclude that devices with active layers fabricated by successive spray deposition of the individual components exhibit a performance

comparable to conventional BHJ devices in which the active layer is rigorously blended in advance. At first glance, this may not seem very intuitive. Considering an average droplet size of a few tens of micrometers in this kind of spray technology, one would expect the intermixing to occur on a scale several orders of magnitude larger than in a BHJ architecture which would lead to a decreased donor/acceptor interface area and hence lower exciton dissociation efficiency. Based on the analysis carried out so far, we attribute the good device performance to two main factors. The existance of a P3HT-rich layer at the hole-extraction interface and a PCBM-rich layer at the electron extraction interface leads to an increased charge carrier selectivity at the respective electrodes. Primarily however, although the spray process itself is expected to generate a coarse intermixing of the two materials on the scale of the droplet size, a further intermixing occurs at the nanometer scale due to diffusion of PCBM into the underlying P3HT layer. Note that in addition to the thermal post-deposition treatment of our devices, there is a short annealing cycle during the deposition phase itself, since deposition is performed at elevated substrate temperature (ca. 150 °C) for accelerated drying of droplets. Similar findings were previously reported as solid-solid intermixing in bilayer devices prepared by stamping transfer [120], or as thermally-induced interdiffusion demonstrated in devices prepared by consecutively spin-cast layers of P3OT and PCBM from different solvents [121]. Spontaneous formation of a BHJ-like nanomorphology upon annealing of model bilayer systems was recently shown to result from PCBM diffusion into disordered P3HT domains without disruption of the crystalline P3HT domains [88], [89]. In contrast to this, our findings suggest that diffusion of PCBM into the P3HT layer disrupts chain ordering. We believe that this discrepancy arises from our significantly different fabrication approach. The interaction with the residual solvent during deposition of PCBM leads to partial dissolving and swelling of the P3HT layer, which together with the elevated temperature enables PCBM diffusion not only into disordered P3HT domains but also into previously crystalline domains. While all results presented here are specific to the common P3HT/PCBM material system, the generality of the proposed fabrication approach for different material systems still has to be investigated.

4.3 Summary

In conclusion, we implemented a simple and low-cost spray-coating test setup using a commercially available automatic air atomizing spray gun. Using this setup we could successfully fabricate different classes of organic thin-film devices exhibiting performances comparable to ones fabricated using other deposition technologies. The technological framework developed based on the deposition approach presented here proved to enhance controllability of the process and reproducibility of the fabricated

devices. For the correct choice of process parameters, the layer formation process can be thought of as a process of successively stacking individual droplets onto the substrate at a certain rate. Further, microscopy investigations indicated that individual droplets in a spray-coated layer can behave to a certain extent as a continuous layer depending on the degree of merging between droplets during deposition and do not necessarily act as isolated domains. Gaining insight into the layer formation process and correlating it to device performance represents an important step towards the realization of arbitrary shaped organic electronic devices fabricated by spray deposition.

We have introduced an alternative deposition approach for the preparation of organic heterojunction photoactive layers by successive spray deposition of the donor and acceptor materials from pristine solutions. The partial dissolving of previously deposited underlying layers was carefully examined using optical and atomic force microscopy. It was shown that P3HT-rich and PCBM-rich layers are expected to form at the vicinity of the hole-extraction and electron-extraction layers, respectively. Optical absorption spectra as well as X-ray reflectivity measurements were utilized to indicate the disruption of P3HT ordering by the subsequently deposited PCBM. Further, cross-sectional TEM investigations, including material analysis with SEAD and EDX, were performed to further support the idea of PCBM penetration into the P3HT layer and the intermixing of both materials within the active layer. Based on performance characteristics of the fabricated organic photodetectors, we can conclude that devices with active layers prepared by successive spray deposition of the individual components exhibit a performance comparable to and can potentially outperform conventional BHJ devices in which the active layer is rigorously blended in advance. Moreover, separate handling of the individual components and their deposition from distinct solutions enables an enhanced control of the active layer composition and hence increases the ability of tuning device characteristics. Although we focused here on the fabrication of organic photodiodes, the proposed fabrication routine is very interesting for different device applications, which require an intermixed layer of different materials while allowing for convenient control over its composition. Our results illustrate the significance of altered fabrication routines on processes predominantly taking place at the nanometer scale. Such processes, like exciton dissociation and charge transport in domains of an interpenetrating network of donor and acceptor molecules, are critical for device performance. From a practical perspective, devices with excellent performance could be fabricated in simple and controllable ways using an industrial relevant high-throughput process.

Chapter 5

CNT Thin-Film Technology

A significant step towards commercialization of novel CNT electronics involves the development of large-area and high-throughput processes for the fabrication of high quality CNT films. In this chapter, we demonstrate a reliable and reproducible spray deposition process for the fabrication of highly uniform CNT films exhibiting state-of-the-art performance. CNT films with average surface roughness as low as 5.8 nm, and conductivities reaching 4000 S/cm for films of 45 nm thickness, are presented. A good trade-off between sheet resistance and transmittance is achieved with best films having 100 Ω/sq at 80 %. Further, a transfer printing process is introduced for the fabrication of CNT thin-films on plastic. A comparison to films fabricated by direct spray deposition onto the same type of substrate material is conducted.

Incorporating this kind of high quality films as resistive networks for gas detection in gas sensors yields devices with high sensitivities. Here we report CNT-based gas sensors with exceptionally high sensitivities and fast response to various test gases. Highly uniform CNT thin-films, prepared using a reliable and reproducible low-cost spray deposition process, are utilized as resistive networks for gas detection. Sensors show a clear and immediate change in resistance as a response to test gas exposure. Sensitivities of 2 % for concentrations as low as 10 ppm and reaching 25 % at a concentration of 100 ppm can be achieved in case of NH_3, yielding the highest sensitivity among our range of test gases. We further demonstrate the potential enhancement in sensitivity achieved through complex impedance characterization of this type of gas sensors.

5.1 Spray Deposition of CNT Thin-Films

Random carbon nanotube (CNT) networks have raised a continuously increasing interest among a broad and multidisciplinary community of researchers throughout the last decade. The remarkable and concurrently diverse properties of such networks have rendered them suitable for a wide range of applications in science and engineering. Among the most promising applications are transparent conductive electrodes [122–124], thin-film transistors and circuits [125], [126], mechanical and chemical sensors [127–129]. The desired functionality of the CNT films produced for different applications depends primarily on the choice of the appropriate raw material. Nevertheless, it is strongly influenced by major process specific aspects. A random CNT network can either be directly grown by chemical vapor deposition (CVD) or processed from a solution of well-dispersed nanotubes. The CVD process involves catalyst nanoparticles acting as seeds for the growth of the CNTs. Although this method leads to films with individually separated tubes and better inter-tube junctions, it is a high vacuum/temperature process not suitable for the emerging field of low-cost flexible electronics. Solution-based methods on the other hand have several advantages. In general, relying on this kind of low temperature processes overrides most constraints on the choice of the substrate material, enabling fabrication even on plastic substrates. The omission of a high-vacuum process further reduces costs significantly.

A significant step towards the commercialization of novel CNT electronics involves the development of large-area and high-throughput processes for the fabrication of high quality CNT films. Among all the different fabrication techniques available, spray deposition is considered to be one of the most competitive in terms of cost-performance ratio. It offers the means for depositing CNT films with high uniformity and low roughness over large areas in a high-throughput (inline) process. The successful adoption of this technique to CNT film fabrication for various applications has been previously reported in literature [124], [130].

In this chapter we demonstrate a reliable and reproducible spray deposition process for the fabrication of CNT films exhibiting state-of-the-art performance. The convenient control of major process parameters enables a fine and accurate tuning of film characteristics, hence rendering this process suitable for a wide range of device applications with different requirements. Films, fabricated using this process, are further applied as resistive networks in gas sensing devices. We demonstrate that such devices, incorporating highly uniform pristine CNT films, exhibit a high sensitivity towards ammonia (NH_3) without the need for any further functionalization of the CNT film, thereby maintaining a simple fabrication process.

5.1.1 Materials and Methods

Spray technology is used in a wide variety of applications such as surface coating, humidification, combustion and many more. Each application area requires different spray nozzles to fulfill the specified criteria and achieve the desired results. The layers deposited here were sprayed by an air atomizing nozzle. This type of nozzles provides, along with ultrasonic spray nozzles, the finest degree of atomization. It is worth mentioning that ultrasonic spray nozzles have also been successfully applied to the deposition of high-uniformity CNT films [124]. For our static test system, a commercially available automatic air atomizing spray gun (Krautzberger GmbH, Germany) was used. The spray gun contains an internal pneumatic control system which is activated by an electromechanical 3/2-way valve connected to a timer for precise spray time adjustment. Other major spray parameters to be adjusted for obtaining desired spray characteristics are material flow rate, atomizing gas (N_2) pressure, nozzle-to-sample distance and substrate temperature. For air-assisted nozzles the diameter of the orifice is one of the most significant dimensions for atomization. Here a nozzle with 0.5 mm orifice diameter was chosen. The atomizing gas (N_2) pressure was kept below 1 bar throughout all experiments in order to obtain the desired spray characteristics and a uniform spray pattern across the area of interest. We use an approach introduced previously for the spray deposition of active polymers in organic photodiodes [96], [111], in which we operate within the wet spraying regime while heating up the substrate in order to speed up the drying of wet droplets arriving at the substrate. This approach allows the formation of dry layers with good thickness control over time, enhancing at the same time reproducibility. Figure 5.1(a) shows a schematic drawing of the test setup, indicating the vertical arrangement of nozzle and substrate.

Solution preparation

In order to disperse CNTs in an aqueous solution, a high molecular weight cellulose derivative, sodium carboxymethyl cellulose (CMC), is used. This kind of dispersant has been reported previously as an excellent agent for dispersing single-walled nanotubes (SWNTs) in water [131]. As a first step, an adequate quantity of CMC is added to Millipore DI water such as to obtain a 0.5 wt% aqueous solution of CMC. This solution is then stirred for ≥12h at room temperature to uniformly dissolve the surfactant in water. The desired amount of SWNTs can then be added to the previously prepared CMC stock solution. Typically, a concentration between 0.03 wt% and 0.05 wt% of SWNTs is used. Actual dispersion of the CNTs is achieved by sonication of the complete solution for 90 min in a bath-sonicator. For dispersions prepared by probe sonication, the duration is reduced to 15 min. The solution is then centrifuged at 15000 rpm for 2 h and the final solution is obtained by decanting the top 80 % of the supernatant.

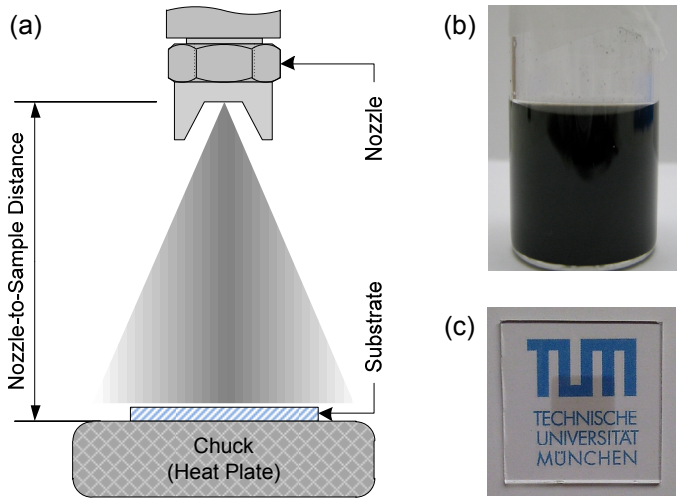

Figure 5.1: (a) Schematic drawing of the test setup, indicating the vertical arrangement of nozzle and substrate. (b) Vial containing a CNT/surfactant aqueous dispersion after sonication and centrifugation, ready for deposition. (c) An image of a CNT film on glass, uniformly deposited over an area of 1 cm^2.

Basic CNT film fabrication

For the fabrication of highly uniform and smooth CNT films, the final CNT solution is spray deposited onto plain glass substrates. Prior to film deposition the substrates are thoroughly cleaned by sonication in acetone and isopropanol. The substrates are then exposed to oxygen plasma for further cleaning and surface treatment. An increased wettability of the glass surface after plasma treatment is beneficial for achieving uniform surface coating during spray deposition of the water-based CNT solution. Chemical post-deposition treatment is necessary to remove the CMC-matrix embedding the CNTs, hence changing film behavior from insulating to conductive. For this purpose, samples are immersed in dilute HNO_3 (13-23 %) for ≥24 h at room temperature. Some samples are additionally immersed in concentrated HNO_3 (65 %) for 1h to further increase conductivity via stronger doping of CNTs [124], [130]. Samples are finally rinsed in DI water and subsequently dried. Note that all steps involved in the CNT film fabrication are performed entirely in ambient conditions.

Basic CNT film characterization

Surface characterization and thickness measurements of fabricated CNT films were performed with an atomic force microscope (AFM) operated in tapping mode. Information on CNT length distribution was extracted from AFM images of low density films using image processing software (ImageJ). Sheet resistances were measured using a four-point collinear probe method on a Keithley 4200 semiconductor parameter analyzer. Optical

transmission was measured using a chopped 300 W xenon arc research source passing through an Oriel Cornerstone 260 1/4 m monochromator and a calibrated silicon photodiode with pre-amplifier connected to an Oriel Merlin digital lock-in radiometry system.

5.1.2 Basic Film Characteristics

Prior to the adoption of CNT films in any specific application, it is necessary to optimize and evaluate the elementary film performance on the basis of some primary figures of merit and their dependence on different process parameters. Among the most important figures are sheet resistance or conductivity, optical transmittance or absorption spectra, mechanical stability, CNT distribution, and surface characteristics. For this reason, we first present an overview of basic film performance and the means for controlling the same before then discussing device specific aspects of gas sensors as one possible application of such CNT films.

As already mentioned in the previous section, we use CMC as surfactant to aid dispersion of the nanotubes in water. This implies that the surfactant will still be present in all deposited films before performing further post-deposition treatments. As-prepared films are therefore composed of a CNT network embedded into a CMC-matrix. Single CNTs and CNT-bundles are suspended within the insulating matrix and hence the film does not exhibit any conductive behavior. Figure 5.2(a) shows an optical microscopy image of an as-prepared film. Note the clearly distinguishable disk-like structures typical for spray deposited layers. Droplets are deformed upon impact onto the substrate and dry rapidly creating the features observed. After removal of the CMC-matrix, the suspended CNT network embedded in the matrix collapses thereby forming the final film of directly interconnected CNTs and exhibiting conductive behavior. This is achieved by chemical post-deposition treatment as described in the experimental section. An optical microscopy image of such a pristine CNT film is shown in Fig. 5.2(b). It is clear from the image that the features previously observed in as-prepared films completely vanish after CMC removal. Moreover, the film seems highly uniform with no agglomerates or other clear particles visible at an optical scale.

An accurate examination of the surface characteristics at the nano-scale is required for a detailed evaluation of the pristine CNT film quality. This involves the characterization of uniformity, surface roughness, and CNT length distribution. Especially surface roughness is of great significance as it can become a crucial factor in certain applications, for example when considering these films as transparent electrodes for optoelectronic devices. The CNT length distribution on the other hand is of relevance for the evaluation of the dispersion quality and understanding the contribution of different process steps in altering

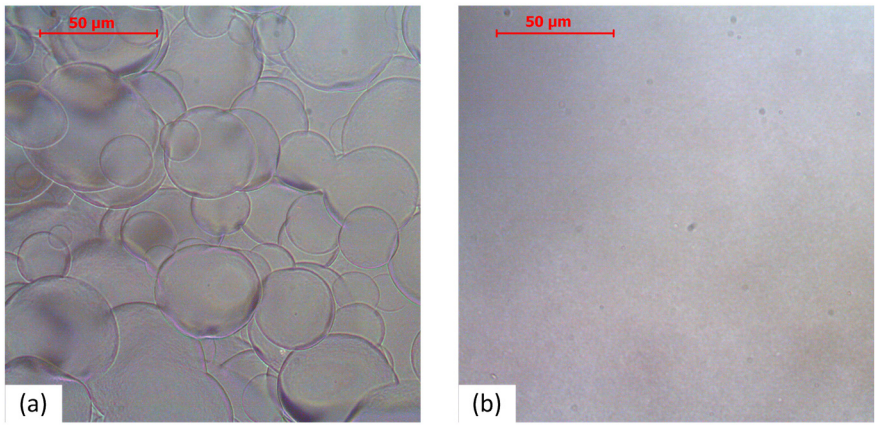

Figure 5.2: (a) Optical microscopy image of an as-prepared film, showing disk-like features originating from spray deposition. (b) Same film after removal of the surfactant-matrix. The final film of directly interconnected CNTs is formed and exhibits a conductive behavior.

the physical properties of the raw CNT material. Sonication during the solution preparation was shown to shorten the CNTs and has therefore to be carefully optimized in terms of power and duration [132]. Figure 5.3 shows two AFM images of the film introduced in Fig. 5.1(c), scanned over a large area of 10x10 μm^2 (left image) as well as a zoom-in of a smaller area of 2x2 μm^2 (right image). For the 10x10 μm^2 scan, the values measured for the average and RMS surface roughness are 5.79 nm and 7.41 nm, respectively. Very similar values (5.64 nm and 7.13 nm) are obtained from the 2x2 μm^2 scan, which demonstrates a high uniformity of the films independent on the total area under investigation.

Another major figure of merit necessary towards a full characterization of CNT films is the sheet resistance (R_{sh}) or DC conductivity (σ_{dc}) and its dependence on the film thickness (d) or density. Due to the percolating nature of CNT films, R_{sh} is expected to vary inversely with film density. Since CNT density is correlated to film thickness, R_{sh} as well is expected to scale inversely with film thickness. Figure 5.4(a) plots the relation between R_{sh}, as determined by four-point probe measurements, and d. One can clearly observe the reduction in sheet resistance with increasing film thickness or density, reaching as low as 60 Ω/sq at approx. 42 nm. DC conductivity can be calculated in a straight-forward manner from the sheet resistance and thickness through $\sigma_{dc}=1/(R_{sh} \cdot d)$. Figure 5.4(b) shows the calculated values of σ_{dc} as a function of d. As opposed to a material specific constant value for the conductivity, as expected from continuous metallic or semiconducting films, σ_{dc} for a CNT thin-film shows a strong dependence on thickness. The conductivities calculated for different films vary by a factor of almost 4 in a range of thicknesses between 10 nm and 50 nm. As more CNTs are deposited, more conduction paths are created through the film and conductivity continues to increase until a thickness of approx. 50 nm is reached, where film conductivity approaches saturation. This behavior is consistent with results previously

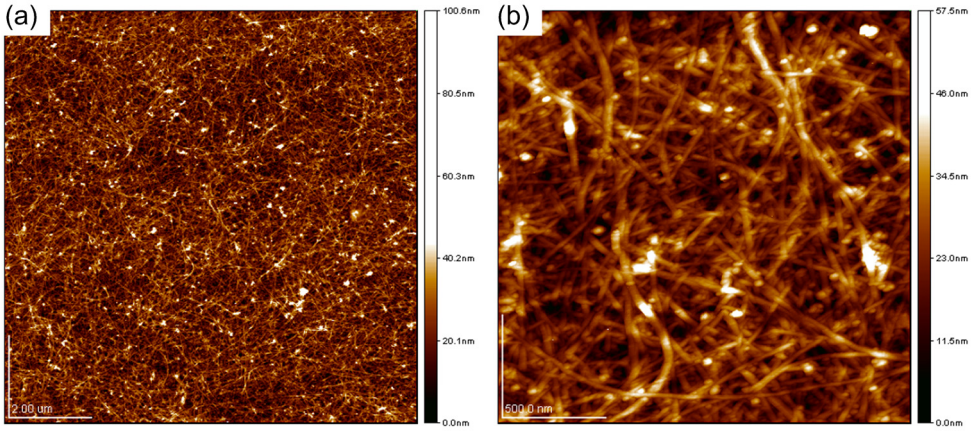

Figure 5.3: AFM images of a CNT film scanned over a large area of 10x10 µm^2 (a) as well as a zoom-in of a smaller area of 2x2 µm^2 (b). The values measured for the average and RMS surface roughness are 5.79 nm and 7.41 nm, respectively.

reported by other groups examining the same CNT material used here [133]. However, there the saturation conductivity reached at 50 nm was 400 S/cm, whereas for our films conductivity approaches 4000 S/cm at 45 nm, thereby being one order of magnitude higher. Besides the choice of a raw material with a given purity and ratio of metallic to semiconducting tubes, numerous other factors influence the conductivity of the films including length and diameter distribution of tubes and bundles, presence of residual surfactants, and doping during post-deposition treatments.

For certain applications of CNT films, evaluation of the electrical properties solely is not sufficient. The optical characterization of fabricated films can give insight into the influence and degree of doping/dedoping through chemical and thermal treatments. This can be achieved by the examination of metallic and semiconducting transitions in the absorption spectrum of films processed differently, as discussed previously. Moreover, in applications requiring optically transparent CNT films, the transmittance in the visible spectral range is of special interest. For this purpose, the transmittance at a wavelength of 550 nm is typically used as a representative value for comparison. As the optical losses increase naturally with increasing film thickness while the electrical losses decrease, a trade-off must be found for applications requiring both, transparency and conductivity. Hence, a common approach for the evaluation of the electro-optical performance of such films is to plot sheet resistance as a function of the transmittance at 550 nm. This relation is plotted in Fig. 5.5 for the fabricated CNT films. A good trade-off between sheet resistance and transmittance is achieved with films having 200 Ω/sq at 80 % or 105 Ω/sq at 65 % transmittance. These values closely match state-of-the-art performance of films fabricated using more common and well established deposition methods, such as spin-coating or even vacuum filtration. Another method to quantify and compare transparent conductive thin-

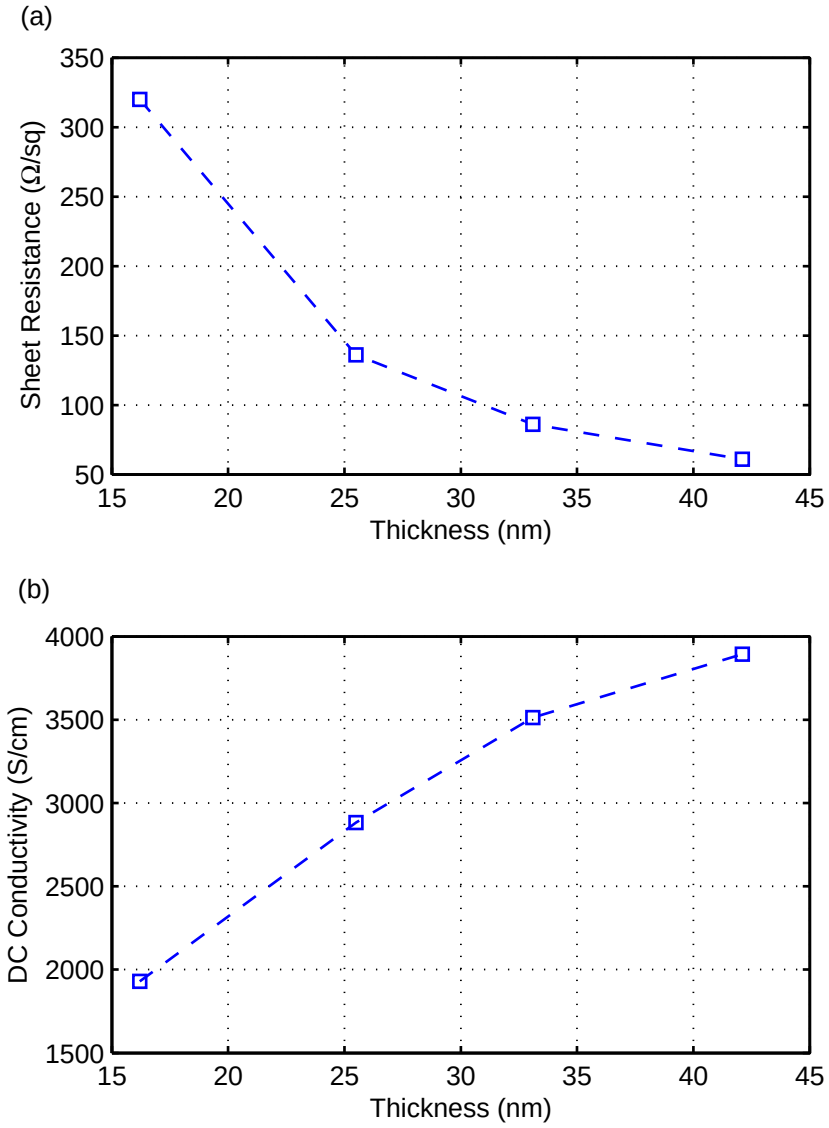

Figure 5.4: (a) Relation between sheet resistance (R_{sh}), as determined by four-point probe measurements, and film thickness. (b) The calculated values of DC conductivity (σ_{dc}) as a function of film thickness.

films is by using the formula defined in Eq. (5.1), where σ_{op} is the optical conductivity and Z0=377 Ω is the impedance of free space [134].

$$T = \left(1 + \frac{Z_0}{2R_{sh}} \cdot \frac{\sigma_{op}}{\sigma_{dc}}\right)^{-2} \tag{5.1}$$

This formula is originally applied to characterize thin metal films where the absorption of the material is significantly lower than the reflectance and the thickness of the film is much smaller than the wavelength of interest. Typically, the value for the optical conductivity of CNT films at 550 nm is chosen to be 200 S/cm, as determined by Ruzicka et al. [135].

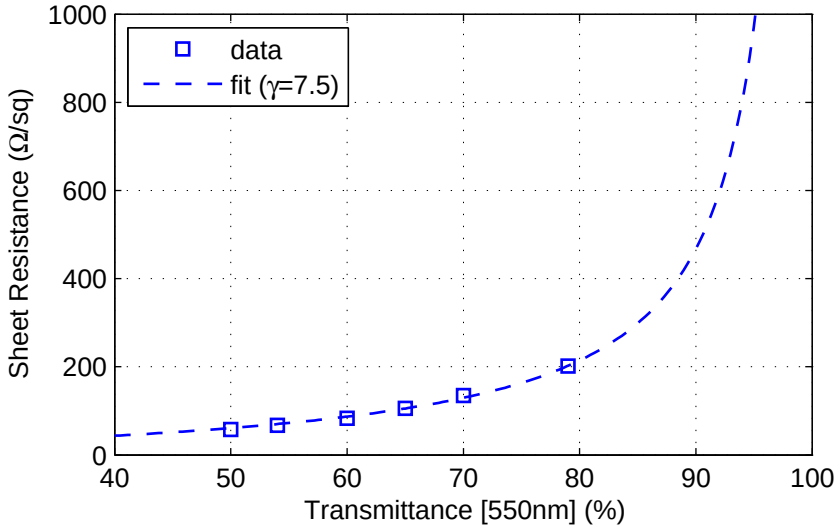

Figure 5.5: Plot of sheet resistance (R_{sh}) as a function of optical transmittance at 550 nm. A good trade-off between sheet resistance and transmittance is achieved with films having 200Ω/sq at 80% or 105Ω/sq at 65% transmittance.

Since optical conductivity is independent of doping levels, this value is assumed to be constant even among differently processed films. By fitting the data plotted in Fig. 5.5 to this formula a value of 7.5 is obtained for the ratio $\gamma=\sigma_{dc}/\sigma_{op}$, which is often used as a figure for quantitative comparison of CNT thin-film performance. This figure should however be considered with caution and may not be suitable for straightforward comparison, since sheet resistance also depends on the type of SWNTs used and the level of doping. Tube diameter, average bundle length, and film roughness are detrimental factors for transmittance as well. The DC to optical conductivity ratio (γ), extracted from relation between sheet resistance and transmittance, is therefore best suitable for the comparison of different films prepared using the same method and under similar conditions. Nevertheless, the values determined above are comparable to those reported for CNT films incorporating the same type of nanotubes (P3-SWNT, Carbon Solutions Inc.), although fabricated using a different method [136].

All figures discussed above demonstrate that the readily scalable air-atomizing spray deposition process presented here yields high quality CNT thin-films with competitive electro-optical performance suitable for different device applications.

5.1.3 Effect of Process Parameter

The previous section was dedicated to a general description of the materials and methods involved in the CNT thin-film technology developed here. Note that a careful optimization of the different process parameters and processing conditions is crucial for achieving

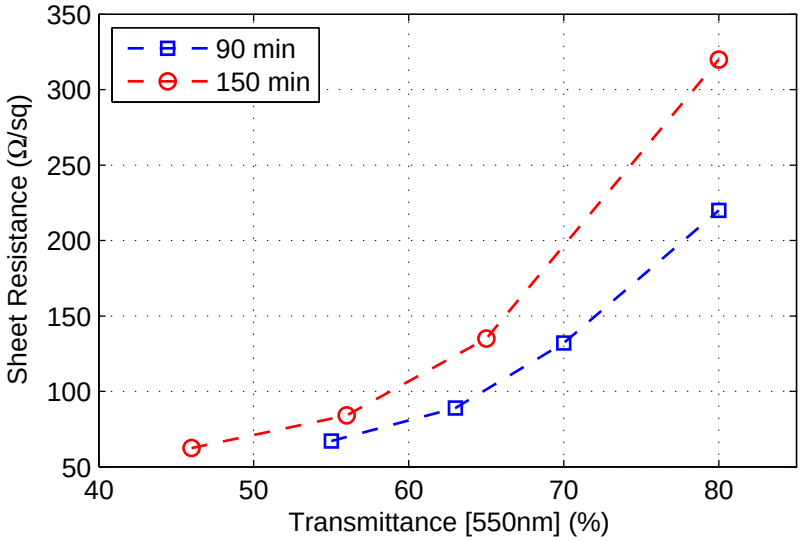

Figure 5.6: Variation of sheet resistance as a function of transmittance at 550nm for SWNT films deposited from solutions with different sonication time. All film were chemically treated in concentrated HNO_3 (65%) for 3 h following CMC removal.

reliable and reproducible results using spray deposition. Several process specific issues have to be addressed for the spray deposition and post-deposition treatment of CNT thin-films based on different types of surfactant.

Sonication Time and CNT Distribution

The effect of sonication power and duration on the quality of the CNT dispersion used for nanotube deposition from solution is of major significance for the performance of the resulting CNT thin-film. It is necessary to differentiate between different sources used for ultrasonic assisted CNT dispersion into solution. The two types typically used in such an application are bath and probe sonicators. While in a bath sonicator the ultrasonic power is generated in a water bath containing a flask with the CNT solution, a probe sonicator is directly immersed into the flask where the ultrasonic power is generated locally. This renders probe sonicators more powerful, hence requiring shorter sonication durations for solution preparation. The results discussed here to demonstrate the effect of sonication time on the characteristics of the final CNT film refer to dispersions prepared by bath sonication. Figure 5.6 compares the relation between sheet resistance and transmittance for a variety of spray deposited films from two CNT solutions prepared with different sonication durations. The data plotted shows a clear shift towards higher values of sheet resistance at any given transmittance. Since excessive sonication introduces tube cutting and hence results in reduction of the average tube length [137], the electro-optical characteristics of the final CNT film suffer. This is a direct consequence of the percolation nature of such a CNT network, being composed of a random arrangement of particles with high aspect ratios, where the percolation threshold scales inversely with the average tube

length. A reduction of the average tube length therefore leads to an increase in the percolation threshold, with shorter sonication allowing for lower sheet resistance at a given optical transmittance or tube density [138].

In order to be able to evaluate the quality of a given CNT dispersion, an analysis of the CNT bundle distribution within the resulting film has to be performed. When considering films with very low CNT density or surface coverage, it is possible to extract information about the CNT length distribution by means of image processing. For this purpose, the CNT solution under investigation is highly diluted and used to spray a CNT network with ultra-low density onto a Si substrate. The sample is then further processed according to the usual procedure and its topography is characterized by AFM. Analysis of CNT bundles and their length distribution is finally performed using the image processing software ImageJ. Figure 5.7 shows the original AFM image obtained for such a sample along with the processed image used to generate the corresponding bundle length distribution. A histogram containing the bundle length distribution obtained for a sample sprayed with the CNT solution of 90 min sonication is plotted in Fig. 5.8. A total of 79 CNTs are counted and considered in this distribution, hence allowing an acceptable statistical analysis. The histogram shows the relative frequency of occurrence for different tube lengths. It is then possible to fit the given tube length data with a log-normal distribution, as represented by the solid red line in the same figure. This is in good agreement with CNT length distributions typically found in literature [124]. For our film, the best fit is obtained using a log-normal distribution with a mean of 744 nm and a standard deviation of 95 nm. Longer SWNT bundles result in lower sheet resistances due to less intertube junctions, which prevail in determining overall film conductivity.

Chemical Treatment with Concentrated HNO_3

Chemical post-deposition treatment with dilute HNO_3 is needed for surfactant (CMC) removal as described above. At the same time however, this treatment introduces an intentional p-type doping of the SWNT film. Treatment with concentrated HNO_3 is found to be effective when a strong doping of the film is desired. We analyzed the reduction in sheet resistance of SWNT films with different thicknesses due to concentrated HNO_3 (65%) treatment. The different samples were directly immersed into the HNO_3 and the sheet resistance was recorded for varying treatment intervals. A graph containing the collected data is shown in Fig. 5.9(a). It is found that treatment with concentrated HNO_3 for 1 h seems already sufficient to approach the lowest value of sheet resistance for any given film, after which only slight reduction is observed. For all films within the thickness range examined here, a stabilization of sheet resistance occurs within 3 h of treatment. Moreover, the absolute change in sheet resistance for thinner films is larger than for thicker films. This is assumed to be due to the fact that thicker films, i.e. ones with higher tube density, contain a larger number of metallic tubes and hence more metallic paths,

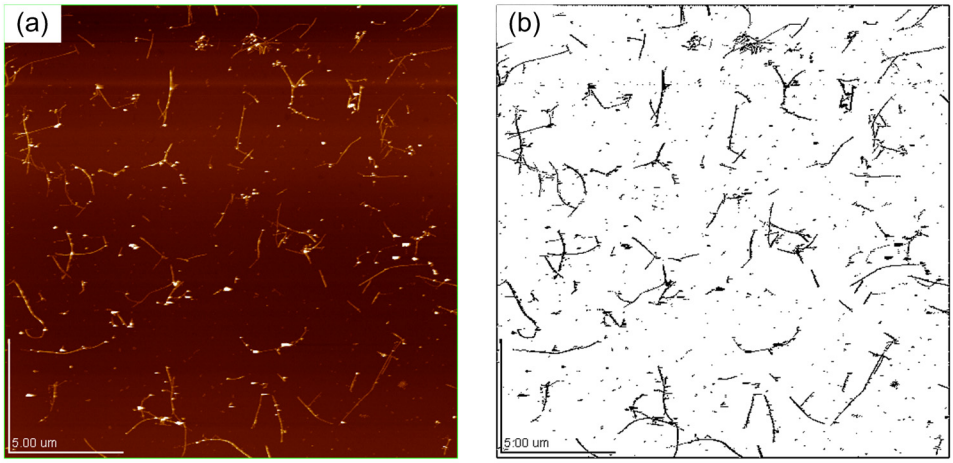

Figure 5.7: (a) AFM image of a CNT film with an extremely low tube density scanned over an area of 20x20 µm^2. (b) The processed image used for bundle length analysis.

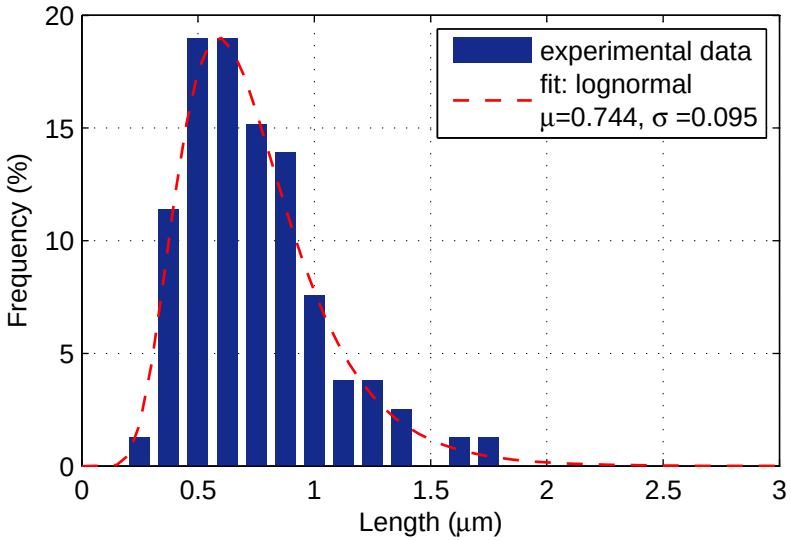

Figure 5.8: Histogram showing the relative frequency of occurrence for different tube lengths. It is possible to fit the given tube length data with a log-normal distribution with a mean of µ=744 nm and a standard deviation of σ=95 nm.

suppressing the effect of doping on the conductivity of semiconducting tubes. The relative change in sheet resistance is however similar for all samples, with reduction by factors of 1.3 to 1.5 after treatment.

Optical Characteristics

In a discussion about the optical properties of CNT thin-films, optical transmittance is of particular interest for organic optoelectronic device applications. As semitransparent electrodes in OLEDs or OPDs, an optimum of sheet resistance and transmittance within the visible range of the optical spectrum has to be carefully determined. Additionally,

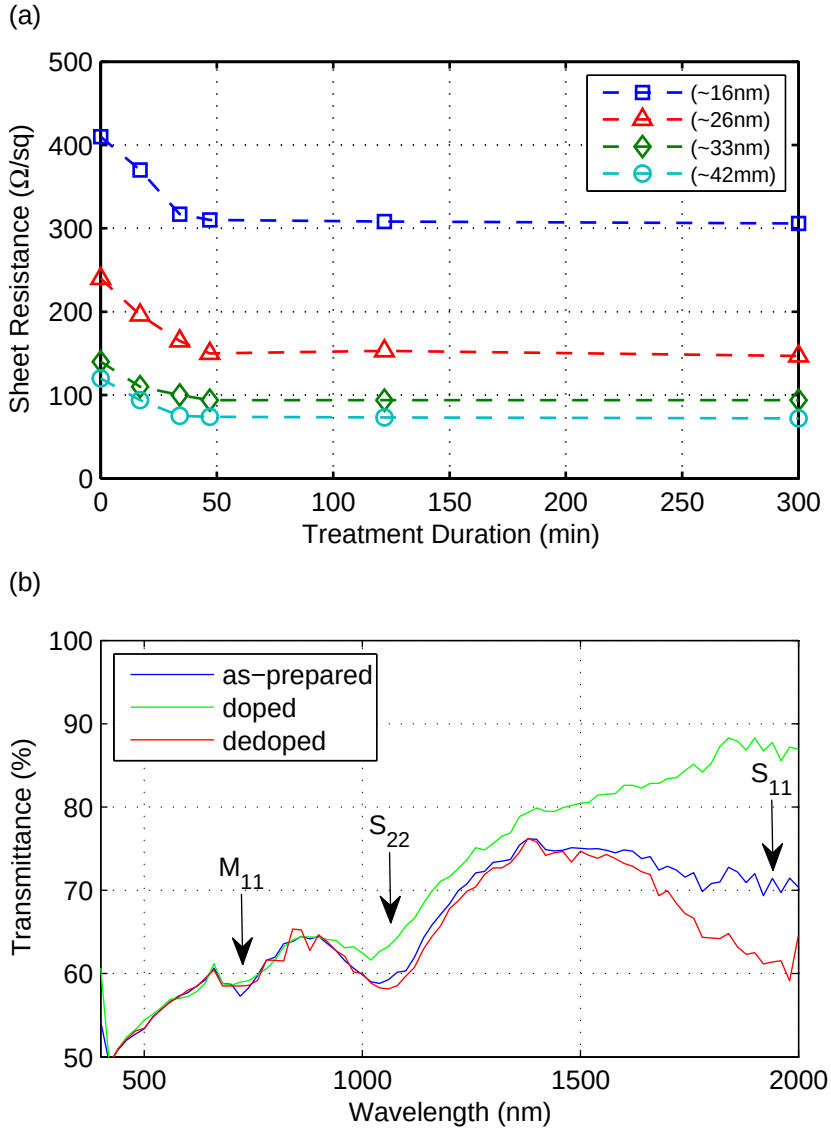

Figure 5.9: (a) Variation of sheet resistance as a function of concentrated HNO_3 (65%) treatment duration for four films of different thicknesses. All films were previously subject to identical treatment in dilute HNO_3 (13-23 %) for CMC removal. (b) Optical transmittance spectra of an as-prepared, doped and dedoped SWNT film.

fundamental information on specific properties of the nanotubes incorporated in a film, such as electronic transitions and doping of nanotubes, can be obtained by the analysis of a broader spectral range extending beyond the visible wavelengths.

The measured optical transmittance decreases with increasing CNT film thickness and is wavelength dependent. It is therefore necessary to define a representative value for the transmittance of any given CNT thin-film. While in some cases this measure is defined as the average transmittance over a certain spectral range, usually including visible and infrared range (400-1800 nm) [124], a more common convention is to use the

transmittance at a fixed wavelength of 550 nm as a representative value. The latter yields moderate values and results in more realistic figures within the context of optoelectronic applications operated in the visible spectral range. Note that this figure can be considered to represent a lower limit, since film transmittance increases considerably in the infrared range. Depending on the application under development, a trade-off between optical and electrical losses must be found such as to fulfill the specifications required.

The characteristic absorption peaks attributed to electronic transitions at van Hove singularities can be observed in the optical transmittance spectrum of SWNT thin-films, thereby deducing information about the extent of doping/dedoping through chemical and thermal treatments. To demonstrate this, a SWNT film was fabricated by spray deposition, which was then characterized once as-prepared and again after performing different post-deposition treatments. Figure 5.9(b) shows the wavelength dependent optical transmittance curve of the as-prepared spray deposited film, where the different transitions are evident as absorption peaks. Interband energy transitions in semiconducting SWNTs are designated by S_{11} and S_{22} while the transition in metallic SWNTs is designated by M_{11}, as typically found literature [139]. As photons are incident onto SWNTs, peak absorption occurs between energies with local maxima of electron density (van Hove singularities). Due to p-type doping, electrons in the valence band are withdrawn and therefore no longer contribute to interband energy transitions. The withdrawal of electrons can be equivalently viewed as the injection of holes. Effects of p-type doping through chemical treatment of the same SWNT film by concentrated HNO_3 (65%) can be seen in Fig. 5.9(b) (doped). A nearly complete bleaching of the S_{11} transition and significant reduction of the S_{22} transition can be observed for the doped film. The preceding observation clearly confirms the occurrence of electron withdrawal from the valance band of the semiconducting SWNTs upon doping with HNO_3. A similar effect is observed when films are chemically treated with $SOCl_2$. The p-type doping of SWNTs can be reversed by a thermal treatment. Here, the film is annealed on a hot plate at 200 °C for 2 h under ambient conditions. A substantial increase of the absorption peak corresponding to the S_{11} energy transition is observed, as seen in the transmittance curve (dedoped) shown in Fig. 5.9(b). Due to partial removal of previously adsorbed oxygen species after thermal annealing of the film, electrons are returned to their initial state in the first van Hove singularity. Consequently, photon energies equal to the S_{11} electronic interband transition are absorbed as indicated by a dip in the transmittance curve located at a wavelength of approx. 1900 nm. The return of electrons to the p-type nanotubes causes a reduction in the excess charge carriers, which in turn leads to reduction of the overall film conductivity. Sheet resistance is hence decreased from 100 Ω/sq for the HNO_3 doped film to 420 Ω/sq by thermally induced dedoping. From the preceding example, we conclude that a qualitative evaluation of the extent of film doping is possible by simple analysis of the optical absorption spectrum in the near infrared range.

	Synthesis Method	Length (μm)	Diameter (nm)	Purity (vol%)
P3-SWNT (Carbon Solutions)	arc discharge	**0.5 – 1.5**	1.3	90
ASP-100F (Hanwha Nanotech)	arc discharge	**5 – 20**	1.0 – 1.2	90

Table 5.1: Specifications of the SWNTs (raw material) utilized in this work, as obtained from two different suppliers.

5.1.4 Changing the Type of SWNTs

Geometrical scaling in CNT thin-films is primarily a consequence of the percolation nature of the network. While CNT-polymer composite systems show 3D percolation behavior, thin-films on flat substrates become a 2D percolation problem. Many experimental studies on the percolation behavior in 2D systems with conducting objects have been carried out and can be found in literature [140]. The most outstanding feature of CNTs in this context is there large aspect ratio, which renders the formation of conducting paths possible at extremely low surface coverage. Hence, the aspect ratio of the CNTs involved in a network is of particular relevance when considering the achievable film conductivity at a given tube density.

Since the overall resistance of CNT films is dominated by the junction resistance between connected tubes, a reduction in the total number of junctions is beneficial for lower film resistance. In other words, reducing the number of tubes required to connect any two points of given distance implies a reduction in the number of junctions included, resulting in a lower resistance of the conducting path. This can be achieved by employing longer tubes in the network. Assuming similar tube and bundle diameter, films containing longer tubes and bundles are expected to reach lower sheet resistances at any given film transmittance. To demonstrate the effect of tube length on film performance, we selected SWNTs from two different suppliers. The first is P3-SWNT (Carbon Solutions Inc.), used in all previously discussed results, while the other is ASP-100F (Hanwha Nanotech). Note that both types of SWNTs are synthesized by electric arc discharge and differ mainly in average tube length, as seen from a comparison in Table 5.1. Thin-films of both types were prepared under similar conditions, as to allow direct comparison in terms of film performance. In general, the same process described above was used for film fabrication. In this case however, a probe sonicator was utilized to achieve proper dispersion during solution preparation.

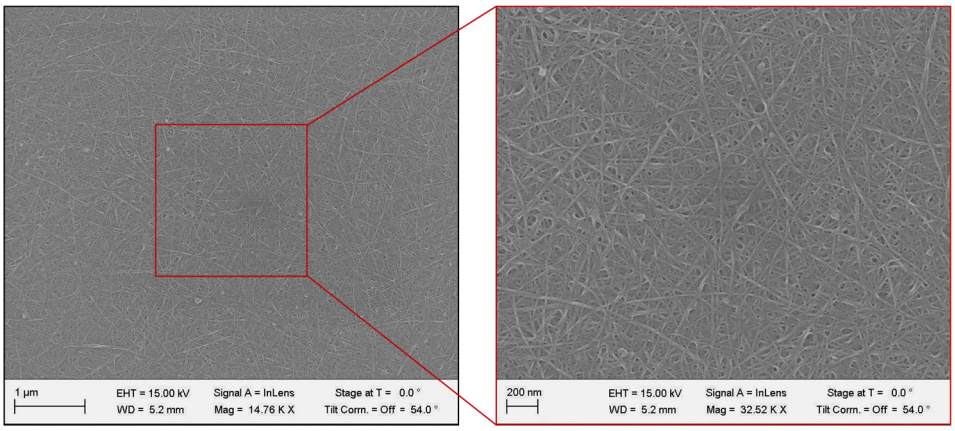

Figure 5.10: An SEM image of a film composed of ASP-100F (Hanwha Nanotech) SWNTs spray deposited onto a Si substrate along with a zoom-in acquired within the same area.

Figure 5.10 shows scanning electron microscopy (SEM) images of a film containing ASP-100F SWNTs spray deposited onto a Si substrate. The relation between sheet resistance and transmittance for films of both types is plotted in Fig. 5.11. It can be seen that, as expected, results obtained for the shorter SWNTs (P3-SWNT) do not differ significantly from the results shown above (Fig. 5.5) for the same type of nanotubes. Considering the longer SWNTs (ASP-100F) show significantly lower sheet resistance at any transmittance, with increasing difference at lower tube density. This is reflected in the values of γ extracted by fitting the shown data using Eq. (5.1). While P3-SWNT films exhibit a value of 6.5, which is similar to the one obtained above, a value of 15.2 is reached for ASP-100F films.

5.1.5 Using Different Dispersants

A major challenge in the fabrication process of CNT thin-films lies in the preparation of high quality dispersions for the deposition from solution. Large van der Waals forces acting between individual CNTs cause them to stick strongly together and form large bundles. Hence, tubes have to be separated without the use of covalent chemistries or other harsh conditions, which could lower their electrical conductivity [4]. This is achieved by adding a dispersant to the coating solution, as described above. In general, post-deposition treatment is required for the removal of dispersants from the fabricated thin-film due to their insulating nature. Since post-deposition treatment depends on the type of dispersant selected, compatibility with all materials involved in the fabrication process has to be ensured. Despite the excellent dispersing capabilities of CMC, the need for dilute HNO_3 treatment in order to efficiently remove it from the film imposes some constraints on the choice of substrate material. Some flexible materials of interest, such as Polyethylene terephthalate (PET) or Polyvinyl chloride (PVC), can withstand the exposure to HNO_3

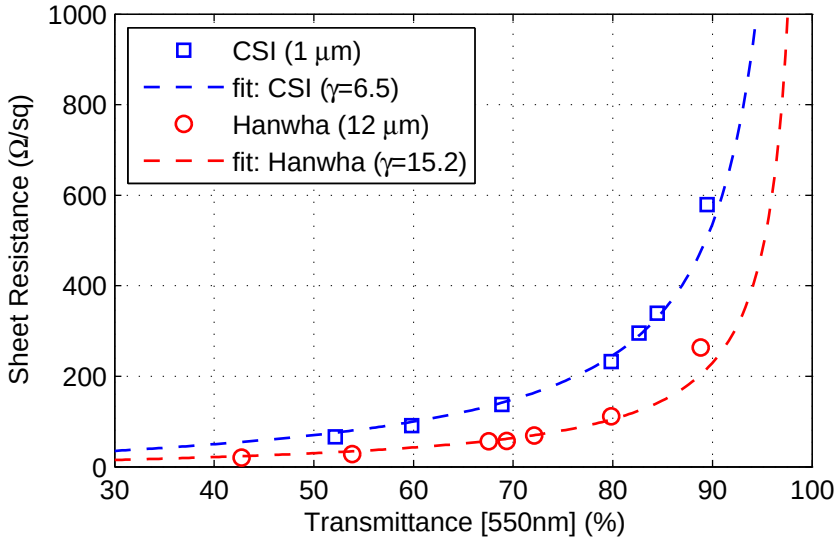

Figure 5.11: Plot of sheet resistance (R_{sh}) as a function of optical transmittance at 550 nm for films deposited from two solutions containing different types of SWNTs. Films with longer SWNTs show significantly lower sheet resistance any transmittance, particularly at lower tube densities.

only for short durations without significant degradation. To use such a substrate it is necessary to adjust the process accordingly, by using different dispersants. One of the most widely used water-soluble surfactants is sodium dodecyl sulfate (SDS). Unlike CMC, films based on SDS readily exhibit conductive behavior upon deposition. Removal of the dispersant can be achieved by simple immersion in water, rendering this process suitable for plastic based substrates.

Process Adjustment

It is important to note that, in terms of processing, SDS based dispersions behave strongly different from CMC based ones. Several process parameters relevant to spray deposition as well as post-deposition treatment have therefore to be readjusted. Nevertheless, the same approach introduced previously is successfully applied to spray deposition of SDS based thin-films, where we operate within the wet spraying regime while heating up the substrate in order to speed up the drying of wet droplets arriving at the substrate. This however has to be performed at lower atomizing pressure and material flow rates, as to generate a softer spray with lower velocity and weaker impact of droplets. Due to the foaming tendency of SDS:H_2O solutions, a softer spray is required to minimize the formation of foam upon impact of solution droplets onto the substrate, leading to more uniform and smoother films. In addition, lowering the substrate temperature during deposition to 60°C further improves film quality by reducing surface roughness. A direct drawback of the above mentioned adjustments is the lower deposition rate achievable, which reduces the throughput of the process. On the other side, the surfactant is simply removed by immersion of as-deposited

films in DI-water for ≥30 min., thereby significantly reducing the duration of post-deposition treatment. This renders the overall fabrication process of CNT thin-films based on SDS easier and less time consuming as compared to CMC. The experimental data presented in this section was collected for P3-SWNT films.

Thin-Film Characteristics

To evaluate the performance of SWNT thin-films fabricated from SDS based dispersions, several sets of samples with different film thicknesses were prepared while varying various process-specific parameters. The relation between sheet resistance and transmittance is plotted in Fig. 5.12(a) for the best set of films. For comparison, the best results obtained using SWNT thin-films fabricated from CMC based dispersions are also shown. Taking a closer look at the characteristics of films based on SDS reveals reasonable performance in terms of the achievable sheet resistance at any given transmittance, with the lowest data point corresponding to 177 Ω/sq at 78 %. The closely matching curves indicate comparable performance in terms of sheet resistance and transmittance for the same type of CNTs and show little effect due to the two different dispersants employed. Note however, that the data points plotted for CMC based films reach significantly lower values, since the film thicknesses achieved are higher. To reach the same thicknesses and hence values with SDS based films, much longer spraying durations are required due to the low deposition rates employed for SDS based dispersions, as described above.

Another important aspect to be evaluated is the surface roughness of the resulting films. We already demonstrated the feasibility of preparing highly uniform SWNT thin-films with very low surface roughness using CMC as a dispersant, where surface roughness is characterized by AFM and values were given for one representative film. This can be extended to include data collected from films of different thicknesses in order to determine a thickness-dependent surface roughness, which is shown for SDS as well as CMC based films in Fig. 5.12(b). In general, surface roughness is observed to increase nearly linear with film thickness within the range examined. Direct comparison of the data plotted for the two different dispersants points out a major issue of SDS based films, which is a significantly higher surface roughness. At a film thickness of approx. 25 nm, a surface roughness of 11 nm is measured for SDS as opposed to 6 nm for CMC, thereby being almost double as high. An AFM image of such an SDS based film spray deposited on glass, scanned over an area of 10x10 μm^2, is presented in Fig. 5.13(a)

Despite the above mentioned drawbacks of spray deposited CNT thin-films from SDS based dispersions, simple post-deposition treatment needed for surfactant removal renders this process applicable to almost any type of substrate material, including plastics with poor chemical resistance. To demonstrate the feasibility of manufacturing SWNT thin-films on conventional flexible substrates using the processing technology discussed in this

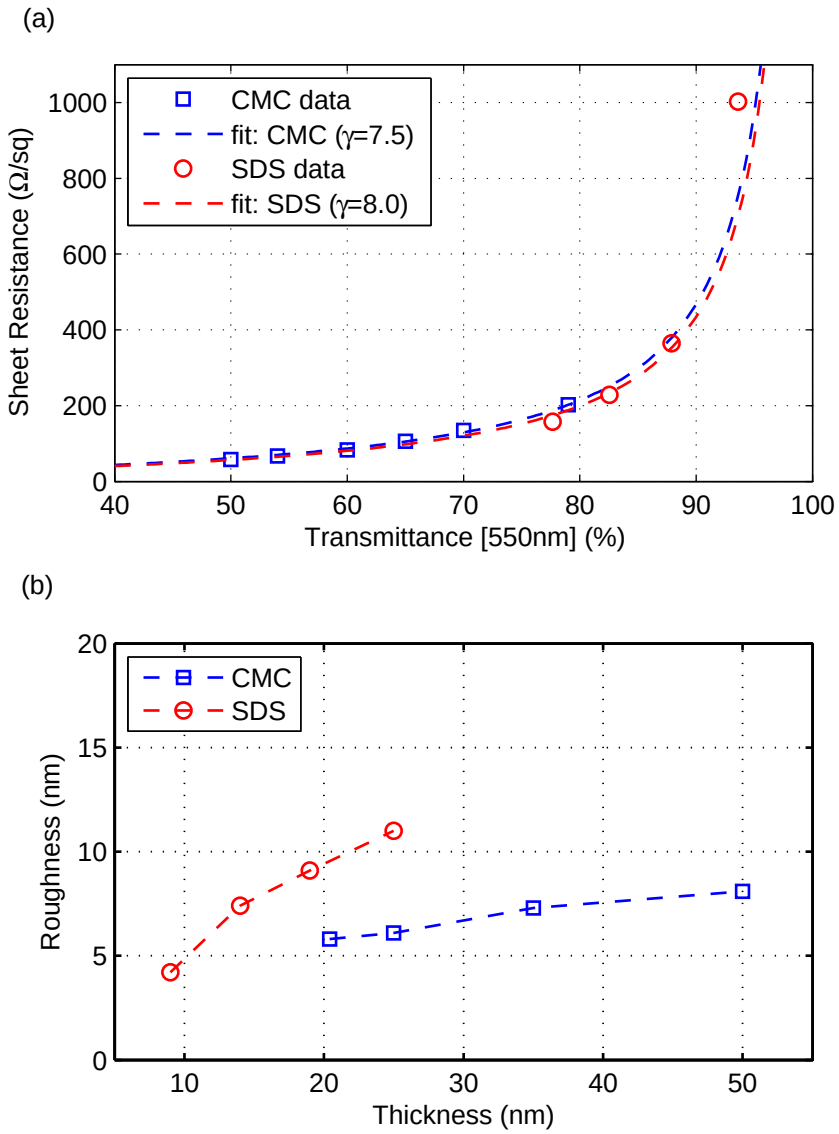

Figure 5.12: (a) Comparison of sheet resistance and transmittance obtained for SWNT films deposited from SDS and CMC based dispersion. (b) The relation between film thickness and surface roughness shows a nearly linear behavior within the measured thickness range for both SDS and CMC based SWNT films, where SDS based films exhibit higher surface roughness.

chapter, P3-SWNT aqueous dispersions based on SDS are spray deposited on commercially available PVC substrates of 200 µm thickness. While minor adjustments of process parameters are applied with respect to deposition on glass substrates, post-deposition treatment remains identical. The relation between measured sheet resistance and film thickness is plotted in Fig. 5.14. for undoped/doped SWNT films deposited on PVC. Doped samples are soaked in concentrated HNO_3 (65%) for 60 min following surfactant removal, which does not cause significant degradation to the substrate material. For direct comparison, the same figure contains results obtained for a doped film on glass prepared using the same process. Films deposited on PVC show a similar characteristic trend with

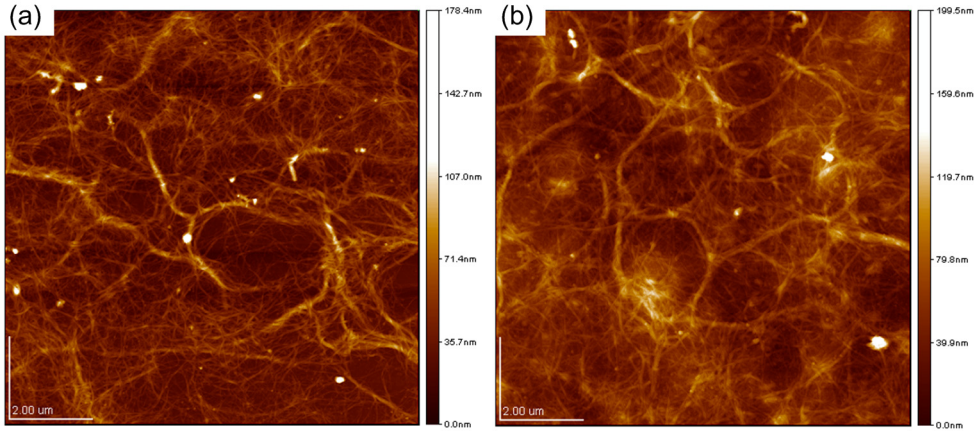

Figure 5.13: AFM images of two CNT films scanned over an area of 10x10 μm^2. The SWNT films shown are directly spray deposited from an SDS based aqueous dispersion onto glass (a) as well as PVC (b).

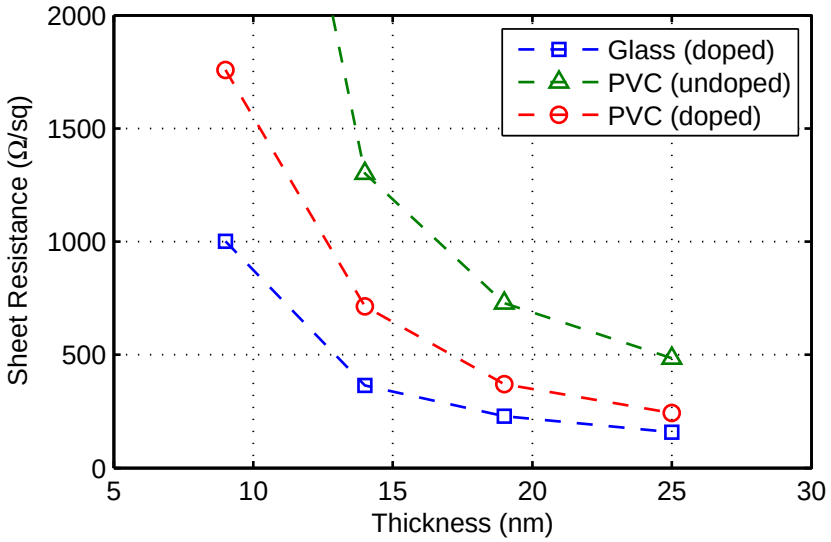

Figure 5.14: Comparison of the sheet resistance of films deposited on glass as well as PVC with respect to film thickness. A reduction in sheet resistance of films deposited on PVC is observed even after short (1 h) treatment in concentrated HNO_3 (65%).

variation in thickness or tube density as those on glass. This behavior is to be expected since it originates from the percolating nature of nanotube networks, as previously described, and are largely independent of substrate material and surface characteristics. Even short doping with HNO_3 leads to significant reduction in sheet resistance, thereby bringing the measured values closer to ones achieved by deposition on glass. Nevertheless, films directly deposited on glass exhibit lower sheet resistance, especially for thinner films. At higher film thickness however, values achieved on PVC approach those on glass. In our

opinion, this can be explained by a less pronounced effect of the substrate surface with increasing film thickness.

The easy and rapid removal of SDS from as-prepared films upon immersion in DI-water introduces however issues of film stability. While initial post-deposition treatment does not cause any problems regarding film adhesion to the substrate, an extension of the treatment duration, repeated treatment, or subsequent HNO_3 treatment for the purpose of doping leads to the release of films in water. This phenomenon was previously utilized by several groups to cause intentional delamination from the substrate and fabricate free standing CNT thin-films floating on the water surface [141]. To ensure proper adhesion and film stability even after complete surfactant removal, the substrate has to be treated with an adhesion promoter prior to film deposition. Here we employ aminopropyltriethoxysilane (APTES) for this purpose [4]. Easy delamination from untreated glass substrates can however be useful for transfer printing of CNT thin-films.

5.1.6 Transfer Printing of CNT Thin-Films

Depending on the materials and processes involved in the fabrication of CNT thin-films, the choice of substrate material can be limited due to compatibility issues. The substrate has to be supported by the selected deposition process as well as withstand any thermal and/or chemical treatments associated with post-deposition processing. The process described above, utilizing spray deposition of a CNT solution based on CMC as a surfactant, requires elevated temperatures during deposition followed by chemical treatment in HNO_3 for several hours. The type of substrate desired for the product under development may not fully support some of the processing conditions or may result in poorer output quality when combined with the spray deposition process presented here. An alternative to the development of an entirely new process lies in introducing some adjustments to the existing and well-developed process, such that readily prepared thin-films can be transferred to the desired substrate in subsequent processing steps.

The general approach to transfer printing was already presented and discussed within the context of polymer thin-films in Chapter 3. Here we adapt the process to the transfer printing of CNT thin-films prepared by spray deposition from a solution based on SDS as a surfactant. A flexible polydimethylsiloxane (PDMS) stamp is utilized to support the CNT film during the transfer process.

Materials and Methods

In order to transfer the desired CNT thin-film to a target substrate, the material is first spray deposited from solution onto a glass substrate. A previously prepared flexible

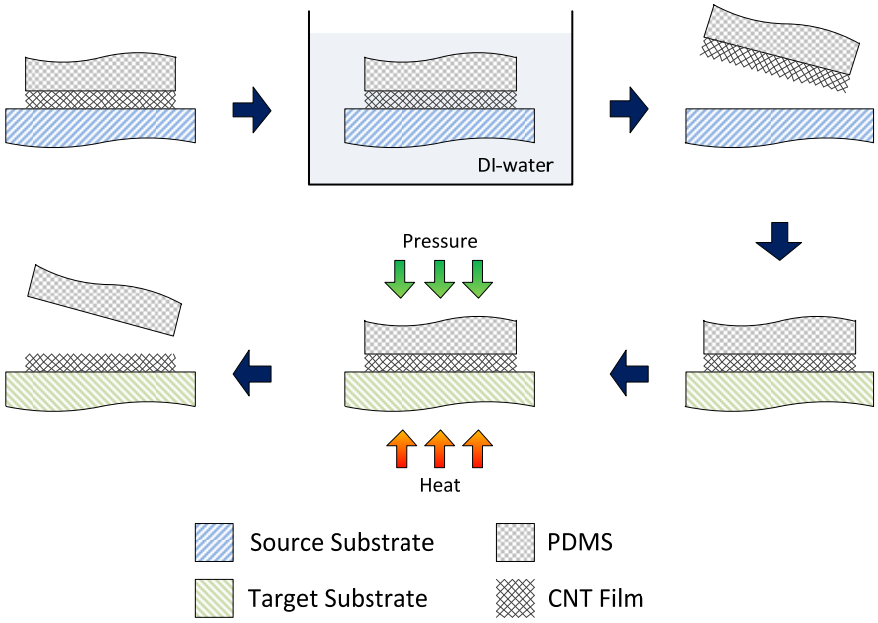

Figure 5.15: Schematic of the major steps involved in the transfer printing process presented here. SWNT thin-films can be transfer printed using a supporting PDMS stamp.

(PDMS) stamp is placed carefully on top of the CNT film while applying little pressure to achieve good adhesion and avoid any air enclosures. Once the PDMS stamp is fully attached to the CNT film, the entire stack is immersed into a bath containing DI-water for a few minutes. After removing it again from the water the PDMS stamp can be easily peeled off the glass substrate, carrying the detached CNT film. This process step relies on the weakened adhesion of SWNTs to the substrate after treatment with HNO_3 [141]. Excellent conformal contact to the PDMS stamp keeps the CNT film attached to the stamp, thereby supporting the sensitive film and enabling convenient handling for a high-yield transfer printing process. The inked stamp is then dried under gentle N_2 flow. To transfer the CNT film to a given target substrate, whether rigid or flexible, the inked PDMS stamp is again placed carefully onto the substrate while applying little pressure to achieve good adhesion and avoid any air enclosures. Finally, the resulting stack is heated up for a defined time interval (approx. 10 min) before the PDMS support is peeled off again, leaving behind the complete CNT film attached to the target substrate. To promote adhesion of the CNT film to the target substrate, the latter has to be treated accordingly before transfer printing. For this purpose, a treatment with APTES is carried out in advance. Figure 5.15 shows a schematic of the major steps involved in the transfer printing process presented here. A photo of a SWNT film successfully transferred from glass to PDMS after 1 min immersion in DI-water is shown in Fig. 5.16(a). The same SWNT film is presented in Fig. 5.16(b) after complete transfer printing from PDMS onto a flexible PVC substrate.

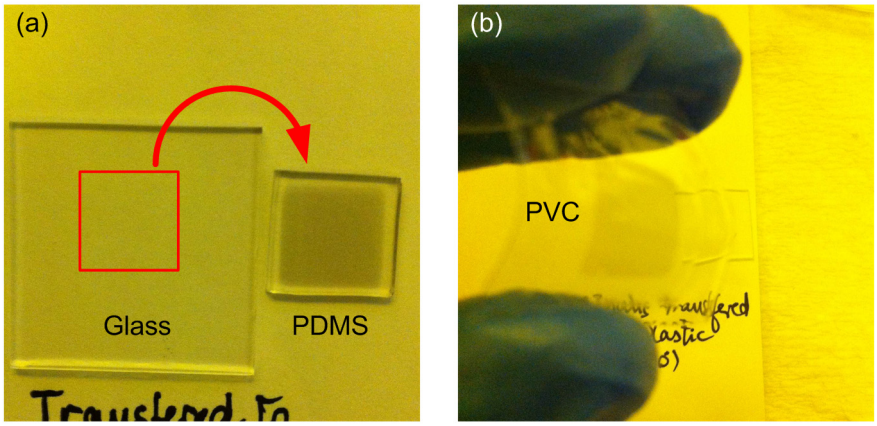

Figure 5.16: (a) Successful SWNT film transfer from glass to PDMS after 1 min immersion in DI-water. (b) Photo of the same SWNT film after complete transfer printing from PDMS onto the flexible PVC substrate.

Characteristics of Transfer Printed CNT Thin-Films

Performance evaluation of transfer printed SWNT thin-films relies on identifying and analyzing implications of the enabling process on basic film characteristics. It is hence necessary to characterize fabricated films after different processing steps. The sheet resistance plotted as a function of optical transmittance for a series of film thicknesses before and after transfer printing is shown in Fig. 5.17. Initial measurement is performed after deposition and surfactant removal on the source substrate (glass). After float-off and transfer printing onto the target substrate (PVC), the film is characterized once again. The sheet resistance at any given transmittance clearly increases by a factor of about 1.5 after the transfer printing process is performed. This can be caused by a combination of a non-perfect transfer process, the poorer surface characteristics of the target substrate, in addition to the thermal treatment involved in the transfer printing process. Further investigations need to be performed in order to clarify the contribution of each of these factors. This is however beyond the scope of the work presented here. A short doping of the film in concentrated HNO_3 (65%) for 60 min. however reduces the sheet resistance again, thereby reaching values even lower than those achieved by direct deposition onto PVC followed by similar treatment, which is also presented in Fig. 5.17 for comparison. It can hence be concluded that a higher film quality due to better surface characteristics of the source substrate is partially maintained even after deposition to a target substrate with poorer surface characteristics. Note that the slight shift in optical transmittance towards lower values, by around 2 %, is a direct effect of the existent substrate material degradation due the chemical post-deposition treatment, despite the short duration of treatment. Considering that the transfer printing process described here is only marginally optimized, the results presented promise high potential for the fabrication of CNT thin-films with

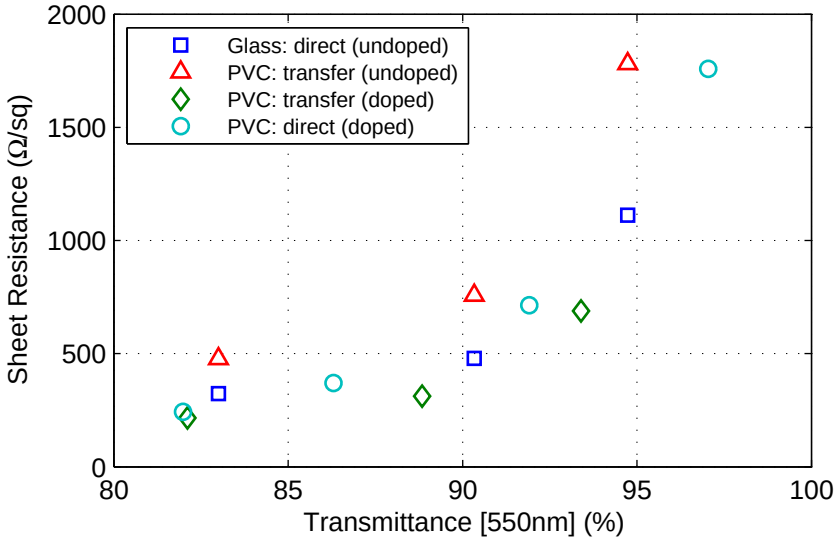

Figure 5.17: Sheet resistance plotted as a function of optical transmittance for a series of films measured before and after transfer printing from glass to PVC. Additionally, a series of transfer printed and directly deposited films on PVC are compared after short doping in HNO_3.

reasonable performance on various substrate materials, which may restrain use of the direct deposition process.

5.2 CNT Networks for Gas Sensing

The inherently reduced dimensionality and hence high surface-to-volume ratio of carbon nanotubes (CNTs) renders them as ideal candidates for environmental sensing applications. For this reason single-walled carbon nanotubes (SWNT) [127], [128], [142] as well as multi-walled carbon nanotubes (MWNT) [143–145] have been repeatedly proposed as sensors for a variety of gases. In general, CNT-based gas sensors have the advantage of being potentially flexible, low-weight and low-cost devices, thereby being attractive for single-use applications such as smart packaging. Food quality, for example, could be monitored in-situ throughout a products lifetime by monitoring the concentration of specific gases inside a package. Implementing CNT networks as conduction channels in different device architectures provides means for detecting even small changes in the local chemical environment as measurable changes in device conductance. Considering that CNTs are p-type under ambient conditions [146], adsorption of electron-donating molecules results in an increase of charge carrier recombination and hence a decrease in conductance. The adsorption of electron-withdrawing molecules on the other hand will result in an increase of the hole concentration and hence an increase in device conductance [142]. Moreover, adsorption can cause a reduction in CNT charge mobility by introducing

additional scattering sites. Sensor architectures based on single CNTs or CNT networks have previously demonstrated good sensitivity to a wide range of gases and volatile organic compounds which are relevant for industrial, environmental, and medical applications. In order to fully exploit the potential of this class of sensors, it is necessary to enable high-throughput, low-cost production onto a wide range of substrate materials of nearly arbitrary geometry. One promising technology capable of fulfilling these requirements is spray deposition. Spray technology has already been successfully utilized for the deposition of conjugated polymer and carbon nanotube thin-films for the fabrication of different device applications [94], [96], [111], [124], [130], [147]. While spray deposited CNT films were primarily employed as transparent electrodes in organic optoelectronic devices and semiconducting channels in CNTFETs, this technology has so far not been applied to the fabrication of CNT-based gas sensors.

Kong et al. were among the first to demonstrate fast and sensitive ChemFETs employing a single semiconducting SWNT working under ambient conditions [142]. Their system exhibited p-type transistor characteristics and significant change in conductance could be measured upon exposure to NO_2 and NH_3. ChemFET sensors based on a random network of SWNTs were successfully used by Novak et al. for the detection of DMMP, a simulant for the nerve agent Sarin [148]. Sub-ppb concentration levels were detectable and fast recovery of the sensor could be achieved by applying a positive gate bias. On the other hand, chemiresistor sensors based on random CNT networks, deposited by plasma-enhanced CVD, were fabricated by Valentini et al. [149]. Their sensor was capable of detecting NO_2 concentrations as low as 10 ppb at an operating temperature of 165 °C. The utilization of CNT networks in both device types, ChemFETs and chemiresistors, can be considered a simple approach to overcome limitations in reproducibility and manufacturing scalability of single CNT devices. In CNT networks the high density of nanotubes leads to an overall averaging of the electronic properties of the individual nanotubes comprising the conduction channel of the sensing device. Further, the decoration of CNTs with metal particles can increase the sensitivity and selectivity of the sensors. Penza et al. reported CNT chemiresistors incorporating CNT networks functionalized with tailored loadings of Au nanoclusters [129]. A significantly enhanced sensitivity to NH_3, NO_2, and H_2S were observed for Au-functionalized CNTs compared to pristine ones, where the highest sensitivities were recorded at an operating temperature of 200 °C. A detailed review on recent progress in the field of CNT-based gas sensors can be found in the work published by the group of Deshusses [17].

Here we report CNT-based gas sensors with exceptionally high sensitivities and fast response to various test gases. Highly uniform CNT thin-films, prepared using a reliable and reproducible low-cost spray deposition process, are utilized as resistive networks for gas detection. The CNT network is composed of commercially available unsorted SWNTs

(33 % metallic, 67 % semiconducting), which maintains the aspect of low-cost fabrication also with respect to the raw materials. The sensitivity towards four different test gases (NH_3, Ethanol, CO, CO_2) is examined along with passive and active recovery routines. It is shown that sensor response, particularly during recovery, depends on the test gas used, and hence can enable the categorization of different gases into pre-defined classes. We further demonstrate the potential enhancement in sensitivity achieved through complex impedance characterization of this type of gas sensors. The high uniformity and low density of the CNT films employed in our chemiresistor provide the means for achieving exceptional sensitivities under ambient conditions and without any further functionalization, rendering them promising for adoption into a wide range of applications, especially where low-cost room-temperature operation is desired.

5.2.1 Materials and Methods

CNT films deposited here were sprayed by an air atomizing nozzle. This type of nozzles provides, along with ultrasonic spray nozzles, the finest degree of atomization. It is worth mentioning that ultrasonic spray nozzles have also been successfully applied to the deposition of high-uniformity CNT films [124]. For our static test system, a commercially available automatic air atomizing spray gun (Krautzberger GmbH, Germany) was used. The spray gun contains an internal pneumatic control system which is activated by an electromechanical 3/2-way valve connected to a timer for precise spray time adjustment. Other major spray parameters to be adjusted for obtaining desired spray characteristics are material flow rate, atomizing gas (N_2) pressure, nozzle-to-sample distance and substrate temperature. For air-assisted nozzles the diameter of the orifice is one of the most significant dimensions for atomization. Here a nozzle with 0.5 mm orifice diameter was chosen. The atomizing gas (N_2) pressure was kept below 1 bar throughout all experiments in order to obtain the desired spray characteristics and a uniform spray pattern across the area of interest. We use an approach introduced previously for the spray deposition of active polymers in organic photodiodes [111], in which we operate within the wet spraying regime while heating up the substrate in order to speed up the drying of wet droplets arriving at the substrate. This approach allows the formation of dry layers with good thickness control over time, enhancing at the same time reproducibility.

Solution Preparation

In order to disperse CNTs in an aqueous solution, a high molecular weight cellulose derivative, sodium carboxymethyl cellulose (CMC), is used. This kind of surfactant has been reported previously as an excellent agent for dispersing SWNTs in water [131]. As a first step, an adequate quantity of CMC is added to Millipore DI water such as to obtain a 0.5 wt% aqueous solution of CMC. This solution is then stirred for ≥12 h at room

temperature to uniformly dissolve the surfactant in water. The desired amount of SWNTs (P3-SWNT, Carbon Solutions Inc.) can then be added to the previously prepared CMC stock solution. Typically, a concentration of 0.05 wt% of SWNTs is used. Actual dispersion of the CNTs is achieved by sonication of the complete solution for 90 min in a bath-sonicator (85 W). The solution is then centrifuged at 15000 rpm for 2 h and the final solution is obtained by decanting the top 80 % of the supernatant.

CNT Gas Sensor Fabrication

The general device architecture of the gas sensors fabricated is illustrated in Fig. 5.18(a). Si wafers with 200 nm of thermally grown SiO_2 are used as substrates. An interdigitated electrode structure (IDES) consisting of a 3 nm thick Ti layer (to promote Au adhesion on Si) followed by a 50 nm Au layer is evaporated on top of the SiO_2. The spacing formed between the two electrodes of this interdigitated structure is chosen to be 100 µm. The substrates are exposed to oxygen plasma for further cleaning and surface treatment. An increased wettability of the sample surface after plasma treatment is beneficial for achieving uniform surface coating during spray deposition of the water-based CNT solution. On top of the IDES a CNT film is spray deposited to form the resistive network for the gas sensing. Chemical post-deposition treatment is necessary to remove the CMC-matrix embedding the CNTs, hence changing film behavior from insulating to conductive. For this purpose samples are immersed in dilute HNO_3 (approx. 16 %) for ≥12 h at room temperature for complete removal of the surfactants, rinsed in DI water and subsequently dried. Note that all steps involved in the CNT film fabrication are performed entirely in ambient conditions.

CNT Sensor Module

The complete sensor module is composed of the CNT based resistive sensing element described above, mounted on a carrier glass together with a Peltier heating element for temperature control and a Pt100 sensor for in-situ temperature monitoring. The heating element is located beneath the glass carrier, whereas the Pt100 sensor is attached right next to the sensing element on top of the glass carrier. This arrangement enables heating of the sensing element during gas exposure and/or recovery cycles up to ca. 150 °C and precise determination of the actual temperature reaching the sensing element. Photos of the front and back side of a readily mounted sensor module are shown Fig. 5.18(b).

CNT Gas Sensor Characterization

Sensor performance was investigated by exposure to different concentrations of the test gas (NH_3, Ethanol, CO, CO_2). The desired concentration is achieved by dilution of the test gas with a carrier gas while maintaining the total gas flux constant. Here, pure nitrogen (N_2) was used as carrier gas for all measurements presented. The duration of each exposure

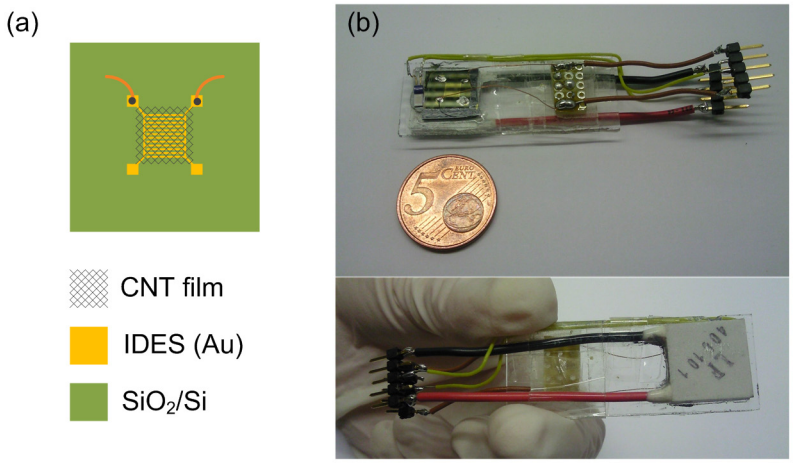

Figure 5.18: (a) The general device architecture of the gas sensors fabricated here, incorporating an interdigitated electrode structure. (b) Photo of the complete sensor module, composed of the CNT based resistive sensing element mounted on a carrier glass together with a Peltier heating element and a Pt100.

cycle was amounting to either 100 sec or 200 sec depending on the test gas, followed by either a passive or active recovery cycle of 900 sec in total.

5.2.2 Gas Sensor Operation

A common implementation for CNT gas sensors consists of an interdigitated electrode structure forming the two contact terminals of the simple resistive architecture, above or beneath which a uniformly distributed resistive random network of carbon nanotubes is deposited. Figure 5.18(a) shows a simple schematic representation of the gas sensor architecture implemented here. It is worth mentioning that the CNT films incorporated in our gas sensors have a significantly lower density/thickness than films typically used as transparent electrodes in organic optoelectronic devices. The utilization of low density films leads to better sensor response and higher sensitivities. This is considered to be a consequence of the more direct exposure of a greater portion of CNTs contributing to current conduction through the film, thereby enhancing the change of the overall film conductance when exposed to a given concentration of the test gas. An AFM image of a typical CNT thin-film deposited onto the IDES, as employed in our sensors, is shown in Fig. 5.19.

Measurement Signal and Sensitivity

Sensor read-out is performed by applying a sensing current and measuring the voltage drop across the two terminals of the device, hence monitoring the relative change in resistance/conductance with respect to different controlled environmental conditions.

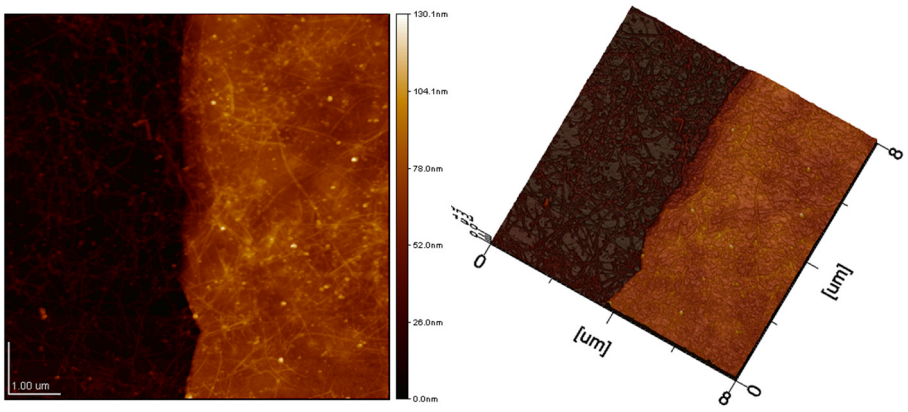

Figure 5.19: AFM image of a typical low density CNT thin-film deposited onto the IDES, as employed in our sensors. The dark region of the image shows a part of the film on SiO_2, while the bright (elevated) region is a part located on top of the Au electrodes.

Before sensor response towards a given test gas is evaluated, the initial resistance of the network is monitored for a specified time in order to determine a baseline for the device under test. Baseline characterization is performed with a sensing current of typically 10 μA under a constant carrier gas (N_2, Air) flux of 200 ml/min at room temperature. A continuous increase in the resistance of the network can be observed during the first hour before a stable state is approached. In our opinion, this effect is attributed to a continuation of the dedoping process due to the flow of a relatively high current density through the network. After reaching a stable initial resistance, the sensor response is investigated by exposing the sensor module inside a gas chamber to different concentrations of the test gas. The main figure used for the evaluation of sensor performance is the sensitivity, defined in Eq. (5.2) as the relative change in resistance, where R_i and R_f are the initial and final resistance values of an exposure cycle, respectively.

$$S = \frac{R_f\text{-}R_i}{R_i} \cdot 100 \tag{5.2}$$

Baseline and Temperature Dependence

In order to adjust the desired concentration of the test gas and to transport it to the test chamber containing the sensor module, the test gas is mixed into a carrier gas flowing through the chamber. By keeping the flow rate constant during all exposure and recovery cycles for any given test gas concentration, one can exclude any effects originating from changes in gas flow. To examine the sensor response to any of the test gases, it is first necessary to characterize its response to the basic testing conditions. This includes the determination of any drift in the baseline signal with time and its response to the carrier gas itself. The immediate change in resistance due to carrier gas flow is however below 1 %,

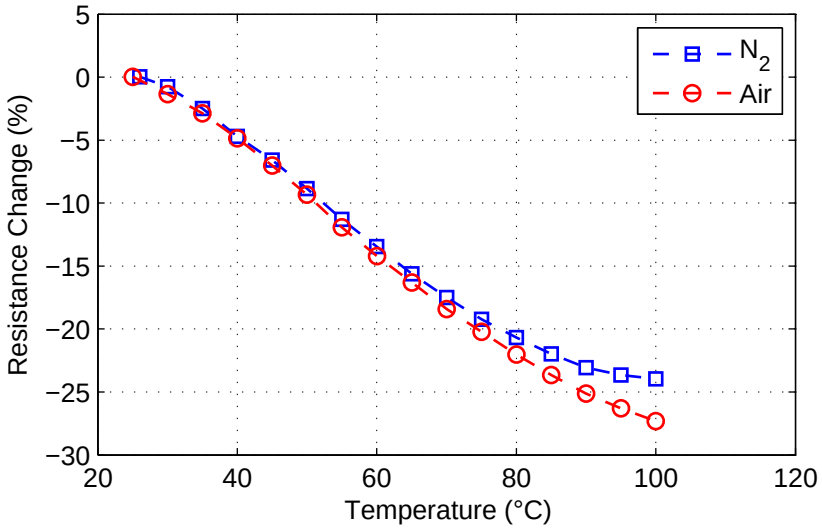

Figure 5.20: The relative change in the resistance of the two-terminal device with respect to its initial temperature at 25 °C plotted against the applied temperature.

and reaches a steady state within 1 min to 3 min depending on the type of carrier gas used. After this short stabilization interval, only a slight drift is observed over time. For later comparison, the drift is calculated over a 300 sec interval, longer than our maximum exposure duration of 200 sec, and lies below 0.2 % for N_2 and 0.4 % for air. This clearly demonstrates that the drift under constant carrier gas flow does not contribute significantly to the overall change in conductance within the typical durations of our exposure cycles and can hence be neglected during sensitivity calculations. It is worth mentioning, that the extent of drift and hence stability of the sensor, primarily during the first days of operation, are strongly influenced by post deposition treatment of the CNT film incorporated and have been adjusted here in a way to minimize drift and enhance sensor stability.

Since it is well known that CNT-based gas sensors suffer from slow recovery rates after exposure to many test gases, the sensor module can be heated during recovery cycles (active recovery) in order to achieve complete recovery within reasonable time [142], [150]. Therefore examination of the CNT network behavior with temperature is necessary to understand the effect of heating on the conductance of the network and to determine a stable operating point for active recovery. For this purpose the resistance of a CNT sensor with initial resistance of ca. 10 kΩ was characterized in a temperature range between 25 °C and 120 °C. Figure 5.20 plots the relative change in the resistance of the two-terminal device with respect to its initial temperature at 25 °C along with the applied temperature. It can be seen that within the temperature range plotted (25 °C – 100 °C) the resistance of the network decreases by approx. 25 %. The increase in conductance with increasing temperature indicates predominantly semiconducting behavior within this temperature regime. Moreover, this characteristic behavior is not significantly affected by the choice of

carrier gas, as seen in Fig. 5.20. Beyond 100 °C the behavior of the film changes and resistance starts increasing again, not shown here. It is worth mentioning that heating beyond this temperature introduces an irreversible change in conductance, probably caused by dedoping effects of the CNT network at such temperatures. A more detailed investigation of this behavior is however beyond the scope of this article. Due to this inflection point, active recovery cycles performed here were limited to a maximum of 90 °C in order to ensure stable and reversible operation of the our sensors.

5.2.3 DC Resistance Characterization

Exposure-Dependent Sensor Resistance

Figure 5.21 depicts the measured sensor resistance over time for the four test gases examined in this work, NH_3, Ethanol, CO, and CO_2. The graph for each test gas is divided into four segments, based on four exposure/recovery cycles at different concentrations. The concentrations tested for NH_3, Ethanol, and CO cover a range between 5 ppm and 100 ppm, achieved by diluting the test gas with pure N_2 as carrier gas. For CO_2 the concentrations tested cover a range between 500 ppm and 5000 ppm and is achieved by diluting the test gas with normal air as carrier gas. Note that in case of CO_2 measurements, normal air used as carrier gas typically contains 390 ppm of CO_2, which is the reason for the high concentration range covered in our tests. Each cycle is composed of an exposure interval followed by a recovery interval. During exposure, the test gas is allowed to enter the chamber along with the carrier gas at room temperature and a constant flux of 200 ml/min for the desired duration. Recovery is then introduced by heating the sensor module to 80 °C and increasing the carrier gas flux to 1000 ml/min for 300 sec, after which heating is stopped again. The high flux is maintained for another 300 sec to accelerate cooling of the sensor and purge any residual test gas molecules out of the chamber. Recovery is then completed by a final 300 sec interval under sensing conditions to restore the initial resistance. As briefly mentioned above, the increase in thermal energy during the heating cycle is necessary to enhance desorption of gas molecules attached to the CNT film and enable complete recovery. One of the most prominent features observed in the response is the clear and immediate change in resistance at the start and end of an exposure cycle even for the lowest concentrations in our test range. The abrupt drop in resistance observed at the beginning of each recovery cycle is due to heating of the CNT film to a temperature of 80 °C, which results in an increase of conductance as described above. Exposure cycles are limited in duration to either 100 sec (NH_3, Ethanol, CO) or 200 sec (CO_2). A longer exposure is chosen particularly for CO_2 due to considerably lower sensitivities achieved with respect to all other test gases in our comparison.

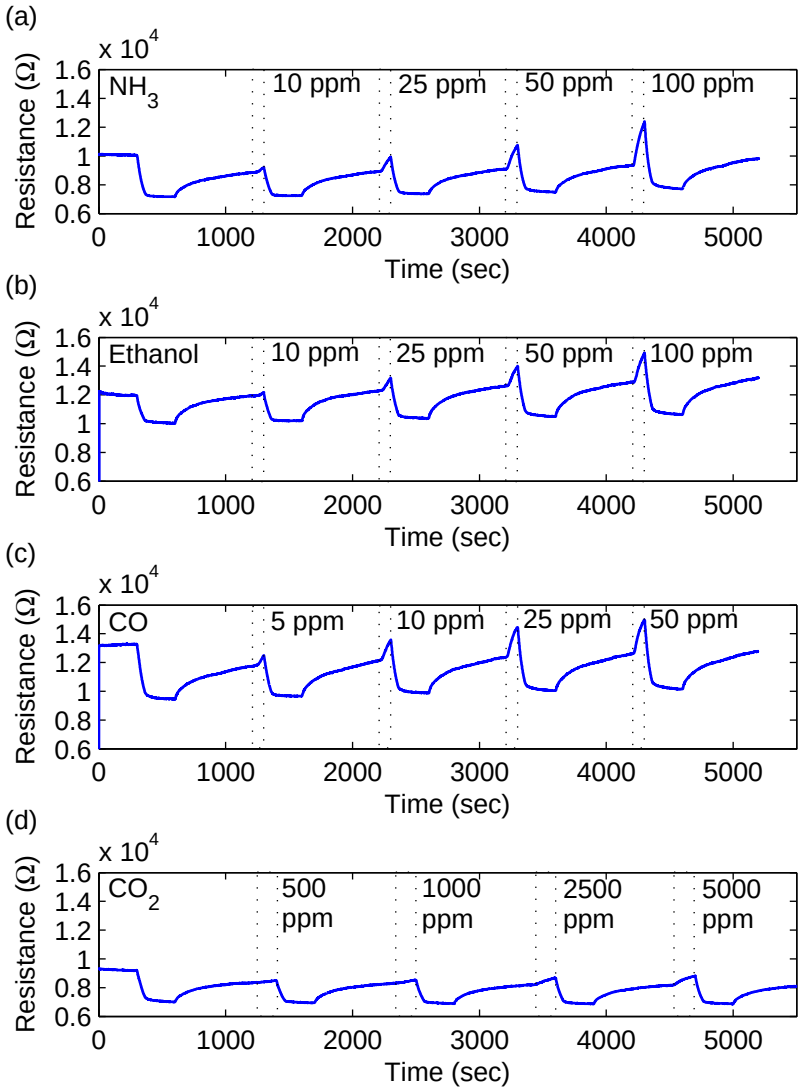

Figure 5.21: Plot of the measured sensor resistance over time. Each graph is divided into four segments, based on four exposure/recovery cycles at different test gas concentrations. The four test gases shown here are NH_3 (a), Ethanol (b), CO (c), and CO_2 (d).

Sensor Speed and Recovery

From the transient response of the sensor it becomes clear that for all four test gases the electrical resistance increases upon exposure due to adsorption of the specific gas molecules. Sensing in CNT films can be considered to originate from the contribution of two mechanisms, charge transfer causing intratube modulation and intertube modulation by gas adsorption [127]. Intratube modulation involves charge transfer in individual nanotubes, whereas for intertube modulation it occurs at the nanotube-nanotube junctions. All four test gases discussed here show electron-donating character, reducing hole density

in the as-prepared p-type CNT film and hence decreasing the overall electrical conductance. It should be noted however that the exact charge transfer mechanisms involved for different gas molecules are not completely understood. Since sensing relies on the adsorption of gas molecules, chemical reactivity of the molecules as well as the strength of the established chemical bonding are expected to influence the response and recovery of the CNT sensors. To gain insight into the transient behavior of our sensors with respect to the different test gases and to determine the speed of such sensors, response and recovery data were further analyzed by extracting the characteristic time constant of the given process. The data acquired during an exposure, following an active recovery cycle, is fitted by the logistic growth function defined in Eq. (5.3). In case of sensor recovery, the data acquired during a passive recovery is fitted by the exponential decay function defined in Eq. (5.4).

$$f_{response}(t) = \frac{a}{1 + e^{(t-t_0)/\tau}} + b \tag{5.3}$$

$$f_{recovery}(t) = a \cdot e^{(t-t_0)/\tau} + b \tag{5.4}$$

Table 5.2 contains the response and recovery parameters extracted from time plots similar to the ones shown in Fig. 5.21. The characteristic time constants associated with response and recovery processes are shown here only at a single concentration for each of the test gases. Since the response characteristics of the sensor are expected to depend on the concentration of the test gas, this parameter only serves as a figure of merit for the quantification of sensor speed for a specific gas at a given concentration. This dependence on concentration was also found in our analysis. From the data summarized in Table 5.2 it is clear that for NH_3, Ethanol, and CO, the variation in the characteristic time constant of the response process at identical concentrations is almost negligible and hence insufficient for clear discrimination between them. The situation becomes different when considering the recovery characteristics of the sensor. Here it is assumed that the characteristic time constant associated with the recovery process is largely independent of the concentration applied during a preceding exposure cycle. Taking a closer look at the corresponding data in our comparison reveals a more prominent variation between the different gases. While the time constants for NH_3, Ethanol, and CO, are close, variations among them are clearly larger than the error in the fit. For CO_2 a significantly larger time constant and hence slower recovery rate is obtained. Although in principle this allows for discrimination between different test gases examined here, it has to be noted that the recovery characteristics are influenced by experimental conditions and are hence potentially prone to strong variations. Moreover, the characteristic time constant can only be reliably extracted for recovery from high concentration exposures as to obtain clear decay characteristics and an acceptable fit. Recovery from low concentration exposures resulted

	NH_3 (50ppm)	Ethanol (50ppm)	CO (50ppm)	CO_2 (5000ppm)
$\tau_{response}$ (sec)	24.9±3	17.3±2	22.4±3	46.0±4
$\tau_{recovery}$ (sec)	323.9±5	249.3±7	385.9±11	556.3±18

Table 5.2: Comparison of response and recovery parameters as extracted from the time plots of different test gases.

in flat recovery characteristics and a bad fit. The above mentioned factors render this parameter insufficient for sole discrimination between test gases. It can however be used for preliminary categorization into classes of gases, as seen from the more significant difference between CO_2 and the rest of the gases in our test range. In combination with a sensor array architecture and functionalization of the CNT film, this can be used to facilitate unambiguous discrimination between gases.

Concentration-Dependent Sensor Sensitivity

Taking a look at the magnitude of change in resistance after exposure to different concentrations reveals a clear increase in sensitivity with increasing concentration, at least within the concentration range shown here. It can be expected that at some point for higher concentrations the sensitivity will eventually approach a certain saturation value, which does depend on the type of test gas. This becomes more evident when displaying the sensitivity to each of the test gases as function of concentration, as plotted in Fig. 5.22 In order to avoid inaccuracies in sensitivity calculations due to delays in the gas system, R_i is recorded with a delay of 10 sec after opening the valve controlling test gas flow. R_f is defined such that the exposure interval considered for the calculation of sensitivity is chosen to be 60 sec (NH_3, Ethanol, CO) or 120 sec (CO_2), which is to our knowledge shorter than the usual exposure intervals reported in literature. Sensitivity is found to have a rather logarithmic dependence on the concentration, but differs between gases and depends on the concentration range recorded. The sensitivity of the sensor to each of the test gases is plotted against concentration for two measurement scenarios, involving either passive or active recovery between the individual exposure cycles. For all test gases one can observe strong enhancement in sensitivity by active recovery, especially at higher gas concentrations. The lower sensitivities achieved under passive recovery conditions are attributed to the incomplete recovery of the sensor from preceding exposure cycles, as described before. Active recovery can therefore enhance sensitivity of the sensor by up to a factor of 3, as seen for CO at a concentration of 50 ppm, using the same sensor architecture in addition to a simple heating element. Sensitivities of 2 % for concentrations as low as

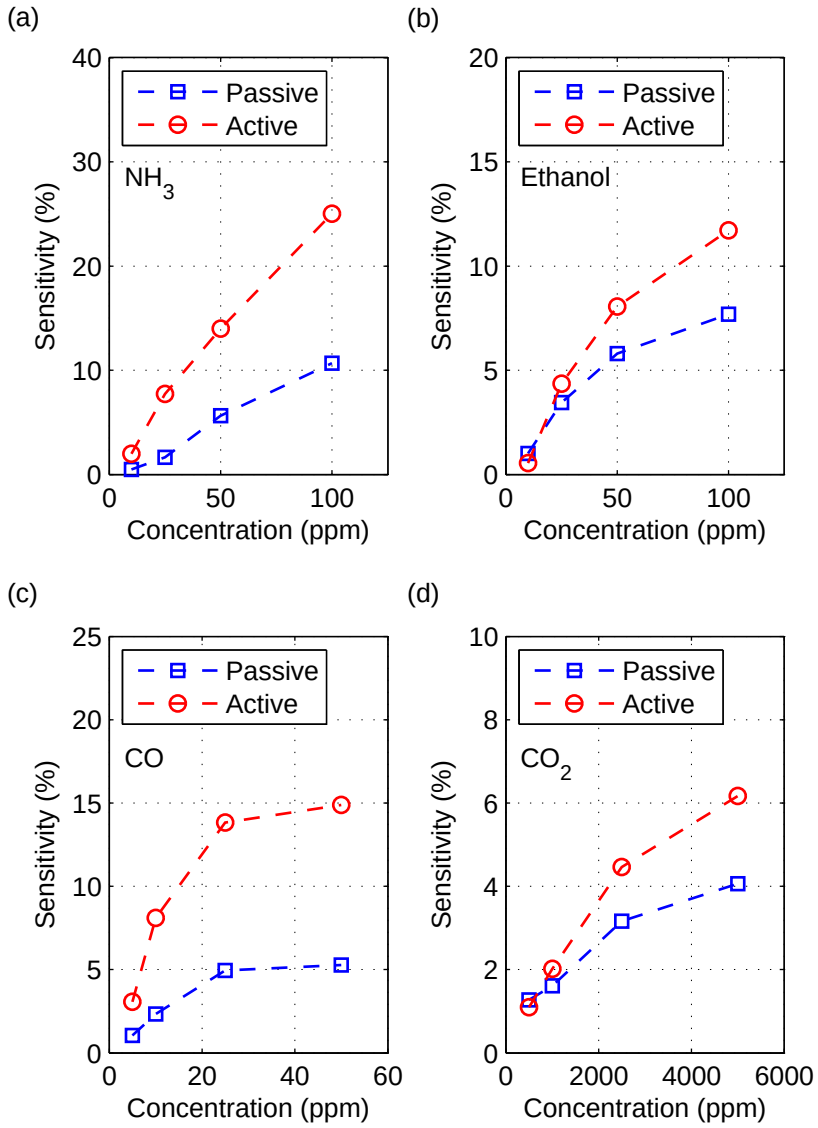

Figure 5.22: Plot displaying the sensitivity of each test gas as a function of concentration. Sensitivities presented here correspond to relative resistance changes in an exposure interval as short as 60 sec (NH_3, Ethanol, CO) or 100 sec (CO_2).

10 ppm and reaching 25 % at a concentration of 100 ppm can be achieved in case of NH_3, yielding the highest sensitivity among our range of test gases. We consider these values for NH_3 sensitivity to be exceptional, taking into account the short exposure intervals of 60 sec [129]. Lowest sensitivity of our sensor was found to be towards CO_2, which results in sensitivities of about 1 % at a concentration of 500 ppm and increases to 6 % for a concentration of 5000 ppm, despite the longer exposure interval of 120 sec considered in sensitivity calculations of CO_2. However, taking into account that the typical concentration of CO_2 in air is ca. 390 ppm, reasonable sensitivities are achieved for concentrations

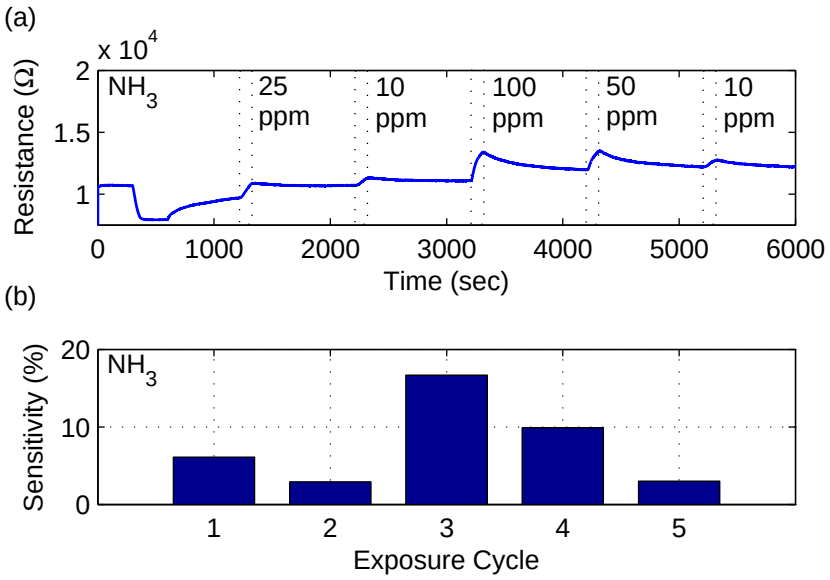

Figure 5.23: Time response of the sensor to a random sequence of exposures with different concentrations of NH_3 ranging from 10 ppm to 100 ppm.

slightly above this value. This allows the detection of CO_2 concentration variations under ambient conditions, needed for applications requiring indoor air quality monitoring.

Exposure to Random Concentration Sequences

In all of the previous discussion, the time response of the senor to any of the test gases was shown only in the case of active recovery between consecutive exposure cycles with ascending concentrations. This well ordered testing conditions may seem unrealistic for a lot of real life applications. While it is clear that the order in which the sensor is exposed to different concentrations is irrelevant in case of active recovery, it is questionable to which extent a random sequence of exposures with different concentrations can be detected in case of passive recovery. For this purpose a random sequence of four different NH_3 concentrations ranging from 10 ppm to 100 ppm was generated. The time response of the sensor to such a random sequence was recorded and is shown in Fig. 5.23. Special attention is to be given to exposure cycles 2 and 5, since those two represent low concentration (10 ppm) exposures following higher concentration ones with only passive recovery. In this case we can observe a sensitivity of ca. 3 % in both cycles. This shows that for NH_3, given the testing conditions used here, the sensitivity does not suffer significantly for incomplete recovery. Note that this is however conditioned by relatively low concentrations that are not sufficient to drive the sensor into saturation within the short exposure intervals. Such a behavior is consistent with the data presented in Fig.5.22(a) for passive recovery, where sensitivity does not approach any saturation and shows almost linear behavior within the concentration rage plotted. It is expected that for higher exposure intervals and/or significantly higher concentrations the sensor is driven towards saturation, which would significantly reduce sensitivity among subsequent exposure

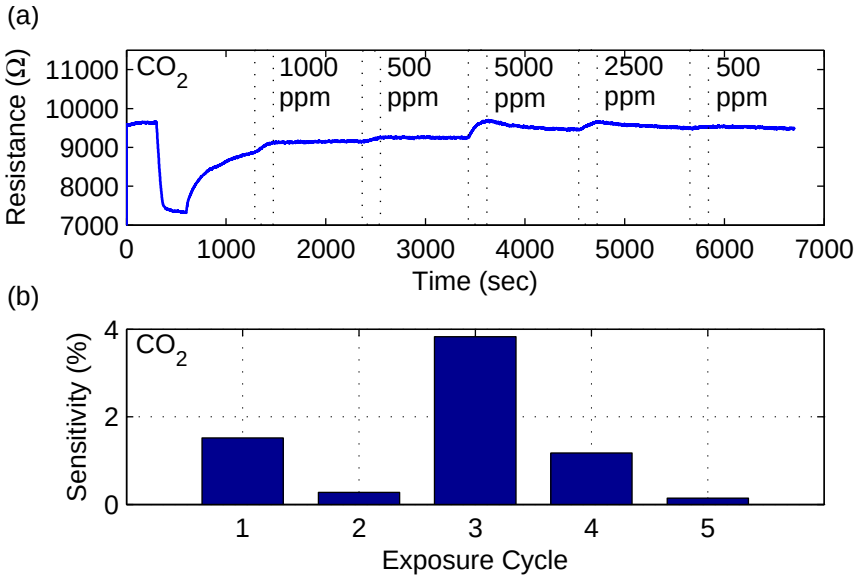

Figure 5.24: Time response of the sensor to a random sequence of exposures with different concentrations of CO_2 ranging from 500 ppm to 5000 ppm.

cycles. This kind of behavior can be easily observed in case of CO_2. Figure 5.24. shows the time response recorded in a similar experiment with random sequence of exposures with different concentrations ranging from 500 ppm to 5000 ppm. In this case it becomes obvious that sensitivity suffers from incomplete recovery from preceding exposures of higher concentration. Sensitivity calculated for exposure cycles 2 and 5 shows a reduction in sensitivity from 0.27 % to 0.14 % for the same concentration (500 ppm). The onset of saturation within the given concentration range could already be observed in the sensitivity data plotted in Fig. 5.22(d). Note that from the results discussed in this section it is difficult to predict the suitability of such a sensor for operation without constantly timed active recovery cycles. A detailed discussion regarding this issue is only possible within the context of a specific application with given monitoring requirements.

5.2.4 Nanotube Density and Senor Response

It is important to understand how CNT film properties influence device performance in the desired application. For the application in gas sensors, the CNT film forms the sensing element and is therefore decisive for device sensitivity. Functionalization can be introduced to enhance sensor selectivity and thereby significantly alter sensitivity towards certain gas molecules [151–153]. In pristine films, the major parameter for tuning device performance, given fixed device architecture, is the tube density. In order to examine the influence of tube density on sensing performance, three different sensors were compared regarding their sensitivity towards NH_3. The three sensors utilize CNT films prepared using the same process, described in the experimental section, but with different tube

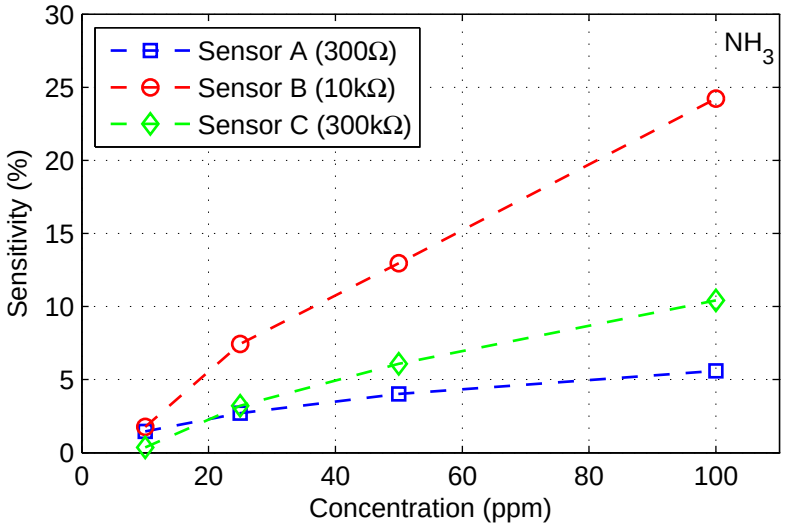

Figure 5.25: Sensitivity plotted against NH_3 concentration for the three sensors with different initial resistance, corresponding to three different tube densities.

densities. The initial resistance of the sensors was found to be 300 Ω, 10 kΩ, and 300 kΩ, for Sensor A, B, and C, respectively. Figure 5.25 depicts sensitivity against NH_3 concentration for each of the three sensors. Almost over the entire concentration range (25 ppm-100 ppm) shown, Sensor B exhibits by far the highest sensitivities, followed by Sensor C, which is in turn followed by Sensor A. As mentioned earlier in this article, the gas sensors presented here utilize CNT films with rather low tube densities. Better sensor response and higher sensitivities are considered to be a consequence of the more direct exposure of a greater portion of CNTs contributing to current conduction through the film. The reduced tube density in Sensor B, as opposed to Sensor A, strongly enhances device sensitivity. A reduced tube density pushes film characteristics towards percolation threshold, thereby reducing the amount of metallic pathways in the network and amplifying the contribution of semiconducting pathways. Since one of the main sensing mechanisms relies on intratube modulation through charge transfer, adsorption of gas molecules mainly affects conduction in semiconducting tubes. The existence of a large number of parallel metallic pathways overrides the modulation in semiconducting tubes by gas adsorption and hence lowers their contribution to the overall conduction in the network. Forming CNT films with predominant semiconducting characteristics by lowering tube density is therefore believed to be a major step towards enhancement of sensitivity. However, reducing density even further, as for Sensor C, adversely affects device sensitivity. This is expected to be caused by a strong reduction in the total number of tubes and junctions contributing to conduction through the network, which in turn lowers the number of available sites for modulation by adsorbed gas molecules. Hence, there is a trade-off between increasing the contribution of semiconducting tubes in the network and maintaining an appropriate amount of available sites. The model described

here predicts an enhancement in device sensitivity by the utilization of sorted semiconducting CNTs. By incorporating film with higher semiconducting tube content, the contribution of semiconducting pathways to the conduction through the network can be increased without reducing tube density. Preliminary data of measurements performed using gas sensors incorporating CNT films with 90 % semiconducting tubes (not presented here) support the aforementioned model.

5.2.5 Complex Impedance Characterization

The main physical quantity measured here for the evaluation of sensor response is the DC Resistance of the CNT film and its dependence on the local chemical environment. A major argument for the choice of this quantity is the simplicity of the measurement circuitry needed for sensor read-out, which is of particular importance for low-cost applications. Another, more powerful but more complicated, tool for the characterization of gas adsorption in semiconducting structures is the complex impedance method. The aim of performing impedance characterization is to model the experimental data with an equivalent circuit usually comprising a combination of parallel and serial resistors and capacitors representing the physical system [154], [155]. By separating the complex impedance response of the sensor into resistive and reactive components, additional information can be obtained to enhance sensitivity and selectivity to the various gases. However, a rigorous investigation of the complex impedance method in CNT-based gas sensors is subject of ongoing work and beyond the scope of this article. Therefore we limit our discussion here to the investigation of the complex sensor response at a single frequency, in order to demonstrate the potential gain in sensitivity obtained by this method. A frequency of 1 kHz was chosen for the excitation signal. Figure 5.26(a) shows the time response in the real and imaginary parts of the complex impedance recorded again during four exposure cycles with different concentrations of CO_2. Considering the response in the resistive component, a very similar behavior as for the DC resistance measurements is observed. The reactive component takes negative values demonstrating the capacitive character of the device. It can be seen that exposure to CO_2 leads to an increase in the absolute value of the reactance, i.e. the reactance is driven towards more negative values with increasing CO_2 concentration. By defining a resistive sensitivity and a reactive sensitivity in analogy to the definition introduced in Eq. (5.2), it is possible to compare the two and visualize their dependence on test gas concentration. This relation is plotted for both components of the complex impedance in Fig. 5.26(b). Note that the resistive sensitivity towards CO_2 at the chosen frequency is only slightly lower than the sensitivity obtained for DC resistance measurements. When examining the reactive sensitivity, significantly higher values are achieved at any given concentration. Sensitivity is almost doubled throughout the entire concentration range examined here. This clearly

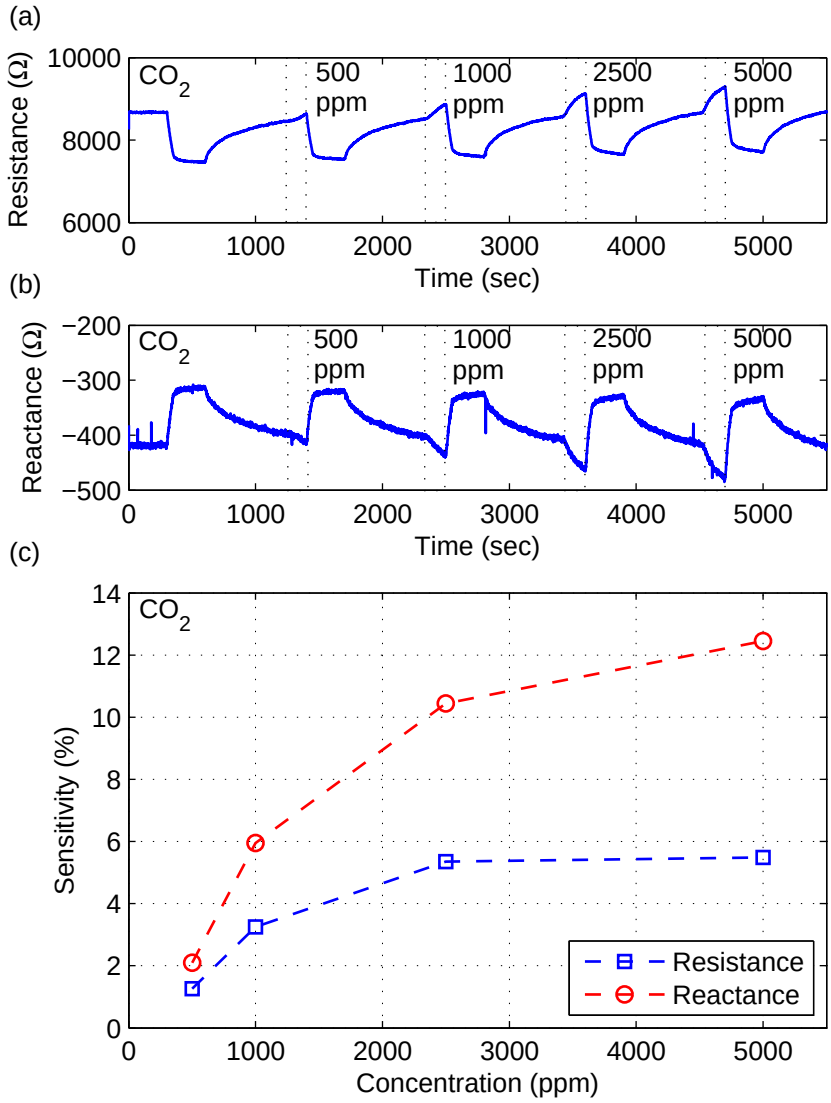

Figure 5.26: (a) Plot of the time response in the real and imaginary parts of the complex impedance recorded during four exposure cycles with different concentrations of CO_2. (b) Dependence on test gas concentration for both components of the complex impedance.

demonstrates the potential of the complex impedance method as a powerful tool for CNT-based gas sensor characterization. Very similar results were also obtained in case of NH_3 as a test gas, which is shown in Fig. 5.27.

5.3 Summary

In conclusion, we presented a reliable and reproducible spray deposition process for the fabrication of highly uniform CNT films exhibiting state-of-the-art performance. The

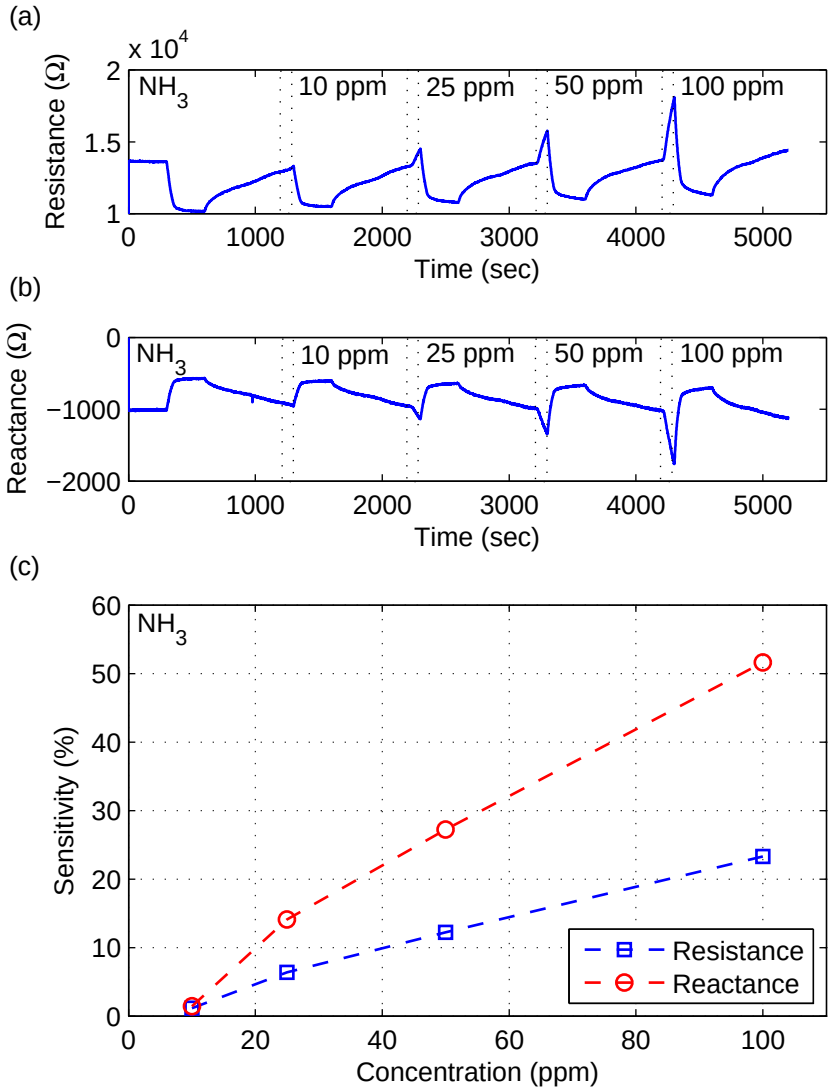

Figure 5.27: (a) Plot of the time response in the real and imaginary parts of the complex impedance recorded during four exposure cycles with different concentrations of NH_3. (b) Dependence on test gas concentration for both components of the complex impedance.

convenient control of major process parameters enables a fine and accurate tuning of film characteristics. Average surface roughness was shown to be 5.79 nm, measured over an area of 10x10 μm^2. The calculated conductivities were shown to vary with film thickness due to the percolating nature of CNT films. Conductivity increases to 4000 S/cm at 45 nm and approaches saturation beyond this thickness. A good trade-off between sheet resistance and transmittance is achieved with best films having 100 Ω/sq at 80 %. A transfer printing process, similar to the one introduced previously in Chapter 3, could be successfully adapted to the fabrication of CNT thin-films on plastic. Considering that the transfer printing process described here is only marginally optimized, the results presented promise

high potential for the fabrication of CNT thin-films with reasonable performance on various substrate materials, which may restrain use of the direct deposition process.

Further, we report the successful implementation of CNT-based gas sensors with exceptionally high sensitivities and fast response to various test gases. Highly uniform CNT thin-films, prepared using a reliable and reproducible low-cost spray deposition process, are utilized as resistive networks for gas detection. The sensitivity towards four different test gases (NH_3, Ethanol, CO, CO_2) is examined along with passive and active recovery routines. Sensors show a clear and immediate change in resistance as a response to test gas exposure. Sensitivities of 2 % for concentrations as low as 10 ppm and reaching 25 % at a concentration of 100 ppm can be achieved in case of NH_3, yielding the highest sensitivity among our range of test gases. We consider these values for NH_3 sensitivity to be exceptional, taking into account the short exposure intervals of 60 sec considered in our sensitivity calculations. It is shown that sensor response, particularly during recovery, depends on the test gas used, and hence can enable the categorization of different gases into pre-defined classes. We further demonstrate the potential enhancement in sensitivity achieved through complex impedance characterization of this type of gas sensors. While the resistive sensitivity towards CO_2 at the chosen frequency (1 kHz) is only slightly lower than the sensitivity obtained for DC resistance measurements, significantly higher values are achieved for the reactive sensitivity at any given concentration. Sensitivity is almost doubled throughout the entire concentration range examined here. Note that the sensors presented here, despite having competitively high sensitivities, are still not rigorously optimized, thereby leaving room for even further improvement.

Chapter 6

Process Development Strategies

In this chapter, we focus on some major aspects of processes involved in manufacturing of solution-processable organic thin-film devices and present a generalized framework for process development. This framework is developed based on the know-how accumulated from all individual processes previously presented as well as literature.

Further, an example of use is given for the development of a process for the fabrication of electronic devices based on CNT thin-films deposited from solution. This involves many of the processes previously described in Chapter 5.

6.1 Generalized Development Framework

Solution-processable organic electronic components, as discussed throughout this thesis, typically comprise layers of different electronic materials in a stack. Their development requires a combination of competences in different technological fields, including material, device design, and processing. It is hence essential to understand the existing interdependencies between material sets, device designs, processes and the resulting functionality of the product under development. Changing device design or materials requires the adjustment of processes involved in manufacturing to ensure proper functionality. Here we focus on major aspects of processes involved in manufacturing of solution-processable organic thin-film devices and present a generalized framework for process development. The product development cycles described above are illustrated in Fig. 6.1. A chart containing all major aspects of the generalized process development framework presented is shown in Fig. 6.2.

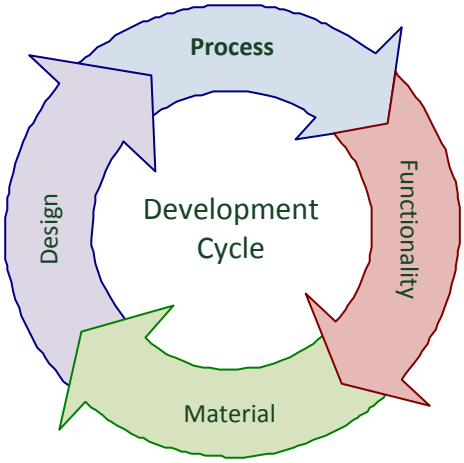

Figure 6.1: Illustration of the product development cycles, describing the interdependencies between material sets, device designs, processes and the resulting functionality

6.1.1 Coating Solution

The first aspect to be considered in the process development of solution-processable thin-film electronics is related to the coating solution containing the functional material to be deposited. All subsequent processing steps and device functionality follow a route initiated by the decisions taken for this part of the process. Consequently, the development of each step has to be performed within the context of the complete manufacturing process, in order to ensure optimal compatibility of all processes involves.

Functional Material

Guided by the desired functionality, it is necessary to choose the most suitable raw material for a given application. This involves the choice between different types of materials which are expected to fulfill the desired functionality according to application-specific requirements, such as efficiency, stability, and cost. Even with one type of material specified, the selection of a particular product from different suppliers of the same type of material with different specifications remains a major decision issue. In semiconducting polymer materials, such as P3HT, material properties strongly influence some process-specific parameters as wells as the electrical characteristics of the resulting thin-film. Molecular weight as well as regioregularity will not only alter solubility of the material and solution properties, but also have a direct effect on film morphology and charge transport properties [98], [156–158]. When dealing with carbon nanotubes on the other hand, the synthesis method is detrimental for conductivity of the resulting thin-films. Arc-discharge SWNTs are known to achieve lower values of sheet resistance for

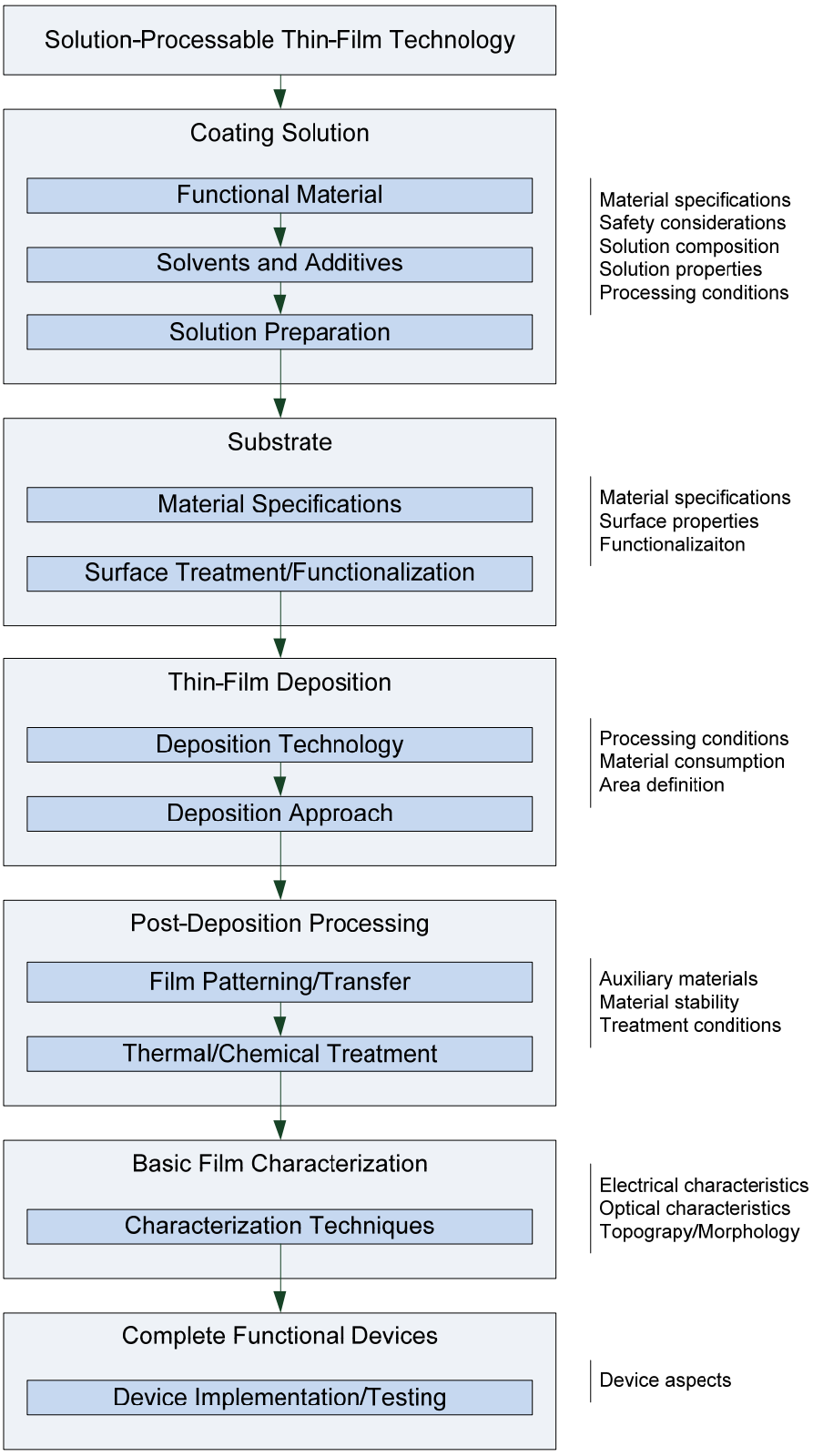

Figure 6.2: Chart containing all major aspects of the generalized process development framework based on the know-how accumulated from all individual processes previously presented here as well as literature.

transparent electrodes [122], [159], as described in the previous chapter. In all cases there is a usually a range of available products among the same type of material with different purities and costs.

Solvents and Additives

Currently there are only few commercially available and ready-to-use ink formulations for solution-processable organic materials specifically developed and optimized for different deposition techniques. One of the most prominent materials available in different formulations is the conducting polymer PEDOT:PSS, which is widely used as a hole injection material in organic optoelectronic devices. In general, the coating solution is self-made and customized to suit a particular deposition technique as well as the surface to be coated. The wide-spread use of spin-coating, the method of choice in most research laboratories, has surely delayed progress in the development of ink formulations [19]. When thinking of the coating solution, then the choice of solvent is an essential issue. Different solvents have to be evaluated according to numerous factors, such as solubility of the functional material at the needed concentration and the deposition technique selected. Some solvent properties like volatility and surface tension have to relate to the deposition technique. Further there are environmental and safety considerations that have to be taken into account, especially in large-scale manufacturing. One particular hazard with solution-processable organic electronics is the volatile organic compounds which develop from the solvent [26]. Water based solutions, as utilized in the previous chapter for CNT thin-film deposition, are the ideal choice from an environmental point of view. Other issues relate to interaction of the coating solution with the substrate surface. Issues regarding the ability to wet the surface for achieving uniform and smooth coating have to be addressed. This can be done through the employment of selected additives to tune solution properties relevant for surface interaction and film drying, such as surface tension and boiling point [95], [160], [161]. Moreover, additives can be employed to tune the resulting electrical or optical thin-film characteristics [162], [163].

Solution Preparation

Actual preparation of the coating solution involves the mixing of all materials, additives, and solvents in specific ratios, in order to obtain a composition leading to best possible functionality. However, this has to be optimized within the context of a given deposition technique and substrate surface, as mentioned above. Depending on the functional material and the solution composition, an appropriate mixing procedure under specified process conditions has to be determined. The preparation of the coating solution can therefore simply rely on stirring at an elevated temperature, as in case of many active polymer materials. Other materials require more powerful tools. Carbon nanotubes may represent one of the best examples for such materials, where high-power sonication is needed to

separate individual tubes and bundles to achieve high-quality dispersions [4]. Since uniformity and hence quality of any deposited thin-film can be strongly improved by minimizing the amount of undissolved particles and large clusters of material in the coating solution, additional processing steps are usually needed. This can extend from simple filtering through membranes of various pore sizes to centrifugation of the coating solution.

6.1.2 Substrate Preparation

The substrate employed in the technology discussed here typically has to serves several purposes. Primarily it acts as carrier and support of the product to be manufactured. For most applications however it also represents part of the encapsulation protecting the product and is therefore detrimental for stability and lifetime.

Material Specifications

Functionality and process both put constraints on the choice of the substrate, since it has to support the desired functionality of the product while being compatible with processes involved in manufacturing. The substrate material can vary from rigid to flexible depending on the application. In any case however it has to fulfill a range of requirements with regards to mechanical and thermal stability, transparency, color, weight, as well as cost. Additionally, surface characteristics are of major significance in the context thin-film deposition. Surface roughness for example can strongly influence device functionality, especially when dealing with thin-films of low thicknesses.

Surface Treatments

As already mentioned before, the interaction of the coating solution and the substrate surface has an influence on the quality of the deposited thin-film. In general, the surface tension of the ink must be lower than the surface energy of the surface [19]. Targeted treatment of the substrate surface in order to increase the surface energy is sometimes necessary for achieving reasonable wetting of the surface. There are different approaches used for the altering surface characteristics of the substrate, such as plasma or chemical treatments [164], [165]. Further, adhesion of certain functional materials can be promoted through functionalization of the surface.

6.1.3 Thin-Film Deposition

The selected thin-film deposition methodology represents the core technology involved in the process of film formation, as described more detailed in Chapter 2. Scalability of the

process is essential for an industrially relevant manufacturing of solution-processable organic electronics. However, this scalability has to be addressed within the context of maintaining the desired functionality of the product with an acceptable performance.

Deposition Technology

Selection of a suitable deposition technique has to be done according to several criteria regarding functionality and manufacturability of the product. Different requirements for the film characteristics, such as thickness range and surface roughness, limit the choice of techniques. Additionally, material consumption is an issue in case of expensive material and can therefore be decisive for the techniques coming into question. There are several other aspects that need to be considered especially when selective deposition is required to achieve desired patterns. Feature size and resolution can further narrow down the choice of techniques.

Operational Mode

Once a suitable deposition technique is chosen, it remains to decide about process-specific operational modes. Some techniques offer the possibility of being operated as both, sheet-fed or web-fed processes. This surely depends partially on the type of substrate used, since a web-fed process is only supported by flexible substrates. Besides the feed type, any large-scale deposition will need a relative movement of substrate and actual deposition tool. This can either involve the movement of only one of the two components while the other remains stationary or the movement of both. A common approach is to move the deposition tool linearly in one dimension while the substrate passes through. The employment of several deposition tools in an array applying the material to the substrate is a possibility provided by some techniques, such as spray deposition.

6.1.4 Post-Deposition Processing

In the context of solution-processable thin-films, post-deposition processing is mostly an elementary part of the process, which is necessary to achieve proper functionality with acceptable performance. The range of processes applicable at this step is broad and varies for different materials and applications. In the following we divide them into two main categories, where the first utilizes patterning and/or transfer techniques, while the second involves thermal and/or chemical treatment of the readily deposited film.

Film Patterning/Transfer

Many applications may involve additional patterning of the deposited thin-film. Depending on the purpose of patterning, this can be on a micrometer or even nanometer scale. Hence

different patterning and structuring techniques must be adjusted and integrated into the process. In CNT thin-film technology, for example, it is sometimes required to remove all unwanted regions of the film in order to precisely define the active device area. One widely used approach involves conventional UV photolithography followed by oxygen plasma or reactive ion etching of the unprotected areas [166], [167]. The employment of surface relief structures serving different purposes have high potential and are of great interest for organic optoelectronic devices [67], [168], [169]. Direct patterning of polymer films by means of nanoimprint lithography is a promising approach, as discussed previously in Chapter 3. Film Transfer on the other side becomes interesting if one or more process steps involved in manufacturing are not fully compatible with the desired type of substrate. In this case part of the fabrication process can be carried out on an intermediate substrate before the film is then transferred onto the target substrate. An example can be found in Chapter 5 for CNT thin-films fabricated on flexible substrates.

Thermal/Chemical Treatment

The classical post-deposition treatments in the context of polymer thin-films are certainly thermal and solvent annealing, usually performed in order to enhance electrical and optical properties of the film and hence reach the required functionality [114], [118], [170], [171]. Even simple drying of wet films and removal of residual solvents by thermal treatment is a common processing step. In CNT thin-film technology, chemical treatment is an essential part of the process through which sufficient removal of the surfactant can be realized, hence establishing complete film functionality. The same chemical treatment may also be employed to introduce doping to the CNT film and increase conductivity [172–174]. Conversely, thermal treatments can contribute to a dedoping of the film [175].

6.1.5 Basic Film Characterization

Calibration and optimization of the different processing parameters is an integral part of the process development. It enables the fabrication of thin-films with given specifications and ensures continuity of the output quality. In order to collect the feedback needed for doing this, characterization of the basic thin-films has to be performed with respect to selected measures before implementation into the device. It is therefore necessary to define and quantify the figures relevant to functionality of the product being manufactured. This may involve electrical, optical, topographical, and more complicated morphological characterization of the deposited thin-films. The results obtained are then analyzed and reflect on the adjustments done to the different processing parameters.

6.1.6 Complete Functional Devices

In solution-processable organic electronics, devices typically comprise layers of different electronic materials in a stack. For each additional layer of the stack a similar process needs to be developed, while taking into consideration any previously deposited layers. Therefore, materials and processes compatible with the entire device have to be selected. In cases where this is not possible, it is necessary to introduce additional process steps in order to bypass the issue. To give an example, thin-films needed to be deposited using coating solutions with cross-solubility can be transfer printed on top of each other, as described in Chapter 3. After fabricating complete devices, testing and benchmarking provide the feedback needed to optimize the process further until acceptable device performance is achieved.

6.2 Example of Use: CNT Thin-Film Technology

The generalized framework for process development proposed in this chapter is thought to serve as a general guiding tool. It is therefore formulated such as to be applicable to a broad range of products based on solution-processable thin-film technology. An example of use is given for the development of a process for the fabrication of electronic devices based on CNT thin-films deposited from solution, which was already successfully implemented in a similar way in Chapter 5. A chart addressing all major aspects involved in solution-processable CNT thin-film technology, constructed in accordance to our generalized framework, is presented in Fig. 6.3. Details to each of the process steps included can be found in Chapter 5.

6.3 Summary

We described existing interdependencies between material sets, device designs, processes and the resulting functionality of the product under development. Further, a generalized framework for process development was presented focusing on some major aspects of processes involved in manufacturing of solution-processable organic thin-film devices. In an example of use, the generalized framework is successfully applied to development of a process for the fabrication of electronic devices based on CNT thin-films deposited from solution.

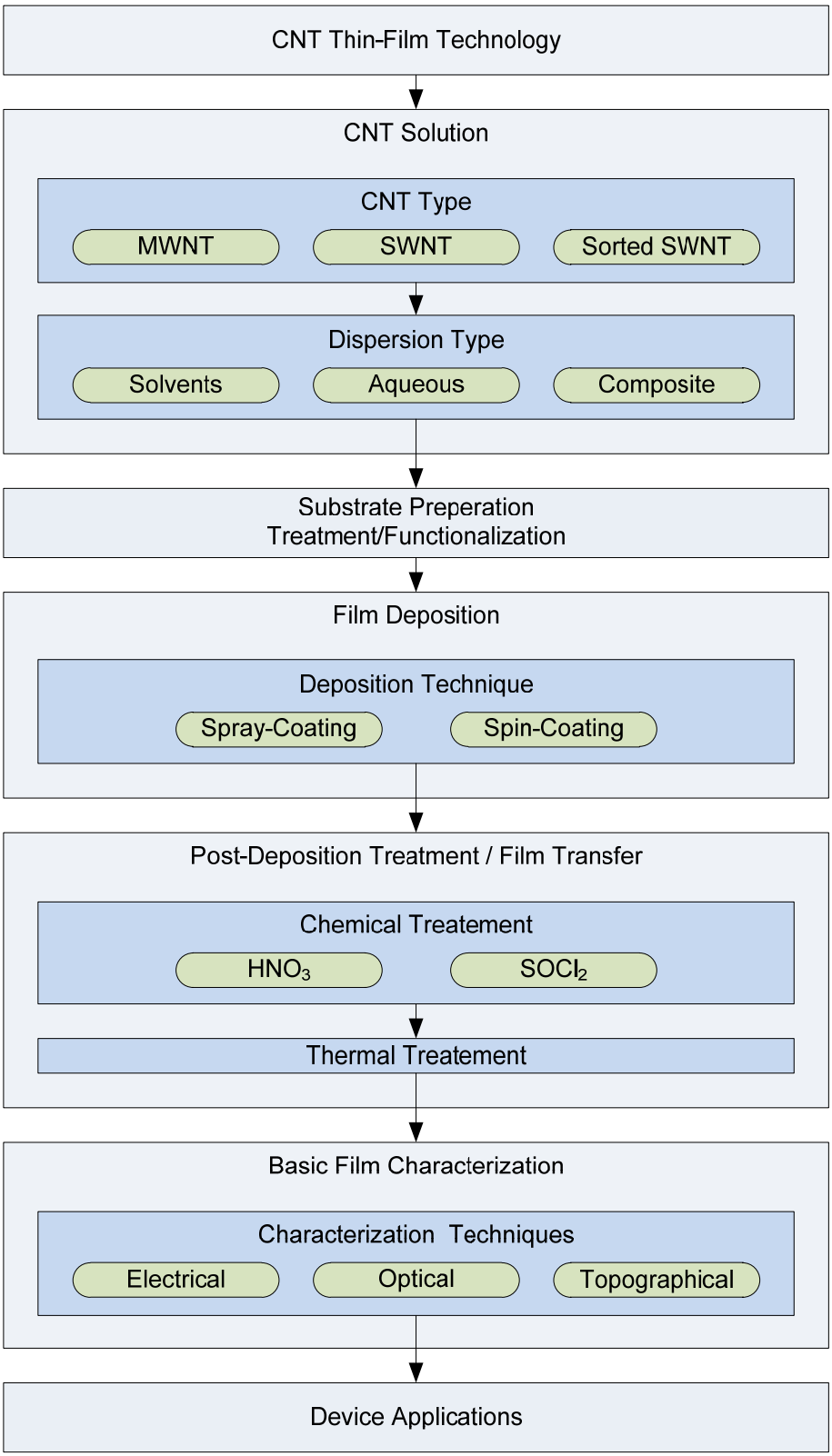

Figure 6.3: Chart addressing all major aspects involved in solution-processable CNT thin-film technology, constructed in accordance to our previously introduced generalized process development framework.

Chapter 7

Conclusion and Outlook

Here, some important conclusions and an outlook on future work are presented. The main findings are summarized, while some novel ideas relevant to the continuation of the work presented within the context of this thesis are discussed.

7.1 Conclusion

In this thesis we started by highlighting the importance of scalable processing technologies for rapid product development and prototyping of solution-processable thin-film electronics. Different film deposition and film patterning techniques were classified according to a proposed scheme. The three core processing technologies, nanoimprint lithography, transfer printing, and spray deposition, investigated throughout this thesis as promising alternatives for scalable manufacturing of solution-processable organic thin-film electronics were described in more detail.

We demonstrated thermal NIL as well as room temperature NIL using organic semiconducting P3HT films as imprint polymer. Commercially available Ni and Si/SiO_2 molds as well as custom built MBE-molds and porous alumina templates enabled imprinting patterns with feature sizes from hundred nanometers down to 20 nm. Our experiments revealed good pattern transfer quality into P3HT layers independent of the presence of other underlying polymer layers or the type of substrate incorporated. Samples with multi-layer structures (e.g including PEDOT:PSS) were also produced to demonstrate process compatibility within more complex device architectures in the future. The future application of this technology to the fabrication of ordered heterojunction organic photovoltaic devices was discussed in detail. Finally, we proved that the NIL step involved

in the fabrication of such kind of devices would not damage the polymer or alter its chemical or electrical properties.

A simple and reliable transfer printing process was developed to enable a solvent-free deposition of organic semiconducting thin-films for the fabrication of bilayer/multilayer based device architectures. We were able to demonstrate that the transfer printing process does not affect any of the desired optical or electrical properties of the materials utilized. Further, organic photodetectors incorporating P3HT/PCBM bilayers fabricated by transfer printing were shown to exhibit a device performance comparable to that of conventional BHJ devices. Device performance improved dramatically upon thermal post-deposition treatment of the bilayers. This performance enhancement was attributed to morphology evolution from a true bilayer towards a bulk heterojunction by intermixing of the materials composing the active layer. We hence conclude that according to the results presented here, the realization of an ordered heterojunction using the given material system of P3HT and PCBM is hardly feasible.

We implemented a low-cost spray-coating test setup using a commercially available automatic air atomizing spray gun. Using this setup we could successfully fabricate different classes of organic thin-film devices exhibiting performances comparable to ones fabricated using other deposition technologies. The technological framework developed based on the deposition approach presented here proved to enhance controllability of the process and reproducibility of the fabricated devices. Gaining insight into the layer formation process and correlating it to device performance represents an important step towards the realization of arbitrary shaped organic electronic devices fabricated by spray deposition.

An alternative deposition approach for the preparation of organic heterojunction photoactive layers by successive spray deposition of the donor and acceptor materials from pristine solutions was introduced. The partial dissolving of previously deposited underlying layers was carefully examined and it was shown that P3HT-rich and PCBM-rich layers are expected to form at the vicinity of the hole-extraction and electron-extraction layers, respectively. Cross-sectional TEM investigations, including material analysis with SEAD and EDX, were performed to further support the idea of PCBM penetration into the P3HT layer and the intermixing of both materials within the active layer. Based on performance characteristics of the fabricated organic photodetectors, we can conclude that devices with active layers prepared by successive spray deposition of the individual components exhibit a performance comparable to and can potentially outperform conventional BHJ devices in which the active layer is rigorously blended in advance.

Further, we presented a reliable and reproducible spray deposition process for the fabrication of highly uniform CNT films exhibiting state-of-the-art performance. The convenient control of major process parameters enables a fine and accurate tuning of film characteristics. Average surface roughness was shown to be 5.79 nm, measured over an area of 10x10 μm^2. The calculated conductivities were shown to vary with film thickness due to the percolating nature of CNT films. Conductivity increases to 4000 S/cm at 45 nm and approaches saturation beyond this thickness. A good trade-off between sheet resistance and transmittance is achieved with best films having 100 Ω/sq at 80 %. Moreover, the transfer printing process already introduced in Chapter 3 was successfully adapted to the fabrication of CNT thin-films on plastic. The results presented promise high potential for the fabrication of CNT thin-films with reasonable performance on various substrate materials, which may restrain use of the direct deposition process.

The implementation of CNT-based gas sensors with exceptionally high sensitivities and fast response to various test gases was successfully demonstrated. Highly uniform CNT thin-films, prepared using a reliable and reproducible low-cost spray deposition process, are utilized as resistive networks for gas detection. The sensitivity towards four different test gases (NH_3, Ethanol, CO, CO_2) is examined along with passive and active recovery routines. Sensors show a clear and immediate change in resistance as a response to test gas exposure. It is shown that sensor response, particularly during recovery, depends on the test gas used, and hence can enable the categorization of different gases into pre-defined classes. We further demonstrate the potential enhancement in sensitivity achieved through complex impedance characterization of this type of gas sensors.

Finally, we described existing interdependencies between material sets, device designs, processes and the resulting functionality of the product under development. A generalized framework for process development was presented focusing on some major aspects of processes involved in manufacturing of solution-processable organic thin-film devices. In an example of use, the generalized framework was applied to the development of a process for the fabrication of electronic devices based on CNT thin-films deposited from solution.

7.2 Outlook

The thermally-assisted spontaneous formation of bulk heterojunction morphology from a P3HT/PCBM bilayer renders the idea of fabricating ordered heterojunction photosensitive devices, as proposed in Chapter 3, rather complicated and hardly feasible. It might however be possible, by careful optimization of treatment temperature and duration, to achieve a kind of guided interdiffusion of PCBM into the patterned P3HT layer. This could

combine the advantages of a tightly interpenetrating network for efficient exciton dissociation along with continuous material paths for efficient charge transport to the electrodes. Further, the transfer method employed here can be extended to new materials and utilized to design more complex stack architectures to enhance device characteristics. This can include the incorporation of active layers from different material systems in organic photosensitive devices thereby covering a broader spectral absorption range.

Polymer thin-films deposited by spray deposition were shown to exhibit comparable performance to other deposition techniques despite the high surface roughness originating from the film formation process governed by droplet drying and surface characteristics. A reduction of surface roughness is expected to further improve performance, in particular for films of low thicknesses where surface coverage can become be an issue. More beneficial surface wetting and drying dynamics can be achieved through the development of special ink formulations containing a combination of different solvents or even the incorporation of certain additive.

Transparent and conductive carbon nanotube thin-films fabricated by spray deposition are ready for integration as anodes into complete organic optoelectronic devices. For successful integration however, some modifications and optimization of the processes involved are required, such as to ensure proper surface wetting of the CNT film as well as film stability throughout all subsequent processing steps. Since spray deposition was individually applied to each of the major layers involved in organic photodetectors, as described within this thesis, the implementation of fully sprayed OPDs is the immediate next step. This involves spray deposition of a CNT film as transparent anode, PEDOT:PSS film as hole injection layer, and P3HT:PCBM blend as active layer. The realization of such a fully sprayed device consequently enables its fabrication on curved substrates.

Successful implementation of CNT-based gas sensors with exceptionally high sensitivities and fast response to various test gases paves the way for the development and evaluation of different approaches for sensitivity/selectivity enhancement. One possibility already mentioned in Chapter 5 relies on performing impedance characterization to model the experimental data with an equivalent circuit usually comprising a combination of parallel and serial resistors and capacitors representing the physical system. By separating the complex impedance response of the sensor into resistive and reactive components, additional information can be obtained to enhance sensitivity and selectivity to the various gases. Functionalization of the sensing CNT films along with the implementation of sensor array architectures represents another major route to the development of discrimination methodologies.

Appendix A

Spray Deposition Tools

A.1 Connection Diagram

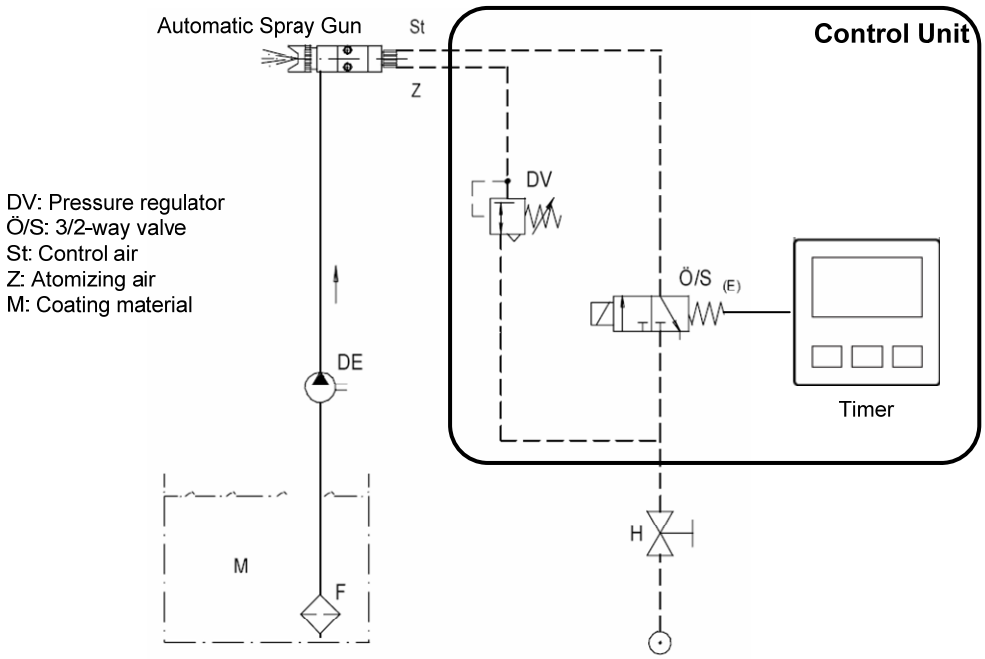

Figure A.1: Connection diagram of the experimental spray deposition setup. The spray gun contains an internal pneumatic control system which is activated by an electromechanical 3/2-way valve connected to a timer for precise spray time adjustment.

A.2 Automatic Spray Gun

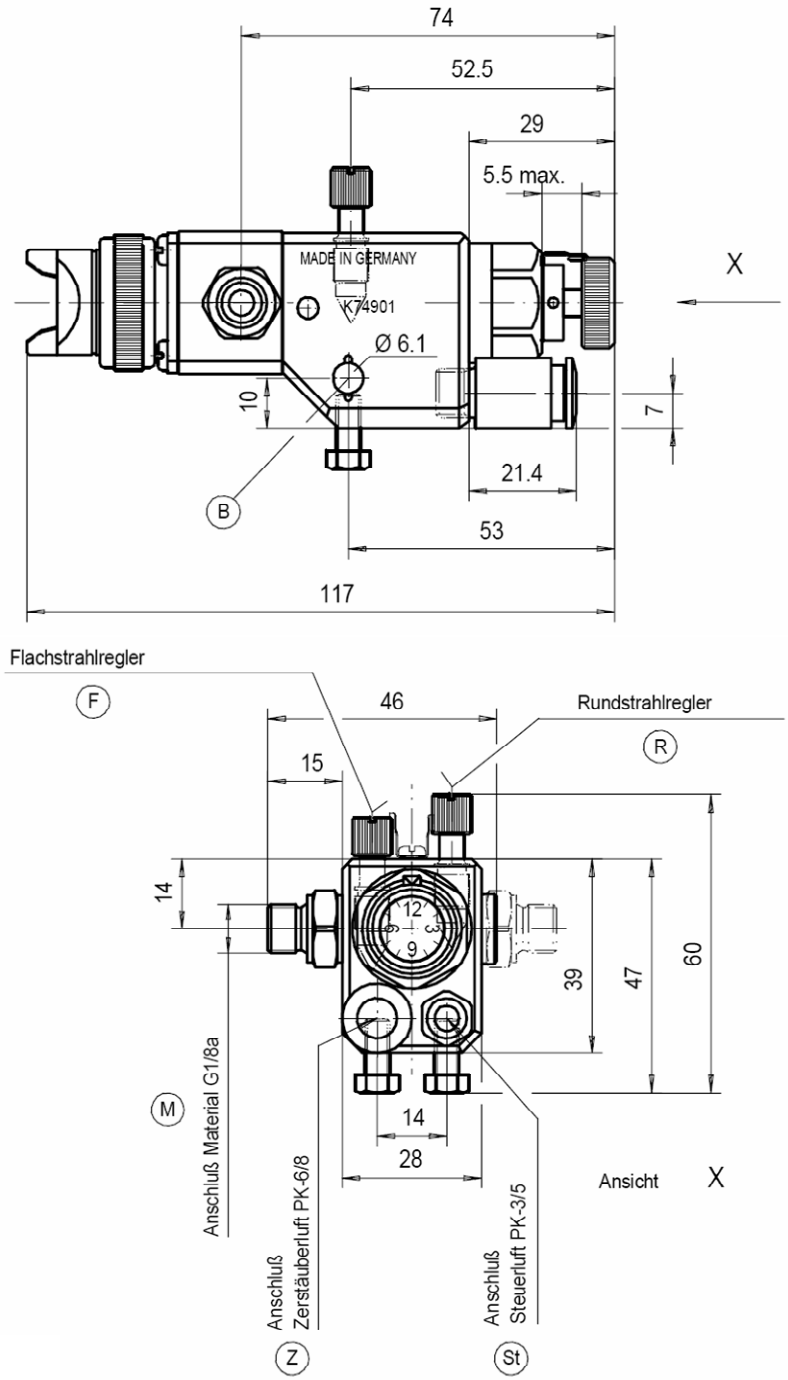

Figure A.2: Dimensional drawing of the commercially available automatic air atomizing spray gun (M10, Krautzberger GmbH, Germany) utilized in our static spray deposition setup.

A.3 Complete Spray Setup

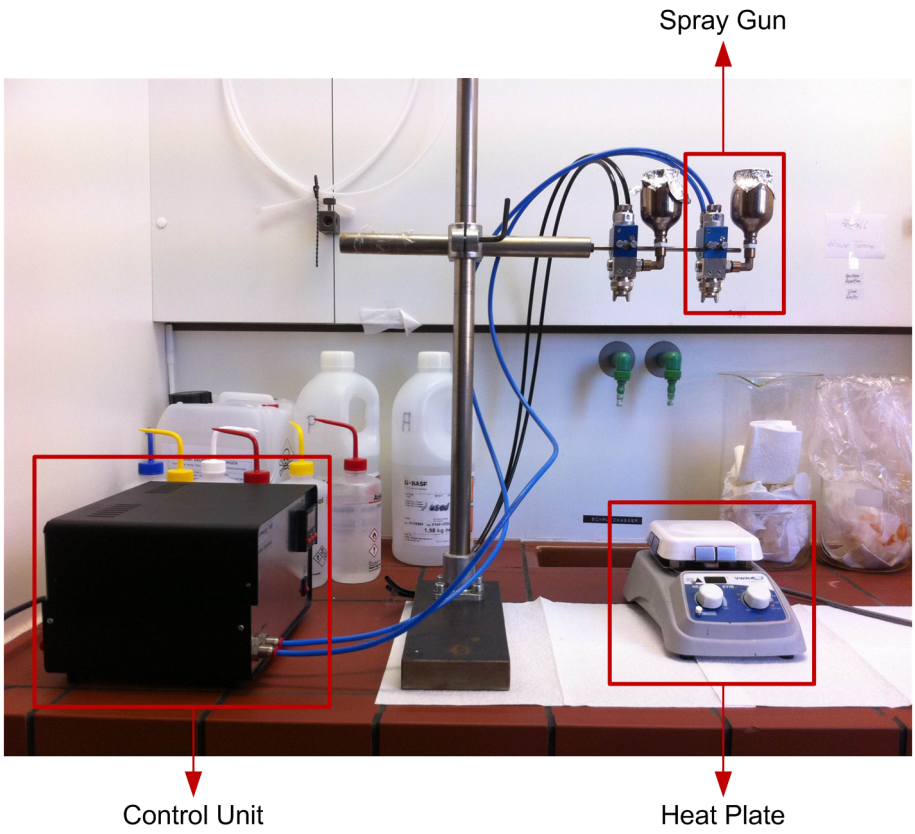

Figure A.3: Photograph of the complete experimental spray deposition setup. The spray gun contains an internal pneumatic control system which is activated by an electromechanical 3/2-way valve connected to a timer for precise spray time adjustment.

Appendix B

Gas Measurement Setup

B.1 Gas Measurement Setup

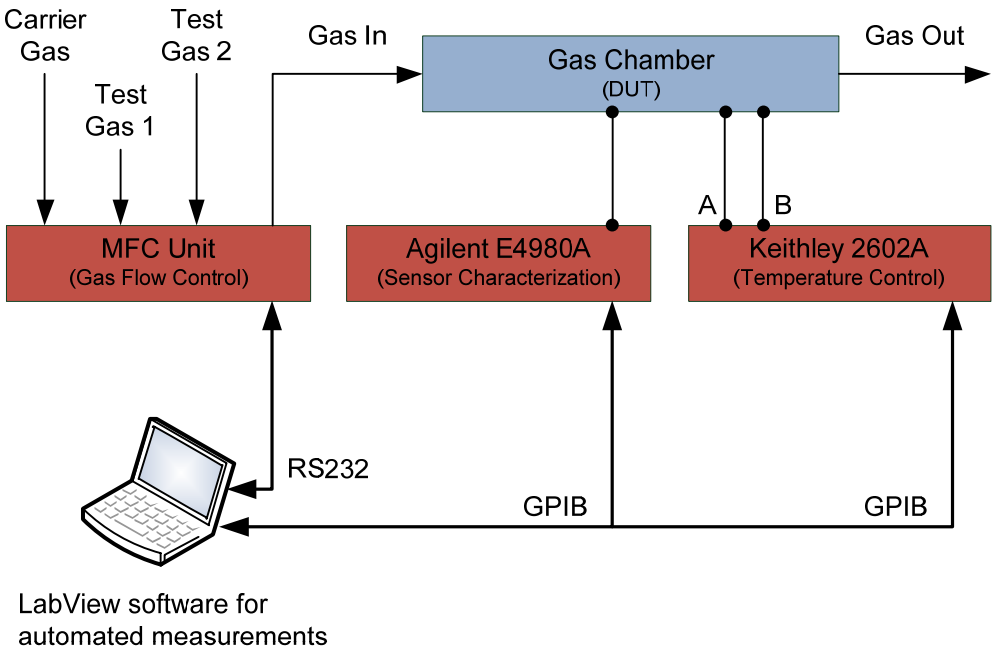

Figure B.1: Block diagram depicting the instrumentation involved in the computer controlled gas measurement setup built for the characterization of carbon nanotube based gas sensors developed within this work.

B.2 Automated Measurement Software

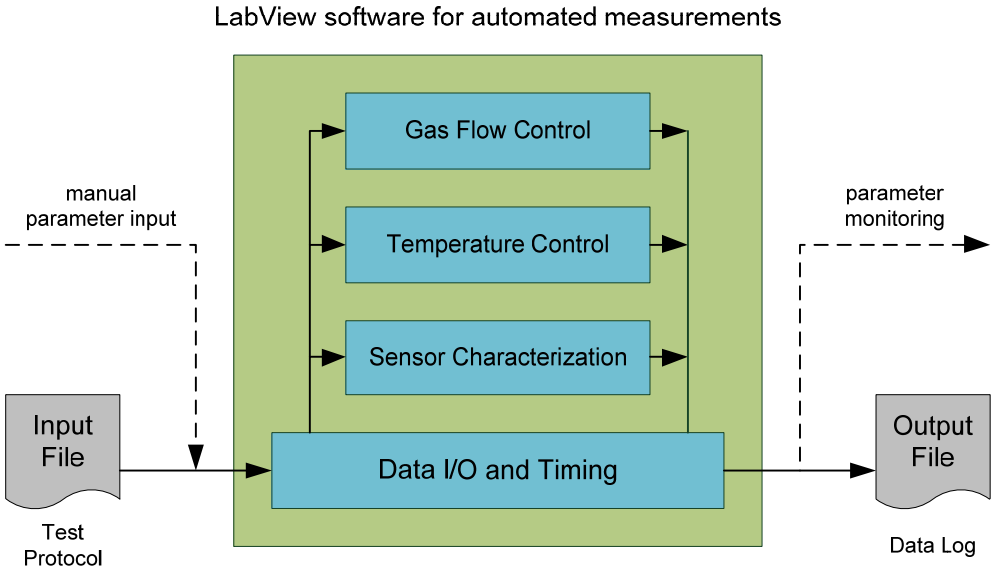

Figure B.2: The general architecture of the software specifically designed and implemented in LabView for automated control of the measurement setup, execution of predefined test protocols, and data acquisition.

B.3 Sensor Response

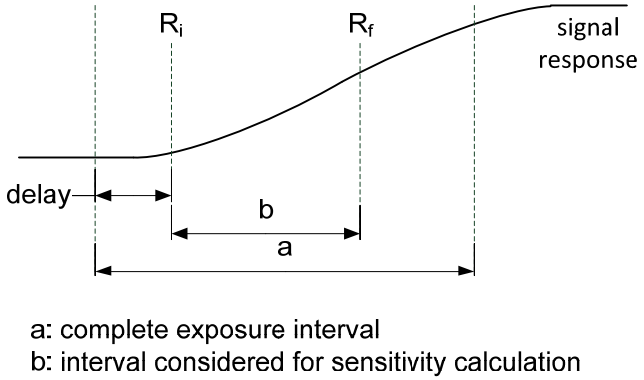

Figure B.3: The main figure used for the evaluation of sensor performance is the sensitivity, defined as the relative change in resistance during any given exposure cycle. R_i and R_f are the initial and final resistance values, respectively, obtained within the interval considered for sensitivity calculation.

References

[1] S. Forrest, P. Burrows, and M. Thompson, "The dawn of organic electronics," *IEEE Spectrum*, vol. 37, no. 8, pp. 29-34, 2000.

[2] S. R. Forrest, "The path to ubiquitous and low-cost organic electronic appliances on plastic," *Nature*, vol. 428, no. 6986, pp. 911-918, Apr. 2004.

[3] S. R. Forrest and M. E. Thompson, "Introduction: Organic Electronics and Optoelectronics," *Chemical Reviews*, vol. 107, no. 4, pp. 923-925, Apr. 2007.

[4] L. Hu, D. S. Hecht, and G. Grüner, "Carbon Nanotube Thin Films: Fabrication, Properties, and Applications," *Chemical Reviews*, vol. 110, no. 10, pp. 5790-5844, Oct. 2010.

[5] Q. Cao and J. A. Rogers, "Ultrathin Films of Single-Walled Carbon Nanotubes for Electronics and Sensors: A Review of Fundamental and Applied Aspects," *Advanced Materials*, vol. 21, no. 1, pp. 29-53, Jan. 2009.

[6] N. K. Patel, S. Cina, and J. H. Burroughes, "High-efficiency organic light-emitting diodes," *IEEE Journal of Selected Topics in Quantum Electronics*, vol. 8, no. 2, pp. 346-361, 2002.

[7] B. W. D'Andrade and S. R. Forrest, "White Organic Light-Emitting Devices for Solid-State Lighting," *Advanced Materials*, vol. 16, no. 18, pp. 1585-1595, Sep. 2004.

[8] C. J. Brabec, N. S. Sariciftci, and J. C. Hummelen, "Plastic Solar Cells," *Advanced Functional Materials*, vol. 11, no. 1, pp. 15-26, Feb. 2001.

[9] S. Gunes, H. Neugebauer, and N. S. Sariciftci, "Conjugated Polymer-Based Organic Solar Cells," *Chemical Reviews*, vol. 107, no. 4, pp. 1324-1338, Apr. 2007.

[10] G. Dennler, M. C. Scharber, and C. J. Brabec, "Polymer-Fullerene Bulk-Heterojunction Solar Cells," *Advanced Materials*, vol. 21, no. 13, pp. 1323-1338, Apr. 2009.

[11] M. M. Ling and Z. Bao, “Thin Film Deposition, Patterning, and Printing in Organic Thin Film Transistors,” *Chemistry of Materials*, vol. 16, no. 23, pp. 4824-4840, Nov. 2004.

[12] H. Sirringhaus, “Device Physics of Solution-Processed Organic Field-Effect Transistors,” *Advanced Materials*, vol. 17, no. 20, pp. 2411-2425, Oct. 2005.

[13] B. S. Ong, Y. Wu, Y. Li, P. Liu, and H. Pan, “Thiophene polymer semiconductors for organic thin-film transistors.,” *Chemistry European Journal*, vol. 14, no. 16, pp. 4766-78, Jan. 2008.

[14] J. T. Mabeck and G. G. Malliaras, “Chemical and biological sensors based on organic thin-film transistors.,” *Analytical and bioanalytical chemistry*, vol. 384, no. 2, pp. 343-53, Jan. 2006.

[15] L. Wang, D. Fine, D. Sharma, L. Torsi, and A. Dodabalapur, “Nanoscale organic and polymeric field-effect transistors as chemical sensors.,” *Analytical and bioanalytical chemistry*, vol. 384, no. 2, pp. 310-21, Jan. 2006.

[16] J. Shinar and R. Shinar, “Organic light-emitting devices (OLEDs) and OLED-based chemical and biological sensors: an overview,” *Journal of Physics D: Applied Physics*, vol. 41, no. 13, p. 133001, Jul. 2008.

[17] T. Zhang, S. Mubeen, N. V. Myung, and M. A. Deshusses, “Recent progress in carbon nanotube-based gas sensors,” *Nanotechnology*, vol. 19, no. 33, p. 332001, Aug. 2008.

[18] G. Gruner, “Carbon nanotube transistors for biosensing applications.,” *Analytical and bioanalytical chemistry*, vol. 384, no. 2, pp. 322-35, Jan. 2006.

[19] F. C. Krebs, “Fabrication and processing of polymer solar cells: A review of printing and coating techniques,” *Solar Energy Materials and Solar Cells*, vol. 93, no. 4, pp. 394-412, Apr. 2009.

[20] F. C. Krebs et al., “A complete process for production of flexible large area polymer solar cells entirely using screen printing—First public demonstration,” *Solar Energy Materials and Solar Cells*, vol. 93, no. 4, pp. 422-441, Apr. 2009.

[21] W. Ma, C. Yang, X. Gong, K. Lee, and a. J. Heeger, “Thermally Stable, Efficient Polymer Solar Cells with Nanoscale Control of the Interpenetrating Network Morphology,” *Advanced Functional Materials*, vol. 15, no. 10, pp. 1617-1622, Oct. 2005.

[22] G. Li et al., “High-efficiency solution processable polymer photovoltaic cells by self-organization of polymer blends,” *Nature Materials*, vol. 4, no. 11, pp. 864–868, Nov. 2005.

[23] F. C. Krebs and H. Spanggaard, “Significant Improvement of Polymer Solar Cell Stability,” *Chemistry of Materials*, vol. 17, no. 21, pp. 5235-5237, Oct. 2005.

[24] J. A. Hauch, P. Schilinsky, S. A. Choulis, R. Childers, M. Biele, and C. J. Brabec, "Flexible organic P3HT:PCBM bulk-heterojunction modules with more than 1 year outdoor lifetime," *Solar Energy Materials and Solar Cells*, vol. 92, no. 7, pp. 727-731, 2008.

[25] M. C. Gather, S. Köber, S. Heun, and K. Meerholz, "Improving the lifetime of white polymeric organic light-emitting diodes," *Journal of Applied Physics*, vol. 106, no. 2, p. 024506, Jul. 2009.

[26] E. Kunnari, J. Valkama, M. Keskinen, and P. Mansikkamäki, "Environmental evaluation of new technology: printed electronics case study," *Journal of Cleaner Production*, vol. 17, no. 9, pp. 791-799, 2009.

[27] A. Schiltz, "A review of planar techniques for multichip modules," *IEEE Transactions on Components, Hybrids, and Manufacturing Technology*, vol. 15, no. 2, pp. 236-244, Apr. 1992.

[28] K. Norrman, A. Ghanbari-Siahkali, and N. B. Larsen, "Studies of spin-coated polymer films," *Annual Reports Section C (Physical Chemistry)*, vol. 101, p. 174, Apr. 2005.

[29] R. Mens et al., "NMR study of the nanomorphology in thin films of polymer blends used in organic PV devices: MDMO-PPV/PCBM," *Journal of Polymer Science Part A: Polymer Chemistry*, vol. 46, no. 1, pp. 138-145, Jan. 2008.

[30] P. Schilinsky, C. Waldauf, and C. J. Brabec, "Performance Analysis of Printed Bulk Heterojunction Solar Cells," *Advanced Functional Materials*, vol. 16, no. 13, pp. 1669-1672, Sep. 2006.

[31] S. E. Shaheen, R. Radspinner, N. Peyghambarian, and G. E. Jabbour, "Fabrication of bulk heterojunction plastic solar cells by screen printing," *Applied Physics Letters*, vol. 79, no. 18, p. 2996, Oct. 2001.

[32] F. C. Krebs, H. Spanggard, T. Kjær, M. Biancardo, and J. Alstrup, "Large area plastic solar cell modules," *Materials Science and Engineering: B*, vol. 138, no. 2, pp. 106-111, Mar. 2007.

[33] J. Birnstock et al., "Screen-printed passive matrix displays based on light-emitting polymers," *Applied Physics Letters*, vol. 78, no. 24, p. 3905, Jun. 2001.

[34] C. N. Hoth, S. a. Choulis, P. Schilinsky, and C. J. Brabec, "High photovoltaic performance of inkjet printed polymer: fullerene blends," *Advanced Materials*, vol. 19, no. 22, pp. 3973–3978, Nov. 2007.

[35] T. Aernouts, T. Aleksandrov, C. Girotto, J. Genoe, and J. Poortmans, "Polymer based organic solar cells using ink-jet printed active layers," *Applied Physics Letters*, vol. 92, no. 3, p. 033306, Jan. 2008.

[36] K. X. Steirer et al., “Ultrasonically sprayed and inkjet printed thin film electrodes for organic solar cells,” *Thin Solid Films*, vol. 517, no. 8, pp. 2781-2786, Feb. 2009.

[37] T. Mustonen et al., “Inkjet printing of transparent and conductive patterns of single-walled carbon nanotubes and PEDOT-PSS composites,” *physica status solidi (b)*, vol. 244, no. 11, pp. 4336-4340, Nov. 2007.

[38] K. Kordás et al., “Inkjet printing of electrically conductive patterns of carbon nanotubes.,” *Small (Weinheim an der Bergstrasse, Germany)*, vol. 2, no. 8–9, pp. 1021-5, Aug. 2006.

[39] P. Beecher et al., “Ink-jet printing of carbon nanotube thin film transistors,” *Journal of Applied Physics*, vol. 102, no. 4, p. 043710, Aug. 2007.

[40] S. Zankovych, T. Hoffmann, J. Seekamp, J.-U. Bruch, and C. M. S. Torres, “Nanoimprint lithography: challenges and prospects,” *Nanotechnology*, vol. 12, no. 2, pp. 91-95, Jun. 2001.

[41] L. J. Guo, “Nanoimprint Lithography: Methods and Material Requirements,” *Advanced Materials*, vol. 19, no. 4, pp. 495-513, Feb. 2007.

[42] S. H. Ahn and L. J. Guo, “Large-area roll-to-roll and roll-to-plate nanoimprint lithography: a step toward high-throughput application of continuous nanoimprinting.,” *ACS nano*, vol. 3, no. 8, pp. 2304-10, Aug. 2009.

[43] B. D. Gates, Q. Xu, M. Stewart, D. Ryan, C. G. Willson, and G. M. Whitesides, “New approaches to nanofabrication: molding, printing, and other techniques.,” *Chemical reviews*, vol. 105, no. 4, pp. 1171-96, Apr. 2005.

[44] A. P. Quist, E. Pavlovic, and S. Oscarsson, “Recent advances in microcontact printing.,” *Analytical and bioanalytical chemistry*, vol. 381, no. 3, pp. 591-600, Mar. 2005.

[45] S. Alom Ruiz and C. S. Chen, “Microcontact printing: A tool to pattern,” *Soft Matter*, vol. 3, no. 2, p. 168, Dec. 2007.

[46] S. Bhattacharya, A. Datta, J. M. Berg, and S. Gangopadhyay, “Studies on surface wettability of poly(dimethyl) siloxane (PDMS) and glass under oxygen-plasma treatment and correlation with bond strength,” *Journal of Microelectromechanical Systems*, vol. 14, no. 3, pp. 590-597, Jun. 2005.

[47] B. A. Langowski and K. E. Uhrich, “Oxygen plasma-treatment effects on Si transfer.,” *Langmuir*, vol. 21, no. 14, pp. 6366-72, Jul. 2005.

[48] A. Lefebvre, *Atomization and Sprays*. CRC Press (Taylor & Francis), 1988, p. 434.

[49] E. J. Lavernia and Y. Wu, *Spray Atomization and Deposition*. John Wiley & Sons, 1996, p. 627.

[50] C. D. Dimitrakopoulos and D. J. Mascaro, “Organic thin-film transistors: A review of recent advances,” *IBM Journal of Research and Development*, vol. 45, no. 1, pp. 11-27, Jan. 2001.

[51] H. Klauk, U. Zschieschang, J. Pflaum, and M. Halik, “Ultralow-power organic complementary circuits.,” *Nature*, vol. 445, no. 7129, pp. 745-8, Feb. 2007.

[52] H. Sirringhaus, N. Tessler, and R. H. Friend, “Integrated Optoelectronic Devices Based on Conjugated Polymers,” *Science*, vol. 280, no. 5370, pp. 1741-1744, Jun. 1998.

[53] G. Wang, J. Swensen, D. Moses, and A. J. Heeger, “Increased mobility from regioregular poly(3-hexylthiophene) field-effect transistors,” *Journal of Applied Physics*, vol. 93, no. 10, p. 6137, May 2003.

[54] G. Scarpa, F. Brunetti, S. Harrer, and P. Lugli, “Nanoimprint Lithography for Optical Components,” in *2007 9th International Conference on Transparent Optical Networks*, 2007, pp. 194-197.

[55] M.-S. Kim, J.-S. Kim, J. C. Cho, M. Shtein, L. J. Guo, and J. Kim, “Flexible conjugated polymer photovoltaic cells with controlled heterojunctions fabricated using nanoimprint lithography,” *Applied Physics Letters*, vol. 90, no. 12, pp. 123113-3, Mar. 2007.

[56] H. D. Goldberg, R. B. Brown, D. P. Liu, and M. E. Meyerhoff, “Screen printing: a technology for the batch fabrication of integrated chemical-sensor arrays,” *Sensors and Actuators B: Chemical*, vol. 21, no. 3, pp. 171-183, Sep. 1994.

[57] Z. Bao, Y. Feng, A. Dodabalapur, V. R. Raju, and A. J. Lovinger, “High-Performance Plastic Transistors Fabricated by Printing Techniques,” *Chemistry of Materials*, vol. 9, no. 6, pp. 1299-1301, Jun. 1997.

[58] D. Pede, G. Serra, and D. Derossi, “Microfabrication of conducting polymer devices by ink-jet stereolithography,” *Materials Science and Engineering: C*, vol. 5, no. 3–4, pp. 289-291, Feb. 1998.

[59] T. R. Hebner, C. C. Wu, D. Marcy, M. H. Lu, and J. C. Sturm, “Ink-jet printing of doped polymers for organic light emitting devices,” *Applied Physics Letters*, vol. 72, no. 5, p. 519, Feb. 1998.

[60] Y. Xia and G. M. Whitesides, “SOFT LITHOGRAPHY,” *Annual Review of Materials Science*, vol. 28, no. 1, pp. 153-184, Aug. 1998.

[61] J. A. Rogers, Z. Bao, A. Makhija, and P. Braun, “Printing Process Suitable for Reel-to-Reel Production of High-Performance Organic Transistors and Circuits,” *Advanced Materials*, vol. 11, no. 9, pp. 741-745, Jun. 1999.

[62] S. Y. Chou, P. R. Krauss, and P. J. Renstrom, “Imprint of sub-25 nm vias and trenches in polymers,” *Applied Physics Letters*, vol. 67, no. 21, p. 3114, Nov. 1995.

[63] M. D. Austin and S. Y. Chou, “Fabrication of 70 nm channel length polymer organic thin-film transistors using nanoimprint lithography,” *Applied Physics Letters*, vol. 81, no. 23, p. 4431, Dec. 2002.

[64] E. Kim, Y. Xia, and G. M. Whitesides, “Polymer microstructures formed by moulding in capillaries,” *Nature*, vol. 376, no. 6541, pp. 581-584, Aug. 1995.

[65] X. YU, R. XING, S. LUAN, Z. WANG, and Y. HAN, “Direct micropatterning of polymer materials by ice mold,” *Applied Surface Science*, vol. 252, no. 24, pp. 8544-8548, Oct. 2006.

[66] C. Balocco, A. G. Jones, J. M. Kingsley, J. R. Chan, X. Q. Huang, and A. M. Song, “Scanning Probe Microscope Based Nanolithography on Conducting Polymer Films,” *Japanese Journal of Applied Physics*, vol. 45, no. 3B, pp. 2095-2098, Mar. 2006.

[67] S.-I. Na et al., “Surface relief gratings on poly(3-hexylthiophene) and fullerene blends for efficient organic solar cells,” *Applied Physics Letters*, vol. 91, no. 17, p. 173509, Oct. 2007.

[68] H. Sirringhaus et al., “Two-dimensional charge transport in self-organized, high-mobility conjugated polymers,” *Nature*, vol. 401, no. 6754, pp. 685-688, Oct. 1999.

[69] S. Hugger, R. Thomann, T. Heinzel, and T. Thurn-Albrecht, “Semicrystalline morphology in thin films of poly(3-hexylthiophene),” *Colloid & Polymer Science*, vol. 282, no. 8, pp. 932-938, Jun. 2004.

[70] B. K. Kuila and A. K. Nandi, “Physical, Mechanical, and Conductivity Properties of Poly(3-hexylthiophene)−Montmorillonite Clay Nanocomposites Produced by the Solvent Casting Method,” *Macromolecules*, vol. 37, no. 23, pp. 8577-8584, Nov. 2004.

[71] S. Harrer, S. Strobel, G. Scarpa, G. Abstreiter, M. Tornow, and P. Lugli, “Room Temperature Nanoimprint Lithography Using Molds Fabricated by Molecular Beam Epitaxy,” *IEEE Transactions on Nanotechnology*, vol. 7, no. 3, pp. 363-370, May 2008.

[72] E. Mele, F. Di Benedetto, L. Persano, R. Cingolani, and D. Pisignano, “Multilevel, room-temperature nanoimprint lithography for conjugated polymer-based photonics.,” *Nano letters*, vol. 5, no. 10, pp. 1915-9, Oct. 2005.

[73] D. Pisignano et al., “Oligomer-based organic distributed feedback lasers by room-temperature nanoimprint lithography,” *Applied Physics Letters*, vol. 83, no. 13, p. 2545, Sep. 2003.

[74] P. Del Carro et al., “Near-infrared imprinted distributed feedback lasers,” *Applied Physics Letters*, vol. 89, no. 20, p. 201105, Nov. 2006.

[75] P. Lugli et al., “Advances in Nanoimprint Lithography,” in *2007 7th IEEE Conference on Nanotechnology (IEEE NANO)*, 2007, pp. 1179-1184.

[76] S. Harrer et al., “Technology Assessment of a Novel High-Yield Lithographic Technique for Sub-15-nm Direct Nanotransfer Printing of Nanogap Electrodes,” *IEEE Transactions on Nanotechnology*, vol. 8, no. 6, pp. 662-670, Nov. 2009.

[77] P. Peumans, A. Yakimov, and S. R. Forrest, “Small molecular weight organic thin-film photodetectors and solar cells,” *Journal of Applied Physics*, vol. 93, no. 7, p. 3693, Apr. 2003.

[78] K. M. Coakley and M. D. McGehee, “Conjugated Polymer Photovoltaic Cells,” *Chemistry of Materials*, vol. 16, no. 23, pp. 4533-4542, Nov. 2004.

[79] D. R. Hines et al., “Nanotransfer printing of organic and carbon nanotube thin-film transistors on plastic substrates,” *Applied Physics Letters*, vol. 86, no. 16, p. 163101, Apr. 2005.

[80] D. R. Hines, V. W. Ballarotto, E. D. Williams, Y. Shao, and S. A. Solin, “Transfer printing methods for the fabrication of flexible organic electronics,” *Journal of Applied Physics*, vol. 101, no. 2, p. 024503, Jan. 2007.

[81] J.-ho Choi, K.-H. Kim, S.-J. Choi, and H. H. Lee, “Whole device printing for full colour displays with organic light emitting diodes,” *Nanotechnology*, vol. 17, no. 9, pp. 2246-2249, May 2006.

[82] T. A. M. Ferenczi et al., “Planar heterojunction organic photovoltaic diodes via a novel stamp transfer process,” *Journal of Physics: Condensed Matter*, vol. 20, no. 47, p. 475203, 2008.

[83] L. Chen, P. Degenaar, and D. D. C. Bradley, “Polymer Transfer Printing: Application to Layer Coating, Pattern Definition, and Diode Dark Current Blocking,” *Advanced Materials*, vol. 20, no. 9, pp. 1679-1683, 2008.

[84] X. Feng, M. A. Meitl, A. M. Bowen, Y. Huang, R. G. Nuzzo, and J. A. Rogers, “Competing fracture in kinetically controlled transfer printing.,” *Langmuir*, vol. 23, no. 25, pp. 12555-60, Dec. 2007.

[85] K.-H. Yim, Z. Zheng, Z. Liang, R. H. Friend, W. T. S. Huck, and J.-S. Kim, “Efficient Conjugated-Polymer Optoelectronic Devices Fabricated by Thin-Film Transfer-Printing Technique,” *Advanced Functional Materials*, vol. 18, no. 7, pp. 1012-1019, Apr. 2008.

[86] M. J. Allen et al., “Soft Transfer Printing of Chemically Converted Graphene,” *Advanced Materials*, vol. 21, no. 20, pp. 2098-2102, May 2009.

[87] V. Shrotriya, J. Ouyang, R. Tseng, G. Li, and Y. Yang, “Absorption spectra modification in poly(3-hexylthiophene):methanofullerene blend thin films,” *Chemical Physics Letters*, vol. 411, no. 1–3, pp. 138-143, 2005.

[88] N. D. Treat et al., “Interdiffusion of PCBM and P3HT Reveals Miscibility in a Photovoltaically Active Blend,” *Advanced Energy Materials*, vol. 1, no. 1, pp. 82-89, Jan. 2011.

[89] D. Chen, F. Liu, C. Wang, A. Nakahara, and T. P. Russell, “Bulk heterojunction photovoltaic active layers via bilayer interdiffusion.,” *Nano letters*, vol. 11, no. 5, pp. 2071-8, May 2011.

[90] P. J. Brown et al., “Effect of interchain interactions on the absorption and emission of poly(3-hexylthiophene),” *Physical Review B*, vol. 67, no. 6, p. 064203, Feb. 2003.

[91] D. Vak et al., “Fabrication of organic bulk heterojunction solar cells by a spray deposition method for low-cost power generation,” *Applied Physics Letters*, vol. 91, no. 8, pp. 081102-3, 2007.

[92] R. Green, A. Morfa, A. J. Ferguson, N. Kopidakis, G. Rumbles, and S. E. Shaheen, “Performance of bulk heterojunction photovoltaic devices prepared by airbrush spray deposition,” *Applied Physics Letters*, vol. 92, no. 3, pp. 033301-3, Jan. 2008.

[93] C. Girotto, B. P. Rand, J. Genoe, and P. Heremans, “Exploring spray coating as a deposition technique for the fabrication of solution-processed solar cells,” *Solar Energy Materials and Solar Cells*, vol. 93, no. 4, pp. 454-458, Apr. 2009.

[94] S. F. Tedde, J. Kern, T. Sterzl, J. Fürst, P. Lugli, and O. Hayden, “Fully Spray Coated Organic Photodiodes,” *Nano Letters*, vol. 9, no. 3, pp. 980-983, Mar. 2009.

[95] C. Hoth, R. Steim, P. Schilinsky, and S. Choulis, “Topographical and morphological aspects of spray coated organic photovoltaics,” *Organic Electronics*, vol. 10, no. 4, pp. 587-593, Jul. 2009.

[96] A. Abdellah, D. Baierl, B. Fabel, P. Lugli, and G. Scarpa, “Exploring spray technology for the fabrication of organic devices based on poly(3-hexylthiophene),” *Nanotechnology, 2009. IEEE-NANO 2009. 9th IEEE Conference on*, pp. 831-934, 2009.

[97] K. X. Steirer et al., “Ultrasonic spray deposition for production of organic solar cells,” *Solar Energy Materials and Solar Cells*, vol. 93, no. 4, pp. 447-453, Apr. 2009.

[98] Y. Kim et al., “A strong regioregularity effect in self-organizing conjugated polymer films and high-efficiency polythiophene:fullerene solar cells,” *Nat Mater*, vol. 5, no. 3, pp. 197-203, Mar. 2006.

[99] E. Klimov, W. Li, X. Yang, G. G. Hoffmann, and J. Loos, “Scanning Near-Field and Confocal Raman Microscopic Investigation of P3HT−PCBM Systems for Solar Cell Applications,” *Macromolecules*, vol. 39, no. 13, pp. 4493-4496, Jun. 2006.

[100] A. Swinnen et al., "Tuning the Dimensions of C60-Based Needlelike Crystals in Blended Thin Films," *Advanced Functional Materials*, vol. 16, no. 6, pp. 760-765, 2006.

[101] M. Campoy-Quiles et al., "Morphology evolution via self-organization and lateral and vertical diffusion in polymer:fullerene solar cell blends," *Nat Mater*, vol. 7, no. 2, pp. 158-164, Feb. 2008.

[102] J.-F. Chang et al., "Enhanced Mobility of Poly(3-hexylthiophene) Transistors by Spin-Coating from High-Boiling-Point Solvents," *Chemistry of Materials*, vol. 16, no. 23, pp. 4772-4776, Nov. 2004.

[103] J. Park, S. Lee, and H. H. Lee, "High-mobility polymer thin-film transistors fabricated by solvent-assisted drop-casting," *Organic Electronics*, vol. 7, no. 5, pp. 256-260, Oct. 2006.

[104] T. Erb et al., "Correlation Between Structural and Optical Properties of Composite Polymer/Fullerene Films for Organic Solar Cells," *Advanced Functional Materials*, vol. 15, no. 7, pp. 1193-1196, Jul. 2005.

[105] C.-W. Liang, W.-F. Su, and L. Wang, "Enhancing the photocurrent in poly(3-hexylthiophene)/[6,6]-phenyl C[sub 61] butyric acid methyl ester bulk heterojunction solar cells by using poly(3-hexylthiophene) as a buffer layer," *Applied Physics Letters*, vol. 95, no. 13, p. 133303, 2009.

[106] A. Kumar, G. Li, Z. Hong, and Y. Yang, "High efficiency polymer solar cells with vertically modulated nanoscale morphology," *Nanotechnology*, vol. 20, no. 16, p. 165202, 2009.

[107] D. H. Wang, H. K. Lee, D.-G. Choi, J. H. Park, and O. O. Park, "Solution-processable polymer solar cells from a poly(3-hexylthiophene)/[6,6]-phenyl C[sub 61]-butyric acidmethyl ester concentration graded bilayers," *Applied Physics Letters*, vol. 95, no. 4, p. 043505, 2009.

[108] A. L. Ayzner, C. J. Tassone, S. H. Tolbert, and B. J. Schwartz, "Reappraising the Need for Bulk Heterojunctions in Polymer- Fullerene Photovoltaics: The Role of Carrier Transport in All-Solution-Processed P3HT/PCBM Bilayer Solar Cells," *The Journal of Physical Chemistry C*, vol. 113, no. 46, pp. 20050–20060, Nov. 2009.

[109] L. M. Chen et al., "Multi-Source/Component Spray Coating for Polymer Solar Cells," *ACS Nano*, vol. 4, no. 8, pp. 4744-4752, 2010.

[110] J. S. Moon, C. J. Takacs, Y. Sun, and A. J. Heeger, "Spontaneous formation of bulk heterojunction nanostructures: multiple routes to equivalent morphologies.," *Nano letters*, vol. 11, no. 3, pp. 1036-9, Mar. 2011.

[111] A. Abdellah, B. Fabel, P. Lugli, and G. Scarpa, "Spray deposition of organic semiconducting thin-films: Towards the fabrication of arbitrary shaped organic electronic devices," *Organic Electronics*, vol. 11, no. 6, pp. 1031-1038, Jun. 2010.

[112] L. G. Parratt, “Surface Studies of Solids by Total Reflection of X-Rays,” *Physical Review*, vol. 95, no. 2, pp. 359-369, 1954.

[113] D. Chirvase, J. Parisi, J. Hummelen, and V. Dyakonov, “Influence of nanomorphology on the photovoltaic action of polymer–fullerene composites,” *Nanotechnology*, vol. 15, no. 9, p. 1317, 2004.

[114] Y. Kim, S. A. Choulis, J. Nelson, D. D. C. Bradley, S. Cook, and J. R. Durrant, “Composition and annealing effects in polythiophene/fullerene solar cells,” *Journal of Materials Science*, vol. 40, no. 6, pp. 1371-1376, 2005.

[115] M. A. Ruderer, E. Metwalli, W. Wang, G. Kaune, S. V. Roth, and P. Müller-Buschbaum, “Thin films of photoactive polymer blends.,” *Chemphyschem : a European journal of chemical physics and physical chemistry*, vol. 10, no. 4, pp. 664-71, Mar. 2009.

[116] G. Kaune and P. Müller-Buschbaum, “Gradient-doping of a conductive polymer film with a layer-by-layer approach,” *physica status solidi (RRL) - Rapid Research Letters*, vol. 4, no. 1–2, pp. 52-54, Feb. 2010.

[117] H. J. Kim, J. H. Park, H. H. Lee, D. R. Lee, and J.-J. Kim, “The effect of Al electrodes on the nanostructure of poly(3-hexylthiophene): Fullerene solar cell blends during thermal annealing,” *Organic Electronics*, vol. 10, no. 8, pp. 1505-1510, Dec. 2009.

[118] M. A. Ruderer et al., “Influence of annealing and blending of photoactive polymers on their crystalline structure.,” *The journal of physical chemistry. B*, vol. 114, no. 47, pp. 15451-8, Dec. 2010.

[119] L. Li, G. Lu, S. Li, H. Tang, and X. Yang, “Epitaxy-Assisted Creation of PCBM Nanocrystals and Its Application in Constructing Optimized Morphology for Bulk-Heterojunction Polymer Solar Cells.,” *The journal of physical chemistry. B*, vol. 112, no. 49, pp. 15651-15658, Nov. 2008.

[120] D. H. Wang, D. G. Choi, K. J. Lee, S. H. Im, O. Ok Park, and J. H. Park, “Unexpected solid-solid intermixing in a bilayer of poly (3-hexylthiophene) and [6, 6]-phenyl C61-butyric acidmethyl ester via stamping transfer,” *Organic Electronics*, vol. 11, no. 8, pp. 1376-1380, Aug. 2010.

[121] M. Kaur, A. Gopal, R. M. Davis, and J. R. Heflin, “Concentration gradient P3OT/PCBM photovoltaic devices fabricated by thermal interdiffusion of separately spin-cast organic layers,” *Solar Energy Materials and Solar Cells*, vol. 93, no. 10, pp. 1779-1784, Oct. 2009.

[122] D. Zhang et al., “Transparent, Conductive, and Flexible Carbon Nanotube Films and Their Application in Organic Light-Emitting Diodes,” *Nano Letters*, vol. 6, no. 9, pp. 1880-1886, 2006.

[123] Y.-M. Chien, F. Lefevre, I. Shih, and R. Izquierdo, "A solution processed top emission OLED with transparent carbon nanotube electrodes," *Nanotechnology*, vol. 21, no. 13, p. 134020, 2010.

[124] R. C. Tenent et al., "Ultrasmooth, Large-Area, High-Uniformity, Conductive Transparent Single-Walled-Carbon-Nanotube Films for Photovoltaics Produced by Ultrasonic Spraying," *Advanced Materials*, vol. 21, no. 31, pp. 3210-3216, 2009.

[125] M. Ha et al., "Printed, sub-3V digital circuits on plastic from aqueous carbon nanotube inks.," *ACS nano*, vol. 4, no. 8, pp. 4388-95, Aug. 2010.

[126] C. Wang, J. Zhang, and C. Zhou, "Macroelectronic Integrated Circuits Using High-Performance Separated Carbon Nanotube Thin-Film Transistors.," *ACS nano*, vol. 4, no. 12, pp. 7123-7132, Nov. 2010.

[127] J. Li, Y. Lu, Q. Ye, M. Cinke, J. Han, and M. Meyyappan, "Carbon Nanotube Sensors for Gas and Organic Vapor Detection," *Nano Letters*, vol. 3, no. 7, pp. 929-933, Jul. 2003.

[128] E. Bekyarova et al., "Chemically Functionalized Single-Walled Carbon Nanotubes as Ammonia Sensors," *The Journal of Physical Chemistry B*, vol. 108, no. 51, pp. 19717-19720, Dec. 2004.

[129] M. Penza, R. Rossi, M. Alvisi, G. Cassano, and E. Serra, "Functional characterization of carbon nanotube networked films functionalized with tuned loading of Au nanoclusters for gas sensing applications," *Sensors and Actuators B: Chemical*, vol. 140, no. 1, pp. 176-184, Jun. 2009.

[130] S. Kim, J. Yim, X. Wang, D. D. C. Bradley, S. Lee, and J. C. DeMello, "Spin-and Spray-Deposited Single-Walled Carbon-Nanotube Electrodes for Organic Solar Cells," *Advanced Functional Materials*, vol. 20, no. 14, pp. 2310–2316, 2010.

[131] T. Takahashi, K. Tsunoda, H. Yajima, and T. Ishii, "Dispersion and Purification of Single-Wall Carbon Nanotubes Using Carboxymethylcellulose," *Japanese Journal of Applied Physics*, vol. 43, no. No. 6A, pp. 3636-3639, Jun. 2004.

[132] D. Hecht, L. Hu, and G. Grüner, "Conductivity scaling with bundle length and diameter in single walled carbon nanotube networks," *Applied Physics Letters*, vol. 89, no. 13, p. 133112, Sep. 2006.

[133] E. Bekyarova et al., "Electronic Properties of Single-Walled Carbon Nanotube Networks," *Journal of the American Chemical Society*, vol. 127, no. 16, pp. 5990-5995, Apr. 2005.

[134] L. Hu, D. Hecht, and G. Grüner, "Percolation in transparent and conducting carbon nanotube networks," *Nano Lett*, vol. 4, no. 12, pp. 2513–2517, Dec. 2004.

[135] B. Ruzicka and L. Degiorgi, “Optical and dc conductivity study of potassium-doped single-walled carbon nanotube films,” *Physical Review B*, vol. 61, no. 4, p. R2468-R2471, Jan. 2000.

[136] Y. Zhou, L. Hu, and G. Grüner, “A method of printing carbon nanotube thin films,” *Applied Physics Letters*, vol. 88, no. 12, p. 123109, Mar. 2006.

[137] M. F. Islam, E. Rojas, D. M. Bergey, A. T. Johnson, and A. G. Yodh, “High Weight Fraction Surfactant Solubilization of Single-Wall Carbon Nanotubes in Water,” *Nano Letters*, vol. 3, no. 2, pp. 269-273, Feb. 2003.

[138] D. Simien, J. A. Fagan, W. Luo, J. F. Douglas, K. Migler, and J. Obrzut, “Influence of nanotube length on the optical and conductivity properties of thin single-wall carbon nanotube networks.,” *ACS nano*, vol. 2, no. 9, pp. 1879-84, Sep. 2008.

[139] S. Niyogi et al., “Chemistry of Single-Walled Carbon Nanotubes,” *Accounts of Chemical Research*, vol. 35, no. 12, pp. 1105-1113, Dec. 2002.

[140] J. C. Grunlan, A. R. Mehrabi, M. V. Bannon, and J. L. Bahr, “Water-Based Single-Walled-Nanotube-Filled Polymer Composite with an Exceptionally Low Percolation Threshold,” *Advanced Materials*, vol. 16, no. 2, pp. 150-153, Jan. 2004.

[141] Q. Liu, T. Fujigaya, H.-M. Cheng, and N. Nakashima, “Free-standing highly conductive transparent ultrathin single-walled carbon nanotube films.,” *Journal of the American Chemical Society*, vol. 132, no. 46, pp. 16581-6, Nov. 2010.

[142] J. Kong et al., “Nanotube Molecular Wires as Chemical Sensors,” *Science*, vol. 287, no. 5453, pp. 622-625, Jan. 2000.

[143] O. K. Varghese, P. D. Kichambre, D. Gong, K. G. Ong, E. C. Dickey, and C. A. Grimes, “Gas sensing characteristics of multi-wall carbon nanotubes,” *Sensors and Actuators B: Chemical*, vol. 81, no. 1, pp. 32-41, Dec. 2001.

[144] Y.-T. Jang, S.-I. Moon, J.-H. Ahn, Y.-H. Lee, and B.-K. Ju, “A simple approach in fabricating chemical sensor using laterally grown multi-walled carbon nanotubes,” *Sensors and Actuators B: Chemical*, vol. 99, no. 1, pp. 118-122, Apr. 2004.

[145] M. Arab, F. Berger, F. Picaud, C. Ramseyer, J. Glory, and M. Maynelhermite, “Direct growth of the multi-walled carbon nanotubes as a tool to detect ammonia at room temperature,” *Chemical Physics Letters*, vol. 433, no. 1–3, pp. 175-181, Dec. 2006.

[146] R. Martel, T. Schmidt, H. R. Shea, T. Hertel, and P. Avouris, “Single- and multi-wall carbon nanotube field-effect transistors,” *Applied Physics Letters*, vol. 73, no. 17, p. 2447, Oct. 1998.

[147] C. Girotto, D. Moia, B. P. Rand, and P. Heremans, “High-Performance Organic Solar Cells with Spray-Coated Hole-Transport and Active Layers,” *Advanced Functional Materials*, vol. 21, no. 1, pp. 64-72, Jan. 2011.

[148] J. P. Novak, E. S. Snow, E. J. Houser, D. Park, J. L. Stepnowski, and R. A. McGill, "Nerve agent detection using networks of single-walled carbon nanotubes," *Applied Physics Letters*, vol. 83, no. 19, p. 4026, Nov. 2003.

[149] L. Valentini, C. Cantalini, I. Armentano, J. M. Kenny, L. Lozzi, and S. Santucci, "Investigation of the NO2 sensitivity properties of multiwalled carbon nanotubes prepared by plasma enhanced chemical vapor deposition," *Journal of Vacuum Science & Technology B: Microelectronics and Nanometer Structures*, vol. 21, no. 5, p. 1996, Sep. 2003.

[150] W. Wongwiriyapan et al., "Ultrasensitive Ozone Detection Using Single-Walled Carbon Nanotube Networks," *Japanese Journal of Applied Physics*, vol. 45, no. 4, pp. 3669-3671, Apr. 2006.

[151] M. Penza et al., "Enhancement of sensitivity in gas chemiresistors based on carbon nanotube surface functionalized with noble metal (Au, Pt) nanoclusters," *Applied Physics Letters*, vol. 90, no. 17, p. 173123, Apr. 2007.

[152] T. Zhang et al., "Poly(m-aminobenzene sulfonic acid) functionalized single-walled carbon nanotubes based gas sensor," *Nanotechnology*, vol. 18, no. 16, p. 165504, Apr. 2007.

[153] T. Zhang, M. B. Nix, B.-Y. Yoo, M. A. Deshusses, and N. V. Myung, "Electrochemically Functionalized Single-Walled Carbon Nanotube Gas Sensor," *Electroanalysis*, vol. 18, no. 12, pp. 1153-1158, Jun. 2006.

[154] N. Barsan and U. Weimar, "Understanding the fundamental principles of metal oxide based gas sensors; the example of CO sensing with SnO2 sensors in the presence of humidity," *Journal of Physics: Condensed Matter*, vol. 15, no. 20, p. R813-R839, May 2003.

[155] T. P. Hülser, H. Wiggers, F. E. Kruis, and A. Lorke, "Nanostructured gas sensors and electrical characterization of deposited SnO2 nanoparticles in ambient gas atmosphere," *Sensors and Actuators B: Chemical*, vol. 109, no. 1, pp. 13-18, Aug. 2005.

[156] R. J. Kline, M. D. McGehee, E. N. Kadnikova, J. Liu, and J. M. J. Fréchet, "Controlling the Field-Effect Mobility of Regioregular Polythiophene by Changing the Molecular Weight," *Advanced Materials*, vol. 15, no. 18, pp. 1519-1522, Sep. 2003.

[157] R. J. Kline, M. D. McGehee, E. N. Kadnikova, J. Liu, J. M. J. Fréchet, and M. F. Toney, "Dependence of Regioregular Poly(3-hexylthiophene) Film Morphology and Field-Effect Mobility on Molecular Weight," *Macromolecules*, vol. 38, no. 8, pp. 3312-3319, Apr. 2005.

[158] C. Goh, R. J. Kline, M. D. McGehee, E. N. Kadnikova, and J. M. J. Fréchet, "Molecular-weight-dependent mobilities in regioregular poly(3-hexyl-thiophene) diodes," *Applied Physics Letters*, vol. 86, no. 12, p. 122110, Mar. 2005.

[159] H.-Z. Geng, K. K. Kim, and Y. H. Lee, “Recent progress in carbon nanotube-based flexible transparent conducting film,” in *Proceedings of SPIE*, 2008, vol. 7037, no. 1, p. 70370A-70370A-14.

[160] C. N. Hoth, S. A. Choulis, P. Schilinsky, and C. J. Brabec, “High Photovoltaic Performance of Inkjet Printed Polymer:Fullerene Blends,” *Advanced Materials*, vol. 19, no. 22, pp. 3973-3978, Nov. 2007.

[161] C. N. Hoth, P. Schilinsky, S. A. Choulis, and C. J. Brabec, “Printing highly efficient organic solar cells.,” *Nano letters*, vol. 8, no. 9, pp. 2806-13, Sep. 2008.

[162] S. H. Eom et al., “High efficiency polymer solar cells via sequential inkjet-printing of PEDOT:PSS and P3HT:PCBM inks with additives,” *Organic Electronics*, vol. 11, no. 9, pp. 1516-1522, 2010.

[163] O. P. Dimitriev, D. A. Grinko, Y. V. Noskov, N. A. Ogurtsov, and A. A. Pud, “PEDOT:PSS films—Effect of organic solvent additives and annealing on the film conductivity,” *Synthetic Metals*, vol. 159, no. 21–22, pp. 2237-2239, 2009.

[164] J. Kim, F. Cacialli, and R. Friend, “Surface conditioning of indium-tin oxide anodes for organic light-emitting diodes,” *Thin Solid Films*, vol. 445, no. 2, pp. 358-366, 2003.

[165] T. P. Burgin, J. C. Lewenstein, and D. Werho, “Investigations into the mechanism of adsorption of carbon nanotubes onto aminopropylsiloxane functionalized surfaces.,” *Langmuir : the ACS journal of surfaces and colloids*, vol. 21, no. 14, pp. 6596-602, Jul. 2005.

[166] K. N. Han, C. A. Li, M.-P. Ngoc Bui, and G. H. Seong, “Patterning of Single-Walled Carbon Nanotube Films on Flexible, Transparent Plastic Substrates,” *Langmuir*, vol. 26, no. 1, pp. 598-602, Jan. 2010.

[167] E. Hye Lee, J. H. Ryu, J. Jang, and K. C. Park, “Patterned Single-Wall Carbon Nanotube Transparent Conducting Films for Liquid Crystal Switching Electrodes,” *Japanese Journal of Applied Physics*, vol. 50, no. 3, p. 03CA04, Mar. 2011.

[168] S.-I. Na, S.-S. Kim, J. Jo, S.-H. Oh, J. Kim, and D.-Y. Kim, “Efficient Polymer Solar Cells with Surface Relief Gratings Fabricated by Simple Soft Lithography,” *Advanced Functional Materials*, vol. 18, no. 24, pp. 3956-3963, 2008.

[169] J. Frischeisen et al., “Light extraction from surface plasmons and waveguide modes in an organic light-emitting layer by nanoimprinted gratings,” *Optics Express*, vol. 19, no. S1, p. A7, Nov. 2010.

[170] D. Mascaro, M. Thompson, H. Smith, and V. Bulovic, “Forming oriented organic crystals from amorphous thin films on patterned substrates via solvent-vapor annealing,” *Organic Electronics*, vol. 6, no. 5–6, pp. 211-220, 2005.

[171] K. C. Dickey, J. E. Anthony, and Y.-L. Loo, "Improving Organic Thin-Film Transistor Performance through Solvent-Vapor Annealing of Solution-Processable Triethylsilylethynyl Anthradithiophene," *Advanced Materials*, vol. 18, no. 13, pp. 1721-1726, Jul. 2006.

[172] U. Dettlaff-Weglikowska et al., "Effect of SOCl2 treatment on electrical and mechanical properties of single-wall carbon nanotube networks.," *Journal of the American Chemical Society*, vol. 127, no. 14, pp. 5125-31, Apr. 2005.

[173] H.-Z. Geng, K. K. Kim, K. P. So, Y. S. Lee, Y. Chang, and Y. H. Lee, "Effect of acid treatment on carbon nanotube-based flexible transparent conducting films.," *Journal of the American Chemical Society*, vol. 129, no. 25, pp. 7758-9, Jun. 2007.

[174] R. Jackson, B. Domercq, R. Jain, B. Kippelen, and S. Graham, "Stability of Doped Transparent Carbon Nanotube Electrodes," *Advanced Functional Materials*, vol. 18, no. 17, pp. 2548-2554, Sep. 2008.

[175] T. M. Barnes, J. L. Blackburn, J. van De Lagemaat, T. J. Coutts, and M. J. Heben, "Reversibility, dopant desorption, and tunneling in the temperature-dependent conductivity of type-separated, conductive carbon nanotube networks.," *ACS nano*, vol. 2, no. 9, pp. 1968-76, Sep. 2008.

Publications

Conference Proceedings

[1] M. Bösing, A. Abdellah, C. Zimmermann, Florian Lindla, F. Jessen, P. van Gemmern, D. Bertram, N. Meyer, D. Keiper, M. Heuken, H. Kalisch, K. Meerholz, and R. H. Jansen, "Influence of Substrate Temperature on Multilayer Thin Film Growth, Charge Carrier Injection and Efficiency of OVPD-processed Organic Light Emitting Diodes," *Mater. Res. Soc. Symp. Proc.*, vol. 1115, 2009.

[2] C. Zimmermann, M. Bösing, F. Lindla, A. Abdellah, F. Jessen, P. van Gemmern, H.-P. Löbl, M. Heuken, H. Kalisch, and R. H. Jansen, "Measurement and Modeling of Hole Transport in Blends of N, N'-diphenyl-N, N'-bis (1-naphthyl)-1, 1'-biphenyl-4, 4'-diamine (NPB) and the Hole-Conducting Material HIM," *Mater. Res. Soc. Symp. Proc.*, vol. 1115, 2009.

[3] O. Wiedenmann, A. Abdellah, G. Scarpa, and P. Lugli, "Design and fabrication of organic solar cells structured via nanoimprint lithography," *Journal of Physics: Conference Series*, vol. 193, no. 1, p. 012115, Nov. 2009.

[4] A. Abdellah, D. Baierl, B. Fabel, P. Lugli, and G. Scarpa, "Exploring spray technology for the fabrication of organic devices based on poly(3-hexylthiophene)," *Nanotechnology (IEEE-NANO), 2009 9th IEEE Conference on*, pp. 831-934, 2009.

[5] P. Lugli, A. Abdellah, E. Albert, G. Csaba, C. Erlen, B. Fabel, Q. Gong, G. Scarpa, M.B. Chan-Park, and P.R. Divina, "Circuit and system implementations of molecular devices," *Integrated Circuits, ISIC'09. Proceedings of the 2009 12th International Symposium on*, pp. 125-128, 2009.

[6] Y. Wang, D.W. Zhao, X.W. Sun, G. Scarpa, A. Abdellah, A. Exner, O. Wiedenmann, and P. Lugli, "Towards the optimization of organic solar cells via controlled morphologies," *Integrated Circuits, ISIC'09. Proceedings of the 2009 12th International Symposium on*, pp. 147-150, 2009.

[7] G. Scarpa, S. Harrer, A. Abdellah, G.P. Blanco, P. Lugli, S. Strobel, G. Abstreiter, and M. Tornow, "Pattern generation by using high-resolution nanoimprinting and nanotransfer printing techniques," *Nanotechnology (IEEE-NANO), 2009 9th IEEE Conference on*, pp. 432-438, 2009.

[8] A. Abdellah, A. Yaqub, C. Ferrari, B. Fabel, P. Lugli, and G. Scarpa, "Spray deposition of highly uniform CNT films and their application in gas sensing," *Nanotechnology (IEEE-NANO), 2011 11th IEEE Conference on*, pp. 1118-1123, 2011.

[9] Q. Gong, E. Albert, B. Fabel, A. Abdellah, P. Lugli, M. Chan-Park, and G. Scarpa, "Solution-processable random carbon nanotube networks for thin-film transistors," *Nanotechnology (IEEE-NANO), 2011 11th IEEE Conference on*, pp. 378-381, 2011.

Peer Reviewed Journals

[1] A. Abdellah, B. Fabel, P. Lugli, and G. Scarpa, "Spray deposition of organic semiconducting thin-films: Towards the fabrication of arbitrary shaped organic electronic devices," *Organic Electronics*, vol. 11, no. 6, pp. 1031–1038, Jun. 2010.

[2] J. Frischeisen, Q. Niu, A. Abdellah, J.B. Kinzel, R. Gehlhaar, G. Scarpa, C. Adachi, P. Lugli, and W. Brütting, "Light extraction from surface plasmons and waveguide modes in an organic light-emitting layer by nanoimprinted gratings," *Optics Express*, vol. 19, no. 1, p. A7, Nov. 2010.

[3] W. Wiedemann, L. Sims, A. Abdellah, A. Exner, R. Meier, K. P. Musselman, J. L. MacManus-Driscoll, P. Müller-Buschbaum, G. Scarpa, P. Lugli, and L. Schmidt-Mende, "Nanostructured interfaces in polymer solar cells," *Applied Physics Letters*, vol. 96, no. 26, p. 263109, 2010.

[4] G. Scarpa, A. Abdellah, A. Exner, S. Harrer, G:P. Blanco, W. Wiedemann, L. Schmidt-Mende, and P. Lugli, "Patterning Poly(3-Hexylthiophene) in the Sub-50-nm Region by Nanoimprint Lithography," *IEEE Transactions on Nanotechnology*, vol. 10, no. 3, pp. 482-488, May 2011.

Acknowledgments

I would like to start by thanking my principle advisor, Prof. Paolo Lugli, for giving me the great opportunity of working with him on this highly exciting and interdisciplinary topic. His continuous interest and academic support contributed to the success of the work presented in this dissertation. Further I want to thank my mentor, Dr.-Ing. Giuseppe Scarpa, for his continuous efforts to provide me all necessary means for successful completion of my work as well as his dedicated guidance.

Moreover, I would like to thank all colleagues who helped me during years of work at the Institute for Nanoelectronics. Special thanks to Rosmarie Heilmann, for her continuous support and efforts in providing an ordered and productive laboratory environment. My special gratitude goes to my friends and colleagues, Anandi Yadav, Muhammad Atyab Imtaar, Simone Locci, Sherif Ahmed, and Sherif Zaidan, who were always a source of motivation and inspiration.

Finally, I am honored to have supervised many students throughout their B.Sc./M.Sc. theses. I am especially thankful to those among them who contributed and added value to my work, Armin Exner, Arhan Yaqub, Ahmed Abdelhalim, Markus Horn, and Ulrich Schwarzenberger.